An analysis of synchrotron radiation from relativistic electrons in the Alcator C-Mod tokamak

by

Roy Alexander Tinguely
BS, Iowa State University, 2014

SUBMITTED TO THE DEPARTMENT OF PHYSICS IN PARTIAL FULFILLMENT OF THE REQUIREMENTS FOR THE DEGREE OF

DOCTOR OF PHILOSOPHY IN PHYSICS
AT THE
MASSACHUSETTS INSTITUTE OF TECHNOLOGY

JUNE 2019

Signature of Author: _____
Department of Physics
17 May 2019

Certified by: _____
Robert S Granetz
Principal Research Scientist, Plasma Science and Fusion Center
Thesis Supervisor

Certified by: _____
Earl S Marmar
Senior Research Scientist, Department of Physics
Thesis Supervisor

Accepted by: _____
Nergis Mavalvala
Professor of Physics
Associate Department Head

An analysis of synchrotron radiation from relativistic electrons in the Alcator C-Mod tokamak

by

Roy Alexander Tinguely

Submitted to the Department of Physics
on 17 May 2019
in Partial Fulfillment of the Requirements
for the Degree of Doctor of Philosophy in Physics

ABSTRACT

In the Alcator C-Mod tokamak, a magnetic confinement fusion experiment, electrons are accelerated to relativistic energies—on the order of tens of MeV—during steady-state conditions of Ohmic, elongated, and diverted plasma discharges. These so-called "runaway" electrons emit synchrotron radiation in their direction of motion due to their gyration in the background toroidal magnetic field, with values of B_0 ranging from 2.7 to 7.8 T at the plasma axis. Two spectrometers, a wide-view camera, and a polarimeter are used to measure time-evolving spectra, images, and polarization information, respectively, of the synchrotron radiation in the visible/near-infrared wavelength range, $\lambda \approx$ 300-1000 nm. The kinetic equation solver CODE [Landreman *et al* 2014 *Comput. Phys. Commun.*, Stahl *et al* 2016 *Nucl. Fusion*] and synthetic diagnostic SOFT [Hoppe *et al* 2018 *Nucl. Fusion*] are used to model the evolution of the runaway electron phase space distribution and to simulate the detected synchrotron emission, respectively. The major contributions of this thesis work to the fields of plasma physics and fusion energy research are the following: Spectral measurements are consistent with runaway electrons' attaining lower energies as the magnetic field increases, a positive sign for future high-field fusion devices. The runaway electron density profile and other spatiotemporal dynamics, such as increased radial transport due to magnetohydrodynamic activity, are inferred from the two-dimensional synchrotron intensity distributions captured in camera images. Finally, for the first time in a tokamak plasma experiment, polarized synchrotron light is used as a novel diagnostic of the pitch angle distribution of runaway electrons. For all three measurements, discrepancies between experiment and theory/simulation are identified, and opportunities for future work are presented.

Thesis Supervisor: Robert S Granetz
Title: Principal Research Scientist, Plasma Science and Fusion Center, MIT

Thesis Supervisor: Earl S Marmar
Title: Senior Research Scientist, Department of Physics

This page intentionally left blank

Acknowledgements

This thesis is dedicated to all who supported me along this journey. I am incredibly grateful to

- my thesis supervisors, Dr. Robert Granetz and Dr. Earl Marmar;
- my thesis readers, Prof. Miklos Porkolab and Prof. John Belcher;
- my funders, the MIT Energy Initiative and US Dept of Energy (Grant DE-FC02-99ER54512);
- the Plasma Theory group at Chalmers University, especially Mathias Hoppe, Ola Embréus, Adam Stahl, Linnea Hesslow, and Prof. Tünde Fülöp;
- the MIT Disruptions group, Kevin Montes, Cristina Rea, Ryan Sweeney, and Jinxiang Zhu;
- my officemate, Adam Kuang, and classmate, Alex Creely;
- the Plasma Physics graduate students, especially Harry Han, Neel Kabadi, Bryan Linehan, Julian Picard, Aaron Rosenthal, Francesco Sciortino, Graeme Sutcliffe, and Libby Tolman;
- my fellow PSFC graduate students, including Sean Ballinger, Norman Cao, Sam Frank, Leigh Ann Kesler, Brandon Lahmann, Pablo Rodriguez-Fernandez, Will McCarthy, Lucio Milanese, Juan Ruiz Ruiz, Alex Sandberg, Raspberry Simpson, Hong Sio, and Muni Zhou;
- previous PSFC graduate students, particularly Evan Davis, Ian Faust, and Chuteng Zhou;
- my PSFC mentors, including Dan Brunner, Eric Edlund, Ted Golfinopolous, Martin Greenwald, Nathan Howard, Amanda Hubbard, Jerry Hughes, Brian LaBombard, Bob Mumgaard, John Rice, Steve Scott, Brandon Sorbom, Jim Terry, Greg Wallace, and Kevin Woller;
- my professors, including Peter Fisher, Jeff Freidberg, Zach Hartwig, Ian Hutchinson, Nuno Loureiro, Anne White, Dennis Whyte, and Bolek Wyslouch;
- the entire Alcator C-Mod team, especially Jim Irby, Rick Murray, Sam Pierson, Ron Rosati, Maria Silveira, Tom Toland, Rui Vieira, and Steve Wolfe;
- the whole Plasma Science and Fusion Center community, especially Anastasia Alexandridis, Lee Berkowitz, Valerie Censabella, Jessica Coco, Matt Fulton, Mark London, Paul Rivenberg, Brandon Savage, Josh Stillerman, Ilavenil Subbiah, Rick Temkin, and Jason Thomas;
- the MIT Physics Department faculty and staff, especially Cathy Modica;
- the students, houseteam, and staff of Simmons Hall, especially John and Ellen, Josh, Nika, Bruno, Elizabeth, Jude, Karisha, Kristen, Michelle, Orlando, and Tina;
- my fellow Graduate Resident Tutors, particularly John Arroyo, Parrish Bergquist, Elise Harrington, James Hawrot, Derek Kita, Takeo Kuwabara, Tedrick Lew, Ruaridh Macdonald, Jere Mladinov, Ashin Modak, Alison Olechowski, Beatrice Soh, and Amanda Vernon;
- the MIT Chamber Chorus and Concert Choir and their director, Dr. Bill Cutter;
- the MIT Graduate Student Council Sustainability Subcommittee and Ruth Davis;
- my siblings, Ashley, Emily, Kristen, Ben, and Ben Bretey;
- my parents, Roy and Debbie, and godparents, Stephen and Mae Tinguely;
- my grandparents, Jerome and JoAnn Sayler and Don Tinguely;
- my friends, including Sameer Abraham, Andrew Birkel, Cheko Cantu, Ani Chiti, Cody Dennett, Ryan Floit, Nick Goodwill, Joshua Hughes, Hao Kang, Hongwan Liu, Owen Morris, Alan (AJ) Mui, Sid Narayanan, Corey O'Bannon, Max Opgenoord, German Parada, Tom Rippenkroeger, Garrett Smith, Jayson Vavrek, Zak Vendeiro, Wonbo Woo, and Liang Yu;
- my best friends, Kelsey Moore and Andrew Turner.

Thank you. – Alex

This page intentionally left blank

Contents

Chapter 1

Introduction

1.1 A need for clean, carbon-free energy

In 2018, the United States' Fourth National Climate Assessment (NCA) [1] reported that without a dedicated effort to curb greenhouse gas emissions, the global average temperature could rise over 5°C by the year 2100. This would be accompanied by a rising sea level, estimated to be at least 30 cm higher than the current global mean by the end of the century [2]. The ramifications of these, among other related climate changes, threaten the health of the environment, economy, and humans. Both the NCA and preceding Climate Science Special Report (CSSR) [2] are clear that it is *"extremely likely"* that human activities are the dominant cause of the increased climate change documented over the last ∼100 years. In fact, 85% of current US carbon emissions come from the burning of fossil fuels. In 2017, the CSSR noted that recent emission rates had slowed, but unfortunately not enough so as to keep the projected global temperature rise below 2°C. To remain below this limit, carbon dioxide emissions must be substantially reduced by 2040 and become net-zero or even net-negative later in the century.

The outlook for humanity is no doubt bleak, that is unless a radical change is made. One path forward is of course the pursuit of clean, carbon-free energy sources. Wind and solar have garnered the most attention as of late; however, windless and sunless days mean that, without adequate battery/energy storage technology, these two energy sources cannot always serve everyday power needs. What is needed is a baseload and load-following energy source which can provide constant baseline power and increase/decrease output as electricity usage demands. *Fusion* energy could be the solution *if* it can be made efficiently and economically.

Making fusion energy a reality has been a global effort for the past ∼70 years. Yet no experimental device[a] has achieved net energy, i.e. more (fusion) power out than (external) power

[a] Not including the hydrogen bomb....

in. Only recently, the US National Academy of Sciences (NAS) commissioned a report on a "Strategic Plan for US Burning Plasma Research." In their 2018 final report [3], the NAS committee recommended that the US set its sights on building a compact[b], net-electric fusion power plant at low capital cost. This would be a stepping stone toward commercial fusion reactors, which could one day produce hundreds of megawatts (MW, i.e. millions of Watts) of power with zero carbon emissions and only short-lived radioactive byproducts. For reference, the US Energy Information Administration reported that the entire state of Massachusetts averaged ∼1500 MW of electric power from burning natural gas (a fossil fuel) in November 2018 [4]. If fusion and other renewable energy sources can replace coal, oil, and gas within the next few decades, some of climate change's worst catastrophes could be avoided.

1.2 Fusion: the star-making business

1.2.1 Nuclear fusion reactants and products

Nuclear fusion is the process by which two atomic nuclei combine—or *fuse*—to form a heavier nucleus of a new element. Usually, the products of fusion are thousands of times more energetic than the initial reactants. This energy comes from the newly-formed nucleus occupying a lower energy state—i.e. having a higher binding energy—and is realized as conversion of mass to energy via Einstein's famous relation $\mathcal{E} = \Delta m c^2$, where $\mathcal{E}$ is the energy, Δm is the total change in *rest* mass, and c is the speed of light.

Consider the fusion of two hydrogrenic isotopes—a deuterium nucleus ${}^{2}_{1}\mathrm{D}$, comprising one proton and one neutron, with a tritium nucleus ${}^{3}_{1}\mathrm{T}$, containing one proton and two neutrons—to produce a helium nucleus (or alpha particle) ${}^{4}_{2}\mathrm{He}$, with two protons and two neutrons, along with a neutron. From the masses of these particles given in table 1.1, the total energy released in this reaction is calculated to be ∼2.8 × 10^{-12} J or ∼17.6 MeV. This is less than one-tenth of the energy produced in a typical nuclear *fission* reaction (which splits large nuclei); however, the energy per particle (or per mass) is almost five times *greater*, making nuclear fusion a more mass-efficient energy source.

From conservation of momentum, the energy is shared in the DT fusion reaction: one-fifth to the alpha particle and four-fifths to the neutron,

$$ {}^{2}_{1}\mathrm{D} \; + \; {}^{3}_{1}\mathrm{T} \; \longrightarrow \; {}^{4}_{2}\mathrm{He}\,(3.5\ \mathrm{MeV}) \; + \; {}^{1}_{0}\mathrm{n}\,(14.1\ \mathrm{MeV}). $$

These high energy neutrons can be used to heat water, producing steam, spinning turbines, and

[b] At least smaller than the current international fusion project ITER.

Table 1.1: Masses of common fusion reactants and products. (1 amu $\approx 1.6605 \times 10^{-27}$ kg)

Particle	Mass (amu)
$^{1}_{1}\mathrm{H}$	1.0073
$^{1}_{0}\mathrm{n}$	1.0087
$^{2}_{1}\mathrm{D}$	2.0141
$^{3}_{1}\mathrm{T}$	3.0160
$^{4}_{2}\mathrm{He}$	4.0026

generating electricity. This is the leading idea for extracting the energy from fusion.

Fusion powers the stars, including our sun. In fact, the light that reaches our eyes and heat we feel on our skin both originated as fusion energy. While we "see" fusion every day, it is actually rather difficult to fuse any material. Nuclei are positively charged due to their proton constituents. Thus, as two nuclei are forced closer together (in an attempt to fuse), they also increasingly repel each other via the Coulomb force; that is, until the nuclei get so close (on the order of 1 fm $= 10^{-15}$ m) that the attractive *strong* force overcomes Coulomb repulsion and holds the fused nucleus together. The reactants must necessarily have significant kinetic energies (on the order of 1-100 keV = 10 million-1 billion K) to surpass this Coulomb energy barrier.[c]

However, high energies are not sufficient to fuse nuclei as two almost-head-on reactants can easily glance past each other. Therefore, a sufficiently large number of particles must be contained within a volume to increase the probability of their interaction and fusion. Moreover, to continually produce fusion energy, the fusion reaction *rate* must be greater than the rate at which energy is lost to the surrounding environment. This is quantified through the Lawson criterion which identifies a minimum "triple product" [5]

$$n\,T\,\tau_{\mathcal{E}} \geq 8 \text{ atm} \cdot \text{s} \tag{1.1}$$

of the reactant temperature T and density n, as well as the energy confinement time $\tau_{\mathcal{E}}$.

1.2.2 An introduction to plasmas

Fusion combines two *nuclei* and not two *atoms*. Recall that the binding energy of the single electron in the hydrogen atom is at most 13.6 eV. Thus, for temperatures[d] higher than that, the electron can easily escape the Coulomb attraction of the hydrogen nucleus. In fact, the

[c] Actually, the nuclei will quantum-mechanically "tunnel" through the Coulomb potential barrier.

[d] Throughout this thesis, the units of temperature are energy; i.e. $T \to k_B T$ where $k_B = 1.381 \times 10^{-23}$ J/K is the Boltzmann constant.

calculation of (1.1) actually assumes a temperature on the order of 10 keV. At this temperature, all materials become a soup of positively and negatively charged particles, an ionized "gas" called a *plasma*. This is the fourth state of matter and the most common form of it in the universe—besides dark matter. Stars, interstellar media, lightning, flames, and fluorescent light bulbs are all examples of plasmas. One of the most interesting properties of plasmas is that the interactions between particles are dominated by long-range electromagnetic forces resulting in small-angle collisions; this is very different from the standard picture of hard-sphere ("billiard-ball") collisions of a neutral gas.

In general, there are three criteria (italicized below) which qualify a substance as a plasma. These are based on three basic parameters described here:

1. The Debye length: Subject to an externally-applied, static electric field, the charged particles in a plasma will rearrange themselves so as to "shield out" the applied field. Because the electrons have much lighter masses compared to the ions (nuclei), they move most readily to cancel out the electric field's effects. The distance over which the electric field amplitude decays from the source location is called the *Debye length* and is computed as

$$\lambda_{\mathrm{De}} = \left(\frac{\epsilon_0 T_{\mathrm{e}}}{e^2 n_{\mathrm{e}}} \right)^{1/2}, \tag{1.2}$$

   where n_{e} and T_{e} are the electron density and temperature, respectively, $e = 1.6 \times 10^{-19}$ C is the electric charge, and $\epsilon_0 = 8.85 \times 10^{-12}$ F/m is the permittivity of free space. A typical value for a fusion plasma with $n_{\mathrm{e}} = 10^{20}$ m^{-3} and $T_{\mathrm{e}} = 10$ keV is $\lambda_{\mathrm{De}} \approx 75$ μm. *The first criterion for a plasma requires that its size a must be much larger than the Debye length, i.e. $a \gg \lambda_{\mathrm{De}}$.*
2. The plasma frequency: Subject to an externally-applied, *dynamic* electric field (like an electromagnetic wave), charged particles in a plasma—electrons, in particular—will oscillate in an attempt to "screen out" the electromagnetic perturbations. However, the inertia of the electrons (and ions) does not allow them to respond instantaneously; instead, they have a characteristic frequency called the *plasma frequency*,

$$\omega_{\mathrm{pe}} = \left(\frac{n_{\mathrm{e}} e^2}{m_{\mathrm{e}} \epsilon_0} \right)^{1/2}. \tag{1.3}$$

   Here, $m_{\mathrm{e}} = 9.11 \times 10^{-31}$ kg is the mass of the electron. Thus, a dynamic field with timescale $\tau > 2\pi/\omega_{\mathrm{pe}}$ is effectively screened by a plasma with density n_{e}.[e] A typical value

[e] In general, a plasma can support electromagnetic waves with many different frequencies, including $\omega < \omega_{\mathrm{pe}}$; however, the details are not discussed here.

for a fusion plasma, with $n_\mathrm{e} = 10^{20}$ m^{-3}, is $f_\mathrm{pe} = \omega_\mathrm{pe}/2\pi \approx 90$ GHz. *The second criterion for a plasma is then that its typical evolution timescale(s) must be much longer than the plasma response time.* This is typically quantified by the transit time of a thermal electron across the plasma; i.e. $a/v_{T\mathrm{e}} \gg 1/\omega_\mathrm{pe}$, where $v_{T\mathrm{e}} = \sqrt{T_\mathrm{e}/m_\mathrm{e}}$.

3. The plasma parameter: The behavior of particles in a plasma is governed primarily by collective effects; in other words, the dynamics of one particle is affected by many neighboring particles instead of binary particle-particle interactions. To quantify this, we require that the mean distance between particles must be much larger than the distance at which their Coulomb potential energies become similar to their kinetic energies. In the end, it is enough to calculate the so-called *plamsa parameter*

$$\Lambda_D = \frac{4\pi}{3} n_\mathrm{e} \lambda_\mathrm{De}^3 \propto \frac{T_\mathrm{e}^{3/2}}{n_\mathrm{e}^{1/2}}, \tag{1.4}$$

which is simply the number of electrons (or ions, by quasi-neutrality) within a sphere of radius λ_De. A typical value for a fusion plasma with $n_\mathrm{e} = 10^{20}$ m^{-3} and $T_\mathrm{e} = 10$ keV is $\Lambda_D \approx 10^8$. *The third criterion for a plasma is that* $\Lambda_D \gg 1$. This may seem slightly counter-intuitive, but note that the dependencies indicate that Λ_D increases with increasing T_e and decreasing n_e.

1.3 Tokamak plasmas: stellar donuts

1.3.1 An introduction to tokamaks

The sun confines its plasma with its own gravity, creating the hot, dense conditions required to satisfy (1.1) and produce net fusion energy. However, since about 1 million Earths could fit inside the sun, gravity cannot be used to keep a plasma in place on Earth. Instead, we can leverage the electromagnetic properties of a plasma, shaping it with magnets. Perhaps the most promising approach to fusion plasma confinement is the donut-shaped "magnetic bottle" called the *tokamak*. See figure 1.1 for a schematic.

The toroidal field (TF) coils are electromagnets producing a magnetic field B_t in the toroidal direction—the long way around the torus—with characteristic radial dependence

$$B_\mathrm{t}(R) = \frac{B_0 R_0}{R}, \tag{1.5}$$

where B_0 is the magnetic field at the major radius R_0, which extends to the center of the plasma. Because charged particles orbit along magnetic field lines, a toroidal magnetic field

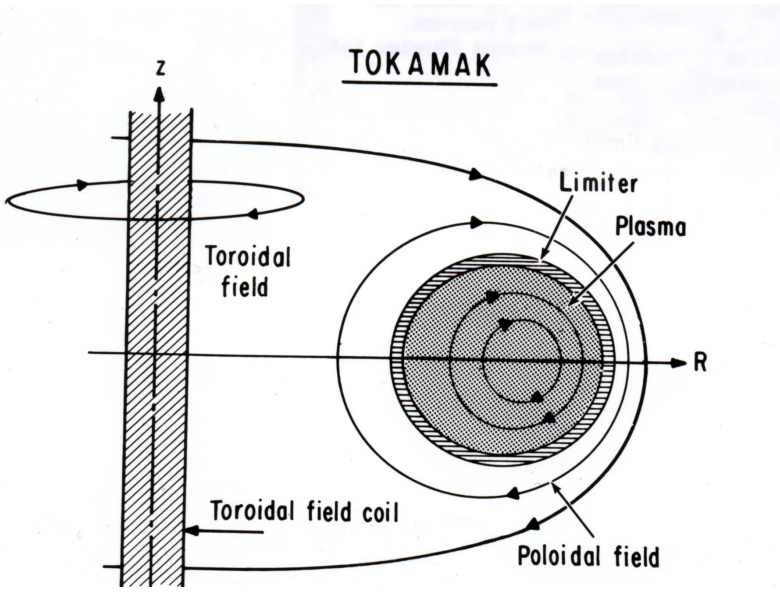

Figure 1.1: A diagram showing a poloidal (vertical) cross-section of an axisymmetric tokamak geometry. The toroidal magnetic field is produced by external coils; the poloidal magnetic field is created by a toroidal plasma current (into the page). The plasma is "confined" by a limiter. From [6].

should keep plasma particles spiraling (gyro-orbiting) within the torus forever. However, both the radial dependence of the magnetic field and the outward centrifugal force from circular motion cause charged particles to drift vertically in a purely toroidal B-field. These drift velocities are appropriately called the *grad-B* drift

$$\boldsymbol{v}_{\nabla B} = \frac{v_\perp^2}{2\omega_B} \frac{\boldsymbol{B} \times \nabla B}{B^2}, \tag{1.6}$$

due to the field gradient, and the *curvature* drift

$$\boldsymbol{v}_\kappa = \frac{v_\parallel^2}{\omega_B} \frac{\boldsymbol{R}_c \times \boldsymbol{B}}{R_c^2 B^2}. \tag{1.7}$$

Here, $v_\parallel$ and $v_\perp$ are the components of the particle velocity $\boldsymbol{v}$ parallel and perpendicular to the magnetic field $\boldsymbol{B}$, R_c is the radius of curvature of the *guiding center* motion (not gyro-motion), and $\omega_B = qB/\gamma m$ is the (relativistic) gyro-frequency of a signed charge q. From (1.6) and (1.7), it is seen that positive and negative charges will separate vertically in a purely-toroidal field $\boldsymbol{B}$. Then the resulting vertical electric field from charge separation would cause a radial $E \times B$ drift

out of the plasma,

$$\boldsymbol{v}_{E\times B} = \frac{\boldsymbol{E}\times\boldsymbol{B}}{B^2}. \tag{1.8}$$

To resolve this, an additional *poloidal* magnetic field B_p can be used to "twist" magnetic field lines such that particle trajectories sample both the high-field ($R < R_0$) and low-field ($R > R_0$) sides of the tokamak. This effectively averages out the vertical particle drifts, adequately confining the plasma.[f] In a tokamak, B_p is created by the plasma itself through its toroidal plasma current I_p, which is typically driven by an externally-applied toroidal loop voltage V_loop induced by varying the magnetic flux of a central solenoid. Plasma currents on the order of mega-amperes (MA, i.e. millions of amps) lead to stored magnetic energies of 100 kJ-100 MJ, tremendous amounts of free energy which must be carefully sustained and contained.

1.3.2 The Alcator C-Mod tokamak

The Alcator C-Mod tokamak was operated from 1992-2016 at the Massachusetts Institute of Technology. Machine and plasma parameters for C-Mod are given in table 1.2. A CAD model and an inside look are shown in figures 1.2 and 1.3, respectively. This compact device operated with one of the highest toroidal magnetic fields in the world, ranging from $B_0 =$ 2-8 T, allowing it to achieve a world-record plasma pressure of 2 atm averaged over the plasma volume. Usually, the B-field on-axis was 5.4 T, slightly higher than the 5.3 T design [8] of ITER, the world's largest tokamak currently under construction in France. C-Mod's usual plasma density, on the order of 10^{20} m^{-3}, is also comparable to ITER's planned density. Two major differences between C-Mod and ITER are the sizes and plasma current: ITER has a major radius of 6 m ($\sim$10$\times$ larger than C-Mod's) and a target plasma current of 15 MA (while C-Mod's was usually $I_\mathrm{p} \approx$ 1-2 MA). Additional machine parameters for ITER, as well as MIT's newest initiative SPARC [9] and the conceptual power plant ARC [10, 11], are provided in table 1.2.

[f] Actually, a vertical magnetic field is also required to achieve radial force balance.

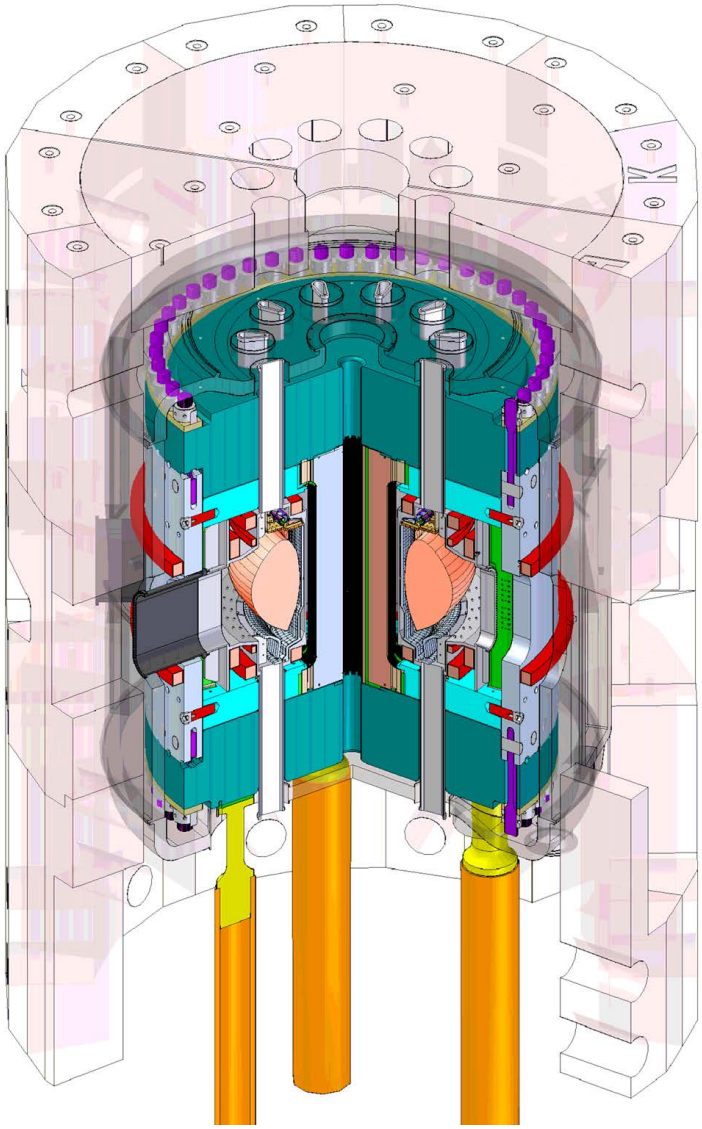

Figure 1.2: An engineering CAD-model of the Alcator C-Mod tokamak. From the center outward: The central solenoid (brown) drives the toroidal plasma current. The plasma (pink) is contained inside the vacuum vessel (grey). The toroidal (cyan) and poloidal/vertical (red) magnetic field coils confine and shape the plasma. The surrounding super-structure (light grey and green) is held together by bolts (purple). The tokamak is surrounded by a cryostat (clear), shielded by a concrete igloo (clear), and supported by three posts (orange). From [7].

Table 1.2: Comparing machine and plasma parameters of Alcator C-Mod with several other tokamaks: ITER, SPARC, and ARC.

Parameter	Symbol	C-Mod	ITER [8, 12]	SPARC [9]	ARC [10, 11]
Major radius (m)	R_0	0.68	6.2	1.65	3.3
Minor radius (m)	a	0.22	2.0	0.5	1.13
Toroidal B-field (T)	B_0	2-8	5.3	12	9.2
Plasma current (MA)	I_p	1-2	15	7.5	7.8
Elongation	κ	0.9-1.8	1.7-1.85	1.8	1.84
Density (10^{20} m^{-3})	n	0.5-2	1	3-6.5	1.3-1.8
Temperature (keV)	T	0.5-8	$\sim$10	15-25	14-27
Edge safety factor	q_{95}	3-5	3	3.05	4.7-7.2
Heating power (MW)	P_ext	10	73	30	38.6
Fusion power (MW)	P_fus	$<$0.001	500	50-100	525
Discharge duration (s)	Δt	2	400	20	∞

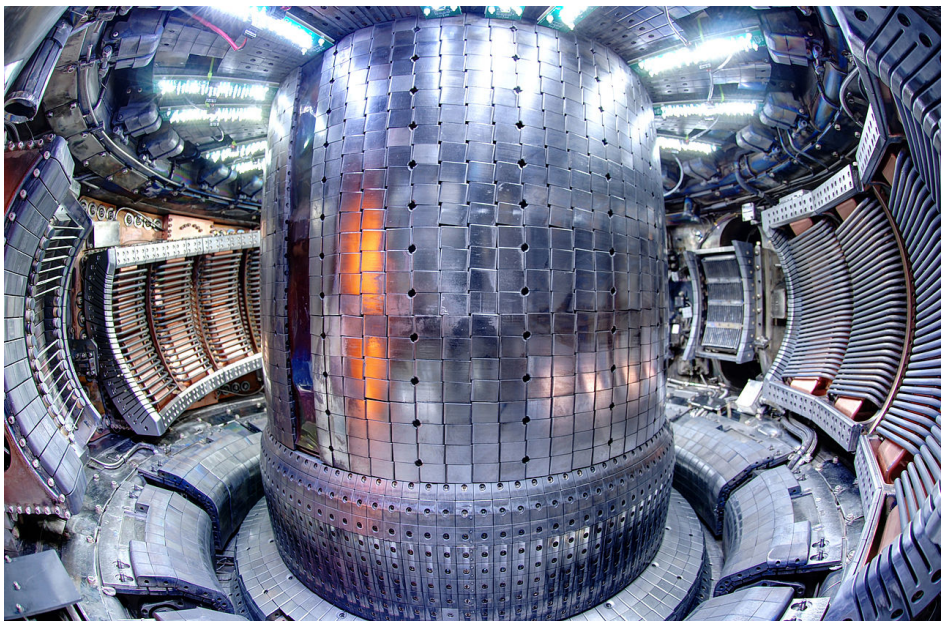

Figure 1.3: A fish-eye view inside the Alcator C-Mod tokamak, taken from F-port. The inner wall (center) is covered with high-Z molybdenum tiles. Radio frequency antennas (copper covered by steel "bars") are on the left and right. The lower hybrid waveguide "grill" is seen to the left of the right antenna. Note that this is approximately the location of the wide-view WIDE2 camera used for the synchrotron radiation studies in this thesis. From [13].

1.4 Disruptive (and eruptive) phenomena

1.4.1 Macroscopic stability

The macroscopic evolution of a plasma is governed by its fluid description, called *magnetohydrodynamics* (MHD). In steady state, ideal MHD gives force balance in the form

$$\nabla \mathrm{P} = \boldsymbol{J} \times \boldsymbol{B} \tag{1.9}$$

where $\mathrm{P} = nT$ is the plasma pressure and $\boldsymbol{J}$ is the current density. In the tokamak configuration, this implies that a hot, dense plasma is confined by the interaction of its own current with the magnetic fields both produced internally and applied externally. By taking the dot product of (1.9) with $\boldsymbol{J}$ and $\boldsymbol{B}$, we see that both $\boldsymbol{J}$ and $\boldsymbol{B}$ lie in surfaces of constant pressure. These so-called *flux surfaces* can be identified by a value called the *safety factor*

$$q(r) = \frac{B_\mathrm{t}}{R_0}\frac{r}{B_\mathrm{p}}, \tag{1.10}$$

which indicates the number of toroidal transits a magnetic field line makes before completing one poloidal revolution. Here, r is the *minor* radius measured from R_0. A typical C-Mod plasma magnetic configuration, from an EFIT [14] reconstruction, is shown in figure 1.4 with several flux surfaces labeled. Note in the figure that all magnetic field lines outside of the last closed flux surface (LCFS) impact the tokamak first wall; therefore the plasma only really "exists" within the LCFS. Moreover, the plasma shown is *diverted* such that there is a poloidal magnetic null at the bottom of the machine; this is used to conduct heat and particles to the lower *divertor*, which is essentially a plasma exhaust system.

There are many ways in which a plasma configuration can become unstable. For instance, an MHD instability can occur when a magnetic field perturbation pushes a small volume of plasma with high P into a region of lower B. Thus, equation (1.9) will not be satisfied locally, and the perturbation will grow continuously. For a perturbation that is periodic poloidally and toroidally, its growth rate is typically greatest for flux surfaces with low, rational values of q. Perturbations on these surfaces have long wavelengths and bend the magnetic field lines the least. As the perturbations grow, adjacent flux surfaces overlap, causing magnetic reconnection and the formation of magnetic islands. Plasma mixing within these islands can then lead to a loss of confinement, stochasticization of the magnetic field, and eventual plasma death.

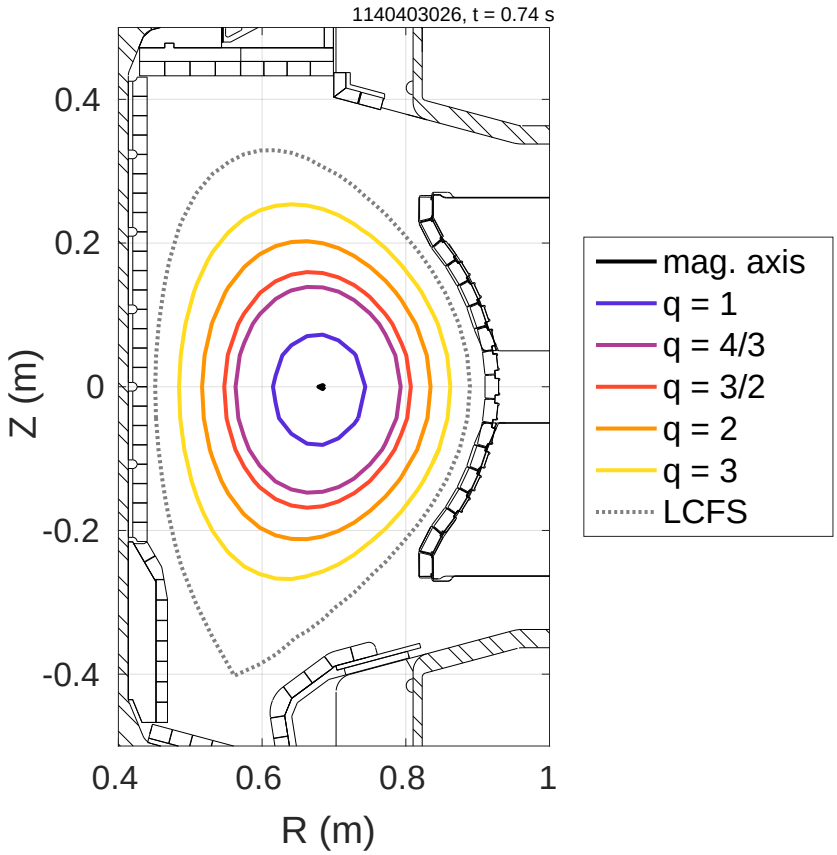

Figure 1.4: A poloidal cross-section of the Alcator C-Mod vacuum vessel (black) with poloidal flux contours labeled for the magnetic axis (center dot), rational surfaces $q = 1$, $4/3$, $3/2$, 2, and 3, and the last closed flux surface (LCFS, dotted). The safety factor at the plasma edge is $q_{95} \approx 4.5$.

1.4.2 Plasma disruptions

The sudden termination of a plasma is appropriately called a *disruption*. Figure 1.5 shows the time-evolution of plasma parameters from the final (ever) plasma discharge of Alcator C-Mod which (unfortunately) ended in a disruption. As is seen in figure 1.5a, the plasma current ramps up to $I_\mathrm{p} \approx 1.4$ MA over $t \approx$ 0-0.5 s, while the density and temperature eventually reach $\sim 2 \times 10^{20}$ m^{-3} and $\sim$3 keV, respectively. The stored thermal energy was about 150 kJ, and approximate magnetic energy was 1.1 MJ. Figure 1.5b zooms in on the disruption which occurs over only a few milliseconds, from $t \approx$ 1.294-1.296 s. Note how the density and temperature start to decrease slightly before the plasma current; this causes an increase in plasma resistivity, which goes like $\eta \propto T^{-3/2}$ in a plasma. What follows is a decay of I_p, usually at a rate consistent with the inductor-resistor $L/\mathcal{R}$ time. A large loop voltage ($\sim$60 times its normal value) is induced from $L\,\mathrm{d}I_\mathrm{p}/\mathrm{d}t$, and a spike in radiated power is observed.

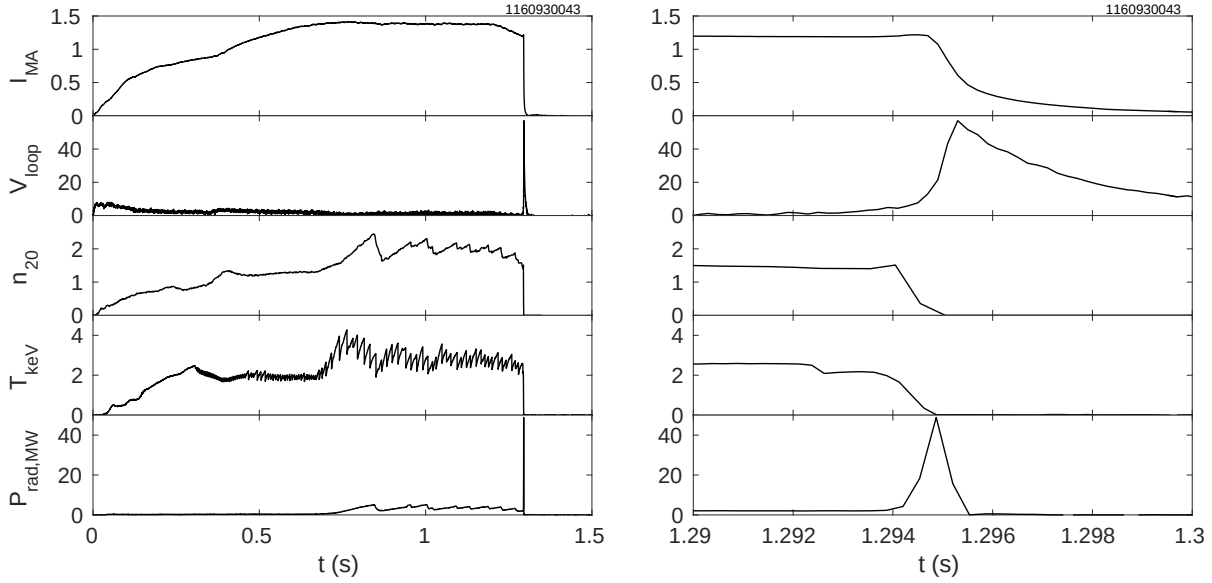

(a) (b)

Figure 1.5: Plasma parameters for C-Mod's final discharge 1160930043 for (a) the entire discharge ($t =$ 0-1.5 s) and (b) zoomed in on the disruption ($t =$ 1.2-1.3 s). From top to bottom: the plasma current (MA), loop voltage (V), density (10^{20} m^{-3}), temperature (keV), and radiated power (MW). ($B_0 = 5.7$ T, $W_\mathrm{th} \approx 150$ kJ, $W_\mathrm{mag} \approx 1.1$ MJ)

As observed in the discharge of figure 1.5, a disruption usually occurs in two stages: the *thermal quench* (TQ) during which essentially all of the plasma thermal energy is conducted, convected, or radiated away, followed by the *current quench* (CQ) during which the magnetic

energy is lost. Timescales of the TQ and CQ of C-Mod disruptions were on the order of 100 μs and 1 ms, respectively. Disruptions not only lead to delays in tokamak (or future power plant) operation, but can also cause serious damage to the machine and plasma-facing components (PFCs). In general, there are three main dangers:

1. High heat fluxes: The rapid loss of thermal energy can lead to high heat loads on the first wall and divertor. In C-Mod, almost 100 kJ of stored thermal energy would be dissipated in ∼100 μs; that's approximately 1 GW of thermal power! Thus, disruptions certainly have the potential to melt PFCs, especially if the radiated and conducted powers are asymmetric. At the beginning of his graduate career, the author of this thesis participated in some experiments measuring radiation asymmetries from both natural and mitigated (i.e. purposefully-triggered) disruptions; the results are published in [15].
2. Halo currents: Diverted and elongated tokamak plasmas are vertically-unstable due to the additional poloidal field coils required to shape/pull the plasma. During a disruption, the plasma can then drift and contact the first wall, allowing a significant fraction of the plasma current, called the *halo current*, to flow through the vacuum vessel. This can lead to large $J \times B$ forces and torques, which can damage PFCs. The author of this thesis has studied the time evolution and poloidal distribution of halo currents from vertical displacement events in C-Mod, using a high spatial resolution poloidal array of Langmuir "rail" probes; the findings are published in [16].
3. Runaway electrons: Large electric fields, induced by the decaying plasma current, can accelerate electrons up to relativistic speeds. These *runaway electrons* can attain energies of tens of MeV ($\sim 10^4$ times the energy of a thermal electron) and sometimes carry a significant fraction of the pre-disruption plasma current: as much as 50% in ASDEX-Upgrade and 66% in COMPASS [17], 60% in JET [18], and 80% in FTU [19]. (All of these are tokamak experiments.) Upon losing confinement, runaway electrons can impact the wall and damage PFCs, as seen in figure 1.6. The dynamics of runaway electrons will be the focus of this thesis work. Papers published and submitted for publication by the author on this topic include [20–23].

Plasma disruptions threaten the operation and success of future tokamaks, like ITER and SPARC. They must be avoided or their deleterious effects at least mitigated. Of course, a disruption must be first be *predicted* with sufficient warning time to allow for avoidance or mitigation efforts. A novel approach to disruption prediction, using the statistical framework of survival analysis and Random Forest machine learning methods, has recently been submitted for publication by the author of this thesis [24].

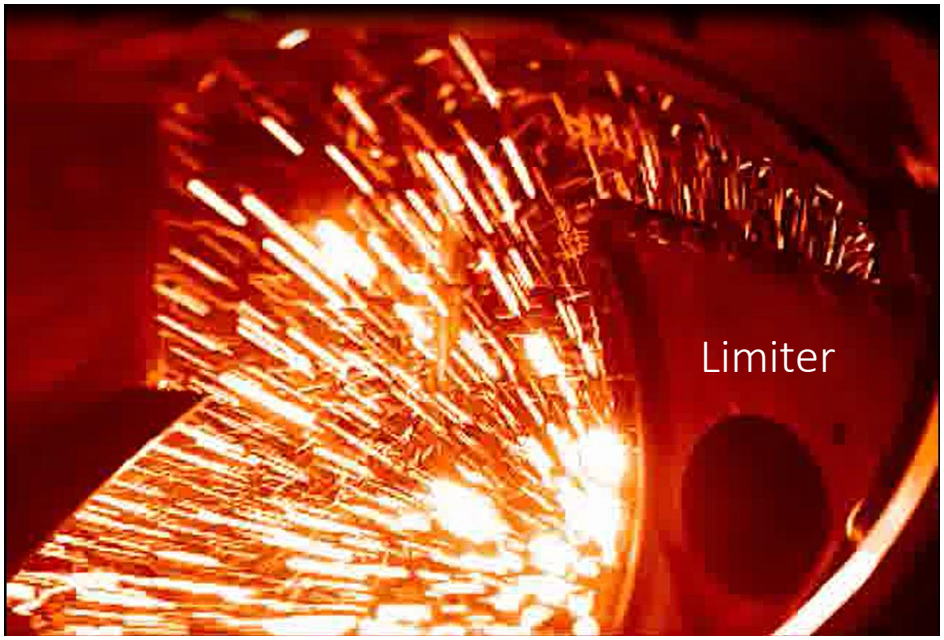

Figure 1.6: A shower of sparks, captured by a false-colored visible camera, resulting from runaways impacting a limiter (labeled) during the plasma current ramp-down at the end of Alcator C-Mod discharge 1160824028. (See the analysis of synchrotron spectra from this discharge in appendix C.)

1.5 Outline

The outline of the rest of this thesis is as follows: Chapter 2 describes the nature of runaway electrons and their generation and evolution in phase space. Then, in chapter 3, a derivation and explanation of synchrotron radiation, which is emitted by runaway electrons, is given. The diagnostics used for detection of runaway electron synchrotron emission are detailed in chapter 4, and overviews of the numerical tools used to compare theory with experiment are provided in chapter 5. The bulk of experimental analyses (and comparisons with synthetic data) are presented in chapters 6, 7, and 8, which focus on spectra, images, and polarization measurements of synchrotron emission, respectively. (The content of these three chapters originates from their respective publications [21], [22], and [23].) Finally, a summary of this thesis work and a future outlook are given in chapter 9.

References—Chapter 1

[1] A. Jay, D.R. Reidmiller, C.W. Avery, D. Barrie, B.J. DeAngelo, A. Dave, M. Dzaugis, M. Kolian, K.L.M. Lewis, K. Reeves, , and D. Winner. Overview. Impacts, Risks, and Adaptation in the United States: Fourth National Climate Assessment, Volume II. *U.S. Global Change Research Program, Washington, DC, USA*, 2018.

[2] D.J. Wuebbles, D.W. Fahey, K.A. Hibbard, B. DeAngelo, S. Doherty, K. Hayhoe, R. Horton, J.P. Kossin, P.C. Taylor, A.M. Waple, and C.P. Weaver. Executive summary. Climate Science Special Report: Fourth National Climate Assessment, Volume I. *U.S. Global Change Research Program, Washington, DC, USA*, pages 12–34, 2017.

[3] National Academies of Sciences, Engineering, and Medicine. *Final Report of the Committee on a Strategic Plan for U.S. Burning Plasma Research*. The National Academies Press, 2018.

[4] US Energy Information Administration. Massachusetts Net Electricity Generation by Source, Nov. 2018. https://www.eia.gov/state/?sid=MA#tabs-4. Accessed: 2019-02-22.

[5] J.P. Freidberg. *Plasma Physics and Fusion Energy*. Cambridge University Press, 2008.

[6] File:hd.6d.768 (13471576805).jpg. https://commons.wikimedia.org/wiki/File:HD.6D.768_(13471576805).jpg#file. Accessed: 2019-02-13.

[7] File:alcator c-mod tokamak engineering diagram.jpg. https://commons.wikimedia.org/wiki/File:Alcator_C-Mod_tokamak_engineering_diagram.jpg. Accessed: 2019-02-13.

[8] M. Shimada, D.J. Campbell, V. Mukhovatov, M. Fujiwara, N. Kirneva, K. Lackner, M. Nagami, V.D. Pustovitov, N. Uckan, J. Wesley, N. Asakura, A.E. Costley, A.J.H. Donné, E.J. Doyle, A. Fasoli, C. Gormezano, Y. Gribov, O. Gruber, T.C. Hender, W. Houlberg, S. Ide, Y. Kamada, A. Leonard, B. Lipschultz, A. Loarte, K. Miyamoto, V. Mukhovatov, T.H. Osborne, A. Polevoi, and A.C.C. Sips. Chapter 1: Overview and summary. *Nuclear Fusion*, 47(6):S1–S17, 2007.

[9] M. Greenwald, D.G. Whyte, P. Bonoli, Z.S. Hartwig, J. Irby, B. LaBombard, E. Marmar, J. Minervini, M. Takayasu, J. Terry, R. Vieira, A.E. White, S. Wukitch, D. Brunner, R.T. Mumgaard, and B.N. Sorbom. The high-field path to practical fusion energy, 2018. https://doi.org/10.7910/DVN/OYYBNU.

[10] B.N. Sorbom, J. Ball, T.R. Palmer, F.J. Mangiarotti, J.M. Sierchio, P. Bonoli, C. Kasten, D.A. Sutherland, H.S. Barnard, C.B. Haakonsen, J. Goh, C. Sung, and D.G. Whyte. ARC: A compact, high-field, fusion nuclear science facility and demonstration power plant with demountable magnets. *Fusion Engineering and Design*, 100:378 – 405, 2015.

[11] A.Q. Kuang, N.M. Cao, A.J. Creely, C.A. Dennett, J. Hecla, B. LaBombard, R.A. Tinguely, E.A. Tolman, H. Hoffman, M. Major, J. Ruiz Ruiz, D. Brunner, P. Grover, C. Laughman, B.N. Sorbom, and D.G. Whyte. Conceptual design study for heat exhaust management in the ARC fusion pilot plant. *Fusion Engineering and Design*, 137:221 – 242, 2018.

[12] A.C.C. Sips, for the Steady State Operation, and the Transport Physics topical groups of the International Tokamak Physics Activity. Advanced scenarios for ITER operation. *Plasma Physics and Controlled Fusion*, 47(5A):A19–A40, 2005.

[13] The interior of Alcator C-Mod as seen from F port. https://commons.wikimedia.org/wiki/Alcator_C-Mod#/media/File:Alcator_C-Mod_Fisheye_from_Fport.jpg. Taken by R. Mumgaard and C. Bolin 2013-09-17. Accessed: 2019-02-13.

[14] L.L. Lao, H. St. John, R.D. Stambaugh, A.G. Kellman, and W. Pfeiffer. Reconstruction of current profile parameters and plasma shapes in tokamaks. *Nuclear Fusion*, 25(11):1611, 1985.

[15] N. Commaux L.R. Baylor D. Brunner C.M. Cooper N.W. Eidietis E.M. Hollmann A.Q. Kuang C.J. Lasnier R.A. Moyer C. Paz-Soldan R. Raman M.L. Reinke D. Shiraki, R.S. Granetz and R.A. Tinguely. Disruption mitigation in the presence of pre-existing MHD instabilities. *Proceedings of the 26th IAEA Fusion Energy Conference*, 2016.

[16] R.A. Tinguely, R.S. Granetz, A. Berg, A.Q. Kuang, D. Brunner, and B. LaBombard. High-resolution disruption halo current measurements using Langmuir probes in Alcator C-Mod. *Nuclear Fusion*, 58(1):016005, 2017.

[17] V.V. Plyusnin, C. Reux, V.G. Kiptily, G. Pautasso, J. Decker, G. Papp, A. Kallenbach, V. Weinzettl, J. Mlynar, S. Coda, V. Riccardo, P. Lomas, S. Jachmich, A.E. Shevelev, B. Alper, E. Khilkevitch, Y. Martin, R. Dux, C. Fuchs, B. Duval, M. Brix, G. Tardini, M. Maraschek, W. Treutterer, L. Giannone, A. Mlynek, O. Ficker, P. Martin, S. Gerasimov, S. Potzel, R. Paprok, P. J. McCarthy, M. Imrisek, A. Boboc, K. Lackner, A. Fernandes, J. Havlicek, L. Giacomelli, M. Vlainic, M. Nocente, U. Kruezi, COMPASS team, TCV team, ASDEX-Upgrade team, EUROFusion MST1 Team, and JET contributors. Comparison of runaway electron generation parameters in small, medium-sized and large tokamaks—a survey of experiments in COMPASS, TCV, ASDEX-Upgrade and JET. *Nuclear Fusion*, 58(1):016014, 2018.

[18] V.V. Plyusnin, V. Riccardo, R. Jaspers, B. Alper, V.G. Kiptily, J. Mlynar, S. Popovichev, E. de La Luna, F. Andersson, and JET EFDA contributors. Study of runaway electron generation during major disruptions in JET. *Nuclear Fusion*, 46(2):277, 2006.

[19] J.R. Martín-Solís, B. Esposito, R. Sánchez, F.M. Poli, and L. Panaccione. Enhanced production of runaway electrons during a disruptive termination of discharges heated with lower hybrid power in the Frascati Tokamak Upgrade. *Phys. Rev. Lett.*, 97:165002, 2006.

[20] M. Hoppe, O. Embréus, R.A. Tinguely, R.S. Granetz, A. Stahl, and T. Fülöp. SOFT: a synthetic synchrotron diagnostic for runaway electrons. *Nuclear Fusion*, 58(2):026032, 2018. SOFT can be downloaded at https://github.com/hoppe93/SOFT, with documentation found at https://soft.readthedocs.io.

[21] R.A. Tinguely, R.S. Granetz, M. Hoppe, and O. Embréus. Measurements of runaway electron synchrotron spectra at high magnetic fields in Alcator C-Mod. *Nuclear Fusion*, 58(7):076019, 2018.

[22] R.A. Tinguely, R.S. Granetz, M. Hoppe, and O. Embréus. Spatiotemporal evolution of runaway electrons from synchrotron images in Alcator C-Mod. *Plasma Physics and Controlled Fusion*, 60(12):124001, 2018.

[23] R.A. Tinguely, M. Hoppe, O. Embréus, R.S. Granetz, S. Scott, and R.T. Mumgaard. Experimental and synthetic measurements of polarized synchrotron emission from runaway electrons in Alcator C-Mod. 2019. Submitted to *Nuclear Fusion*.

[24] R.A. Tinguely, K.J. Montes, C. Rea, R. Sweeney, and R.S. Granetz. An application of survival analysis to disruption prediction via Random Forests. 2019. Submitted to *Plasma Physics and Controlled Fusion*.

Chapter 2

Runaway electrons

2.1 Runaway electron generation

2.1.1 Threshold electric fields

Charged particles in a plasma interact primarily via the long-range ($\sim 1/r^2$) Coulomb force. Therefore, "collisions" between particles are typically *small*-angle deflections, as opposed to the large-angle, hard-sphere collisions idealized in a neutral gas. Recall that a single charge only feels the electric force from neighboring charges within a Debye sphere, with radius equal to the Debye length given in (1.2). The typical collision frequency ν of an electron with mass m_e and speed v moving through such a plasma is calculated (i) using the well-known Rutherford scattering cross-section and (ii) including only impact parameters $b < \lambda_\mathrm{De}$. The frequency ν_ei of an electron colliding with a plasma ion is given by equation (9.48) in [1],

$$\nu_\mathrm{ei} \approx \frac{1}{4\pi}\frac{ne^4\ln\Lambda}{\epsilon_0^2 m_\mathrm{e}^2}\frac{1}{v^3+1.3v_{T\mathrm{i}}^3}. \tag{2.1}$$

Here, $v_{T\mathrm{i}} = \sqrt{T_\mathrm{i}/m_\mathrm{i}}$ is the thermal speed of an ion with mass m_i and temperature T_i, the assumption $n \approx n_\mathrm{e} \approx n_\mathrm{i}$ is made for a single ion species plasma due to quasi-neutrality, and the parameter $\ln\Lambda \approx$ 10-20 is the Coulomb logarithm where

$$\Lambda = \frac{12\pi(\epsilon_0 T_\mathrm{e})^{3/2}}{e^3 n^{1/2}}. \tag{2.2}$$

The collision frequency of an electron with another electron ν_ee takes a similar form,

$$\nu_\mathrm{ee} \approx \frac{1}{2\pi}\frac{ne^4\ln\Lambda}{\epsilon_0^2 m_\mathrm{e}^2}\frac{1}{v^3+1.3v_{T\mathrm{e}}^3}, \tag{2.3}$$

where $v_{T\mathrm{e}} = \sqrt{T_\mathrm{e}/m_\mathrm{e}}$ is the electron thermal speed.

An important (and fascinating) property of plasmas is contained in (2.1) and (2.3): As a particle's speed increases ($v \gg v_{T\mathrm{e}} \gg v_{T\mathrm{i}}$), its probability of colliding with another particle *decreases*. Thus, provided a sufficiently strong force, a charged particle can continuously accelerate, i.e. "run away," to relativistic velocities $v \to c$. Due to their light masses ($m_\mathrm{e} \ll m_\mathrm{i}$), electrons are most susceptible to this behavior and are then called "runaway" electrons, hereafter referred to as runaways.

The first postulation of runaways is attributed to Dreicer in 1959-1960 [2, 3]. Following a derivation similar to that in those works, consider a plasma in which an electron moves with velocity $\boldsymbol{v}$ exactly parallel to the background magnetic field $\boldsymbol{B}$—i.e. there is no gyro-motion. If an external electric field $\boldsymbol{E}$ is applied parallel to $\boldsymbol{B}$, then the 1D non-relativistic equation of motion along $\boldsymbol{B}$ is

$$m_\mathrm{e}\frac{\mathrm{d}v}{\mathrm{d}t} = -eE - m_\mathrm{e}v\left(\nu_{\mathrm{ei}} + \nu_{\mathrm{ee}}\right). \tag{2.4}$$

Solving for force balance gives a threshold electric field

$$E_\mathrm{thr} = |E| = \frac{1}{4\pi}\frac{ne^3\ln\Lambda}{\epsilon_0^2 m_\mathrm{e}}v\left(\frac{1}{v^3 + 1.3\,v_{T\mathrm{i}}^3} + \frac{2}{v^3 + 1.3\,v_{T\mathrm{e}}^3}\right). \tag{2.5}$$

Note that (2.4) and (2.5) constitute "test-particle" equations; that is, they consider only a test electron interacting with distinct populations of electrons and ions. However, in [2, 3], Dreicer argues that the *total* momentum and energy of one particle species does not change from interactions between *like*-particles. Neglecting the second term[a] of (2.5) and assuming $v \gg v_{T\mathrm{i}}$ gives the new threshold field

$$E_\mathrm{thr} \approx \frac{mv}{e}\nu_{\mathrm{ei}} = \frac{ne^3\ln\Lambda}{4\pi\epsilon_0^2 m_\mathrm{e}v^2}. \tag{2.6}$$

From this, we can calculate the critical (Dreicer) field at which the *bulk* population of (thermal) electrons would run away by substituting $v = v_{T\mathrm{e}} = \sqrt{T_\mathrm{e}/m_\mathrm{e}}$,

$$E_\mathrm{D} = \frac{ne^3\ln\Lambda}{4\pi\epsilon_0^2 T_\mathrm{e}}. \tag{2.7}$$

When the entire population of electrons runs away in experiment, it is called electron "slide-away." This can often happen during plasma start-up when densities n are quite low.

[a] Because ν_{ei} and ν_{ee} are of similar order, neglecting ν_{ee} only changes the final result by a factor of order unity.

Naturally, relativistic effects will come into play as electrons run away to $v \approx c$. In [4], Connor and Hastie derived the critical electric field below which *no* electrons could run away,

$$E_{\mathrm{C}} = \frac{ne^3 \ln \Lambda}{4\pi\epsilon_0^2 m_{\mathrm{e}} c^2}, \tag{2.8}$$

which is simply (2.6) with $v \to c$, or $E_{\mathrm{C}} = E_{\mathrm{D}} \times T_{\mathrm{e}}/m_{\mathrm{e}}c^2$. Note that with $m_{\mathrm{e}}c^2 = 511$ keV and a temperature of $T_{\mathrm{e}} \sim 5$ keV, the ratio $E_{\mathrm{D}}/E_{\mathrm{C}} \sim 100$. In more practical units, the Connor-Hastie critical field is

$$E_{\mathrm{C}}\,[\mathrm{V/m}] \approx 0.005\, n_{20}\, \ln \Lambda, \tag{2.9}$$

where n_{20} is the density measured in units of 10^{20} m^{-3}. Since $\ln \Lambda$ is relatively insensitive to changes in density and temperature, we see that the electric field required for runaway production is really just a function of density, and $E > E_{\mathrm{C}}$ can be attained in different phases of the plasma discharge: For example, if the plasma density is sufficiently low, the normal loop voltage V_{loop} driving the plasma current could also drive runaways. In addition, during plasma disruptions, the induced electric field often exceeds E_{C} by factors of 10-100.

Note that this calculation—and the results, (2.7) and (2.8)—included only collisions with singly-charged ions, but no other damping effects, such as collisions with high-Z impurities, radiation reaction, or wave-particle interactions. For multiply-charged ions (resulting from impurities), the *effective charge*,

$$Z_{\mathrm{eff}} = \frac{\sum_i Z_i^2 n_{\mathrm{i}}}{\sum_i Z_i n_{\mathrm{i}}}, \tag{2.10}$$

will be used, where the sum is over all ion species.

Two groundbreaking studies in [5] and [6] showed that the electric field needed for runaway generation and suppression was several (∼2-5) times higher than E_{C}. This is perhaps unsurprising since other runaway power loss mechanisms make it more difficult for runaway populations to form. This may bode well for future devices. The ratio E/E_{C} for more recent runaway experiments on C-Mod will be explored later in this thesis, in chapters 6 and 7.

2.1.2 Runaway electron growth rates

While the previous section discussed the plasma conditions required for runaways to be born, nothing was mentioned about their population growth rates. A simple formulation of the bulk runaway density evolution is

$$\frac{\mathrm{d}n_{\mathrm{r}}}{\mathrm{d}t} = \Gamma_{\mathrm{lin}} n + \Gamma_{\mathrm{exp}} n_{\mathrm{r}}, \tag{2.11}$$

where Γ_{lin} and Γ_{exp} are linear and exponential growth rates, respectively.

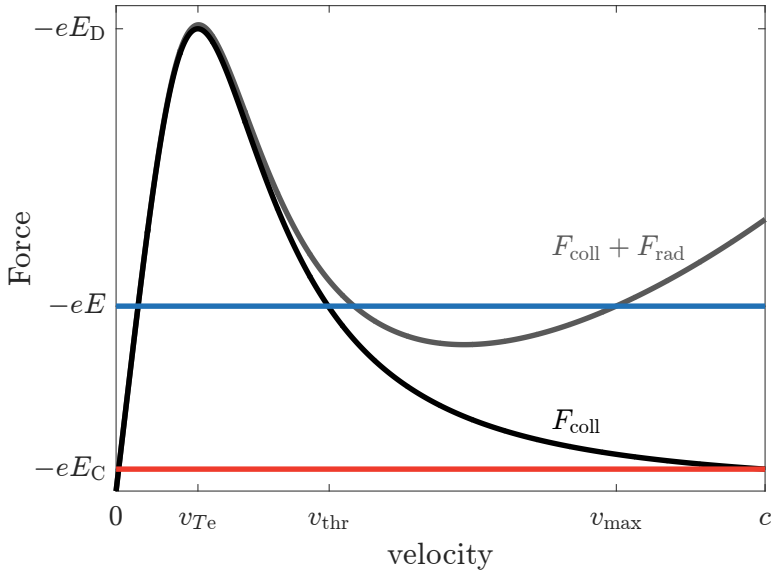

Figure 2.1: A diagram depicting the *magnitude* of forces experienced by an electron in a plasma. Note how collisional friction *decreases* as the particle's speed *increases*. The friction force F_{coll} (black) is calculated from (2.5). If an external electric field $E > E_{\mathrm{C}}$ is applied, all electrons with velocities $v > v_{\mathrm{thr}}$, from (2.12), will run away. If radiation or other deceleration mechanisms are included, represented as $F_{\mathrm{coll}} + F_{\mathrm{rad}}$, then runaways can only accelerate to $v = v_{\mathrm{max}}$. (Not to-scale.)

Consider first the linear, or primary (Dreicer), growth rate. Rearranging (2.6) gives the threshold velocity

$$v_{\mathrm{thr}} = \left(\frac{ne^3 \ln \Lambda}{4\pi\epsilon_0^2 m_{\mathrm{e}} E} \right)^{1/2} \tag{2.12}$$

For a given electric field E, electrons with velocities $v > v_{\mathrm{thr}}$ should run away to c, thus depleting that same region of (1D) velocity space. Connor and Hastie, in [4], performed the relativistic calculation of the rate at which the thermal electron population "diffuses" into (or "feeds") the runaway regime. The result is given as equations (62)-(64) in [4],

$$\Gamma_{\mathrm{lin}} = C\,\nu(v_{Te}) \left(\frac{E_{\mathrm{D}}}{E} \right)^{h(\hat{E}, Z_{\mathrm{eff}})} \exp\left[-f(\hat{E}) \frac{E_{\mathrm{D}}}{E} - g(\hat{E}, Z_{\mathrm{eff}}) \sqrt{\frac{2E_{\mathrm{D}}}{E}} \right] \tag{2.13}$$

where C is a constant of order unity, $\nu(v_{Te})$ is the collision frequency evaluated at the electron

thermal speed, $\hat{E} = E/E_{\mathrm{C}}$ (recall $E_{\mathrm{C}} = E_{\mathrm{D}} \times T_{\mathrm{e}}/mc^2$), and

$$f(\hat{E}) = 2\hat{E}\left(\hat{E} - \frac{1}{2} - \sqrt{\hat{E}(\hat{E}-1)}\right), \tag{2.14}$$

$$g(\hat{E}, Z_{\mathrm{eff}}) = \sqrt{\frac{(Z_{\mathrm{eff}}+1)\hat{E}^2}{8(\hat{E}-1)}}\left[\frac{\pi}{2} - \arcsin\left(1 - \frac{2}{\hat{E}}\right)\right], \tag{2.15}$$

$$h(\hat{E}, Z_{\mathrm{eff}}) = \frac{1}{16(\hat{E}-1)}\left[\hat{E}(Z_{\mathrm{eff}}+1) - Z_{\mathrm{eff}} + 7 + 2\sqrt{\frac{\hat{E}}{\hat{E}-1}}(Z_{\mathrm{eff}}+1)(\hat{E}-2)\right]. \tag{2.16}$$

No doubt, equation (2.13) is complex, but it is included here for completeness as it is utilized later in chapter 6. From equation (67) in [4], the non-relativistic limit can be written as

$$\Gamma_{\mathrm{lin}} \approx C\,\nu(v_{T\mathrm{e}})\left(\frac{E_{\mathrm{D}}}{E}\right)^{3(Z_{\mathrm{eff}}+1)/16}\exp\left(-\frac{1}{4}\frac{E_{\mathrm{D}}}{E} - \sqrt{(Z_{\mathrm{eff}}+1)\frac{E_{\mathrm{D}}}{E}}\right) \tag{2.17}$$

In general, it is found that Γ_{lin} increases with increasing temperature through the ratio $E_{\mathrm{D}}/E \propto T_{\mathrm{e}}/E$, specifically when $E/E_{\mathrm{D}} \ll 1$, which is generally the case in experiment (at least for this thesis work). In addition, Γ_{lin} decreases with increasing effective charge Z_{eff}. These dependencies make sense intuitively as higher values of T_{e} provide a larger population of electrons available to run away, while high Z_{eff} leads to increased collisional friction and damping.

The exponential growth term Γ_{exp} in (2.11) is the secondary generation mechanism called "avalanching." This is the process by which a runaway electron with velocity $v_1 > v_{\mathrm{thr}}$ collides with a thermal electron with velocity $v_2 < v_{\mathrm{thr}}$; after the collision, the runaway electron has lost energy but maintains $v_1' > v_{\mathrm{thr}}$, while the second electron's speed has increased such that now $v_2' > v_{\mathrm{thr}}$. In this way, the runaway electron has "knocked" the thermal electron into the runaway regime without leaving the regime itself, and a runaway avalanche process occurs.

Based on the work of Jayakumar [7], it was first shown that the avalanching mechanism was exponentially sensitive to the bulk plasma current. The number of e-folds expected during a disruption—in which all of the magnetic energy could be converted to runaway electron energy—was given by

$$\Gamma_{\mathrm{exp}}\,\Delta t \approx \frac{I_{\mathrm{p}}}{I_A \ln\Lambda} \tag{2.18}$$

where $I_A = 4\pi\epsilon_0 m_{\mathrm{e}} c^3/e \approx 17$ kA. For C-Mod with $I_{\mathrm{p}} \approx 1$ MA, an exponential increase of e^3 might be expected, whereas for ITER, with $I_{\mathrm{p}} = 15$ MA, the factor could be as large as e^{40}!

The most well-known calculation of the runaway avalanche growth rate was carried out by Rosenbluth and Putvinski [8], with the result given by equation (18) therein,

$$\Gamma_{\rm exp} = \frac{eE_{\rm C}}{m_{\rm e}c\ln\Lambda}\sqrt{\frac{\pi\alpha}{3(Z_{\rm eff}+5)}}\left(\hat{E}-1\right)\left(1-\frac{1}{\hat{E}}+\frac{4\pi(Z_{\rm eff}+1)^2}{3\alpha(Z_{\rm eff}+5)(\hat{E}^2+4/\alpha^2-1)}\right)^{-1/2}. \tag{2.19}$$

Here, $\alpha \sim 1$ in the high aspect ratio limit ($a/R \to 0$), and $\hat{E} = E/E_{\rm C} > 1$ is assumed. Again, this is a complicated formula but is included for completeness as it is used in chapter 6. In the limit that $E/E_{\rm C} \gg Z_{\rm eff}+1$, we obtain

$$\Gamma_{\rm exp} \approx \frac{eE_{\rm C}}{mc\ln\Lambda}\frac{1}{\sqrt{Z_{\rm eff}+5}}\left(\hat{E}-1\right) \tag{2.20}$$

As one might expect, $\Gamma_{\rm exp}$ is found to increase with increasing $\hat{E} \propto E/n$ and decrease with increasing $Z_{\rm eff}$.

2.1.3 Other runaway generation mechanisms

The previous sections described how runaways can be generated as electrons are (i) accelerated from the tail of the distribution function via the Dreicer mechanism or (ii) boosted to relativistic speeds via a collision with an already-formed runaway. In addition, there are several other ways that runaways can form. These are not the focus of this thesis, but they are noted here. First, the non-thermal, yet non-relativistic electron population ($v_{T\rm e} < v \ll c$) can be enhanced from wave-particle interactions, like electron cyclotron heating (ECH) or lower hybrid current drive (LHCD). In fact, LH was often used on C-Mod to encourage runaway growth during runaway experimental studies. In this scenario, a higher fraction of the electron population is available to run away for lower values of an applied electric field, when compared to a Maxwellian distribution. This is slightly worrisome as future fusion devices will likely rely on ECH or LHCD for steady-state operation. During a disruption, these "hot-tail" electrons will slow down less efficiently than the bulk population—see (2.1) and (2.3)—potentially exacerbating the runaway problem.

The nuclear/radiation environment of future machines unfortunately provides other opportunities for runaway generation [9]: The beta-decay of tritium can result in an electron with an energy up to 18.6 keV. Thermal electrons can also gain energy through collisions with the 3.5 MeV alpha particles produced from DT reactions. Gamma radiation from neutron-irradiated wall materials can inverse Compton scatter with cold electrons. All of these potential non-thermal electron sources need further investigation, as noted in [9], especially to assess their possible impacts on machines like ITER and SPARC. However, as also noted in [9], some of these effects—the first

two, in particular—may be negligible for a sufficiently hot tail of the Maxwellian distribution, which could remain even after a disruption.

2.2 Momentum space evolution of runaway electrons

The analysis of the previous section was only one-dimensional, considering electron velocities $\boldsymbol{v}$ and applied electric fields $\boldsymbol{E}$ parallel to the background magnetic field $\boldsymbol{B}$. Of course, there are three components of $\boldsymbol{v}$, but it is enough to consider just two: the velocity components parallel ($v_\parallel$) and perpendicular ($v_\perp$) to $\boldsymbol{B}$. This is the guiding center "picture"; the precise angle of the electron in its gyro-orbit about the magnetic field line is inconsequential and averaged out.

The perpendicular velocity $v_\perp$ is needed to understand the full picture of runaway dynamics. In particular, even if $v_\parallel$ decreases due to, say, collisions with other particles, energy can be transferred into $v_\perp$, so the total energy is not actually lost. This is a process called *pitch angle scattering*, where the pitch angle is defined as $\tan\theta_\mathrm{p} = v_\perp/v_\parallel$. In addition, it is $v_\perp$ (gyro-motion) that most readily produces synchrotron radiation which acts as a power loss mechanism for runaways. The details of synchrotron radiation will be handled in chapter 3. For now, we need only consider the total synchrotron power radiated by a gyrating electron, given by the Larmor formula

$$P_\mathrm{synch} = \frac{e^4\gamma^2 v_\perp^2 B^2}{6\pi\epsilon_0 m_\mathrm{e}^2 c^3}, \tag{2.21}$$

where $\gamma = 1/\sqrt{1-v^2/c^2}$ is the relativistic Lorentz factor. Note that a characteristic radiation timescale can be extracted from (2.21), defined as

$$\tau_\mathrm{rad} = \frac{6\pi\epsilon_0 m_\mathrm{e}^3 c^3}{e^4 B^2}. \tag{2.22}$$

This timescale is often compared to the runaway collisional timescale, calculated from (2.4) and (2.8),

$$\tau_\mathrm{coll} = \frac{m_\mathrm{e} c}{eE_\mathrm{C}} = \frac{4\pi\epsilon_0^2 m_\mathrm{e}^2 c^3}{e^4 n\ln\Lambda}. \tag{2.23}$$

The ratio $\hat{\tau}_\mathrm{rad} = \tau_\mathrm{rad}/\tau_\mathrm{coll}$ is then used to indicate the relative strengths of synchrotron radiation reaction compared to collisional damping on runaways,

$$\hat{\tau}_\mathrm{rad} = \frac{3m_\mathrm{e} n\ln\Lambda}{2\epsilon_0 B^2} \approx 280\frac{n_{20}}{B^2}. \tag{2.24}$$

Here, n_{20} is measured in units of 10^{20} m^{-3}. Thus, for low values of $\hat{\tau}_\mathrm{rad}$, the power loss from synchrotron radiation dominates over that from friction. However, this ratio is slightly misleading

since $\hat{\tau}_{\mathrm{rad}} = 1$ does not necessarily mean that the damping mechanisms are of equal magnitude. We are really interested in the ratio of powers

$$\frac{P_{\mathrm{synch}}}{P_{\mathrm{coll}}} = \left(\frac{\gamma v_\perp}{c}\right)^2 \frac{1}{\hat{\tau}_{\mathrm{rad}}}, \tag{2.25}$$

which is energy-dependent. If runaway energies are not known *a priori*—which is the case in experiment—only estimates of $P_{\mathrm{synch}}/P_{\mathrm{coll}}$ can only be made.

2.2.1 A test-particle model

One way to calculate the trajectories of runaways in momentum space $(v_\parallel, v_\perp)$ is using a test-particle model (TPM), through which the equation of motion of a single test electron is solved given bulk plasma parameters. The TPM used for this thesis work was developed by Martín-Solís *et al* [10] and incorporates the effects of both collisions and synchrotron radiation. The evolution of the *parallel* runaway momentum is given by equation (1) of [10],

$$\frac{\mathrm{d}p_\parallel}{\mathrm{d}t} = eE_\parallel - \frac{n_{\mathrm{e}} e^4 m_{\mathrm{e}} \ln\Lambda}{4\pi\epsilon_0^2}\frac{\gamma^2}{p^2}\left(1 + \frac{Z_{\mathrm{eff}}+1}{\gamma}\right)\frac{p_\parallel}{p} - \frac{e^2}{6\pi\epsilon_0}\beta^3\gamma^4\left\langle R^{-2}\right\rangle\frac{p_\parallel}{p}, \tag{2.26}$$

Here, $p_\parallel = \gamma m_{\mathrm{e}} v_\parallel$ is the parallel relativistic momentum, $p = \gamma m_{\mathrm{e}} v$ is the total relativistic momentum, and $\beta = v/c$ is the normalized velocity. The first term corresponds to the electric force in the direction of the magnetic field, where $E_\parallel$ is the component of the electric field parallel to $\boldsymbol{B}$. The second term is recognizable as collisional friction, with the additional factor $(Z_{\mathrm{eff}}+1)/\gamma$, computed by Fussmann [11], including pitch angle scattering from multiply-charged ions. The last term is the gyro-averaged synchrotron reaction force, where $\langle R^{-2}\rangle$ is the inverse-square of the radius of curvature, calculated by Kurzan *et al* [12], accounting for both gyro- and toroidal motion in a tokamak. This is approximated as

$$\left\langle \frac{1}{R^2} \right\rangle \approx \frac{1}{R_0^2} + \frac{\sin^4(\theta_{\mathrm{p}})}{\rho_L^2}, \tag{2.27}$$

where R_0 is the tokamak major radius and $\rho_L = p_\perp/eB$ is the Larmor gyro-radius. Note that for a runaway electron in Alcator C-Mod, ρ_L is usually on the order of mm (certainly sub-cm), so synchrotron radiation is typically gyro-motion dominated.

The *total* runaway momentum is given by equation (2) of [10],

$$\frac{\mathrm{d}p}{\mathrm{d}t} = eE_\parallel\frac{p_\parallel}{p} - \frac{n_{\mathrm{e}} e^4 m_{\mathrm{e}} \ln\Lambda}{4\pi\epsilon_0^2}\frac{\gamma^2}{p^2} - \frac{e^2}{6\pi\epsilon_0}\beta^3\gamma^4\left\langle R^{-2}\right\rangle. \tag{2.28}$$

The evolution of the perpendicular momentum ($\mathrm{d}p_\perp/\mathrm{d}t$) can be computed from (2.26) and (2.28) if needed.

This set of coupled momentum equations can be solved with a standard ordinary differential equation solver, like the Runge-Kutta methods, given time-dependent parameters $E_\parallel$, n_e, Z_eff, and B. Examples of test-particle trajectories in momentum space, solved using time-*independent* parameters, are shown in figure 2.2. The initial electron momentum was set to $(p_{\parallel 0},\, p_{\perp 0})/m_\mathrm{e}c = (1,\, 10^{-3})$[b], and the plasma density set to $n_\mathrm{e} = 10^{19}$ m^{-3}. Then, equations (2.28) and (2.26) were evolved from $t =$ 0-1 s. The dots in figure 2.2 represent time intervals of $\Delta t = 0.1$ s. As is seen in the figure, the distance between points along each trajectory decreases in time, indicating that the test particle is approaching an "attractor" or equilibrium in momentum space.

The dependencies of the test-particle trajectories on input parameters are intuitive: As the ratio E/E_C increases, the electric field increasingly dominates over collisional friction; thus, as shown in figure 2.2a, the runaway momentum increases, mostly parallel but also perpendicular to the magnetic field. As the magnetic field strength increases, a smaller perpendicular momentum $p_\perp$ is required to radiate the same synchrotron power—see (2.21); for the case shown in figure 2.2b, both the total runaway momentum and pitch angle decrease with increasing B. Increasing Z_eff results in higher collisionality and pitch angle scattering; this is seen as an increase in $p_\perp$ and decrease in $p_\parallel$ in figure 2.2c.

2.2.2 The kinetic equation

An advantage of the TPM presented in the previous section is that it is computationally inexpensive to solve, allowing many scans over different plasma parameters. However, the result of the TPM is a delta function $\delta(\boldsymbol{p})$ in momentum space, when in reality the runaway population will have an entire *distribution* of energies and pitch angles. The distribution function $f(\boldsymbol{p})$ of runaways in momentum space can be calculated from the kinetic equation which takes the general form

$$\frac{\mathrm{d}f_\mathrm{e}}{\mathrm{d}t} = \frac{\partial f_\mathrm{e}}{\partial t} + \frac{\mathrm{d}\boldsymbol{r}}{\mathrm{d}t}\cdot\frac{\partial f_\mathrm{e}}{\partial \boldsymbol{r}} + \frac{\mathrm{d}\boldsymbol{p}}{\mathrm{d}t}\cdot\frac{\partial f_\mathrm{e}}{\partial \boldsymbol{p}}. \tag{2.29}$$

Here, $f_\mathrm{e}(t, \boldsymbol{r}, \boldsymbol{p})$ is actually the *phase* space distribution of electrons, including position space effects through $\partial f_\mathrm{e}/\partial \boldsymbol{r}$. In the case of no spatial dependence, e.g. in an infinite homogeneous plasma, the kinetic equation can be rewritten as

$$\frac{\partial f_\mathrm{e}}{\partial t} - e\left(\boldsymbol{E} + \boldsymbol{v}\times\boldsymbol{B}\right)\cdot\frac{\partial f_\mathrm{e}}{\partial \boldsymbol{p}} = \sum_i C_{ei}\left\{f_\mathrm{e}, f_i\right\}. \tag{2.30}$$

[b] Note that if $p_{\perp 0} = 0$, then $p_\perp = 0$ for all time.

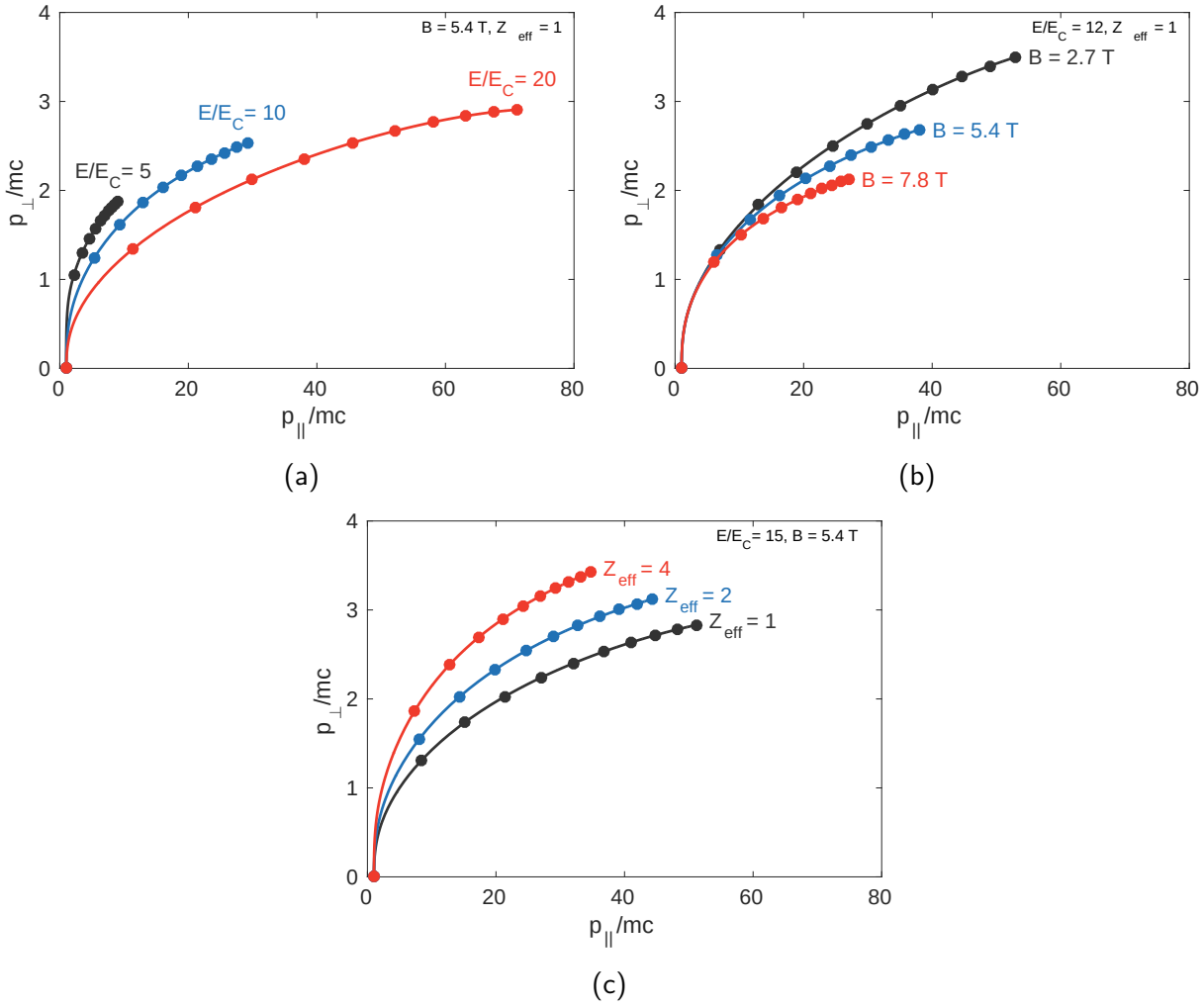

Figure 2.2: TPM trajectories in momentum space from (2.26) and (2.28), varying parameters (a) E/E_{C}, (b) B, and (c) Z_{eff}. All parameters are constant in time; the dots denote time intervals $\Delta t = 0.1$ s from $t = 0$-1 s. The initial momentum is $p_{\parallel 0}/m_{\mathrm{e}}c = 1$ and $p_{\perp 0}/m_{\mathrm{e}}c \approx 10^{-3}$. Note that for $B = 2.7$, 5.4, and 7.8 T, the ratio $\hat{\tau}_{\mathrm{rad}} \approx 4$, 1, and 0.5, respectively, for $n_{\mathrm{e}} = 10^{19}$ m^{-3}.

Here, the Lorentz force was substituted, and C_{ei} is the operator representing collisions between electrons and all ion species i. This can be solved numerically given an appropriate form of C_{ei}. The code *COllisional Distribution of Electrons* (CODE) [13, 14] was used for this task, and its details are discussed further in chapter 5.

It should be noted that there are certain cases in which a TPM *is* sufficient to capture runaway evolution and dynamics and to explain diagnostic measurements. This is the case in the analysis of chapter 6 which utilizes a *bulk* measurement of the runaways, so fine details of the full runaway distribution are unresolvable. Other times, the full distribution is required to adequately match theory and experiment, as is the case in chapters 7 and 8 for which effects of the full spatial and pitch angle distributions are diagnosed.

2.3 Position space dynamics of runaway electrons

The previous section considered runaway dynamics in momentum space, but neglected any position space (real space) effects. These play an important role in runaway evolution—e.g. spatially-varying plasma parameters, radial transport, and drifts—as well as the diagnosis of runaways—e.g. is the emission from runaways even within a detector's field-of-view? The following sections will focus specifically on runaway drift orbits and radial diffusion. The former will be needed when comparing experimental and synthetic data in chapter 6. The latter is *observed* in and inferred from experimental measurements of chapters 7 and 8, but detailed calculations are left for future work.

2.3.1 Drift orbits

As mentioned in chapter 1, charged particles experience drifts in a tokamak magnetic geometry due to the curvature of magnetic field lines as well as the radially-decreasing magnetic field strength. The total vertical drift velocity, summing (1.6) and (1.7), can be expressed as

$$v_d = \frac{1}{\omega_B R}\left(v_\parallel^2 + \frac{v_\perp^2}{2}\right), \tag{2.31}$$

where $\omega_B = qB/\gamma m_\mathrm{e}$ is the cyclotron frequency. Following the derivation performed by Knoepfel and Spong [15], the drift radius—i.e. the radial deviation from the flux surface—can be calculated as $r_\mathrm{d}/r = v_\mathrm{d}/v_\mathrm{p}$, where r is the minor radial position and v_p is the poloidal velocity given by the rotational transform

$$v_\mathrm{p} = v_\parallel \frac{B_\mathrm{p}(r)}{B_\mathrm{t}}. \tag{2.32}$$

Thus, the drift radius can be expressed as

$$r_{\mathrm{d}} = \frac{r}{R_0}\frac{\gamma m_{\mathrm{e}}}{eB_{\mathrm{p}}(r)}\frac{1}{v_{\parallel}}\left(v_{\parallel}^2 + \frac{v_{\perp}^2}{2}\right). \tag{2.33}$$

Because runaway motion is primarily in the toroidal direction, we expect that $v_{\parallel}^2 \gg v_{\perp}^2$. Thus, the second term in (2.33) can usually be neglected, so that

$$r_{\mathrm{d}} \approx \frac{p_{\parallel}\, q(r)}{eB_{\mathrm{t}}}, \tag{2.34}$$

where $q(r) = B_{\mathrm{t}} r / B_{\mathrm{p}} R$ is the safety factor. Note that the drift radius in (2.34) is essentially the same as those derived in later works, such as [16–18].

To approximate $q(r)$ and $B_{\mathrm{p}}(r)$, first consider the current profile of a cylindrical plasma of the form $J(r) = J_0\left(1 - (r/a)^{\mathrm{n}}\right)$ where n is a positive number and a is the maximum minor radius. The total current in the plasma is given by

$$I_{\mathrm{p}} = \int_0^{2\pi} \mathrm{d}\theta \int_0^a J(r)\, r\, \mathrm{d}r = 2\pi J_0 \int_0^a \left[1 - \left(\frac{r}{a}\right)^{\mathrm{n}}\right] r\, \mathrm{d}r. \tag{2.35}$$

Solving this integral gives the appropriate form of J_0

$$J_0 = \frac{\mathrm{n}+2}{\mathrm{n}}\frac{I_{\mathrm{p}}}{\pi a^2}. \tag{2.36}$$

In a similar way, the poloidal field can be calculated through Ampere's law

$$2\pi r\, B_{\mathrm{p}}(r) = 2\pi\mu_0 a^2 J_0 \left[\frac{1}{2}\left(\frac{r}{a}\right)^2 - \frac{1}{\mathrm{n}+2}\left(\frac{r}{a}\right)^{\mathrm{n}+2}\right]. \tag{2.37}$$

Rearranging and substituting for J_0 gives

$$B_{\mathrm{p}}(r) = \frac{\mu_0 I_{\mathrm{p}} r}{\pi a^2}\left\{\frac{1}{2} + \frac{1}{\mathrm{n}}\left[1 - \left(\frac{r}{a}\right)^{\mathrm{n}}\right]\right\}. \tag{2.38}$$

Finally, the approximate drift orbit radius can be written in its final form

$$r_{\mathrm{d}} = \frac{\pi}{e\mu_0}\frac{a^2}{R_0}\frac{p_{\parallel}}{I_{\mathrm{p}}}\left(1 + \frac{\tan^2\theta_{\mathrm{p}}}{2}\right)\left\{\frac{1}{2} + \frac{1}{\mathrm{n}}\left[1 - \left(\frac{r}{a}\right)^{\mathrm{n}}\right]\right\}^{-1}, \tag{2.39}$$

where $\tan\theta_{\mathrm{p}} = v_{\perp}/v_{\parallel}$ was substituted.

A particle will lose confinement when its drift orbit leaves the plasma, i.e. $r + r_\mathrm{d} + \rho_L > a$. In the small gyro-radius limit (neglecting ρ_L), the parallel momenta for which particles are confined are given by

$$p_\parallel \leq \frac{e\mu_0}{\pi}\frac{R_0}{a}I_\mathrm{p}\left(1-\frac{r}{a}\right)\left\{\frac{1}{2}+\frac{1}{\mathrm{n}}\left[1-\left(\frac{r}{a}\right)^\mathrm{n}\right]\right\}, \tag{2.40}$$

where the $\tan^2\theta_\mathrm{p} \ll 1$ was assumed. The ratio of threshold energy to plasma current for several profiles are shown in figure 2.3. As the current profile peaks (low n), the local B_p increases and higher energy runaways are better confined. For a parabolic current profile ($\mathrm{n} = 2$) and C-Mod machine parameters, this reduces to

$$\frac{p_\parallel}{m_\mathrm{e}c} \leq 724\, I_\mathrm{MA}\left(1-\frac{r}{a}\right)\left[1-\frac{1}{2}\left(\frac{r}{a}\right)^2\right] \tag{2.41}$$

which implies that runaways generated on the magnetic axis ($r = 0$) require energies $\mathcal{E} \geq 360$ MeV to lose confinement in a C-Mod plasma with $I_\mathrm{p} = 1$ MA. This threshold is quite high, reflecting the impressive confining "power" of the poloidal magnetic field. Note however that, in practice, runaways could not reach this energy during a standard ∼2 s plasma discharge (or disruption) in C-Mod. This also does not account for diffusion/transport of runaways or magnetic perturbations.

2.3.2 Diffusion and radial transport

Because runaways experience far fewer collisions than thermal electrons, their radial diffusion and transport are primarily influenced by magnetic perturbations and wave-particle interactions. The effect of magnetic fluctuations on runaway dynamics has been studied extensively in theory [19–21], simulation [22–25], and experiment [17, 26].[c] Here, a brief overview of runaway diffusion is given.

In their seminal paper on electron transport in stochastic fields [19], Rechester and Rosenbluth suggested that the radial diffusion coefficient for high energy electrons should scale like

$$D_\mathrm{r} \approx vR\left(\frac{\delta B}{B}\right)^2 \tag{2.42}$$

where v is the velocity ($v \approx c$ for runaways), R is the major radius, and δB is the amplitude of magnetic fluctuations (at a particular flux surface) in the background magnetic field B. The experimentally-measured confinement times of runaways in the LT-3 tokamak [27] could be matched for $\delta B/B \sim 10^{-4}$. Later works—for instance, see [16, 20, 21]—considered the effects of

[c] This is a non-exhaustive list of references.

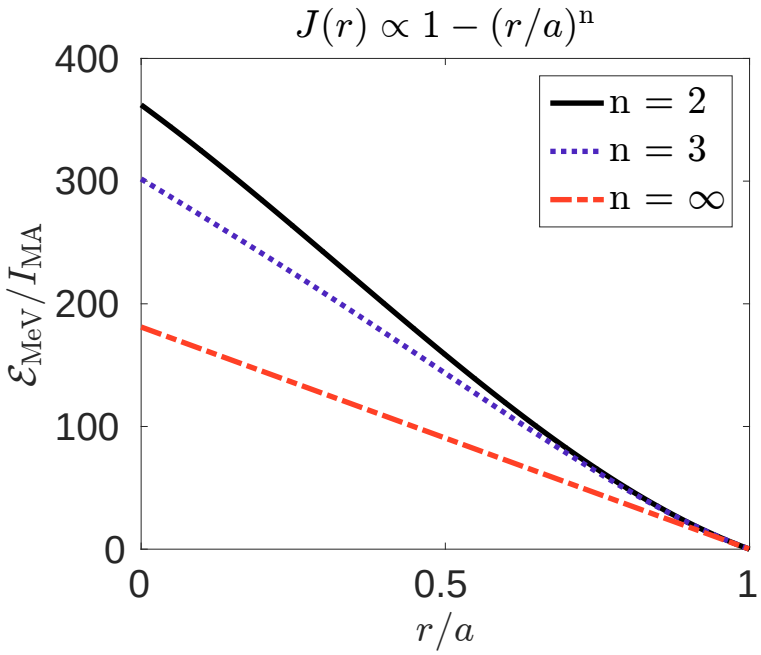

Figure 2.3: The maximum confined runaway energy (in MeV) for a given plasma current (in MA) versus normalized minor radius, calculated from (2.40), for three current density profiles of the form $J(r) \propto 1-(r/a)^{\mathrm{n}}$: parabolic ($\mathrm{n}=2$, solid), cubic ($\mathrm{n}=3$, dotted), and uniform ($\mathrm{n}=\infty$, dot-dashed).

the finite Larmor radius[d] and drift velocity, concluding that runaway diffusion should be *reduced* compared to (2.42). In [21], it was estimated that fluctuation amplitudes of $\delta B/B \geq 10^{-3}$ would be required to suppress a runaway avalanche; that is, for the diffusion rate to be greater than the avalanche growth rate. A similar value was also found from simulations by Papp *et al* [23].

A thorough analysis of runaway diffusion is *not* performed in this thesis due to uncertainties in measured $\delta B/B$. The diagnostics measuring magnetic fluctuations, like the Mirnov coils, are located outside the plasma in the vacuum vessel wall and are not always appropriately calibrated. Thus, it is difficult—or practically impossible—to estimate the amplitude of magnetic perturbations at specific locations within the plasma. The cumulative errors accrued in estimating $\delta B/B$ would then propagate to the calculations of the diffusion coefficient. Nevertheless, the effects of MHD activity, measured as high frequency magnetic oscillations, on runaway dynamics have been observed in C-Mod and are explored further in chapters 6, 7, and 8.

[d]The Larmor radius of a runaway electron can be up to $\gamma c/v_{T\mathrm{e}}$ larger than that of a thermal electron.

2.4 Other energy and particle loss mechanisms

In this section, we briefly discuss some other runaway energy and particle loss mechanisms which are observed in experiment and could play important roles in the dynamics of runaway beams in future tokamaks. However, these mechanisms are not major foci of this thesis work because they were either not relevant to or not directly measured in the runaway experiments of Alcator C-Mod.

2.4.1 Bremsstrahlung

Bremsstrahlung is the "braking radiation" emitted by a charged particle as it is deflected (and often decelerated) by a charged nucleus. Runaway electrons produce bremsstrahlung when either colliding with plasma ions (typically the high-Z impurities) or impacting the tokamak first wall after loss of confinement. The energy of a bremsstrahlung photon is at maximum the energy of the runaway itself, meaning that hard X-rays (HXR) and gammas are often emitted. These signals will be used later in chapters 6-8 to indicate the generation of runaways. As will be discussed, HXR measurements are recorded outside of the C-Mod vacuum vessel, meaning that much of the detected bremsstrahlung is likely produced through runaway-wall impacts. A radially-viewing HXR camera was also available to measure bremsstrahlung from runaway-ion interactions; however, overwhelming photon fluxes caused signal saturation and resulted in inaccurate pulse-height analysis. Thus, the HXR camera data were never analyzed.

Almost all studies of runaways in tokamak plasmas make some use of HXR bremsstrahlung signals. A literature review will not be presented in this section; instead, we argue here that synchrotron radiation is a more significant power loss mechanism for runaways compared to bremsstrahlung. Therefore, it is allowable to neglect bremsstrahlung in the above runaway momentum space evolution of section 2.2 and throughout the rest of this thesis. From [28], the bremsstrahlung reaction *force*, in the high runaway energy limit, is given by

$$F_{\text{brems}} = \frac{\alpha(Z_{\text{eff}}+1)eE_{\text{C}}}{\pi \ln\Lambda}\,(\gamma-1)\left(\ln 2\gamma - \frac{1}{3}\right), \tag{2.43}$$

where $\alpha \approx 1/137$ is the fine-structure constant, and γ is again the relativistic factor. As one might expect, this drag force increases with both Z_{eff} (impurities) and density through $E_{\text{C}} \propto n$.

Note that (2.43) also depends on the runaway energy through γ, just like the synchrotron radiation reaction forces in (2.26) and (2.28). This indicates that there are runaway energies at which synchrotron power loss will dominate that from bremsstrahlung, and vice versa. In [28], a parameter scan of kinetic simulations (using CODE [13, 14], to be described in chapter 5) found

that the effect of synchrotron radiation on the runaway momentum space distribution function is *more significant* than that of bremsstrahlung when

$$B^2 \gtrsim n_{20} \frac{E}{E_{\mathrm{C}}}. \tag{2.44}$$

Here, B is the magnetic field strength in Tesla, n_{20} is the plasma (electron) density in 10^{20} m^{-3}, and E/E_{C} is the typical ratio of the electric and critical [4] fields. For typical runaway discharges in C-Mod, with $B \approx 5$ T, $n_{20} \approx 0.5$, and $E/E_{\mathrm{C}} \approx 5$, we see that synchrotron radiation dominates bremsstrahlung by an order of magnitude. However during disruptions, when densities increase multifold due to impurity injections and the induced electric field is $E/E_{\mathrm{C}} \gg 1$, bremsstrahlung could become comparable to or surpass even synchrotron radiation as a power loss mechanism for runaways.

Interestingly, there is no Z_{eff} dependence in (2.44). As described in [28], while synchrotron power does not explicit depend on Z_{eff}, increased collisions lead to pitch angle scattering, which enters the Larmor formula (2.21) through $v_\perp = v \sin\theta_{\mathrm{p}}$. Thus, the Z_{eff} dependencies of synchrotron radiation and bremsstrahlung effectively cancel each other out.

2.4.2 Kinetic instabilities

As discussed in section 2.3, magnetic fluctuations can enhance runaway electron losses due to increased radial transport. Sometimes, these magnetic perturbations are even excited by the runaway beam itself, through kinetic instabilities and wave-particle interactions. Runaway-driven waves and modes are an active area of research, and the purpose of this section is *not* to provide an exhaustive review of the topic. Rather, we will give a general physical picture for how these excitation processes occur, note some recent theoretical and experimental work on runaway-related instabilities, and mention possible future applications for runaway mitigation strategies.

A good physical picture of the runaway beam instability was given in the early theoretical work of Parail and Pogutse [29] and was well-summarized in a later experimental study by Luckhardt *et al* [30]: Subject to a sufficiently strong external electric field or other electron-heating mechanisms (such as lower hybrid current drive), the plasma electron distribution function becomes increasingly elongated in the direction of acceleration, parallel to the magnetic field. For sufficient densities of energetic electrons, wave-particle resonances can occur, satisfying

$$\omega - k_\parallel v_\parallel - \ell\omega_B = 0, \tag{2.45}$$

where ω and $k_\parallel$ are the frequency and parallel wavevector of excited wave, respectively; $v_\parallel$ is the electron parallel velocity; ℓ is an integer; and ω_B is again the relativistic gyro-frequency. The

anomalous Doppler, Cherenkov, and Doppler resonances occur when $\ell =$ -1, 0, and 1, respectively.

From [29], as electrons accelerate to higher parallel velocities, the anomalous Doppler resonance will cause pitch angle scattering, thereby transferring parallel to perpendicular energy and making the distribution function more isotropic. This effective decrease in the population of high-$v_\parallel$ electrons can then trigger a Cherenkov resonance, which further reduces the energetic electron population. If the driving force is still present, this population can reform, and the cycle continues. The loss of confinement of this hot electron tail, due to this resonance cycle, has been observed, for instance, on the Versator II tokamak [30].

Note that sufficiently large pitch angle scattering could lead to *trapped* electron orbits. Recall that the *classical* trapped particle criterion is

$$\sin\theta_{\rm p} \geq \left(\frac{B_{\rm min}}{B_{\rm max}}\right)^{1/2}, \tag{2.46}$$

where $B_{\rm min}$ and $B_{\rm max}$ are the minimum and maximum strengths of the magnetic field along the particle's trajectory. For a tokamak with aspect ratio $A \approx 3$, a particle must have a pitch angle $\theta_{\rm p} \geq \pi/4$ rad in order to be trapped. As will be seen in upcoming chapters, runaways with such large pitch angles are either too low in number or low enough in energy that their synchrotron radiation is not measurable by our detectors. Thus, trapped runaways are not treated explicitly in this thesis work. Even so, kinetic instabilities are still likely excited and may even be observed in C-Mod, as discussed in chapter 7.

Recently, high frequency magnetic fluctuations have been observed and correlated with runaway electrons in the DIII-D tokamak. For the first time in a tokamak plasma, runaway-driven Whistler waves were detected, in the range 100-200 MHz [31].[e] The generation of these Whistlers was attributed to runaways, with energies $\geq$7 MeV, exciting an anomalous Doppler resonance. Furthermore, magnetic fluctuations, with frequencies of a few MHz, were measured during the formation of a runaway plateau in DIII-D [32]. It was inferred from these observations that runaways with energies $\geq$2.5-3 MeV were required to excite this kinetic instability, although the exact type of wave was not determined. In the former study [31], the Whistler waves were correlated with oscillations in electron cyclotron emission, indicating increased pitch angle scattering; the latter study [32] concluded that the excited modes were correlated with runaway losses. Thus, future runaway mitigation strategies could involve injecting Whistler waves or exciting appropriate plasma modes in order to increase runaway power and particle losses.

[e] To the author's knowledge, C-Mod does not have magnetic probes that can measure such high frequencies.

References—Chapter 2

[1] J.P. Freidberg. *Plasma Physics and Fusion Energy*. Cambridge University Press, 2008.

[2] H. Dreicer. Electron and ion runaway in a fully ionized gas. I. *Physical Review*, 115:238–249, 1959.

[3] H. Dreicer. Electron and ion runaway in a fully ionized gas. II. *Physical Review*, 117:329–342, 1960.

[4] J.W. Connor and R.J. Hastie. Relativistic limitations on runaway electrons. *Nuclear Fusion*, 15(3):415, 1975.

[5] J.R. Martín-Solís, R. Sánchez, and B. Esposito. Experimental observation of increased threshold electric field for runaway generation due to synchrotron radiation losses in the FTU tokamak. *Phys. Rev. Lett.*, 105:185002, 2010.

[6] R.S. Granetz, B. Esposito, J.H. Kim, R. Koslowski, M. Lehnen, J.R. Martín-Solís, C. Paz-Soldan, T. Rhee, J.C. Wesley, L. Zeng, and ITPA MHD Group. An ITPA joint experiment to study runaway electron generation and suppression. *Physics of Plasmas*, 21(7):072506, 2014.

[7] R. Jayakumar, H.H. Fleischmann, and S.J. Zweben. Collisional avalanche exponentiation of runaway electrons in electrified plasmas. *Physics Letters A*, 172(6):447 – 451, 1993.

[8] M.N. Rosenbluth and S.V. Putvinski. Theory for avalanche of runaway electrons in tokamaks. *Nuclear Fusion*, 37(10):1355, 1997.

[9] A.H. Boozer. Runaway electrons and ITER. *Nuclear Fusion*, 57(5):056018, 2017.

[10] J.R. Martín-Solís, J.D. Alvarez, R. Sánchez, and B. Esposito. Momentum-space structure of relativistic runaway electrons. *Physics of Plasmas*, 5(6):2370–2377, 1998.

[11] G. Fussmann. On the motion of runaway electrons in momentum space. *Nuclear Fusion*, 19(3):327–334, 1979.

[12] B. Kurzan, K.-H. Steuer, and G. Fussmann. Dynamics of runaway electrons in the magnetic field of a tokamak. *Phys. Rev. Lett.*, 75:4626–4629, 1995.

[13] M. Landreman, A. Stahl, and T. Fülöp. Numerical calculation of the runaway electron distribution function and associated synchrotron emission. *Computer Physics Communications*, 185(3):847 – 855, 2014.

[14] A. Stahl, O. Embréus, G. Papp, M. Landreman, and T. Fülöp. Kinetic modelling of runaway electrons in dynamic scenarios. *Nuclear Fusion*, 56(11):112009, 2016.

[15] H. Knoepfel and D.A. Spong. Runaway electrons in toroidal discharges. *Nuclear Fusion*, 19(6):785, 1979.

[16] J.R. Myra and P.J. Catto. Effect of drifts on the diffusion of runaway electrons in tokamak stochastic magnetic fields. *Physics of Fluids B: Plasma Physics*, 4(1):176–186, 1992.

[17] B. Esposito, J.R. Martín Solís, P. van Belle, O.N. Jarvis, F.B. Marcus, G. Sadler, R. Sánchez, B. Fischer, P. Froissard, J.M. Adams, E. Cecil, and N. Watkins. Runaway electron measurements in the JET tokamak. *Plasma Physics and Controlled Fusion*, 38(12):2035, 1996.

[18] J.R. Martín-Solís, R. Sánchez, and B. Esposito. Effect of magnetic and electrostatic fluctuations on the runaway electron dynamics in tokamak plasmas. *Physics of Plasmas*,

6(10):3925–3933, 1999.

[19] A.B. Rechester and M.N. Rosenbluth. Electron heat transport in a tokamak with destroyed magnetic surfaces. *Phys. Rev. Lett.*, 40:38–41, 1978.

[20] H.E. Mynick and J.D. Strachan. Transport of runaway and thermal electrons due to magnetic microturbulence. *The Physics of Fluids*, 24(4):695–702, 1981.

[21] P. Helander, L.-G. Eriksson, and F. Andersson. Suppression of runaway electron avalanches by radial diffusion. *Physics of Plasmas*, 7(10):4106–4111, 2000.

[22] A. Wingen, S.S. Abdullaev, K.H. Finken, M. Jakubowski, and K.H. Spatschek. Influence of stochastic magnetic fields on relativistic electrons. *Nuclear Fusion*, 46(11):941, 2006.

[23] G. Papp, M. Drevlak, T. Fülöp, P. Helander, and G.I. Pokol. Runaway electron losses caused by resonant magnetic perturbations in ITER. *Plasma Physics and Controlled Fusion*, 53(9):095004, 2011.

[24] G. Papp, M. Drevlak, T. Fülöp, and G.I. Pokol. The effect of resonant magnetic perturbations on runaway electron transport in ITER. *Plasma Physics and Controlled Fusion*, 54(12):125008, 2012.

[25] G. Papp, M. Drevlak, G.I. Pokol, and T. Fülöp. Energetic electron transport in the presence of magnetic perturbations in magnetically confined plasmas. *Journal of Plasma Physics*, 81(5):475810503, 2015.

[26] O.J. Kwon, P.H. Diamond, F. Wagner, G. Fussmann, and ASDEX Team and NI Team. A study of runaway electron confinement in the ASDEX tokamak. *Nuclear Fusion*, 28(11):1931, 1988.

[27] J.D. Strachan. Runaway electron transport in the LT-3 tokamak. *Nuclear Fusion*, 16(5):743–751, 1976.

[28] O. Embréus, A. Stahl, S. Newton, G. Papp, Ee. Hirvijoki, and T. Fülöp. Effect of bremsstrahlung radiation emission on distributions of runaway electrons in magnetized plasmas. *arXiv preprint arXiv:1511.03917*, 2015.

[29] V.V. Parail and O.P. Pogutse. The kinetic theory of runaway electron beam instability in a tokamak. *Nuclear Fusion*, 18(3):303–314, 1978.

[30] S.C. Luckhardt, K-I. Chen, M.J. Mayberry, M. Porkolab, Y. Terumichi, G. Bekefi, F.S. McDermott, and R. Rohatgi. Particle confinement and the anomalous Doppler instability during combined inductive and lower-hybrid current drive. *The Physics of Fluids*, 29(6):1985–1993, 1986.

[31] D.A. Spong, W.W. Heidbrink, C. Paz-Soldan, X.D. Du, K.E. Thome, M.A. Van Zeeland, C. Collins, A. Lvovskiy, R.A. Moyer, M.E. Austin, D.P. Brennan, C. Liu, E.F. Jaeger, and C. Lau. First direct observation of runaway-electron-driven Whistler waves in tokamaks. *Phys. Rev. Lett.*, 120:155002, 2018.

[32] A Lvovskiy, C Paz-Soldan, N W Eidietis, A Dal Molin, X D Du, L Giacomelli, J L Herfindal, E M Hollmann, L Martinelli, R A Moyer, M Nocente, D Rigamonti, D Shiraki, M Tardocchi, and K E Thome. The role of kinetic instabilities in formation of the runaway electron current after argon injection in DIII-d. *Plasma Physics and Controlled Fusion*, 60(12):124003, nov 2018.

This page intentionally left blank

Chapter 3

Synchrotron radiation

As a non-relativistic charged particle executes circular motion due to its presence in a magnetic field, it emits quasi-isotropic *cyclotron* radiation primarily at low-integer harmonics of its rotation frequency. However, if its speed should approach that of light, the now relativistic particle emits velocity-directed *synchrotron* emission in a continuum of frequencies much higher than its now relativistically-lowered gyro-frequency. The properties of observed synchrotron emission—including intensity, wavelength, polarization, and spatial distribution—can reveal properties of the emitting relativistic particle, like its position and momentum.[a] Ultimately, synchrotron emission will be used in this work to study properties of the entire phase-space distribution of relativistic runaway electrons in a magnetized (tokamak) plasma.

This chapter is organized as follows: In section 3.1, we will derive the relativistic equations of motion of an electron in a magnetic field. Section 3.2 will follow the derivation of polarized synchrotron radiation (spectra) from Westfold [1]. Synchrotron radiation spectra, from Schwinger [2] and Pankratov [3], will be discussed in section 3.3, with a (synthetic) calculation of the expected spectral radiance (or brightness) presented in section 3.4.

3.1 Relativistic gyro-motion

Consider an electron with (rest) mass m and charge $-e$ moving in a background magnetic field $\boldsymbol{B}$ (assuming no electric field, $\boldsymbol{E} = 0$).[b] The relativistic equation of motion is given by the Lorentz force,

$$\frac{\mathrm{d}\boldsymbol{p}}{\mathrm{d}t} = -e\boldsymbol{v} \times \boldsymbol{B}, \tag{3.1}$$

[a] Uncertainties still governed by the Heisenberg principle.

[b] Note that we drop the subscript e from $m_\mathrm{e} \to m$ in this chapter.

where $\boldsymbol{p} = \gamma m \boldsymbol{v}$ is the relativistic momentum, $\gamma = 1/\sqrt{1 - v^2/c^2}$ is the relativistic factor, $\boldsymbol{v}$ is the electron velocity, and c is the vacuum speed of light. Normalizing by c and assuming conservation of energy ($\mathcal{E} = \gamma m c^2 =$ constant),

$$\frac{\mathrm{d}}{\mathrm{d}t}\frac{m\boldsymbol{\beta}}{\sqrt{1-\beta^2}} = \frac{m}{\sqrt{1-\beta^2}}\frac{\mathrm{d}\boldsymbol{\beta}}{\mathrm{d}t} = -e\boldsymbol{\beta} \times \boldsymbol{B}. \tag{3.2}$$

Note how the acceleration is always perpendicular to the both the velocity and magnetic field. Define the relativistic gyro-frequency to be $\omega_B = eB/\gamma m$ so that

$$\dot{\boldsymbol{\beta}} = -\boldsymbol{\omega_B} \times \boldsymbol{\beta}. \tag{3.3}$$

This is just helical motion, with a constant velocity parallel to $\boldsymbol{B}$ and cyclotron motion perpendicular to $\boldsymbol{B}$. Let the Cartesian coordinate system be such that the electron starts at $z = 0$ on the x-axis, with initial perpendicular velocity in the y-direction and $\boldsymbol{B} = B_0\hat{z}$. Define the pitch angle as $\tan\theta_\mathrm{p} = \beta_\perp/\beta_\parallel$, where $\beta_\perp$ and $\beta_\parallel$ are the components of the velocity parallel and perpendicular to $\boldsymbol{B}$, respectively. Let the gyro-angle be $\chi = \omega_B t$, where t is time. Then the position vector is

$$\boldsymbol{r}(t) = \frac{\beta c}{\omega_B}\left[(\hat{x}\,\cos\chi + \hat{y}\,\sin\chi)\sin\theta_\mathrm{p} + \hat{z}\,\chi\cos\theta_\mathrm{p}\right], \tag{3.4}$$

and velocity vector is

$$\boldsymbol{\beta}(t) = \beta\left[(-\hat{x}\,\sin\chi + \hat{y}\,\cos\chi)\sin\theta_\mathrm{p} + \hat{z}\,\cos\theta_\mathrm{p}\right]. \tag{3.5}$$

The instantaneous curvature can be related to (3.5) via the tangent vector $\hat{\beta} = \boldsymbol{\beta}/\beta$ and

$$\dot{\hat{\beta}} = -\omega_B \sin\theta_\mathrm{p}\,(\hat{x}\,\cos\chi + \hat{y}\,\sin\chi + 0\hat{z}\,). \tag{3.6}$$

The radius of curvature is constant in this case,

$$R_\mathrm{c} = \frac{1}{\kappa} = \frac{|\boldsymbol{v}|}{|\dot{\hat{\beta}}|} = \frac{\beta c}{\omega_B \sin\theta_\mathrm{p}}. \tag{3.7}$$

The *total* power radiated by the particle is given by the relativistic Larmor formula,

$$P = \frac{q^2}{6\pi\epsilon_0 c}\gamma^6\left[\dot{\boldsymbol{\beta}}^2 - \left(\boldsymbol{\beta}\times\dot{\boldsymbol{\beta}}\right)^2\right], \tag{3.8}$$

Inserting (3.5) and (3.6), we find the familiar relation

$$P = \frac{e^4 p_\perp^2 B^2}{6\pi\epsilon_0 m^4 c^3}. \tag{3.9}$$

For an electron with energy $\mathcal{E} = 30$ MeV ($\gamma \approx 60$) and pitch angle $\theta_\mathrm{p} = 0.1$ rad inside Alcator C-Mod ($B_0 = 5.4$ T), the power radiated away is over 100 MeV/s!

3.2 Polarized synchrotron radiation

This section follows the derivation of the polarization and spectrum of synchrotron radiation performed by Westfold in 1959 [1]. Note that the synchrotron spectrum had already been calculated by Scwhinger in 1949 [2], but polarization had not been considered. There are several other ways to perform the following derivation—some even more straightforward, like that in [4]. However, the following gives a solution in a form typically used when modeling runaway electrons.

3.2.1 Geometric considerations

An accelerating charge, like a gyrating electron, always emits electromagnetic radiation. The aim of this chapter is to calculate the frequency-dependent, oscillating electric field $\boldsymbol{E}$, observed at position $\boldsymbol{r}_\mathrm{o}$ and produced by one electron at position $\boldsymbol{r}$ with energy $\mathcal{E} = \gamma mc^2$ and pitch angle θ_p. As will be described in the next section, this cyclotron radiation becomes highly-directional for relativistic particles ($\beta \approx 1$) with the peak of emission along $\boldsymbol{\beta}$; this is then called synchrotron radiation. The geometry to consider is shown in figure 3.1.

The gyro-motion of the electron is shown at right in figure 3.1, with gyro-angle χ. As in the previous section, the instantaneous perpendicular velocity at $t = 0$ is in the $\hat{y}$-direction, and the magnetic field $\boldsymbol{B}$ is in the $\hat{z}$-direction. The pitch angle between $\boldsymbol{B}$ and $\boldsymbol{\beta}$ is θ_p. The synchrotron emission is shown schematically in grey with a *finite* angular width $\xi \approx 1/\gamma$, which will be derived in the next section. The vector from the electron position to the observation point is $\boldsymbol{R} = \boldsymbol{r}_\mathrm{o} - \boldsymbol{r}$, with unit vector $\hat{n}$ in that direction. The angle between $\boldsymbol{\beta}$ and $\hat{n}$ *at this moment in time* is called ψ; for other gyro-angles χ this angle will be called ϑ. This notation is chosen for consistency with the original sources, e.g. [1].

The following calculation will rely on the smallness of certain quantities: For $\gamma \gg 1$, it follows that $\xi \ll 1$, and because $\hat{n}$ must lie within this angular width for any radiation to be observed, $\psi \sim O(\xi) \ll 1$. The gyro-motion will ultimately sweep the emission to produce a "cone," but there is only a small range of $\chi \ll 1$ which will direct emission toward $\boldsymbol{r}_\mathrm{o}$. Finally, a far-field approximation is assumed such that $|\boldsymbol{r}_\mathrm{o}| \gg |\boldsymbol{r}|$, which leads to the approximation

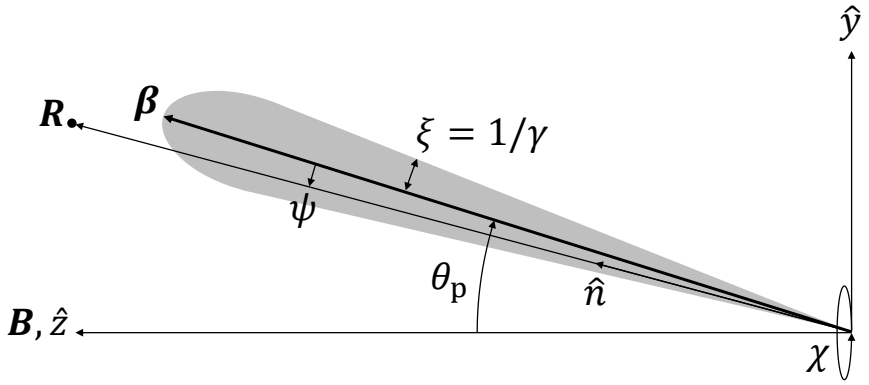

Figure 3.1: A schematic representation of synchrotron emission (in grey) at one moment in time t. A relativistic electron, instantaneously located at the origin, executes gyro-motion in a magnetic field $\boldsymbol{B} = B_0\hat{z}$ with normalized velocity $\boldsymbol{\beta} = \hat{y}\,\beta_\perp + \hat{z}\,\beta_\parallel$, pitch angle $\theta_{\rm p}$, and gyro-angle $\chi = \omega_B t$. The emission, with angular width $\xi \sim 1/\gamma$, is observed at position $\boldsymbol{R}$ along line-of-sight $\hat{n}$, with angle ψ from $\boldsymbol{\beta}$ to $\hat{n}$.

$R = |\boldsymbol{R}| \approx r_{\rm o} - \hat{n}\cdot\boldsymbol{r}$. Therefore, in the following section, expansions will be carried out for ξ, ψ, and χ, but not for the pitch angle $\theta_{\rm p}$.

3.2.2 Electric field calculation

The oscillating electric field observed at position $\boldsymbol{r}_{\rm o}$ and time t arising from a arbitrarily-moving charge (electron) is given by the Liénard-Wiechert field,

$$\boldsymbol{E}(\boldsymbol{r}_{\rm o}, t) = \frac{\mu_0 e c}{4\pi}\left[\frac{c}{\gamma^2}\frac{\hat{n}-\boldsymbol{\beta}}{R^2(1-\boldsymbol{\beta}\cdot\hat{n})^3} + \frac{\hat{n}\times\left((\hat{n}-\boldsymbol{\beta})\times\dot{\boldsymbol{\beta}}\right)}{R(1-\boldsymbol{\beta}\cdot\hat{n})^3}\right]_{t_{\rm r}}. \tag{3.10}$$

Here, all terms within the brackets are evaluated at the *retarded* time $t_{\rm r} = t - R(t_{\rm r})/c$, and μ_0 is the permeability of free space. The corresponding magnetic field is just $\boldsymbol{B} = \hat{n}\times\boldsymbol{E}/c$, assuming propagation in free space.[c] We are interested in electromagnetic *radiation*, which means that energy must be transported by the waves to arbitrary distances. That is,

$$\int 4\pi R^2\,\boldsymbol{S}\cdot\mathrm{d}\boldsymbol{R} > 0 \tag{3.11}$$

[c]Electromagnetic wave propagation in plasmas is quite complex; however, we are ultimately interested in visible/infrared light frequencies far greater than the plasma frequency.

for $R \to \infty$. Here, $\boldsymbol{S} = \boldsymbol{E} \times \boldsymbol{B}/\mu_0$ is the Poynting vector. The first term in (3.10) is proportional to $1/R^2$, whereas the second goes like $1/R$; thus, we only consider the second term

$$\boldsymbol{E}(\boldsymbol{r}_{\rm o}, t) \approx \frac{\mu_0 e c}{4\pi R} \left[\frac{\hat{n} \times \left((\hat{n} - \boldsymbol{\beta}) \times \dot{\boldsymbol{\beta}} \right)}{(1 - \boldsymbol{\beta} \cdot \hat{n})^3} \right]_{t_{\rm r}}. \tag{3.12}$$

To show that this radiation will be highly-directional for relativistic particles, let the angle between $\boldsymbol{\beta}$ and $\hat{n}$ be ϑ, so that the denominator goes like $(1 - \beta \cos\vartheta)^3$. For $\beta \approx 1$, this implies that the peaks of emission occur at $\vartheta = 0$, i.e. when $\boldsymbol{\beta}$ and $\hat{n}$ are parallel. The angular width of the emission can be estimated in the "ultra-relativistic" limit (i.e. $\gamma \gg 1$, $\beta \to 1$). Rearranging the relativistic factor and Taylor expanding in terms of $\xi = 1/\gamma$ gives

$$\beta = \sqrt{1 - \gamma^{-2}} \approx 1 - \frac{1}{2}\xi^2. \tag{3.13}$$

For small values of ϑ, we Taylor expand and compute

$$1 - \beta \cos\vartheta \approx 1 - \left(1 - \frac{1}{2}\xi^2\right)\left(1 - \frac{1}{2}\vartheta^2\right) \approx \frac{1}{2}\left(\xi^2 + \vartheta^2\right) \tag{3.14}$$

For fixed $\gamma = 1/\xi$, a "threshold" is reached when $\vartheta \sim \xi$. Thus, $\vartheta \sim 1/\gamma$ is taken to be the approximate angular width of the "cone" of synchrotron emission produced from the gyro-motion.

The total electric field received at $\boldsymbol{r}_{\rm o}$ can be represented as a superposition of the harmonics $\rm n$ of ω_B:

$$\boldsymbol{E}(\boldsymbol{r}_{\rm o}, t) = \sum_{\rm n=-\infty}^{\infty} \boldsymbol{E}_{\rm n} \exp(-in\omega_B t). \tag{3.15}$$

Therefore, an individual harmonic can be selected via

$$\boldsymbol{E}_{\rm n}(\boldsymbol{r}_{\rm o}) = \frac{\omega_B}{2\pi} \int_0^{2\pi/\omega_B} \boldsymbol{E}(\boldsymbol{r}_{\rm o}, t) \exp(i{\rm n}\omega_B t) {\rm d}t. \tag{3.16}$$

Plugging in (3.12) for $\boldsymbol{E}(\boldsymbol{r}_{\rm o}, t)$ and converting to the particle (retarded) time yields

$$\boldsymbol{E}_n(\boldsymbol{r}_{\rm o}) = \frac{\mu_0 e c \omega_B}{8\pi^2 r_{\rm o}} \int_0^{2\pi/\omega_B} \frac{\hat{n} \times \left((\hat{n} - \boldsymbol{\beta}) \times \dot{\boldsymbol{\beta}} \right)}{(1 - \boldsymbol{\beta} \cdot \hat{n})^3} \exp\left[i{\rm n}\omega_B \left(t_{\rm r} + \frac{r_{\rm o} - \hat{n} \cdot \boldsymbol{r}}{c} \right) \right] \frac{{\rm d}t_{\rm r}}{{\rm d}t} {\rm d}t_{\rm r} \tag{3.17}$$

Here, all quantities are evaluated at the retarded time $t_{\rm r}$, the derivative ${\rm d}t_{\rm r}/{\rm d}t = 1 - \boldsymbol{\beta} \cdot \hat{n}$, and the far-field approximation has been used. Removing (and dropping) the phase factor $\exp(in\omega_B r_{\rm o}/c)$

from the integral and simplifying leaves

$$\boldsymbol{E}_n(\boldsymbol{r}_\mathrm{o}) = \frac{\mu_0 e c \omega_B}{8\pi^2 r_\mathrm{o}} \int_0^{2\pi/\omega_B} \frac{\hat{n} \times \left((\hat{n} - \boldsymbol{\beta}) \times \dot{\boldsymbol{\beta}}\right)}{(1 - \boldsymbol{\beta} \cdot \hat{n})^2} \exp\left[i n \omega_B \left(t_\mathrm{r} - \frac{\hat{n} \cdot \boldsymbol{r}}{c}\right)\right] \mathrm{d}t_\mathrm{r} \tag{3.18}$$

This is the equation we need to solve. Using the geometry described in the previous section, define

$$\begin{aligned} \hat{n} &= 0\hat{x} + \hat{y}\,\sin(\theta_\mathrm{p} - \psi) + \hat{z}\,\cos(\theta_\mathrm{p} - \psi) && (3.19)\\ &= 0\hat{x} + \hat{y}\,(\sin\theta_\mathrm{p}\cos\psi - \cos\theta_\mathrm{p}\sin\psi) + \hat{z}\,(\cos\theta_\mathrm{p}\cos\psi + \sin\theta_\mathrm{p}\sin\psi) && (3.20) \end{aligned}$$

where the second line results from the double angle formulas. Next, define the unit vector in the direction of $\boldsymbol{\beta}$,

$$\hat{\beta} = \boldsymbol{\beta}/\beta = -\hat{x}\,\sin\theta_\mathrm{p}\cos\chi + \hat{y}\,\sin\theta_\mathrm{p}\sin\chi + \hat{z}\,\chi\cos\theta_\mathrm{p}. \tag{3.21}$$

The denominator of (3.18) can then be calculated via

$$1 - \boldsymbol{\beta}\cdot\hat{n} \approx 1 - \left(1 - \frac{1}{2}\xi^2\right)\cos\vartheta \approx 1 - \left(1 - \frac{1}{2}\xi^2\right)\left(1 - \frac{1}{2}\vartheta^2\right) \approx \frac{1}{2}\left(\vartheta^2 + \xi^2\right) \tag{3.22}$$

where expansions were carried out in ϑ and ξ. Furthermore, a direct computation of $\boldsymbol{\beta}\cdot\hat{n}$ gives

$$\begin{aligned} \boldsymbol{\beta}\cdot\hat{n} &= \sin(\theta_\mathrm{p} - \psi)\sin\theta_\mathrm{p}\cos\chi + \cos(\theta_\mathrm{p} - \psi)\cos\theta_\mathrm{p} && (3.23)\\ 1 - \frac{1}{2}\vartheta^2 &\approx 1 - \frac{1}{2}\psi^2 - \frac{1}{2}\chi^2\sin^2\theta_\mathrm{p}\left(1 - \frac{1}{2}\psi^2\right) + \frac{1}{2}\psi\chi^2\sin\theta_\mathrm{p}\cos\theta_\mathrm{p} && (3.24) \end{aligned}$$

Keeping only terms to second order gives $\vartheta^2 \approx \psi^2 + \chi^2\sin^2\theta_\mathrm{p}$; thus, the denominator of the integral is

$$(1 - \boldsymbol{\beta}\cdot\hat{n})^2 \approx \frac{1}{4}(\xi^2 + \psi^2 + \chi^2\sin^2\theta_\mathrm{p})^2 \tag{3.25}$$

Next, consider the exponent in (3.18), $\omega_B(t_\mathrm{r} - \hat{n}\cdot\boldsymbol{r}/c) = \chi - \omega_B\hat{n}\cdot\boldsymbol{r}/c$. The second term can be computed from (3.4) and (3.20):

$$\begin{aligned} \frac{\omega_B}{c}\hat{n}\cdot\boldsymbol{r} &= \beta\left(\sin(\theta_\mathrm{p} - \psi)\sin\theta_\mathrm{p}\sin\chi + \chi\cos(\theta_\mathrm{p} - \psi)\cos\theta_\mathrm{p}\right)\\ &\approx \left(1 - \frac{1}{2}\xi^2\right)\left[\chi\left(1 - \frac{1}{2}\psi^2\right) - \frac{1}{6}\chi^3\sin^2\theta_\mathrm{p}\left(1 - \frac{1}{2}\psi^2\right)\right] && (3.26) \end{aligned}$$

Keeping terms up to third order gives

$$\chi - \frac{\omega_B}{c}\hat{n}\cdot\boldsymbol{r} \approx \frac{1}{2}\chi(\xi^2+\psi^2) + \frac{1}{6}\chi^3\sin^2\theta_\mathrm{p} \tag{3.27}$$

The numerator of (3.18) gets quite messy, so I quote it directly from equation (17) of [1]:

$$\begin{aligned}\boldsymbol{E}_n(\boldsymbol{r}_\mathrm{o}) = \frac{\mu_0 ec\omega_B \sin\theta_\mathrm{p}}{4\pi^2 r_\mathrm{o}} \int_{-\infty}^{\infty} \mathrm{d}\chi \exp\left[\frac{1}{2}i\mathrm{n}\chi\left(\xi^2+\psi^2+\frac{1}{3}\chi^2\sin^2\theta_\mathrm{p}\right)\right] \\ \times \frac{\hat{x}\,\left(\xi^2+\psi^2+\chi^2\sin^2\theta_\mathrm{p}\right) + 2\psi\chi\sin\theta_\mathrm{p}\left(\hat{y}\,\cos\theta_\mathrm{p} - \hat{z}\,\sin\theta_\mathrm{p}\right)}{\left(\xi^2+\psi^2+\chi^2\sin^2\theta_\mathrm{p}\right)^2}.\end{aligned} \tag{3.28}$$

Here, the integration variable $\chi = \omega_B t_\mathrm{r}$ has been substituted, and the integration is performed over all possible values.

Westfold [1] and others [2] recognized that (3.28) takes the form of a modified Bessel function of the second kind $\mathrm{K}_\nu[z]$. From equation (19) of [1], one harmonic of the electric field can be recast as

$$\begin{aligned}\boldsymbol{E}_n(\boldsymbol{r}_\mathrm{o}) = &\frac{\mu_0 ec}{4\sqrt{3}\pi^2 r_\mathrm{o}} \frac{\mathrm{n}\omega_B}{\sin\theta_\mathrm{p}} \exp\left(i\mathrm{n}\omega_B\frac{r_\mathrm{o}}{c}\right) \\ &\times\left\{\hat{x}\,\left(\xi^2+\psi^2\right)\mathrm{K}_{2/3}[z] + \left(\hat{y}\,\cos\theta_\mathrm{p} - \hat{z}\,\sin\theta_\mathrm{p}\right) i\psi\left(\xi^2+\psi^2\right)^{1/2}\mathrm{K}_{1/3}[z]\right\},\end{aligned} \tag{3.29}$$

where

$$z = \frac{\mathrm{n}}{3\sin\theta_\mathrm{p}}\left(\xi^2+\psi^2\right)^{3/2}. \tag{3.30}$$

In (3.29), the extra phase factor has been added back in for completeness. To reiterate, given one electron with energy $\gamma = 1/\xi$ and pitch angle θ_p, the total electric field observed at the far-field position $\boldsymbol{r}_\mathrm{o}$, where the angle between the electron velocity vector and viewing direction is ψ, is the sum over all harmonics $\mathrm{n}\omega_B$, using (3.29) in (3.15). From this, the polarization of the observed synchrotron emission can be calculated, and the power spectrum can be related to the integral of the Poynting vector.

Recall that the relativistic gyro-frequency is a factor $1/\gamma$ smaller than the classical gyro-frequency. Therefore, a relativistic electron with $\gamma = 50$, gyrating in C-Mod's typical toroidal magnetic field $B_0 = 5.4$ T, has a relativistic gyro-frequency of $\omega_B/2\pi \approx 3$ GHz; this corresponds to a fundamental ($\mathrm{n} = 1$) radiation frequency of $\sim$3 GHz and corresponding wavelength of $2\pi c/\omega_B \approx 10$ cm. The radiation wavelengths of interest in this thesis are in the visible/near-infrared range, i.e. $\lambda \approx$ 300-1000 nm or $f \approx$ 300-1000 THz. At these high frequencies, with $\mathrm{n} \sim O(10^6)$, the harmonics are so closely spaced that the spectrum is effectively a continuum, i.e. $\mathrm{n}\omega_B \to \omega$.

3.2.3 Stokes parameters

As the electromagnetic wave travels toward the observer/detector, we assume that its polarization angle does not change. In fact, for such high frequency visible light ($\lambda \approx$ 400-1000 nm), an effect like Faraday rotation would only cause a change in angle of

$$\Delta\theta_{\rm pol} \approx \frac{e^3 nBR}{2\epsilon_0 m^2 c\omega^2} \approx 0.001 \text{ rad},$$

for typical C-Mod parameters. The measured polarization angle $\theta_{\rm pol}$ will depend on the orientation of the detector. Let the detector normal be $\hat{n}_{\rm d}$. Note that $\hat{n}_{\rm d}$ does not necessarily have to be (anti)-parallel to $\hat{n}$; instead, we require that $\hat{n}_{\rm d} \cdot (-\hat{n}) \geq \cos\alpha$, where α is the opening *half*-angle of the detector field-of-view.

To find the projection of $\boldsymbol{E}$ onto the detector plane, define unit vector $\hat{e}_1$ to be perpendicular to $\hat{n}_{\rm d}$ and lie in the horizontal plane, i.e. $\hat{e}_1 \times \hat{n}_{\rm d} = \hat{e}_1 \times \hat{Z} = 0$. Similarly, define unit vector $\hat{e}_2 = \hat{e}_1 \times \hat{n}_{\rm d}$ to form a *left*-handed coordinate system, i.e. $\hat{e}_1 \times \hat{e}_2 = -\hat{n}_{\rm d}$.[d] The components of $\boldsymbol{E}$ along the new axes are simply $E_1 = \boldsymbol{E} \cdot \hat{e}_1$ and $E_2 = \boldsymbol{E} \cdot \hat{e}_2$. The polarization angle $\theta_{\rm pol}$ measured from $\hat{e}_1$ toward $\hat{e}_2$—i.e. from the horizontal—is then $\tan\theta_{\rm pol} = E_2/E_1$.

To include the contribution from all runaways throughout the plasma, all E-field vectors reaching the detector would need to be summed, i.e. $\boldsymbol{E}_{\rm tot} = \sum_i \boldsymbol{E}_i$. However, a more convenient way to keep track of amplitude and polarization information is in the form of a Stokes vector $[I, Q, U, V]$ in which the Stokes parameters are

$$I = |E_1|^2 + |E_2|^2, \tag{3.31}$$
$$Q = |E_1|^2 - |E_2|^2, \tag{3.32}$$
$$U = 2\text{Re}(E_1 E_2^*), \tag{3.33}$$
$$V = -2\text{Im}(E_1 E_2^*), \tag{3.34}$$

where the asterisk (*) means the complex conjugate, and subscripts 1 and 2 refer to an arbitrary orthogonal basis $(\hat{e}_1, \hat{e}_2)$. Conveniently, the total Stokes vector from $\boldsymbol{E}_{\rm tot}$ is the sum of all individual Stokes vectors from each $\boldsymbol{E}_i$. We see that I is just the total intensity. The intensities of linearly and circularly-polarized light are given by $L = \sqrt{Q^2 + U^2}$ and V, respectively. Thus, the *degrees* or *fractions* of linearly and circularly-polarized light are $\text{f}_{\rm lin} = L/I$ and $\text{f}_{\rm circ} = V/I$. Finally, the polarization angle is given by $\tan(2\theta_{\rm pol}) = U/Q$, measured from $\hat{e}_1$ toward $\hat{e}_2$.[e] Note that $\theta_{\rm pol}$ is degenerate with $\theta_{\rm pol} + \pi$ due to the oscillatory nature of $\boldsymbol{E}$.

[d] This is done as a matter of convenience since the motional Stark effect diagnostic measures the polarization angle from $\hat{Z}$ toward $\hat{R}$. For $\hat{\phi}$ counterclockwise, $(\hat{R}, \hat{Z}, \hat{\phi})$ is left-handed.

[e] This is the *opposite* of typical C-Mod MSE measurements, where $\theta_{\rm pol}$ is measured from $\hat{e}_2$ toward $\hat{e}_1$.

3.3 Synchrotron radiation spectra

Calculated by Schwinger in 1949, the angular and spectral synchrotron power density is given by equation (II.34) of [2],

$$\frac{\mathrm{d}P}{\mathrm{d}\Omega \mathrm{d}\omega} = \frac{3e^2}{4\pi^2 \epsilon_0 R_c} \left(\frac{\omega}{\omega_\mathrm{c}}\right)^2 \gamma^2 \left(1+\gamma^2\psi^2\right)^2 \left[\mathrm{K}^2_{2/3}\left(\bar{z}\right) + \frac{\gamma^2\psi^2}{1+\gamma^2\psi^2}\mathrm{K}^2_{1/3}\left(\bar{z}\right)\right], \tag{3.35}$$

where R_c is the radius of curvature given by (3.7), $\omega_\mathrm{c} = 3\gamma^3 c/2R_\mathrm{c}$, and

$$\bar{z} = \frac{\omega}{2\omega_\mathrm{c}}\left(1+\gamma^2\psi^2\right)^{3/2} \approx \frac{n}{3\sin\theta_\mathrm{p}}\left(\xi^2+\psi^2\right)^{3/2}. \tag{3.36}$$

The approximation assumes $\beta \approx 1$ and $\omega = n\omega_B$. As expected, (3.35) shares many similarities with (3.29). This can be integrated over all solid angles to obtain the spectral power density in equation (II.16) of [2],

$$\frac{\mathrm{d}P}{\mathrm{d}\omega} = \frac{3\sqrt{3}e^2\gamma^4 c}{4\pi\epsilon_0 R_c^2}\frac{\omega}{\omega_\mathrm{c}^2}\int_{w/\omega_\mathrm{c}}^{\infty} \mathrm{K}_{5/3}\left[z\right]\mathrm{d}z. \tag{3.37}$$

This equation is *general*, accounting for any radius of curvature R_c. In [3], Pankratov computed (3.37) for particle motion in a tokamak magnetic geometry, including the effect of the vertical centrifugal drift and averaging over gyro-angles. The final form of the synchrotron power spectra can be found in equation (15) of [3], but is more conveniently expressed as a function of wavelength λ in equations (2)-(4) of [5]:

$$\begin{aligned}\frac{\mathrm{d}P}{\mathrm{d}\lambda} = \frac{ce^2}{\epsilon_0\lambda^3\gamma^2}\Bigg\{ &-\frac{\pi}{2} + \int_0^\infty \frac{\mathrm{d}y}{y}\left(1+2y^2\right)J_0\left(ay^3\right)\sin\left[\frac{3}{2}\zeta\left(y+\frac{y^3}{3}\right)\right] \\ &- \frac{4\eta}{1+\eta^2}\int_0^\infty \mathrm{d}y\, y J_0'\left(ay^3\right)\cos\left[\frac{3}{2}\zeta\left(y+\frac{y^3}{3}\right)\right]\Bigg\}\end{aligned} \tag{3.38}$$

where $J_0(z)$ is a Bessel function of the first kind, $J_0'(z) = \mathrm{d}J_0(z)/\mathrm{d}z = -J_1(z)$,

$$a = \zeta\eta/(1+\eta^2), \tag{3.39}$$

$$\zeta = \frac{4\pi}{3}\frac{R_0}{\lambda\gamma^3\sqrt{1+\eta^2}}, \tag{3.40}$$

$$\eta = \omega_B R_0 \frac{\beta_\perp}{\beta_\parallel^2}, \tag{3.41}$$

and R_0 is the tokamak major radius.

Wrapped up in (3.38) are the runaway energy ($\mathcal{E} = \gamma mc^2$), runaway pitch angle ($\tan\theta_\mathrm{p} = \beta_\perp/\beta_\parallel$), and magnetic field ($\omega_B = eB/\gamma m$). The synchrotron power spectra, scanned over these three parameters, are plotted in figure 3.2 for the visible and infrared wavelength ranges. The calculations were performed with the code SYRUP, first introduced in [5], which numerically integrates the strongly-oscillating integrands of (3.38).

As seen in figure 3.2, the spectral amplitude increases with p/mc, θ_p, and B while holding all other variables constant; this means that the total power radiated—the area under the curve—also increases, as expected. Note that the spectral peak shifts toward shorter ("bluer") wavelengths as these same parameters increase. Therefore, for the range of toroidal fields on Alcator C-Mod of $B_0 \approx$ 2-8 T, we expect a non-negligible fraction of synchrotron light to be observed in the visible/near-IR wavelength range, $\lambda \approx$ 300-1000 nm. Moreover, the spectral peak is even predicted to move within this range for high enough energies, pitch angles, and/or magnetic fields. The observation of visible synchrotron emission by in-vessel cameras ($\lambda \approx$ 400-900 nm) and the motional Stark effect diagnostic ($\lambda \approx$ 660 nm) motivated the purchase of two visible spectrometers to specifically study runaway spectra. The prospect of measuring this spectral peak motivated this thesis work.

3.4 Synthetic brightness calculations

The quantity measured by spectrometers is usually *not* the spectral power density $\mathrm{d}P/\mathrm{d}\lambda$, but rather a brightness or spectral radiance $\mathcal{B} = \mathrm{d}^3P/\mathrm{d}A\mathrm{d}\Omega\mathrm{d}\lambda$ in terms of power emitted (or received) per unit area per unit solid angle per unit wavelength (μW/m^2/sr/m). Thus, a "synthetic diagnostic" calculation is required to connect the spectral power density to typical spectral measurements. To my knowledge, the first attempt is given in [6] as equation (10) therein,

$$\mathcal{B}_\mathrm{syn} = \frac{2\pi R_0}{ec}\frac{I_\mathrm{r}}{\Omega_\mathrm{r} A_\mathrm{r}}\left.\frac{\mathrm{d}P}{\mathrm{d}\lambda}\right|_{\lambda_\mathrm{max}}. \tag{3.42}$$

Here, R_0 is the major radius of the tokamak, I_r is the runaway current, λ_max is the wavelength at which $\mathrm{d}P/\mathrm{d}\lambda$ is maximum, $\Omega_\mathrm{r} = \pi/\gamma$ is the solid angle into which synchrotron radiation is emitted, and A_r is the poloidal cross-sectional area of the runaway beam. Note that $I_\mathrm{r} \approx n_\mathrm{r} ecA_\mathrm{r}$, where n_r is the (average) runaway density, giving

$$\mathcal{B}_\mathrm{syn} = 2R_0 n_\mathrm{r}\gamma\left.\frac{\mathrm{d}P}{\mathrm{d}\lambda}\right|_{\lambda_\mathrm{max}}. \tag{3.43}$$

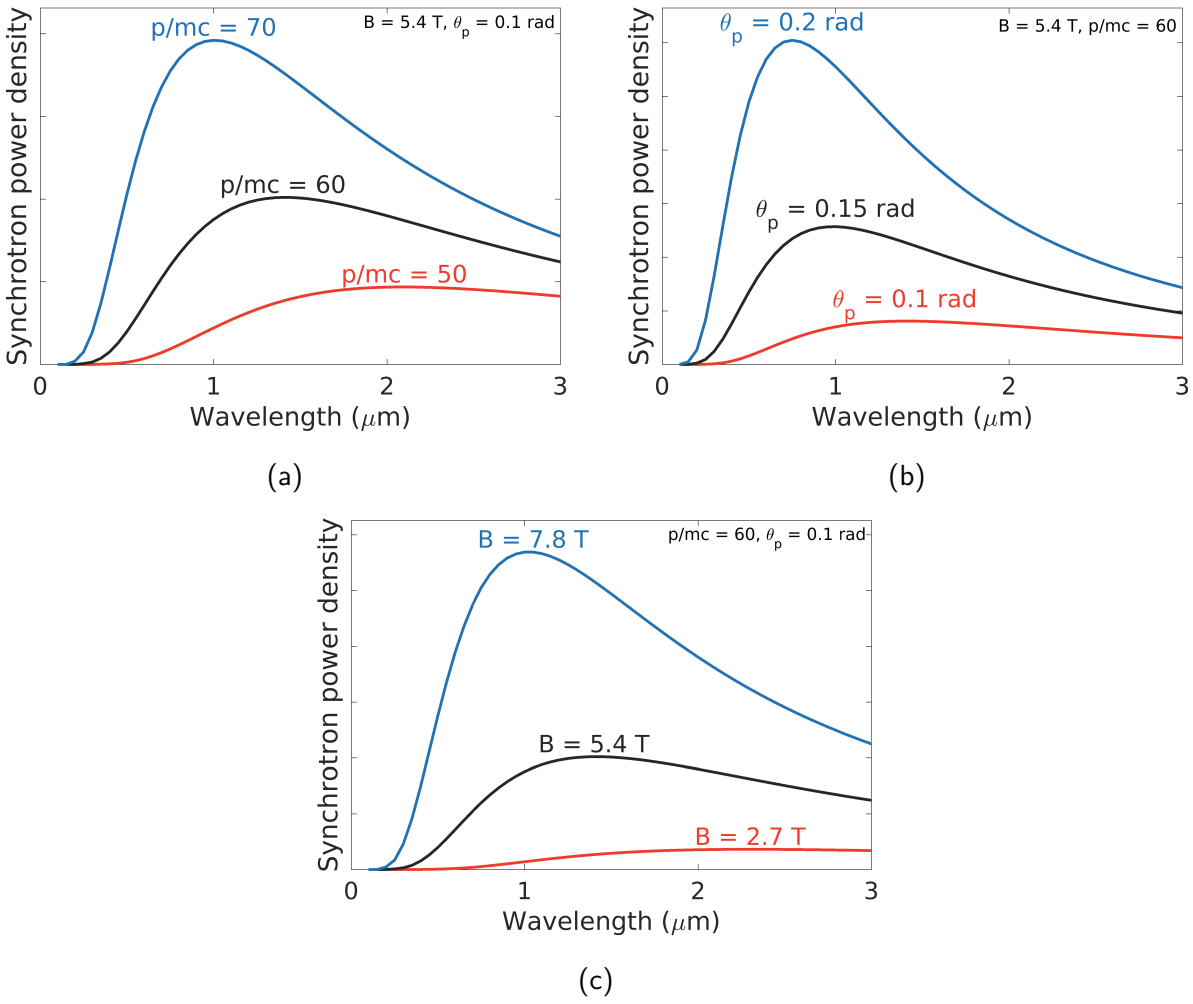

Figure 3.2: Synchrotron spectral power density $\mathrm{d}P/\mathrm{d}\lambda$ (a.u.) versus wavelength over the visible and infrared ranges, varying (a) runaway momentum p/mc, (b) runaway pitch angle θ_p, and (c) toroidal magnetic field strength B. Note how the peak of the power spectrum increases in magnitude and shifts toward shorter (bluer) wavelengths for increasing p/mc, θ_p, and B. (Computed using SYRUP [5].)

A more detailed and intuitive derivation of the synthetic brightness is given in [7], with the result differing slightly from that above. The observed brightness is determined from the spectral power density *per electron* $\mathrm{d}P/\mathrm{d}\lambda$, the number of those runaways observed N_obs, the area of the detector A_det, and solid angle subtended by it Ω_det. This calculation assumes a single-energy distribution for simplicity. In principle, the contributions from different numbers of runaways observed at different energies could be summed together.

Consider the "cone" of synchrotron radiation, with an opening half-angle θ_p and angular spread $\sim 1/\gamma$. Assuming that $\theta_\mathrm{p} \ll 1$ and $1/\gamma \ll \theta_\mathrm{p}$, the solid angle of emission per runaway is[f]

$$\Omega_\mathrm{r} = 2\pi(1 - \cos\theta_\mathrm{p}) \approx \pi\theta_\mathrm{p}^2. \tag{3.44}$$

The highly-directional nature of synchrotron emission also implies that only runaways within a small toroidal "wedge" are observed by the detector; the observed fraction is estimated to be

$$f_\mathrm{obs} \approx 2\theta_\mathrm{p}/2\pi = \theta_\mathrm{p}/\pi. \tag{3.45}$$

Note that this assumption is most accurate for collimated views looking near the magnetic axis, where there is little-to-no poloidal field and the total field is nearly toroidal.

The *total* number of runaways can be related to the runaway density n_r and beam cross-section A_r (as before) by $N_\mathrm{tot} \approx 2\pi R_0 A_\mathrm{r} n_\mathrm{r}$. Thus,

$$N_\mathrm{obs} = f_\mathrm{obs} N_\mathrm{tot} = 2\pi R_0 A_\mathrm{r} n_\mathrm{r} \times \frac{\theta_\mathrm{p}}{\pi}, \tag{3.46}$$

and

$$\mathcal{B}_\mathrm{syn} = 2R_0\theta_\mathrm{p} n_\mathrm{r} \frac{\mathrm{d}P}{\mathrm{d}\lambda} \frac{A_\mathrm{r}}{A_\mathrm{det}\Omega_\mathrm{det}}. \tag{3.47}$$

By conservation of etendue, $A_\mathrm{det}\Omega_\mathrm{det} = A_\mathrm{r}\Omega_\mathrm{r}$, so that the final formulation as given by equation (2) in [7] is

$$\mathcal{B}_\mathrm{syn} = \frac{2R_0}{\pi\theta} n_\mathrm{r} \frac{\mathrm{d}P}{\mathrm{d}\lambda}. \tag{3.48}$$

Note that (3.48) differs from (3.42) due to the different approximations of the solid angle; (3.44) assumes that synchrotron radiation is "smeared" over the entire solid angle of the cone, which could in some way be due to helical runaway trajectories. Regardless, the spectral shape will remain the same because (3.42) is just (3.48) scaled by a factor of $\pi\gamma\theta_\mathrm{p}$, which is independent of wavelength.

In [5], the calculation of (3.48) is extended to account for a distribution of runaway energies $f(p_\parallel, p_\perp)$. This involves an integration over momentum-space,

$$\mathcal{B}_\mathrm{syn} = \frac{2R_0}{\pi} \int \frac{\mathrm{d}P}{\mathrm{d}\lambda} \frac{1}{\theta_\mathrm{eff}} f(\boldsymbol{p})\, \mathrm{d}^3 p \tag{3.49}$$

[f] In what follows, the notation $\theta \equiv \tan(\theta_\mathrm{p})$ of [5–7] is not used, since $\theta_\mathrm{p} \approx \theta$ for small values. (And it's confusing!)

where

$$\theta_{\mathrm{eff}} = \sqrt{\theta_{\mathrm{p}}^2 + \gamma^{-2} + (r_{\mathrm{ap}}/r_{\mathrm{o}})^2} \tag{3.50}$$

is the *effective* pitch angle, accounting for such geometric effects as the pitch angle θ_{p}, angular width of the cone $1/\gamma$, and approximate solid angle subtended by an aperture of radius r_{ap} at a distance r_{o} from the point of synchrotron emission.

The equations for $\mathcal{B}_{\mathrm{syn}}$ in this section were a first important step in the analysis of synchrotron spectra. However, for wide-view detectors/spectrometers, helical trajectories and other spatial effects complicate the picture. Thus, more advanced synthetic diagnostics, like SOFT [8] and KORC [9], have been developed and incorporate the magnetic field topology, detector geometry and spectral response, and both momentum and spatial distributions of runaways. SOFT is used in this thesis work for the detailed analysis of experimental results.

References—Chapter 3

[1] K.C. Westfold. The Polarization of Synchrotron Radiation. *The Astrophysical Journal*, 130:241, 1959.

[2] J. Schwinger. On the classical radiation of accelerated electrons. *Phys. Rev.*, 75:1912–1925, 1949.

[3] I.M. Pankratov. Analysis of the synchrotron radiation spectra of runaway electrons. *Plamsa Physics Reports*, 25(2):145–148, 1999.

[4] I.H. Hutchinson. *Principles of Plasma Diagnostics: Second Edition*. Cambridge University Press, 2002.

[5] A. Stahl, M. Landreman, G. Papp, E. Hollmann, and T. Fülöp. Synchrotron radiation from a runaway electron distribution in tokamaks. *Physics of Plasmas*, 20(9):093302, 2013.

[6] R. Jaspers, N.J. Lopes Cardozo, A.J.H. Donné, H.L.M. Widdershoven, and K.H. Finken. A synchrotron radiation diagnostic to observe relativistic runaway electrons in a tokamak plasma. *Review of Scientific Instruments*, 72(1):466–470, 2001.

[7] J.H. Yu, E.M. Hollmann, N. Commaux, N.W. Eidietis, D.A. Humphreys, A.N. James, T.C. Jernigan, and R.A. Moyer. Visible imaging and spectroscopy of disruption runaway electrons in DIII-D. *Physics of Plasmas*, 20(4):042113, 2013.

[8] M. Hoppe, O. Embréus, R.A. Tinguely, R.S. Granetz, A. Stahl, and T. Fülöp. SOFT: a synthetic synchrotron diagnostic for runaway electrons. *Nuclear Fusion*, 58(2):026032, 2018. SOFT can be downloaded at https://github.com/hoppe93/SOFT, with documentation found at https://soft.readthedocs.io.

[9] L. Carbajal and D. del Castillo-Negrete. On the synchrotron emission in kinetic simulations of runaway electrons in magnetic confinement fusion plasmas. *Plasma Physics and Controlled Fusion*, 59(12):124001, 2017.

Chapter 4

Synchrotron diagnostics

This chapter will detail the diagnostics used for measurements of visible synchrotron emission in Alcator C-Mod. Sections 4.1, 4.2, and 4.3 will describe the spectrometers, wide-view camera, and motional Stark effect (MSE) diagnostic which measured synchrotron spectra, images, and polarization information, respectively.

A top-down schematic of the positions and views of each diagnostic are shown in figure 4.1.[a] Together, the diagnostics provide good coverage of the entire plasma with both clockwise (CW) and counter-clockwise (CCW) views for the spectrometers at the In-Vessel Platform (IVP) and wide-view (WIDE2) camera. Unfortunately, as will be discussed, these diagnostics rarely collected (good) synchrotron data on the same discharges; reasons included particulate matter building up on windows, data acquisition systems malfunctioning, diagnostics viewing the wrong direction (i.e. experimenter error), or simply being turned off.

4.1 Visible spectrometers

For the study of synchrotron radiation spectra from runaway electrons, two visible spectrometers were installed and absolutely calibrated on Alcator C-Mod. This section will detail their specifications, installation, viewing geometry, calibration, and operation.

4.1.1 Spectrometer specifications and installation

Two Ocean Optics visible spectrometers, model USB2000+, were used to measure synchrotron emission in the wavelength range $\lambda \approx$ 350-1000 nm during the 2015 and 2016 Alcator C-Mod experimental campaigns. Table 4.1 contains the spectrometer specifications. Figure 4.2 shows

[a] Note there is no I-port; it's *imaginary*.

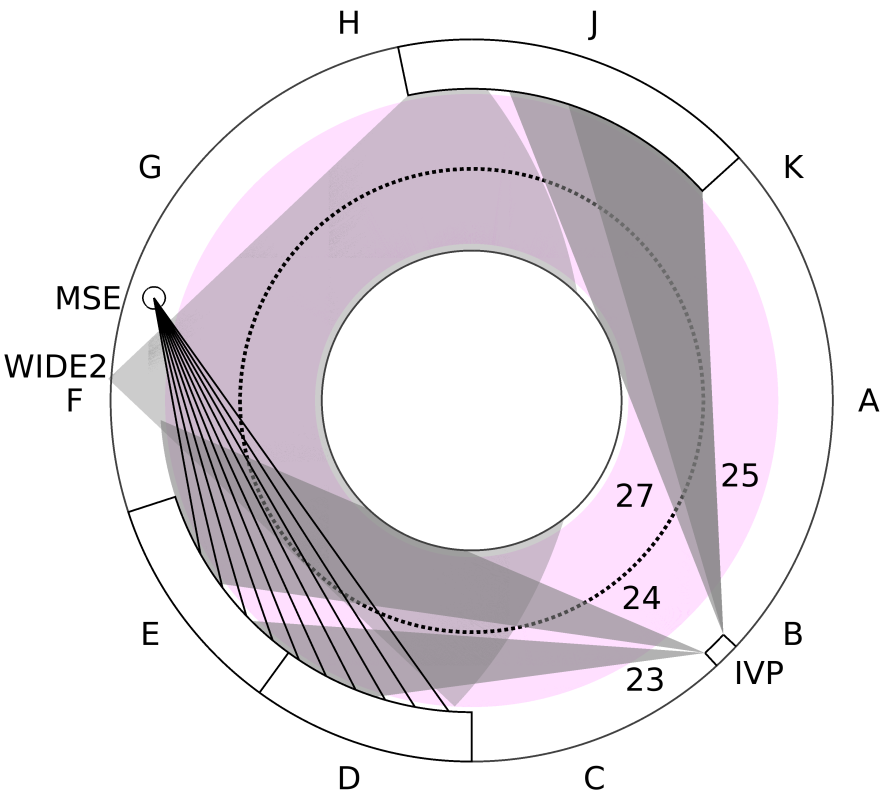

Figure 4.1: A top-down schematic of the tokamak midplane. The ten ports A-K are labeled, with RF antennas depicted at D, E, and J-ports. The plasma is pink, with the major radius of the plasma axis dotted. The spectrometer views (CW: 23/24, and CCW: 25/27) are located on the In-Vessel Platform (IVP). Note that the field-of-view of IVP25 lies *within* that of IVP27. The wide-view (WIDE2) camera views both CW and CCW directions. The MSE diagnostic has ten CCW views; here, only the lines-of-sight are shown.

the laboratory setup of the spectrometers. Trigger wires were connected to the plasma control system (PCS) for synchronized timing with the plasma discharge. Several bundles of silica optical fibers (400 μm in diameter) were connected to different apertures inside the tokamak; these could be easily connected to and switched between the spectrometers in the lab.

Table 4.1: Specifications for Ocean Optics spectrometers installed on Alcator C-Mod.

Specification	Spectrometer 1/2
Serial number	USB2+H14948/14949
Wavelength range (nm)	348-1024/349-1022
Grating (lines/mm)	600
Slit width (μm)	100
FWHM spectral resolution (nm)	∼4
Minimum integration time (ms)	1
Minimum duty cycle (ms)	10

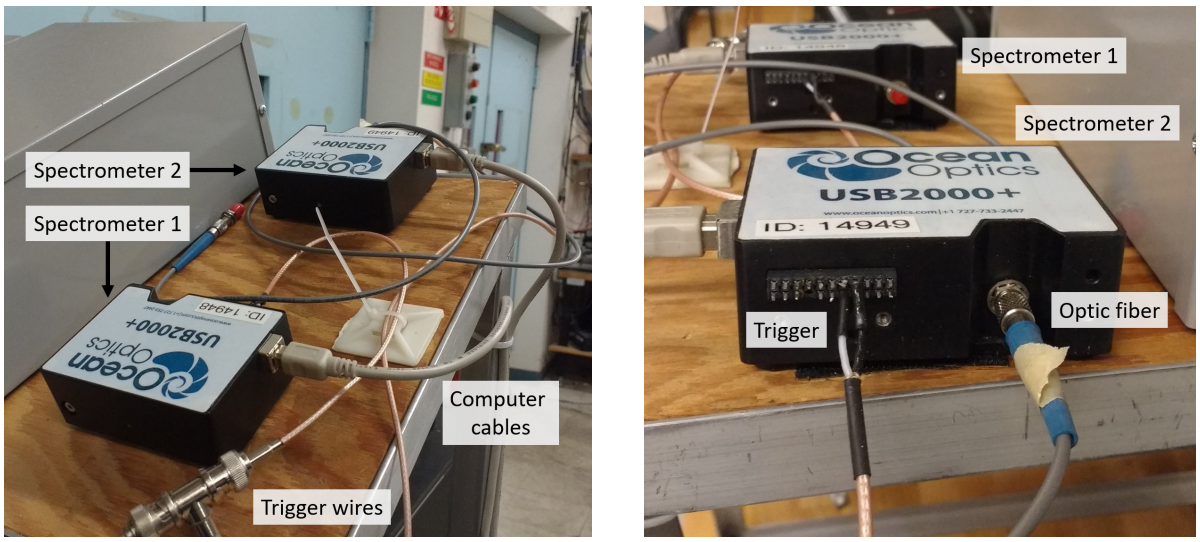

(a) (b)

Figure 4.2: Laboratory setup of Ocean Optics spectrometers. Labeled are spectrometers 1 and 2, trigger wires, computer cable connections, and optic fibers.

4.1.2 Spectrometer viewing geometries

Four apertures (23, 24, 25, and 27) on the In-Vessel Platform (IVP), located between B and C-ports, were used for synchrotron spectral measurements. Refer to table 4.2 for IVP geometry specifications. As seen in figure 4.3, IVP23 and IVP24 view the CW toroidal direction (when viewed from above), whereas IVP25 and IVP27 view CCW. Each view was backlit with a bright light source to determine the line-of-sight (LOS) and total viewing angle. Enhanced images of this backlighting are shown in figure 4.4. IVP23 and 24 view the right straps of the two-strap D- and E-port radio frequency (RF) antennas, respectively; IVP25 and 27 both view the right two straps of the four-strap J-antenna. Note that the IVP24 field-of-view (FOV) also extends

to the inner wall, seen on the right side of figure 4.4b. Additionally, comparing figures 4.4c and 4.4d, IVP27 has a wider viewing angle than 25. In fact, the IVP25 FOV is contained *within* that of IVP27. Thus, IVP24 and 27 were used for most spectral analyses as they viewed the largest portion of the plasma and received most light.

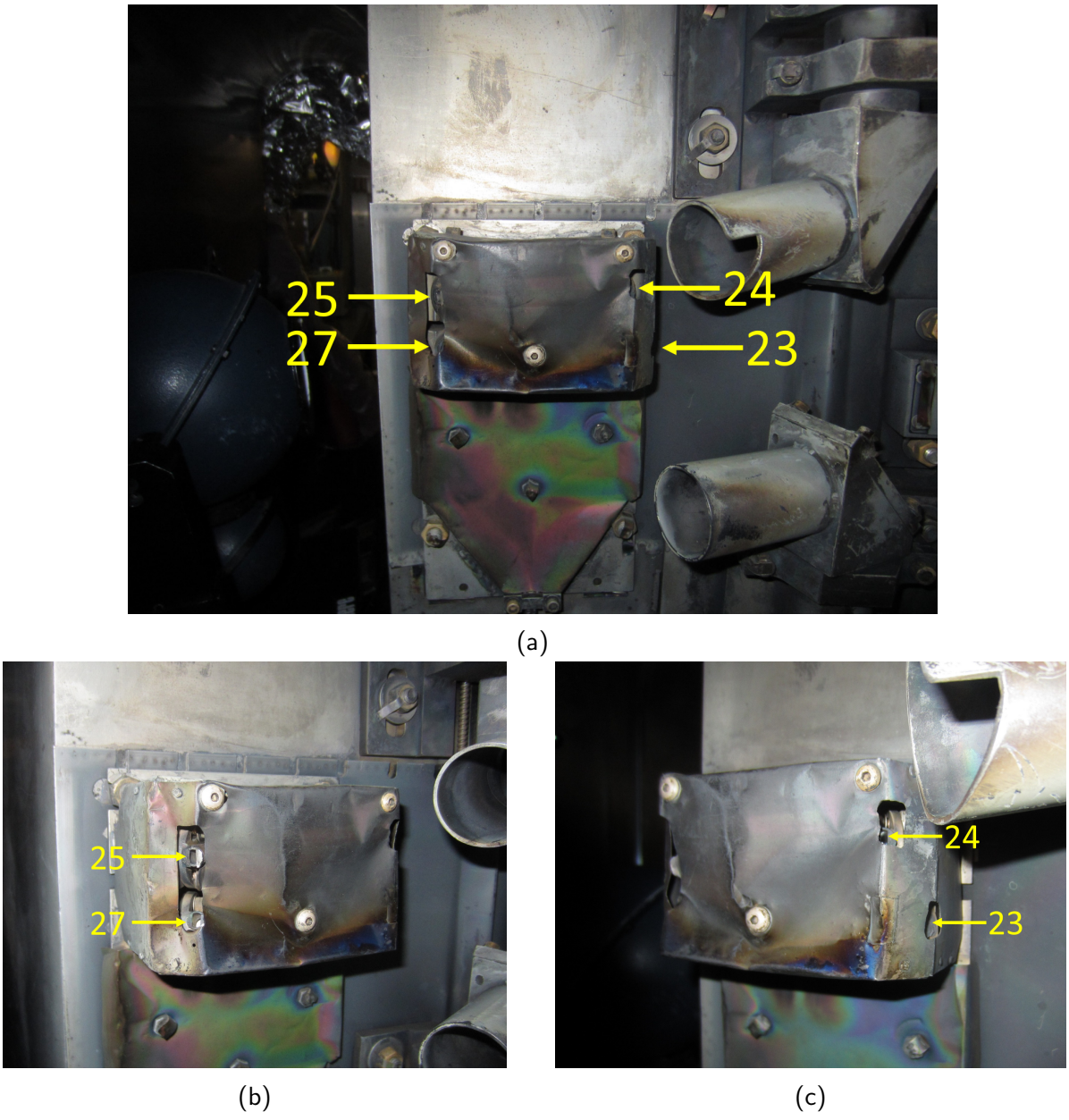

(a)

(b)

(c)

Figure 4.3: The In-Vessel Platform apertures: IVP23, 24, 25, and 27.

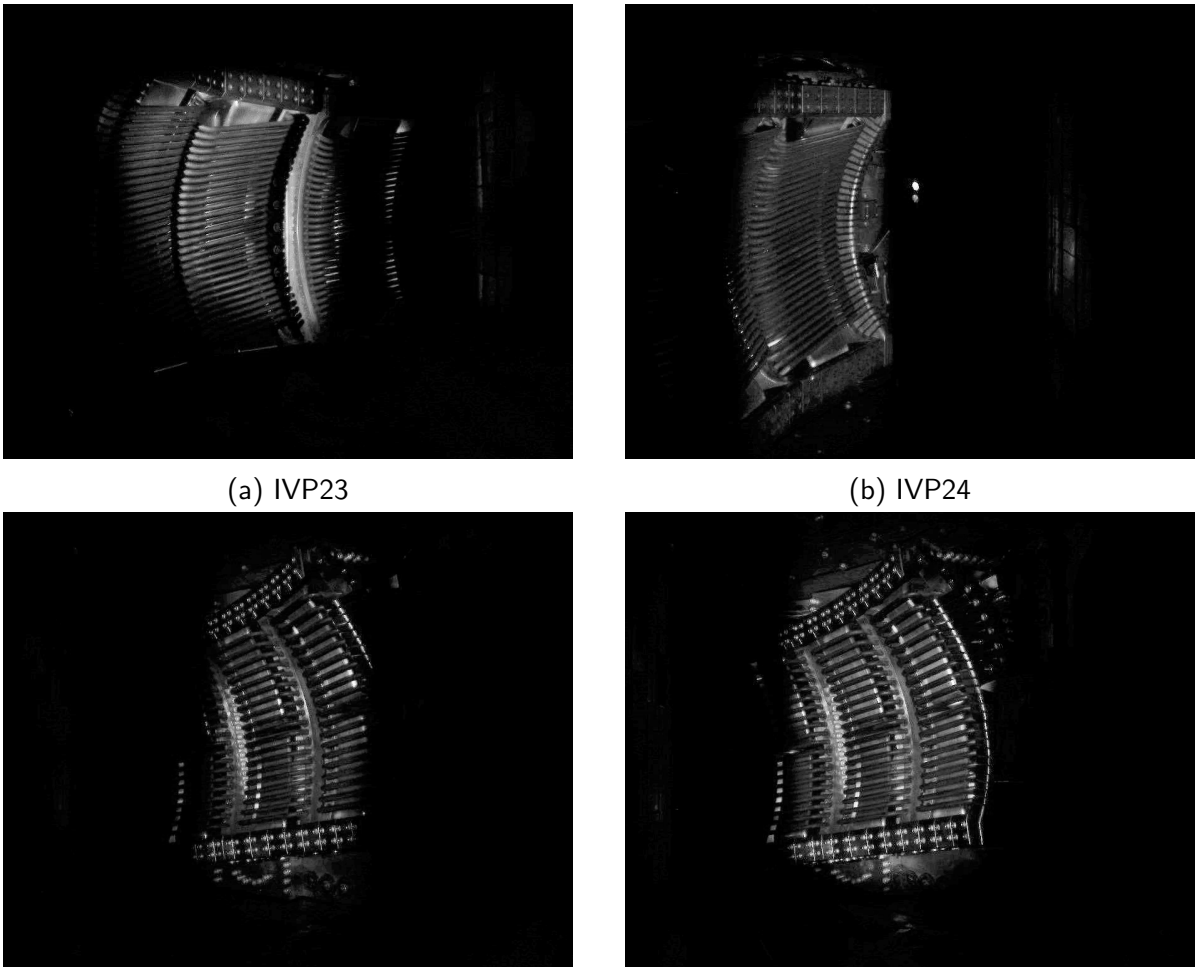

(a) IVP23 (b) IVP24

(c) IVP25 (d) IVP27

Figure 4.4: Backlighting of In-Vessel Platform (IVP) views (a) 23, (b) 24, (c) 25, and (d) 27. Note that images have been converted to greyscale and enhanced to highlight illuminated areas.

Table 4.2: Specifications of the IVP apertures. Lines-of-sight are assumed to be horizontal (parallel to the midplane). The major radius of all apertures is $R \approx 1.01$ m. Note that here the center of A-port is regarded as $\phi = 0°$.

Specification	IVP23/24	25/27
Toroidal angle (ϕ)	-47.3°	-42.9°
FOV opening angle	11.6°/15.0°	13.6°/18.8°
Vertical positions (cm)	2.5/3.8	3.8/2.5

4.1.3 Spectrometer calibration

The absolute calibration of the spectrometers was facilitated by the use of a Labsphere USS-600V Uniform Source System, hereafter referred to simply as the "labsphere." Inside the 6 inch diameter spherical shell of the labsphere, white light from a photodiode reflects off the inner surface and is emitted almost uniformly through an aperture $\sim$2 inches in diameter. For these calibrations, two labspheres were used and are pictured in figure 4.5. The uncalibrated labsphere, with portable power supply, could be taken inside the tokamak to perform in-vessel calibrations. The absolutely-calibrated labsphere was used for cross-calibrations in the lab; its known spectral radiance is shown in figure 4.6b.

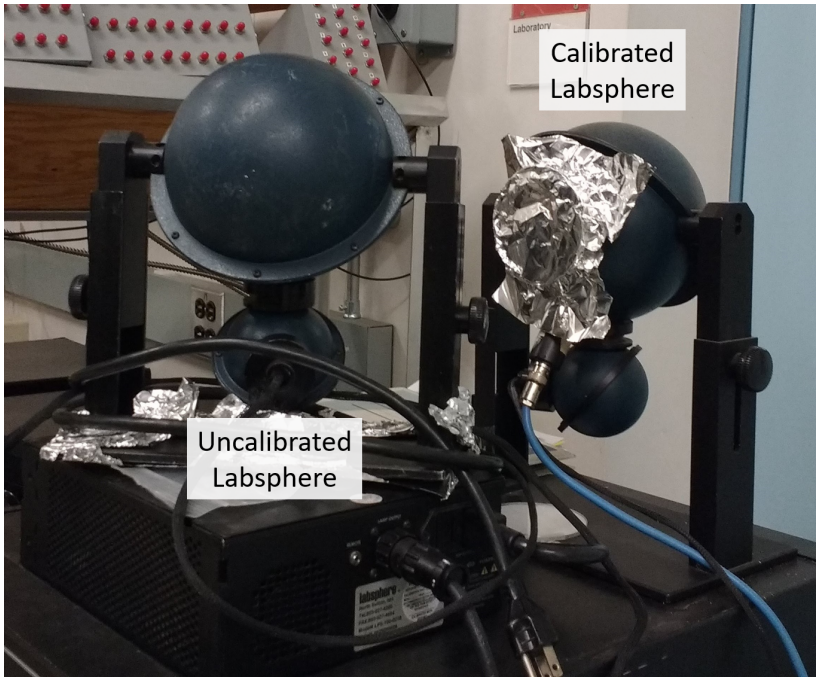

Figure 4.5: Uncalibrated and calibrated labspheres used in-vessel and in-lab, respectively, for spectrometer absolute calibration. Aluminum foil is covering the aperture of the calibrated labsphere to keep out contaminants.

The procedure for calibration of the spectrometers through each of the IVP views was as follows: First, "dark" spectra were obtained by recording data with all vessel lights turned off; this background noise would later be subtracted from all signals. Second, the uncalibrated labsphere was positioned in-vessel so that the IVP FOV was totally contained within the labsphere opening; in other words, the spectrometer only received light emitted by the labsphere. Third, two hundred spectra were measured at $\Delta t = 10$ ms intervals, with integration times varying between 3-7 ms to increase photon counts and improve counting statistics. These spectra were then averaged

together and smoothed over the wavelength resolution of ∼4 nm to produce the curves shown in figure 4.6a. Note that absorption features from the silica optical fibers can be seen at $\lambda \approx 600$ and 740 nm. In the lab, spectra were also measured to cross-calibrate the uncalibrated and calibrated labspheres as well as spectrometers 1 and 2.

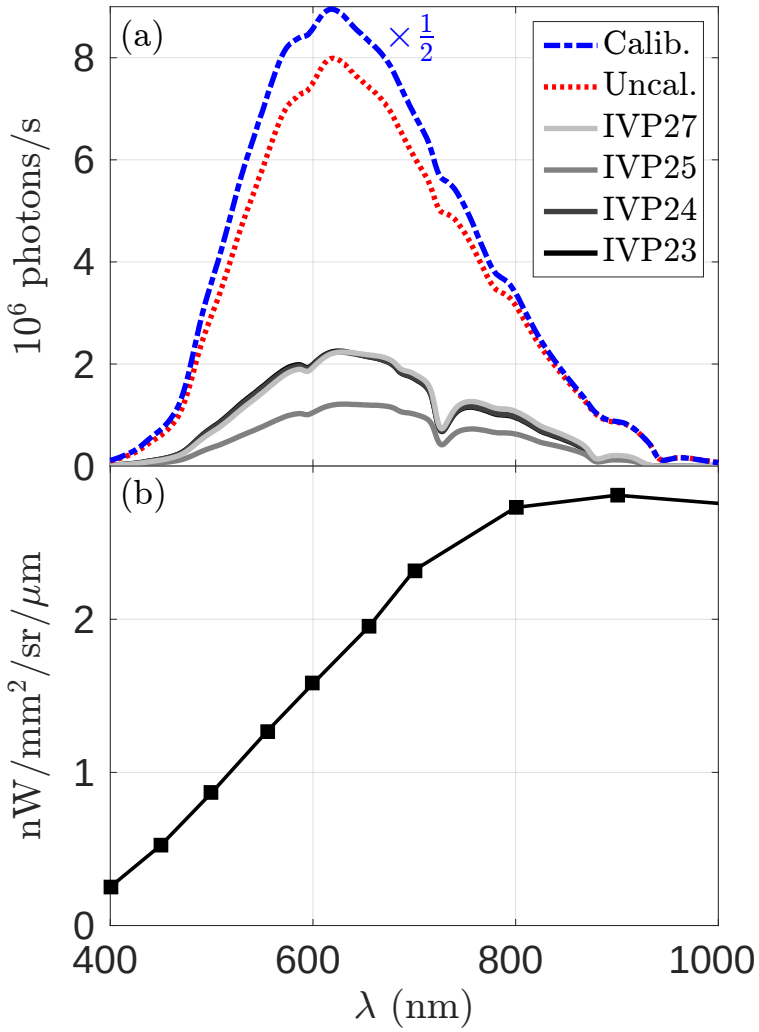

Figure 4.6: (a) Averaged spectra (normalized to integration time) measured by spectrometer 1 for each of the IVP views. (Note that IVP23, 24, and 27 have almost overlapping curves.) Spectra from the calibrated (dot-dashed blue) and uncalibrated (dotted red) labspheres are also shown; the former is scaled by a factor of 1/2. (b) The linear interpolation of spectral radiance (black squares) known to be emitted by the calibrated labsphere.

4.1.4 Spectrometer operation

The operation of the Ocean Optics spectrometers and their integration into the PCS was non-trivial. First, proprietary Ocean Optics software was required to run the spectrometers, and while many spectral measurements could be triggered in succession by an external source, the initiation of "waiting" for the triggers was a manual click of a "Go" button. Moreover, parameters such as the integration time, number of spectra to measure, data output folder, etc. were also required to be manually written into GUI's text boxes. Making matters even more complicated, this program was run on a Windows computer next to the spectrometers in the lab, which could only be controlled through a virtual connection.

The work-around was the following: A MATLAB script read spectrometer settings, like the integration time or fiber view, from the `spectroscopy.ocean_optics` MDStcl tree; these were written into a text file accessible by the Windows computer controlling the spectrometers. A `Python` script running on Windows read those settings, manually "clicked" in the appropriate text boxes of the Ocean Optics GUI, and entered the inputs. The same `Python` program also clicked the "Go" button so that the spectrometers were waiting for an external trigger synchronized with the plasma discharge. After the plasma discharge, spectral data were written to text files, which were collected and stored back in the tree.

4.2 Wide-view camera

This section will detail the calibration and distortion correction of the wide-view video camera which was used to measure images of runaway electron synchrotron emission. The following sections will include the camera specifications, viewing geometry, in-vessel calibration, distortion correction, data acquisition, and comparison/validation with the synthetic diagnostic SOFT [1].

4.2.1 Camera specifications

The wide-view WIDE2 video camera was used in Alcator C-Mod to capture images of visible and near-infrared emission from the plasma and plasma-facing components inside the tokamak. Located at F-port, the camera viewed both co- and counter-current directions, so visible synchrotron emission from relativistic runaway electrons could be observed as coming from (only) the counter-I_p side. Specifications for the camera are given in table 4.3. The black-and-white camera measured intensities in 256 levels or bins, and Auto Gain Control was always turned off. This unfortunately led to some saturated images, but more importantly allowed comparisons of relative intensities from frame-to-frame and even discharge-to-discharge, assuming the camera window stayed clean. The camera LOS is nominally parallel to the radial vector through the center of F-port; however, as will be shown in later sections, calibration determines that this is slightly off.

Table 4.3: Specifications for the wide-view video camera. Note that a toroidal angle of $\phi = 0°$ is defined at the center of A-port, and in this case a positive angle is measured in the CCW direction from a top-down view.

Specification	Value
Model	ELMO QN42H
Aperture diameter (mm)	7
Pixel dimensions	640 × 480
Spectral range (nm)	∼400-900
Major radius (cm)	106.9
Vertical position (cm)	-20.655
Toroidal angle (degrees)	176.6
Frame rate (fps)	59.94

4.2.2 Camera calibration and distortion correction

Due to its fish-eye lens, the wide-view camera image has barrel distortion, i.e. straight lines in real space appear bent outward near the edges of the image. To glean physical understanding from these images and compare them to synthetic diagnostics, a proper calibration was performed to correct for the distortion. A 3 cm $\times$ 3 cm grid was printed in the shape of the poloidal cross-section of the vacuum vessel, as shown in figure 4.7. The grid was placed in-vessel at three locations: extending approximately radially at E and G-ports, as well as lying approximately tangent to the inner wall at F-port. A bright LED light source was used to illuminate the grid, and calibration images can be seen in figure 4.8.

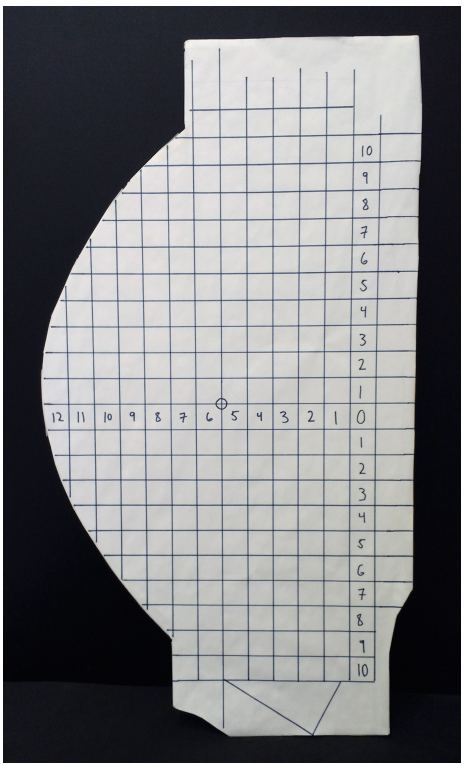

Figure 4.7: A foam board cut-out of a C-Mod vacuum vessel poloidal cross-section used for calibration of the wide-view camera. Each square is 3 cm $\times$ 3 cm.

The procedure for distortion correction was as follows[b]: The pixel locations, (x_i, y_i), of 439 total grid points were identified in the distorted calibration images and can be seen overlaying the grids in figure 4.8. The real-space positions of these grid points were also computed using knowledge of the grid's location in each calibration image. These data provided a discrete

[b]There are software packages available for such distortion correction procedures; however, the author was unfamiliar with them, and a cursory attempt to learn was abandoned for the adopted, straightforward method.

mapping from distorted image pixel locations to real-space positions; however, a general relation was required to correct the entire image. To simplify the analysis, it was assumed that the camera lens—and thus the distortion—was cylindrically symmetric. Therefore, pixel radii $r_i = \sqrt{x_i^2 + y_i^2}$ were mapped to angles θ_i between the camera LOS and vectors from the camera to real-space positions, while the pixel angles $\phi_i = \arctan(y_i/x_i)$ were treated as a constant. Here, the camera LOS was calculated as the vector from the camera position to the real-space location at the image center (0,0). To be agnostic of the absolute number of pixels, pixel radii were normalized by half the horizontal extent of the image. This mapping from θ_i to ρ_i is plotted for all grid points in figure 4.9. Since $\theta = 0°$ should correspond with $\rho = 0$, a linear regression through the origin was performed, determining that $\rho \approx \theta/C$, where $C = 0.7423$.

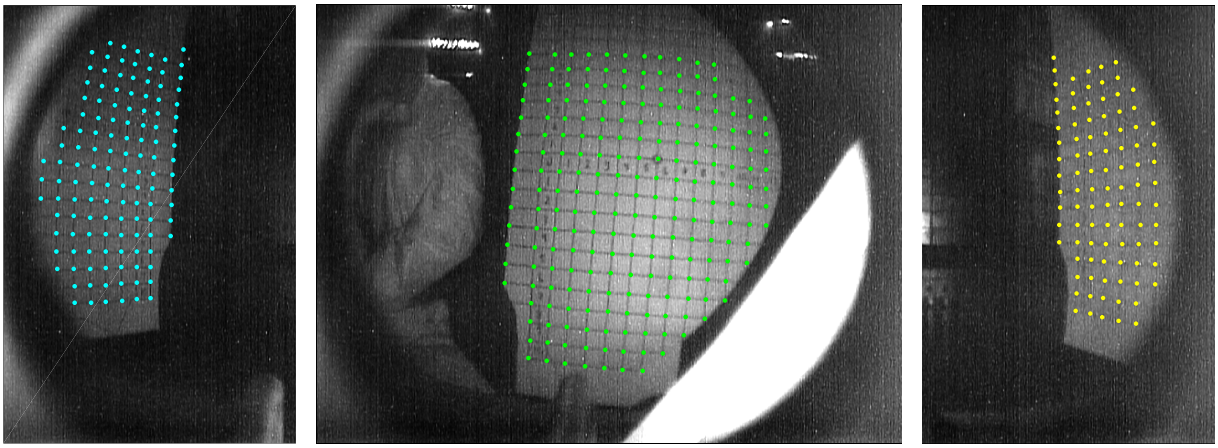

(a) G-port. (b) F-port. (c) E-port.

Figure 4.8: Camera images of the calibration grid located at (a) G, (b) F, and (c) E-ports, respectively. Colored dots indicate the pixel locations of grid points used in the calibration. Note that the images in (a) and (c) are cropped, the grid in (b) is slightly tilted, and the author is also captured by the camera at left in (b).

For a pinhole camera, the relationship between image height h and distance d from the pinhole is simply given by $h/d = \tan(\theta)$, with θ defined previously. Thus, to produce a rectilinear image from the distorted data, the new normalized pixel radius is given by $\rho' = \tan(\theta(\rho))/\tan(C)$, where ρ is the distorted normalized pixel radius, and the normalization factor is used such that $\rho' = 1$ when $\rho = 1$. This relation is shown in figure 4.9 as the dot-dashed line. Note that all distorted data points lie above the rectilinear relation; this implies that for an object at a given position in real space (i.e. a given θ), the distorted image shows this object at a radius greater than in real life, consistent with the expected barrel distortion.

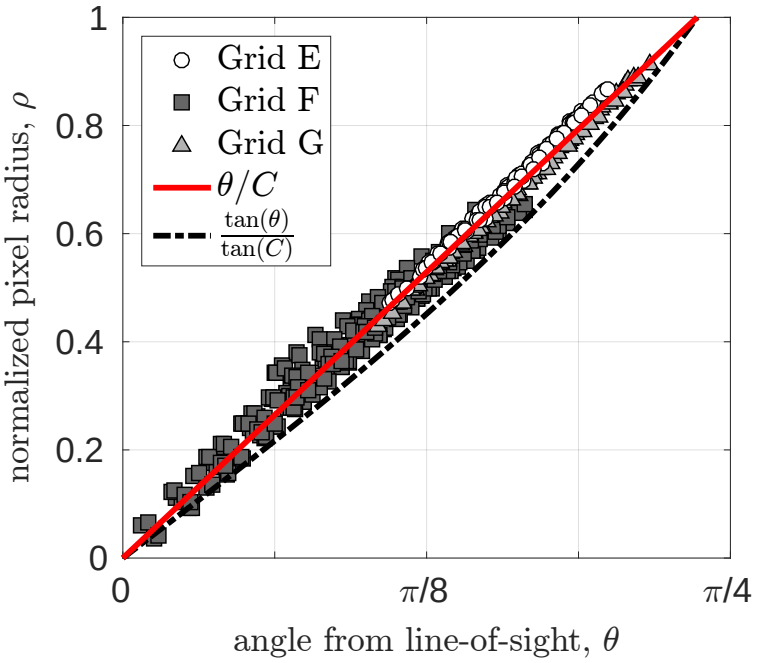

Figure 4.9: Normalized pixel radius ρ (from the center of the image) as a function of angle θ from the camera LOS vector to the location in real space for grid points at ports E (circles), F (squares), and G (triangles). Overlaid lines are the linear regression of all data through the origin (solid) and the relation for a rectilinear image (dot-dashed), where $C = 0.7423$.

4.2.3 Comparisons of corrected and synthetic camera images

After correcting for barrel distortion, the camera images can be compared to those generated by synthetic diagnostics like the *Synchrotron-detecting Orbit Following Toolkit* (SOFT) [1]. In order to accurately assess the camera viewing direction, tilt angle, and total viewing angle, a simple synthetic camera was used to "see" the vacuum vessel walls as the wide-view camera would; by varying camera geometry parameters, the walls could be "fit" to the distortion-corrected camera images. From this analysis, the best-fit camera parameters are given in table 4.4. The tilt angle, or roll, was determined simply by aligning the inner wall in the camera image with the vertical axis; for the 2014 and 2015 campaigns, it was $\sim$3.9°. The yaw, defined here as the angle in the midplane between the LOS and the local major radial vector $\hat{R}$, was varied to move the horizontal position of the synthetic inner wall left and right, while the total viewing angle, defined from the left to right side of the image, was increased/decreased to grow/shrink the synthetic inner wall size. The yaw was found to be about half of that predicted from engineering drawings, but the total viewing angle was similar to that expected from the calibration. Finally, the angle of

Table 4.4: WIDE2 camera parameters determined using a SOFT synthetic camera system. Note that the tilt angle (roll) applies for the 2014 and 2015 campaigns.

Parameter	Value
Tilt/roll	3.9°
Yaw	1.9°
Inclination/pitch	1.7°
Total viewing angle	86.8°

inclination, or pitch, of the camera was used from the in-vessel calibration. The resulting synthetic vacuum vessel is shown overlaying a distortion-corrected experimental image in figure 4.10. Good agreement is observed.

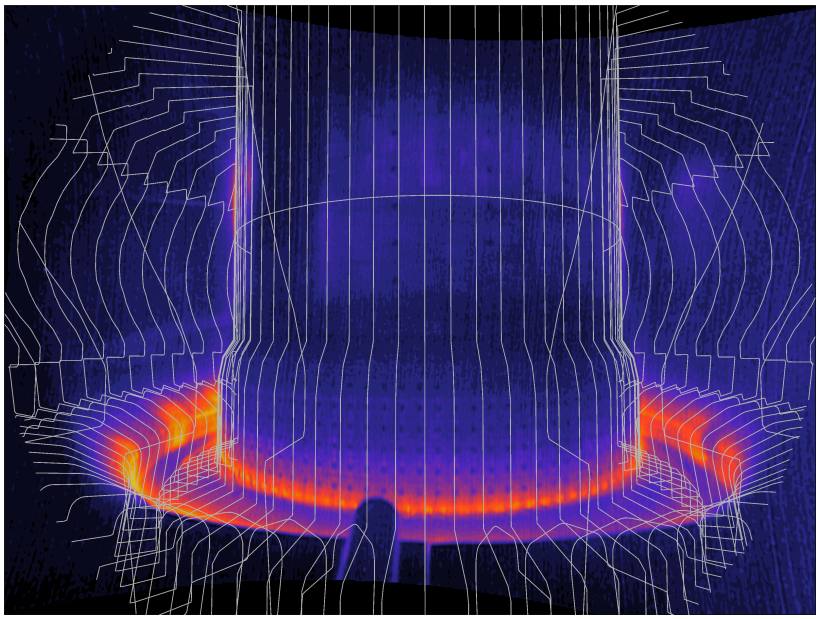

Figure 4.10: The "synthetic" vacuum vessel wall is plotted in toroidal angle increments of $\Delta\phi = 5°$ over a corrected experimental image (averaging all frames from C-Mod discharge 1140403014). The "horizontal" line corresponds to the plasma midplane $Z = 0$. Note the slight disagreement around the divertor in the camera's near view.

When simulating this wide-view camera in SOFT, the parameters of tables 4.3 and 4.4 were used with the exception of the total viewing angle. This is because SOFT defines the opening angle α_{diag} of its camera as that of the circular cone within which the resulting *square* image is inscribed. Since the experimental images are rectangular, we defined the total opening angle α_{horiz} as that covering the horizontal extent of the image itself. Thus, the two angles can be related by $\tan(\alpha_{\text{diag}}/2) = \sqrt{2}\tan(\alpha_{\text{horiz}}/2)$.

4.2.4 Camera data acquisition

Because the wide-view camera captures spatiotemporal dynamics of runaway electron synchrotron emission, the timing of data acquisition must also be calibrated. Disruptions provide a convenient way to mark time: In one frame, a plasma is visible; in the next frame, it's gone. An analysis of 50 disruptions from 2014-2016 was performed, comparing the disruption time reported by the wide-view camera (with an error of $\pm$1 frame $\approx \pm$16.7 ms) and the disruption time as calculated by the fast decay of the plasma current (with an error on the order of 1 ms). From this, it was found that the WIDE2 camera captures its first image at $t \approx$ (-42 $\pm$ 14) ms, when the plasma current ramp-up begins at $t \approx 0$ s. The standard EFIT calculations are performed every 20 ms, so the uncertainty in image capture time is approximately one EFIT time.[c] One other subtlety of the WIDE2 camera data acquisition is that images are actually stored as the combination of two frames; each frame captured is 640 $\times$ 240 pixels, and then the two frames are "interwoven" to form the full 640 $\times$ 480 pixel image at a reduced frame rate of $\sim$30 Hz. To improve the time resolution, images were split into their original frames and then interpolated over 640 $\times$ 480 pixels to fill in the "gap" rows.

[c] Fun fact: The author also discovered that the WIDE2 camera frames were being stored in the order $(t_2, t_1, t_4, t_3, ...)$ instead of $(t_1, t_2, t_3, t_4, ...)$.

4.3 Motional Stark Effect diagnostic

This section will detail the Motional Stark Effect (MSE) diagnostic, which has been used to measure *polarized* synchrotron radiation from runaway electrons. The following sections will include an overview of the motional Stark effect, as well as the specifications, geometry, and measurement capabilities of the MSE system on Alcator C-Mod.

4.3.1 An overview of the motional Stark effect

The Stark effect is the quantum process by which atomic energy levels split due to the presence of a background electric field. In a similar way, the *motional* Stark effect (MSE) arises due to the *effective* electric field ($\boldsymbol{E} = \boldsymbol{v} \times \boldsymbol{B}$) arising from particle motion (with velocity $\boldsymbol{v}$) in a background magnetic field $\boldsymbol{B}$. A transformation from the lab frame to particle rest frame shows how the magnetic field can be experienced as an electric field.

In a tokamak plasma, radiation is emitted as excited, bound electrons transition between Stark-split energy levels; this can be used to diagnose the local magnetic field, from which the safety factor and current density profile can be inferred. An MSE device was first deployed on the PBM-X tokamak for this purpose [2]. Typically, a diagnostic neutral beam (DNB) of neutral hydrogen or deuterium is injected into the plasma. (See figure 4.11a, for an illustration.) Before complete ionization, these neutral particles collide with the background plasma, exciting electrons into higher energy states. Of particular interest is the quantum $\mathrm{n} = 3$ state, which is split into $2\mathrm{n}-1 = 5$ distinct energy levels. The electron can then decay—through collisions or spontaneously—to one of the three levels of the $\mathrm{n} = 2$ state. Thus, there are fifteen possible transitions corresponding to fifteen distinct photon energies; however, only nine are easily measureable: six "π" lines and three "σ" lines, all separated by the same $\Delta\lambda$. The wavelengths are all near the normal Balmer-α wavelength, $\lambda \approx 656$ nm. These lines are also shifted by the Doppler effect, which depends on the geometry and beam energy, usually on the order of 50 keV.

Of the nine observable lines, some are polarized perpendicular to the local (motional) electric field, while others have parallel polarization. Thus, analyzing the polarization angle θ_{pol} of different wavelength ranges allows inference of the local magnetic field pitch. To do this, light from the plasma passes in series through two photo-elastic modulators (PEMs), i.e. birefringent materials with tuneable, polarization-dependent refractive indices. Slightly different high-frequency (tens of kHz) voltages are applied to each PEM, thereby varying the linear polarization of passing light which is incident on a final, stationary polarization filter. The resulting amplitude modulation, measured at the appropriate harmonics of the PEM frequency, can then be decomposed into $\sin\theta_{\mathrm{pol}}$ and $\cos\theta_{\mathrm{pol}}$. This procedure and calculation are described in detail in [3]. While the

synchrotron radiation spectrum is quite different from line radiation, it is still polarized and falls into the MSE wavelength range. Thus, the MSE system can be used to measure the polarization of synchrotron light.

4.3.2 MSE detector specifications and geometry

The MSE system on Alcator C-Mod measures radiation in the visible wavelength range, within a $\Delta\lambda \approx 0.8$ nm band around $\lambda = 660$ nm. See table 4.5 (and references [4–6], among others) for additional diagnostic specifications. Therefore, during runaway electron discharges, this diagnostic can capture visible synchrotron emission. There are ten MSE channels which span the plasma across major radii $R > 59$ cm, approximately on the midplane, as seen in figure 4.11b. Thus, the MSE system can provide spatiotemporal information of runaway evolution and the underlying runaway distribution function.

Table 4.5: Specifications of the MSE diagnostic in Alcator C-Mod. Note that ϕ is the toroidal angle measured CCW with $\phi = 0°$ at A-port.

Specification	Value
Major radial position	$R \approx 98.1$ cm
Vertical position	$Z \approx 2.9$ cm
Toroidal location	$\phi \approx 162.1°$
Wavelength range	$\lambda \in 660 \pm 0.4$ nm
Time resolution	$\Delta t \sim 1$ ms
FOV opening angle	$2\alpha \sim 1.7°$

Light is collected by the MSE diagnostic through an in-vessel periscope which has a CCW view of the plasma (as depicted in figure 4.11a). The periscope is situated slightly above the midplane such that the ten LOS have a slight downward orientation—i.e. an inclination $\delta \approx$ -3°—to intersect the DNB (which is approximately horizontal on the midplane). The opening angle of each channel was estimated from the radial extent of the beam observed by each channel FOV.

Further specifications for the ten channel views are provided in table 4.6. For normal MSE operation, the geometric quantities of interest are the following: (i) the "geometric" major radius R_{geo} at which each MSE chord intersects the DNB trajectory, and (ii) the angle Ω between the MSE LOS and the *local* toroidal unit vector $\hat{\phi}$. However, when considering synchrotron emission—which is forward-directed, parallel to the runaway velocity vector—the geometric quantities of interest are (i) the "tangency" radius R_{tan} at which each channel LOS is orthogonal to the local radial vector $\hat{R}$ (and thus tangent to a toroidal circular orbit) and (ii) the LOS direction, which can be described by the angle ψ between the LOS and the MSE radial vector $\boldsymbol{R}_{\text{MSE}}$.

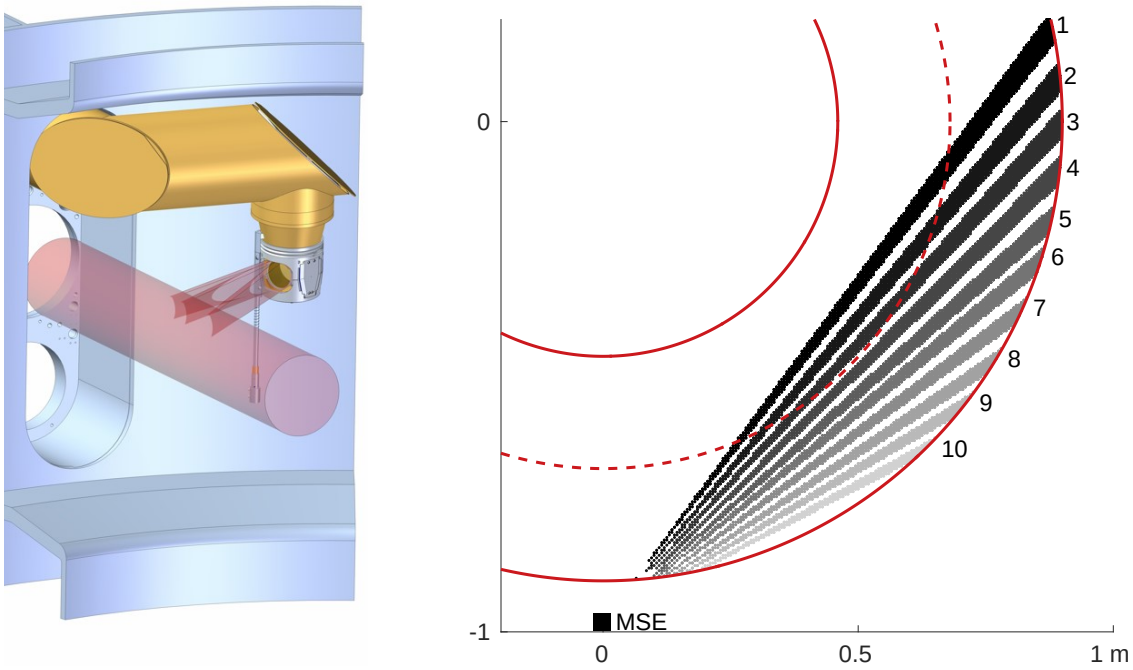

(a) (b)

Figure 4.11: (a) CAD model of the MSE periscope in-vessel with three channels' fields-of-view (FOV) intersecting a schematic DNB. (Courtesy of R. Mumgaard.) (b) A top-down view of the ten channels' FOV overlaying a plasma with boundary (solid) and major radius (dashed) shown.

To calculate $R_{\tan}$ and ψ from known R_{MSE}, R_{geo}, and Ω, consider the schematic shown in figure 4.12. We see that

$$R_{\tan} = R_{\mathrm{geo}} \sin\left(\frac{\pi}{2} - \Omega\right) = R_{\mathrm{geo}} \cos\Omega \tag{4.1}$$

and

$$\sin\psi = \frac{R_{\tan}}{R_{\mathrm{MSE}}} = \frac{R_{\mathrm{geo}}}{R_{\mathrm{MSE}}} \cos\Omega. \tag{4.2}$$

The calculated values for $R_{\tan}$ and ψ are reported in table 4.6.

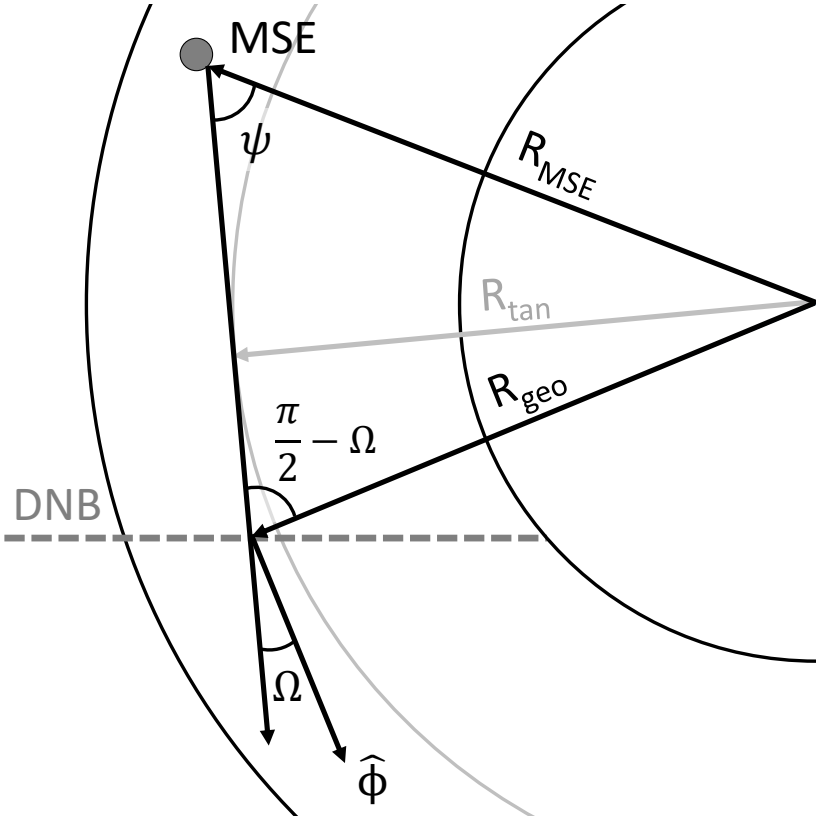

Figure 4.12: A schematic top-down view of the MSE diagnostic geometry, with relevant geometric quantities labeled and described in the text.

Table 4.6: Specifications for the ten LOS of the MSE diagnostic on Alcator C-Mod. Note that ψ is the angle measured CW from a radially-inward vector ($-\hat{R}$) at the periscope location toward the channel LOS in the horizontal plane ($Z = 0$). An inclination of $\delta < 0$ implies a *downward* view. These specific values were taken for shot 1140403026 and can vary slightly for different experimental campaigns.

Channel	1	2	3	4	5	6	7	8	9	10
$R_{\tan}$ (cm)	59.1	63.0	66.3	69.7	73.0	75.6	78.7	81.6	84.0	86.4
ψ (°)	37.1	40.0	42.6	45.3	48.1	50.5	53.4	56.3	59.0	61.7
δ (°)	-2.8	-3.3	-3.1	-2.9	-3.4	-3.4	-3.4	-3.2	-3.2	-3.1

4.3.3 MSE measurement capabilities

While the MSE system calculates the Stokes parameters $[I, Q, U, V]$, encoding all intensity and polarization information of the incoming light, the data stored in the MDStcl tree are

(i) the intensity of linearly-polarized light $L = \sqrt{Q^2 + U^2}$ (*atot*),
(ii) the degree of linearly-polarized light $\mathrm{f_{lin}} = \mathrm{f_{pol}} = L/I$ (*pf_linear*),
(iii) the degree of circularly-polarized light $\mathrm{f_{circ}} = V/I$ (*pf_circular*), and
(iv) the polarization angle $2\theta_{\mathrm{pol}} = \arctan(U/Q)$ (*a_mse*).

Here, the node names in the tree are given in parentheses.

Unfortunately, the absolute calibration of L varies from channel-to-channel, so it is most useful to consider the other intensity-independent quantities (ii)-(iv). The noise floor used for data analysis is $L \leq 10^{-3}$ (a.u.). It is important to note that the MSE system measures θ_{pol} from the vertical axis downward, i.e. approximately $\hat{Z}$ toward $\hat{R}$ as viewed by the detector. Also, there is a 180° degeneracy of θ_{pol}. Finally, since synchrotron radiation is primarily linearly-polarized, we will only consider the fraction $\mathrm{f_{lin}} = \mathrm{f_{pol}}$ in our experimental analyses.

References—Chapter 4

[1] M. Hoppe, O. Embréus, R.A. Tinguely, R.S. Granetz, A. Stahl, and T. Fülöp. SOFT: a synthetic synchrotron diagnostic for runaway electrons. *Nuclear Fusion*, 58(2):026032, 2018. SOFT can be downloaded at https://github.com/hoppe93/SOFT, with documentation found at https://soft.readthedocs.io.

[2] F.M. Levinton, R.J. Fonck, G.M. Gammel, R. Kaita, H.W. Kugel, E.T. Powell, and D.W. Roberts. Magnetic field pitch-angle measurements in the PBX-M tokamak using the motional Stark effect. *Phys. Rev. Lett.*, 63:2060–2063, 1989.

[3] G.R. Boyer, B.F. Lamouroux, and B.S. Prade. Automatic measurement of the Stokes vector of light. *Appl. Opt.*, 18(8):1217–1219, 1979.

[4] R.T. Mumgaard. Engineering upgrades to the Motional Stark Effect diagnostic on Alcator C-Mod, 2015.

[5] R.T. Mumgaard. *Lower Hybrid Current Drive on Alcator C-Mod: Measurements with an upgraded MSE diagnostic and comparisons to simulation*. PhD thesis, Massachusetts Institute of Technology, 2015.

[6] R.T. Mumgaard, S.D. Scott, and M. Khoury. A ten sightline multi-spectral line-polarization MSE system for Alcator C-Mod. *Review of Scientific Instruments*, 87, 2016. https://doi.org/10.1063/1.4959793.

This page intentionally left blank

Chapter 5

Simulations of runaway electrons and synchrotron radiation

Ultimately, the goal of this thesis is to infer properties of the runaway electron phase space distribution from experimental measurements of synchrotron emission. To do this, we must also understand which regions of phase space we are interrogating or "seeing"; that is, synchrotron emission from runaways within only certain regions of phase space will be observed. This is really a convolution or integration of the runaway phase space distribution, synchrotron power density, and detector response function. Solving the full *inverse* problem—i.e. inferring the entire runaway phase-space distribution from synchrotron data—is intractable as there is almost never a unique solution. For example, many runaway energies and pitch angles can result in the same synchrotron spectrum, as discussed in chapter 6. On the other hand, completely solving the *forward* problem requires (i) accurate theories of runaway electron phase space dynamics and (ii) good synthetic diagnostic simulations. Oftentimes, it is useful to meet somewhere in the middle. For instance, we can use experimentally-measured plasma parameters to either evolve a test-particle model (TPM) or solve the kinetic equation for the runaway momentum space distribution, and then invert a density profile by comparing synthetic and experimental measurements, as is done in chapter 7.

Either way, simulations are needed to perform these tasks. Two codes in particular have been used extensively throughout this thesis, and the analyses performed would not have been possible without them. These are the kinetic equation solver *COllisional Distribution of Electrons* [1, 2] and the synthetic diagnostic *Synchrotron-detecting Orbit Following Toolkit* [3], hereafter referred to as CODE and SOFT. These were developed by the Plasma Theory group, at Chalmers University in Göteborg, Sweden, with whom the author of this thesis has kept a close collaboration. The codes will be described in the following sections, with supplemental sections showing the

dependencies of the outputs (e.g. runaway momentum space distribution functions and synthetic measurements) on the inputs (e.g. plasma, runaway, and detector parameters).

5.1 CODE simulations

A test-particle model, as described in chapter 2, is one way of calculating the energies and pitch angles of runaways, i.e. as delta functions in momentum space. As will be discussed, this can sometimes be sufficient to reproduce and explain experimental data. However, to explore the full *distributions* of runaway energies and pitch angles, we need to calculate the full momentum space distribution function.

5.1.1 Solving the kinetic equation

The general kinetic equation, describing the evolution of a distribution of particles in phase space, was introduced in chapter 2 in (2.29). Here, it is rewritten in the form

$$\frac{\partial f_{\mathrm{e}}}{\partial t} + \frac{\mathrm{d}\boldsymbol{r}}{\mathrm{d}t} \cdot \frac{\partial f_{\mathrm{e}}}{\partial \boldsymbol{r}} + \frac{\mathrm{d}\boldsymbol{p}}{\mathrm{d}t} \cdot \frac{\partial f_{\mathrm{e}}}{\partial \boldsymbol{p}} = \sum_i C_{ei}\left\{f_{\mathrm{e}}, f_i\right\} + S. \tag{5.1}$$

The left-hand side (LHS) takes into account spatial variations $(\partial f_{\mathrm{e}}/\partial \boldsymbol{r})$ and forces acting on the population $(\mathrm{d}\boldsymbol{p}/\mathrm{d}t)$, while the right-hand side accounts for collisions between different species (C_{ei}) and particle sources (S). Several assumptions and approximations are sometimes made in order to make the computation of $f_e(t, \boldsymbol{r}, \boldsymbol{p})$ tractable:

(i) Spatial homogeneity is sometimes assumed in order to eliminate the second term on the LHS of (5.1). While a tokamak plasma is spatially inhomogeneous, this assumption can hold in some limits; for instance, in the case of large aspect ratio, i.e. $R_0/a \gg 1$.

(ii) In a magnetized plasma, the fast gyro-motion of charged particles motivates the averaging over gyro-angles, so that momentum space is reduced from three dimensions to two: $p_\parallel$ and $p_\perp$, momenta parallel and perpendicular to the magnetic field.

(iii) As discussed in chapters 1 and 2, interactions between particles in a plasma are dominated by small-angle deflections. Therefore, the Fokker-Planck collision operator can be used to approximate C_{ei}.

(iv) However, as noted in chapter 2, large-angle collisions *can* occur during the runaway electron avalanching process, significantly affecting the distribution function. Because C_{ei} now only accounts for small angle collisions, these large momentum transfers can be included in S.

(v) The collision operator can also be *linearized* when the total distribution function f_e is only a slight modification of a known distribution; i.e. $f_e = f_{e0} + f_{e1}$, and $f_{e1} \ll f_{e0}$. For these analyses, f_{e0} is taken to be a Maxwellian distribution.

The code CODE [1, 2] was developed to solve the time-dependent, spatially-homogeneous, linearized Fokker-Planck equation for the distribution of electrons $f(t, \boldsymbol{p})$, where the subscript e has been dropped for convenience. The forces on electrons are those due to an applied electric field $\boldsymbol{E}$ and the (synchrotron) radiation reaction force, also called the Abraham-Lorentz-Dirac force [4],

$$\boldsymbol{F}_{\mathrm{rad}} = \frac{e^2\gamma^2}{6\pi\epsilon_0 c^2}\left\{\ddot{\boldsymbol{\beta}} + 3\gamma^2\left(\boldsymbol{\beta}\cdot\dot{\boldsymbol{\beta}}\right)\dot{\boldsymbol{\beta}} + \gamma^2\left[\boldsymbol{\beta}\cdot\ddot{\boldsymbol{\beta}} + 3\gamma^2\left(\boldsymbol{\beta}\cdot\dot{\boldsymbol{\beta}}\right)^2\right]\boldsymbol{\beta}\right\}. \tag{5.2}$$

The relativistic factor γ and normalized velocity $\boldsymbol{\beta}$ are familiar, with dots representing time derivatives $\mathrm{d}/\mathrm{d}t$. Typically, the $\boldsymbol{\beta}\cdot\dot{\boldsymbol{\beta}}$ terms can be ignored because the velocity and acceleration are almost perpendicular.

Small-angle collisions of (i) runaways on thermal electrons and (ii) thermal electrons on runaways are taken into account in CODE, but the collisions of runaways with other runaways are neglected as it they are of second order, $O(f_1^2)$. Pitch angle scattering from collisions between electrons and ions is also included, although essentially no energy is exchanged between the light electrons and massive ions.

Primary (Dreicer) generation of runaways is accounted for in (5.1) through the electric field acceleration, embedded in $\mathrm{d}\boldsymbol{p}/\mathrm{d}t$, and momentum space diffusion through small angle collisions, in $C_{ei}\{f_\mathrm{e}, f_i\}$. The avalanche source term S, however, must be specified explicitly. That from Rosenbluth and Putvinski (RP) [5], as described in chapter 2 and given in (2.19), is implemented in CODE. Recall, from chapter 2, that avalanching occurs through knock-on collisions, in which an incident runaway electron collides with a thermal electron; post-collision, both electrons are relativistic runaways. One limitation of the RP growth rate is that "outgoing" runaways are produced with artificially high energies; this is a result of simplifications made in the mathematics of [5].

A more realistic avalanching operator was derived by Chiu *et al* [6], where the outgoing runaway momentum is limited by the incident runaway's, i.e. $p_{\mathrm{out}} \leq p_{\mathrm{in}}$.[a] This so-called Chiu-Harvey (CH) operator is also available in CODE. Once again, due to assumptions made in the mathematics, the CH source term (like the RP operator) does *not* conserve momentum because the primary runaway momentum p_{in} does not decrease after the interaction. In addition, while a number of runaway electrons are *created* by the RP and CH source terms, the same number

[a] Note that momentum of the thermal electron, pre-collision, is much smaller than the incident runaway's, i.e. $p_{\mathrm{th}} \ll p_{\mathrm{in}}$.

of thermal electrons are not removed from the bulk population; thus, particle number is not conserved. This assumption is only allowable when the runaway population is small compared to the bulk. See [7] for a more in-depth discussion.

The inputs to CODE are the time-evolutions of bulk plasma temperature T and density n, electric field E parallel to the magnetic field of strength B,[b] and effective charge Z_{eff}. The avalanching source term—like RP, CH, or none at all—can also be specified. Numerically, momentum space is decomposed into the total momentum p and cosine of the pitch angle $\cos\theta_{\text{p}}$; the former has a finite difference discretization, while the latter is expanded in Legendre polynomials. Details can be found in [1, 2]. CODE is written in MATLAB, and computation times range from CPU-seconds to CPU-hours.

5.1.2 Momentum space distributions

A sample momentum space distribution function calculated with CODE is shown in figure 5.1. The *time-independent* parameters used are similar to those measured for low-density C-Mod discharges: $n = 10^{19}$ m^{-3}, $T = 1$ keV, $Z_{\text{eff}} = 4$, $E/E_{\text{C}} = 15$, and $B = 5.4$ T. The RP avalanche source was enabled, and the distribution function was evolved from $t = 0$-1 s, with initial condition $f(t = 0, \boldsymbol{p})$ a Maxwellian at temperature T. Figure 5.1a shows the distribution function at one time $t = 1$ s; as is seen, the electrons in the tail of $f(\boldsymbol{p})$ have been accelerated along the magnetic field to relativistic energies ($p_\parallel/mc \gg 1$) with relatively small pitch angles ($p_\perp \ll p_\parallel$). While there is a significant fraction of runaways with $p_\parallel/mc \approx$ 10-30, the gradient $\partial f/\partial p_\parallel$ becomes much steeper for $p_\parallel/mc \geq 30$.

The time evolution of the runaway distribution is depicted in figure 5.1b. Each curve is the contour $\log_{10}(f) =$ -12 with colors indicating steps from $t = 0$-1 s in steps $\Delta t = 0.1$ s. Note how the change in parallel momentum $\Delta p_\parallel/mc$ is fairly constant for each time interval; this is due to the constant electric field accelerating runaways along the magnetic field. The change in *perpendicular* momentum $\Delta p_\perp/mc$ between time steps, however, *decreases* as time increases. Through collisions with ions (Z_{eff}), parallel momentum can be transferred to perpendicular momentum; this is pitch angle scattering. But as both runaway energies and pitch angles increase, so too does the power lost due to synchrotron radiation. (Recall that $P_{\text{synch}} \propto p_\perp^2 B^2$.) Therefore, $p_\perp$ is limited in a way that $p_\parallel$ is not, and the gradient $\partial f/\partial p_\perp$ is much steeper than $\partial f/\partial p_\parallel$.

It should be noted that the distribution functions calculated for this thesis work are all monotonically-decreasing, i.e. $\partial f/\partial p_\perp \leq 0$ and $\partial f/\partial p_\parallel \leq 0$. However, in principle, CODE distribution functions can exhibit non-monotonic features if runaways "pile up" at an energy which is balanced by the electric force, collisional friction, and synchrotron damping, as well as

[b] In CODE, E can be time-dependent, but B must be time-independent.

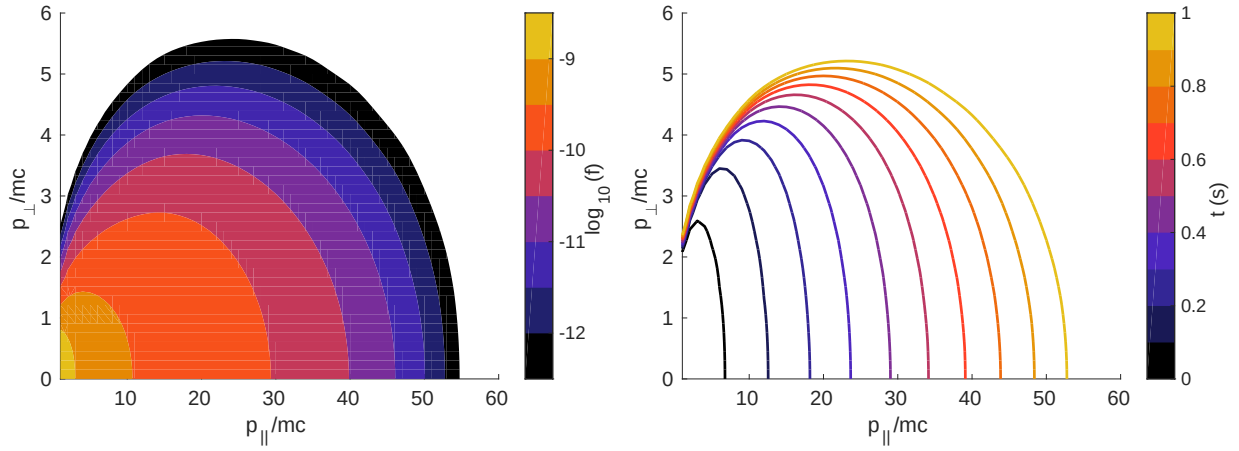

(a) $t = 1$ s (b) $\log_{10}(f) = -12$

Figure 5.1: (a) The electron momentum space distribution function $f(\boldsymbol{p})$, calculated from CODE, for one time $t = 1$ s. (b) The time-evolution of the contour $\log_{10}(f) = -12$ from $t = 0$-1 s in time steps $\Delta t = 0.1$ s. Parameters used were $n = 10^{19}$ m^{-3}, $T = 1$ keV, $Z_{\text{eff}} = 4$, $E/E_{\text{C}} = 15$, and $B = 5.4$ T, and the RP avalanche source term was enabled.

diffusion into and out of that region of momentum space. It is not known whether such momentum space distribution functions are achievable in reality, but it is thought that such a "bump" in the distribution function would soon excite kinetic instabilities and be smoothed out via processes similar to inverse Landau damping; see [8, 9], for example. The effects of kinetic instabilities and wave-particle interactions are not included in CODE, which is likely why non-monotonic features in $f(\boldsymbol{p})$ can be obtained.

5.1.3 Regions of peak synchrotron emission

Our measurements of synchrotron radiation will not be able to probe the entire runaway electron distribution in momentum (or phase) space. Instead, we will only "see" a region of it: the part that "shines brightest," emitting the most synchrotron radiation. Even this is not completely true as our detector will respond differently to light emitted by runaways within various regions of momentum space, depending on the detector geometry and specifications. Discussing these diagnostic effects is left for the section 7.1.4, in which the synthetic diagnostic SOFT is described. Here, we assume that the *entire* momentum space distribution $f(\boldsymbol{p})$ can be probed.

Recall that the synchrotron power spectrum $\mathrm{d}P/\mathrm{d}\lambda$ from a *single* runaway electron, given in (3.38), depends on the runaway's energy and pitch angle as well as the magnetic field strength. The spectra of figure 3.2 indicate how the spectral peak increases in amplitude and shifts toward shorter wavelengths as p, θ_{p}, and B all increase. Now, instead of a delta function in momentum

space (i.e. one energy and one pitch angle), there is a *distribution* of p and θ_p for the runaway electron population. The synchrotron power emitted by runaways within a small region of momentum space into a small wavelength range $\mathrm{d}\lambda$ is given by

$$\mathrm{d}P = \frac{\mathrm{d}P}{\mathrm{d}\lambda}\mathrm{d}\lambda\; f(\boldsymbol{p})\mathrm{d}\boldsymbol{p}\,\mathrm{d}\boldsymbol{r} = \frac{\mathrm{d}P}{\mathrm{d}\lambda}\mathrm{d}\lambda\; f(p_\parallel, p_\perp)\, p_\perp \mathrm{d}p_\parallel \mathrm{d}p_\perp\, \mathrm{d}V, \tag{5.3}$$

where $\mathrm{d}V$ is taken to be a small volume of position space, and $p_\perp = p\sin\theta_\mathrm{p}$ is the Jacobian. It is instructive to compute the quantity $P \times f(p_\parallel, p_\perp) \times p_\perp$ to find the region of momentum space within which runaways emit the most synchrotron emission. When considering a specific wavelength range of interest $\lambda \in [\lambda_\mathrm{min}, \lambda_\mathrm{max}]$ (e.g. of a detector), this quantity is calculated as

$$I(p_\parallel, p_\perp) = p_\perp\, f(p_\parallel, p_\perp) \int_{\lambda_\mathrm{min}}^{\lambda_\mathrm{max}} \frac{\mathrm{d}P(p_\parallel, p_\perp, \lambda)}{\mathrm{d}\lambda}\mathrm{d}\lambda. \tag{5.4}$$

Here, I is just a dummy variable.

The momentum space distribution function in figure 5.1a is plotted again in figure 5.2a.[c] Note that the color-scale limits of the logarithmic plot are different, but the domain is similar. The calculation of I in (5.4) is shown in figures 5.2b and 5.2c for two wavelength ranges: visible/near-infrared (λ = 500-1000 nm) and infrared (λ = 2-3 μm). These are both normalized to their respective maxima and have the same linear color-scale. The region of peak emission is highly localized in momentum space. We denote this momentum $\boldsymbol{p}_\mathrm{c}$ as that of a "super-particle," or dominant runaway electron. In other words, the synchrotron power radiated by the entire distribution function $f(\boldsymbol{p})$ in figure 5.2a is quite similar to that of a delta function $n_\mathrm{r}\,\delta(\boldsymbol{p} - \boldsymbol{p}_\mathrm{c})$ of runaways, with density n_r appropriate to match the amplitude. The values of $\boldsymbol{p}_\mathrm{c}$ are slightly different for the two wavelength ranges investigated: $\boldsymbol{p}_\mathrm{c}/mc = (p_{\parallel\mathrm{c}}, p_{\perp\mathrm{c}})/mc \approx$ (33, 3.9) for λ = 500-1000 nm and (26, 3.3) for λ = 2-3 μm.

The localization of maximum synchrotron emission in momentum space is one of the motivations for using a TPM—described in chapter 2—for estimations of synchrotron measurements when calculations of the full distribution function are infeasible or too computationally-intensive. Referring to figure 2.2c, we can compare the momentum of the test electron from the TPM calculation to the momenta of the super-particles in figure 5.2. For the same plasma parameters, the TPM momentum is $(p_\parallel, p_\perp)/mc \approx$ (35, 3.5); this differs from the super-particles of figures 5.2b and 5.2c by ∼10-30%. This close agreement is actually quite fortuitous since the TPM calculation does not account for any wavelength dependencies. The TPM estimation of the runaway energy to within 30% is likely sufficient for our purposes. When evaluating mitigation

[c] The plots in figure 5.2 were made using `codeviz`, a visualization tool for CODE, which can be downloaded at https://github.com/hoppe93/codeviz.

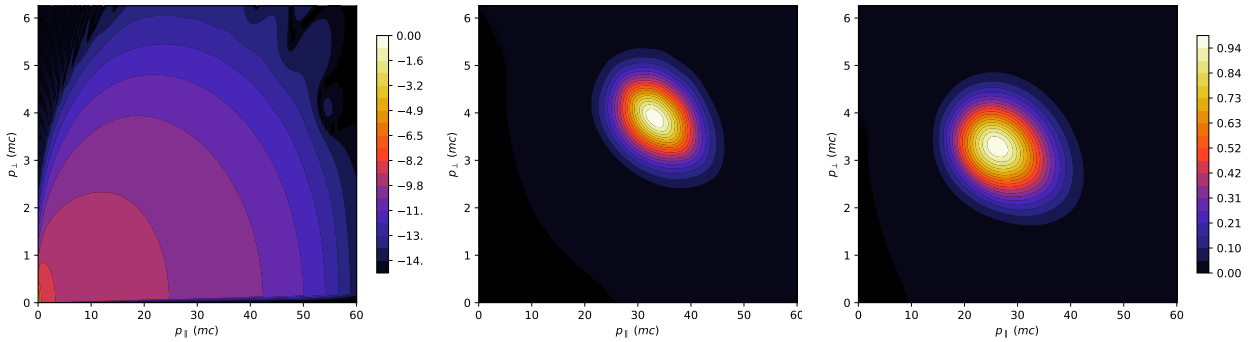

(a) $\log_{10}(f)$ (b) $\lambda =$ 500-1000 nm (c) $\lambda =$ 2-3 μm

Figure 5.2: (a) The same electron momentum space distribution function $\log_{10}(f)$ from figure 5.1a, but with a different logarithmic color-scale. The convolutions $f \times p_\perp \times P$, from (5.4), for wavelength ranges (b) $\lambda =$ 500-1000 nm and (c) $\lambda =$ 2-3 μm. Note that (b) and (c) have the same linear color-scale. These plots were made using `codeviz`.

strategies for machine protection, an experimental runaway energy resolution of $\Delta\mathcal{E} \sim 5$ MeV ($\Delta p/mc \sim 10$) is probably good enough. For example, the author opines that it is more important to know if there are numerous runaways with energies of 20, 30, or 40 MeV in your plasma than to distinguish among individual energies of 28, 30, and 32 MeV.

5.2 Parameter scans in CODE

This section will explore further the dependencies of the electron momentum space distribution on driving, damping, and source terms. For each of the following CODE simulations, all input parameters—n, T, E/E_C, B, and Z_eff—are time-independent, and the distribution function $f(t, \boldsymbol{p})$ is allowed to evolve from t = 0-1 s, starting from a Maxwellian with temperature T. The plasma density and temperature are always $n = 10^{19}$ m^{-3} and $T = 1$ keV. "Base case" parameters are $B = 5.4$ T and $Z_\mathrm{eff} = 1$, and the RP avalanche source term is used, unless otherwise noted. Finally, the distribution function is always shown for the last time, $t = 1$ s, in the following figures.

5.2.1 Driving force, E/E_C

Figure 5.3 shows the resulting electron distribution function for three ratios of the electric to critical field [10]: $E/E_\mathrm{C} = 5$, 10, and 20. Note that because the avalanche growth rate increases with E/E_C—refer to (2.19)—each distribution function $f(\boldsymbol{p})$ must be normalized to the runaway density n_r in order for them all to be plotted with the same color-scale. As expected, $f(\boldsymbol{p})$ is elongated in the parallel direction ($p_\parallel/mc$) for higher values of E/E_C since the electric field accelerates runaways parallel to the magnetic field. The perpendicular extent of $f(\boldsymbol{p})$ increases only slightly with increasing E/E_C.

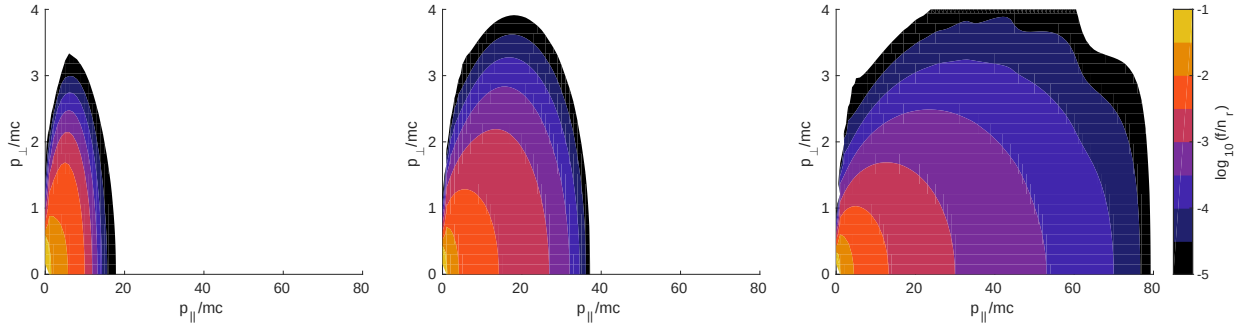

(a) $E/E_\mathrm{C} = 5$ (b) $E/E_\mathrm{C} = 10$ (c) $E/E_\mathrm{C} = 20$

Figure 5.3: Electron momentum space distribution functions, calculated with CODE, for three ratios of the applied to critical electric field: $E/E_\mathrm{C} =$ (a) 5, (b) 10, and (c) 20. The distribution function $f(\boldsymbol{p})$ is normalized to the calculated runaway density n_r so that all color-scales are the same. Compare to the TPM of figure 2.2a. ($B = 5.4$ T, $Z_\mathrm{eff} = 1$, RP avalanche source.)

Note also the "wiggles" of the contour $\log_{10}(f) \approx$ -5 in figure 5.3c; these are artifacts of the pitch angle discretization via Legendre polynomial expansion in CODE. This is typically only

seen at low values of $f(\boldsymbol{p})$ so that it has little effect on the expected synchrotron measurement; the pitch angle resolution in the simulation can also be increased, if necessary.

5.2.2 Radiation reaction, B

The effect of increasing magnetic field strength B on the electron distribution function is shown in figure 5.4. CODE simulations were run with $B = 2.7$, 5.4, and 7.8 T. These are three fields at which runaways were generated in Alcator C-Mod; synchrotron spectral measurements from these discharges are analyzed in chapter 6. The distribution functions $f(\boldsymbol{p})$ are all plotted on the same logarithmic color-scale, so that they can be compared directly. As is seen, the pitch angle (and perpendicular momentum) distribution narrows significantly as B increases. Again, this is due to synchrotron power growing like $p_\perp^2 B^2$: for higher B, smaller $p_\perp$ is required to radiate away the same power. The parallel momentum also decreases slightly with B. This implies that total runaway energies *decrease* as the magnetic field *increases*, a hopeful outlook for future high-field tokamaks.

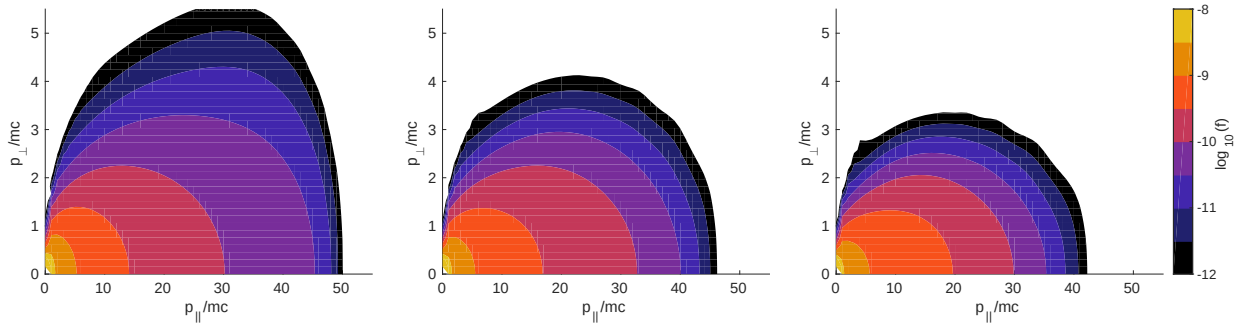

(a) $B = 2.7$ T (b) $B = 5.4$ T (c) $B = 7.8$ T

Figure 5.4: Electron momentum space distribution functions, calculated with CODE, for three magnetic fields: $B =$ (a) 2.7 T, (b) 5.4 T, and (c) 7.8 T. All color-scales and axes are the same. Compare to the TPM of figure 2.2b. ($E/E_C = 12$, $Z_{\text{eff}} = 1$, RP avalanche source.)

5.2.3 Pitch angle scattering, Z_{eff}

In figure 5.5, the effect of increasing Z_{eff} on the electron distribution function is depicted. As Z_{eff} is increased from 1 to 2 to 4, the runaway population decreases in parallel momentum and density. This matches expectations because Z_{eff} contributes to collisional friction and also decreases the primary and secondary growth rates—see (2.13) and (2.19). However, the perpendicular momentum decreases only slightly with increasing Z_{eff}, meaning that the pitch angle remains approximately constant or even increases. This is a result of higher Z_{eff} leading to increased pitch angle scattering.

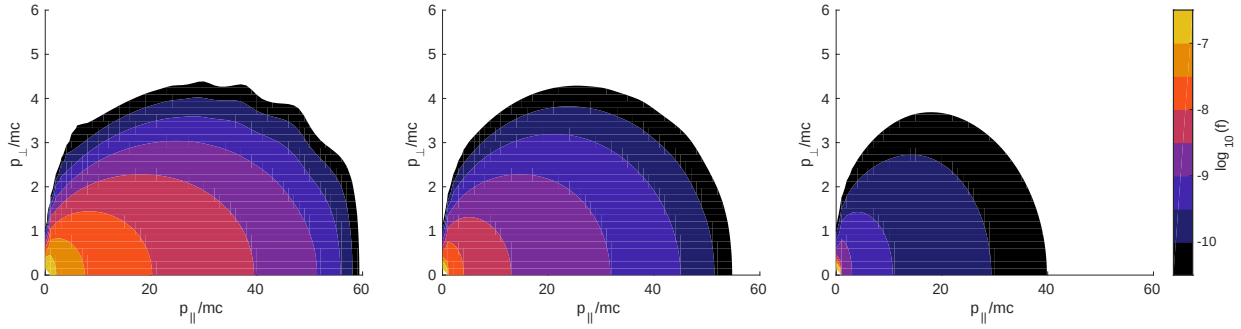

(a) $Z_{\mathrm{eff}} = 1$ (b) $Z_{\mathrm{eff}} = 2$ (c) $Z_{\mathrm{eff}} = 4$

Figure 5.5: Electron momentum space distribution functions, calculated with CODE, for three effective charges: $Z_{\mathrm{eff}} =$ (a) 1, (b) 2, and (c) 4. All color-scales and axes are the same. Compare to the TPM of figure 2.2c. ($E/E_{\mathrm{C}} = 15$, $B = 5.4$ T, RP avalanche source.)

5.2.4 Avalanche sources

In CODE, the avalanche source term S in (5.1) can be turned on and off. If off, then primary (Dreicer) generation [10] is the only mechanism accelerating runaways from the tail of $f(\boldsymbol{p})$. The resulting distribution function, shown in figure 5.6a, is highly elongated along $p_\parallel/mc$ since runaways are primarily diffusing from the region of the Maxwellian distribution aligned with the magnetic field.

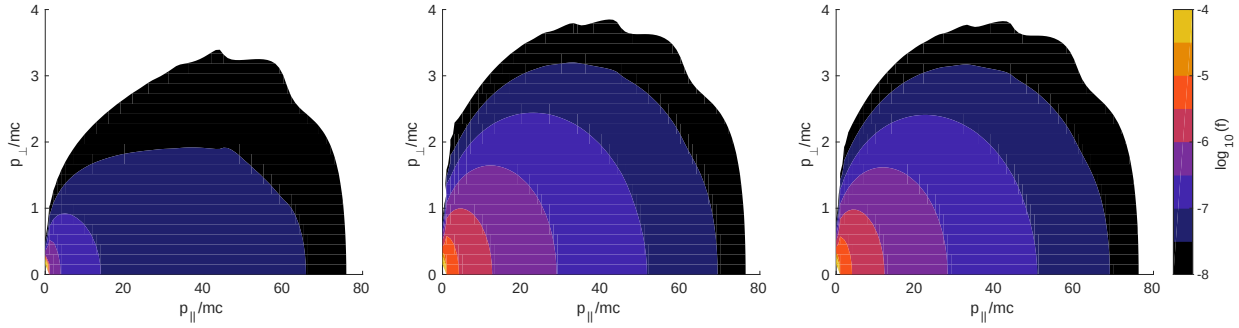

(a) Dreicer generation [10] (b) Rosenbluth-Putvinski [5] (c) Chiu-Harvey [6]

Figure 5.6: Electron momentum space distribution functions, calculated with CODE, using (a) no avalanche source term (i.e. only primary generation from [10]) or the avalanche source terms from (b) Rosenbluth and Putvisnki [5] and (c) Chiu *et al* [6]. All color-scales and axes are the same. ($E/E_\mathrm{C} = 20$, $B = 5.4$ T, $Z_\mathrm{eff} = 1$.)

Figures 5.6b and 5.6c show the resulting runaway distributions when secondary avalanching is enabled, using the RP [5] and CH [6] source terms, respectively. Notice that these two distribution functions are almost indistinguishable from each other, indicating that the RP term is often an allowable approximation. However, a large discrepancy is seen when comparing with the no-avalanche case in figure 5.6a. With avalanching on, the density of runaways is greatly increased at larger values of $p_\parallel/mc$ and $p_\perp/mc$ as secondary runaways are knocked into these regions via large-angle collisions. Note that the color-scales for all three plots are the same, so that they can be compared directly.

5.3 SOFT simulations

The versatile synthetic diagnostic SOFT is needed to adequately reproduce and explain the experimental measurements of synchrotron radiation analyzed in this thesis. SOFT takes as inputs the detector geometry and specifications, magnetic topology, and runaway phase space distribution and then outputs the desired synthetic signal, such as the spectrum, image, or polarization information of the modeled synchrotron emission. Detector properties are normally determined from installation and calibration. A magnetic reconstruction, like EFIT [11], which uses experimental magnetic measurements, is usually sufficient if the runaway current is small compared to the plasma current, i.e. $I_\mathrm{r} \ll I_\mathrm{p}$. This is inferred from loop voltage measurements in C-Mod. However, if I_r is a significant fraction of I_p, which can happen in post-disruption runaway beams, then the magnetic geometry must be determined by another method. The runaway distribution in phase space can either be (i) forward-modeled using CODE, a TPM, or other numerical tools or (ii) *inverted* using Green's functions, as discussed below. The former allows validation of theoretical models of runaway evolution; however, if they cannot fully reproduce experiment, then inferring some aspects of the phase space distribution can provide insight into missing physics.

5.3.1 Synchrotron detection

The full details of the calculations in SOFT can be found in [3]. Here, they are briefly overviewed. Consider a detector (observer) located at position $\boldsymbol{r}_\mathrm{o}$ with detector normal $\hat{n}_\mathrm{d}$ and opening half-angle α. All lines-of-sight (LOS) with unit vectors $\hat{n}_k$ such that $\hat{n}_k \cdot \hat{n}_\mathrm{d} \geq \cos\alpha$ have the potential to detect radiation. This is depicted in figure 5.7, which has been updated from figure 3.1 to include the detector geometry. The synchrotron power *detected* per unit area per unit solid angle in the wavelength interval $[\lambda, \lambda + \mathrm{d}\lambda]$ along LOS $\hat{n}_k$ is given by equation (1) of [3]

$$\frac{\mathrm{d}^3 P_\mathrm{o}(\boldsymbol{r}_\mathrm{o}, \hat{n}_k, \lambda)}{\mathrm{d}A\,\mathrm{d}\Omega_k\,\mathrm{d}\lambda} = \int \mathrm{d}\boldsymbol{r}\,\mathrm{d}\boldsymbol{p}\,\delta(\boldsymbol{X}/X - \hat{n}_k)\,\frac{\hat{n}_k \cdot \hat{n}_\mathrm{d}}{X^2}\,\frac{\mathrm{d}^2 P(\boldsymbol{r}, \boldsymbol{p}, \lambda)}{\mathrm{d}\Omega\,\mathrm{d}\lambda}\,f(\boldsymbol{r}, \boldsymbol{p}). \tag{5.5}$$

Here, the notation is kept as close as possible to that in chapter 3, except now $\boldsymbol{X} = \boldsymbol{r} - \boldsymbol{r}_\mathrm{o}$, and R is reserved for the major radius, to be used later. The delta function selects out radiation along the LOS, and the dot product relates the detector area and subtended solid angle via $\mathrm{d}\Omega/\mathrm{d}A = \hat{n}_k \cdot \hat{n}_\mathrm{d}/X^2$. The runaway phase space distribution is $f(\boldsymbol{r}, \boldsymbol{p})$, and $\mathrm{d}^2P/\mathrm{d}\Omega\mathrm{d}\lambda$ is the power radiated per unit solid angle per unit wavelength from [12] given in (3.35). Note that $\mathrm{d}^2P/\mathrm{d}\Omega\mathrm{d}\lambda$ can be decomposed into power radiated along each axis of an orthogonal basis via the electric field calculations from [13] and given in (3.29). The actual implementation in SOFT, however, is slightly different than the derivation provided in chapter 3; further details are provided

in appendix B and [14].

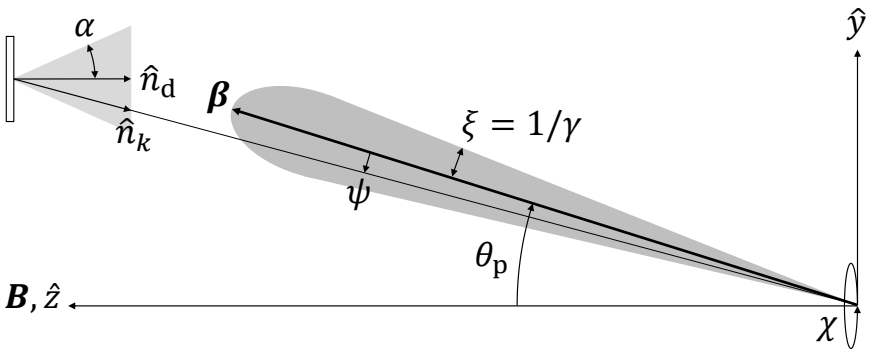

Figure 5.7: An updated version of figure 3.1, now with a detector at left with detector normal $\hat{n}_\mathrm{d}$ and opening half-angle α. Synchrotron radiation will be visible along the LOS with unit vector $\hat{n}_k$. See figure 3.1 for the definitions of the other parameters.

As discussed previously in chapter 3 and shown in figure 5.7, the angular distribution of synchrotron radiation at one instant in time has a characteristic width $\xi \sim 1/\gamma$. Therefore, the small gyro-radius and fast gyro-frequency of a runaway effectively produces a *cone* of synchrotron emission, with the direction determined by the runaway's parallel velocity $v_\parallel$ and opening half-angle approximately equal to the runaway pitch angle $\theta_\mathrm{p} = \arctan(v_\perp/v_\parallel)$. Calculating the full angular distribution of emission in SOFT is possible but also computationally-expensive. Synthetic data can be approximated more efficiently using the so-called *cone model*, for which *all* of the synchrotron power is emitted along the runaway velocity vector $\boldsymbol{v} = \boldsymbol{\beta}c$; this is the limit when $\gamma \gg 1$, so that $\xi \to 0$. In SOFT, the cone model is implemented as

$$\left\langle \frac{\mathrm{d}^2 P}{\mathrm{d}\Omega \mathrm{d}\lambda} \right\rangle = \frac{1}{2\pi} \frac{\mathrm{d}P}{\mathrm{d}\lambda} \delta(1 - \cos\psi), \tag{5.6}$$

where $\langle \cdot \rangle$ denotes averaging over the gyro-motion, $\mathrm{d}P/\mathrm{d}\lambda$ is given by (3.37), and ψ is the angle between the runaway velocity $\boldsymbol{\beta}$ and detector viewing direction $\hat{n}_k$, as shown in figure 5.7. Simulations using the cone model can run over 100 times faster than those using the full angular distribution. As will be described in the next section, the cone model adequately approximates the full calculation and is typically sufficient when producing synthetic data to compare with experiment.

5.3.2 Particle trajectories

The integral of (5.5) is carried out numerically in SOFT. While the detector geometry is encoded in $\boldsymbol{r}_{\rm o}$, $\hat{n}_{\rm d}$, and $\hat{n}_k$, the locations of the runaways $\boldsymbol{r}$ are determined from the magnetic topology, which is modeled as axisymmetric. Zeroth-order guiding center motion is used to follow particle trajectories, reducing $\boldsymbol{p}$ from three to two dimensions, i.e. $(p_\parallel, p_\perp, \chi)$ to $(p_\parallel, p_\perp)$, by averaging over the gyro-angle χ. Therefore, only the initial position—the major radius R on the outboard midplane, in this case—is needed to follow the helical orbits. Note that drift orbits are *not* yet included in SOFT because the effect on the synthetic signal is estimated to be similar to that caused by *first*-order corrections to guiding center motion, e.g. non-circular gyro-orbits.

When running SOFT, a discretization in phase space must be provided. The discretization of position space is dictated by the FOV of each pixel; for the wide-view camera in C-Mod, at least 1 particle/mm (i.e. $\Delta R \leq 1$ mm) was sufficient for the radial resolution. Typically, the runaways are "initiated" at points of minimum magnetic field in the simulation; since these are usually on the outer midplane, the prescribed R of each runaway is the maximum major radius experienced on any single trajectory. The phase space distribution $f(R, \boldsymbol{p})$ does not evolve in time in a SOFT simulation; that is, SOFT provides a "snapshot" in time, and $f(R, \boldsymbol{p})$ is assumed to be approximately constant on the transit timescale: one toroidal period is $\tau_{\rm t} \approx 2\pi R_0/c \approx 10^{-8}$ s, while the energy loss timescales $\tau_{\rm rad}$ and $\tau_{\rm coll}$ are on the order of 100 ms in C-Mod discharges—see equations (2.22) and (2.23). Thus, energy is conserved, and so is the (classical) magnetic moment

$$\mu = \frac{m v_\perp^2}{2B}. \tag{5.7}$$

Even though the total velocity is relativistic, the perpendicular velocity is not: $v_\perp^2 \ll v_\parallel^2$. Additionally, using the relativistic mass, i.e. $m \to \gamma m$, does not change the conservation law since γ (energy) is conserved. Thus, it is adequate to use the classical magnetic moment here.

The conservation of magnetic moment will play an important role in the production of synchrotron emission by runaways in a non-uniform magnetic field. We already know from the Larmor formula that $P_{\rm synch} \propto p_\perp^2 B^2$. From (5.7), we also have that $p_\perp^2/B =$ constant on the transit timescale. Thus, $P_{\rm synch} \propto B^3$, which means that runaways will produce much more synchrotron power on the high-field side of their helical orbit than on the low-field side. Note that this cubic scaling is even greater for finite wavelength ranges of the synchrotron spectrum, as described in [15].

5.3.3 Green's functions

Before performing the full integration of (5.5), we can first integrate over known geometric dependencies: (i) the detector area and all acceptable $\hat{n}_k$ acquired from the detector specifications; (ii) the toroidal and poloidal angles, since the trajectories follow field lines; and (iii) gyro-angles due to the guiding center approximation. Thus, a measured signal at detector pixel[d] (i, j) can be calculated from the integral

$$\frac{\mathrm{d}P_{ij}}{\mathrm{d}\lambda} = \int \mathrm{d}R\,\mathrm{d}\boldsymbol{p}\, f(R,\boldsymbol{p})\,\frac{\mathrm{d}\hat{G}_{ij}(R,\boldsymbol{p},\lambda)}{\mathrm{d}\lambda}, \tag{5.8}$$

where $\boldsymbol{p}$ is now two-dimensional, and $\hat{G}_{ij}$ represents the *Green's* function calculated by SOFT. (Compare (5.8) to (5.5).) This Green's function is essentially a detector response function which incorporates all geometric effects like the detector setup and magnetic geometry. It is a very powerful feature of SOFT; once $\hat{G}_{ij}$ is computed, two avenues can be explored: (i) Many distribution functions $f(R,\boldsymbol{p})$ can be integrated via (5.8) to best match synthetic and experimental signals, or (ii) the properties of $\hat{G}_{ij}$ itself, along with experimental data, can be studied to better constrain $f(R,\boldsymbol{p})$.

Unless spectral information is required, SOFT can also integrate over wavelength such that (5.8) can be simplified as

$$P_{ij} = \int \mathrm{d}R\,\mathrm{d}\boldsymbol{p}\, f(R,\boldsymbol{p})\,\hat{G}_{ij}(R,\boldsymbol{p}), \tag{5.9}$$

where $\mathrm{d}\lambda$ has been absorbed into $\hat{G}_{ij}$. It is important to note that the momentum space Jacobian is *not* absorbed into $\hat{G}_{ij}$; instead, it is included in $\mathrm{d}\boldsymbol{p}$. In chapters 6 and 7, the distribution function will be given in terms of $f(R, p_\parallel, p_\perp)$ so that $\mathrm{d}\boldsymbol{p} = p_\perp\,\mathrm{d}p_\parallel\,\mathrm{d}p_\perp$. However, in chapter 8, the pitch angle distribution will be explored so that the distribution function is $f(R, p, \theta_\mathrm{p})$ and $\mathrm{d}\boldsymbol{p} = p^2 \sin\theta_\mathrm{p}\,\mathrm{d}p\,\mathrm{d}\theta_\mathrm{p}$.

[d] Note that non-camera data just has one pixel, i.e. $i = 1$, $j = 1$.

5.4 Parameter scans in SOFT

The purpose of this section is to explore the dependencies of SOFT outputs (i.e. synchrotron spectra, images, and polarization measurements) on SOFT inputs (e.g. detector geometry and spectral range, runaway phase space distribution, etc.). The following parameter scans will help the reader better understand the experimental measurements analyzed in chapters 6, 7, and 8. The magnetic geometry used for all of these SOFT simulations is shown in the poloidal cross-section of figure 5.8a. The toroidal field $B_0 = 5.4$ T and plasma current $I_\mathrm{p} = 800$ kA are directed *into* the page in figure 5.8a, so that both are counter-clockwise in the top-down schematic of figure 5.8b. This direction of I_p means that the poloidal magnetic field is in the clockwise direction in figure 5.8a.

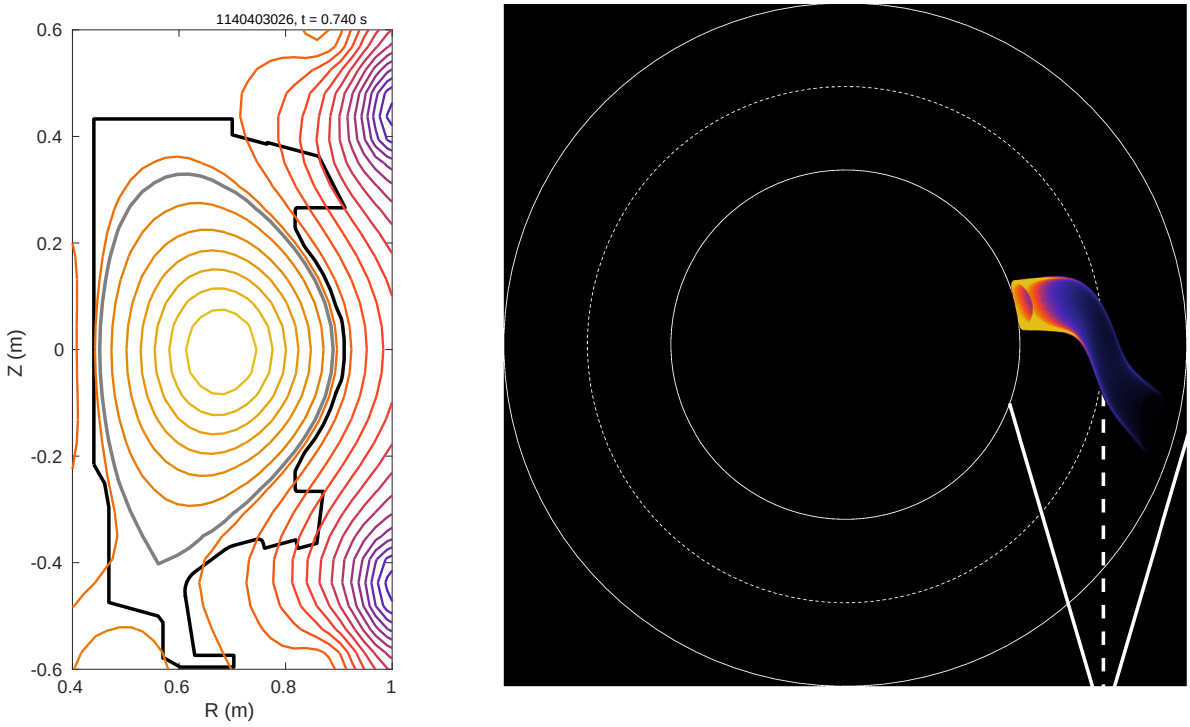

(a) (b)

Figure 5.8: (a) Poloidal flux contours, including the last closed flux surface (grey), overlay a vertical cross-section of the C-Mod vacuum vessel (black). (b) A top-down view of the reference SOFT simulation; the radial/toroidal intensity distribution corresponds to the intensity of synchrotron radiation detected by the detector *located in the midplane*, with field-of-view (solid) and line-of-sight (dashed) indicated by the thick lines. This is *not* the synchrotron radiation pattern that would be measured by a detector looking down on the tokamak. The midplane major radii of the last closed flux surface (solid) and magnetic axis (dashed) are shown as thin-lined circles.

The "reference" position of the detector is on the midplane ($Z = 0$) with line-of-sight (LOS) tangent to the major radius of the plasma axis ($R = R_0 = 68$ cm), as shown by the thick dashed line in figure 5.8b. The detector is located 1 m from the poloidal cross-section to which the LOS is normal. The total opening angle modeled in SOFT is $2\alpha = \pi/4$. However, as mentioned previously in chapter 4, this is the angle spanning the *diagonal* of the output square image, meaning that the angle spanning the horizontal (or vertical) extent of the square image is given by

$$\tan(\alpha_{\text{diag}}) = \sqrt{2}\tan(\alpha_{\text{horiz}}). \tag{5.10}$$

Here, α is again the opening *half*-angle. The detector field-of-view (FOV) falls within the thick solid lines of figure 5.8b.

The detector modeled in SOFT is really an *imaging spectropolarimeter* in that it captures an image along with spectral and polarization information; i.e. the Stokes parameters can be calculated for each pixel and wavelength.[e] The synthetic image is 400×400 pixels and has an aperture of 1 cm^2; the reference wavelength range is in the visible/near-infrared, $\lambda =$ 500-1000 nm. The reference runaway phase space distribution has the following properties: All runaways have the same momentum $p/mc = 60$ ($\mathcal{E} \approx 30$ MeV) and pitch angle $\theta_{\text{p}} = 0.1$ rad, and the runaway density profile decreases linearly from the magnetic axis to plasma edge, $R =$ 68-88 cm. The cone model is used unless noted otherwise.

5.4.1 Reference image and radial structure

The reference *image* of synchrotron radiation intensity (from the reference scenario) is shown in figure 5.9a, with the high-field side (HFS) on the left. Note that this plot and all others in this section are false-colored. This is really a greyscale image because the intensity has been integrated over the visible wavelength range. The colormap[f] used is perceptually-uniform, allowing the eye to distinguish features while maintaining the perceived brightness if converted to greyscale.

Figure 5.9a is chopped up into radial bands in figure 5.9b, in which synchrotron emission is only shown for runaways within eleven radial bands of width $\Delta R = 1$ cm at radial steps of 2 cm from $R =$ 68-88 cm. Here, the emission is normalized within each band to highlight the structure. The center-most ring corresponds to runaways nearest the magnetic axis; the reason that this appears as a ring, instead of a dot, is because runaways were not populated directly at the magnetic axis. While this is not physically-realistic, it is useful in this analysis as the center of the runaway beam can be identified by this black dot (i.e. no emission).

[e] To my knowledge, such an imaging spectropolarimeter has never been used for synchrotron studies, but could be very useful.

[f] Credit goes to Geri Papp, who introduced this colormap to me.

As expected, the synchrotron pattern expands outward from the center for runaways at larger minor radii. For helical trajectories near the magnetic axis, runaways are visible on the entire flux surface, which is seen as a ring. However, as the minor radius increases, there are only certain sections of a runaway's trajectory along which its synchrotron emission is directed into the detector's FOV. Since runaways travel in the counter-I_{p} direction, their poloidal motion is counter-clockwise here (see figure 5.8a). Therefore, synchrotron emission is directed into the detector's FOV by runaways at the top-left and bottom-right; this creates the backward-$\mathcal{S}$-like pattern in the synthetic images. Due to the major-radially-decreasing magnetic field strength, the measured synchrotron emission is brighter on the high field side (HFS, left) compared to the low field side (LFS, right).

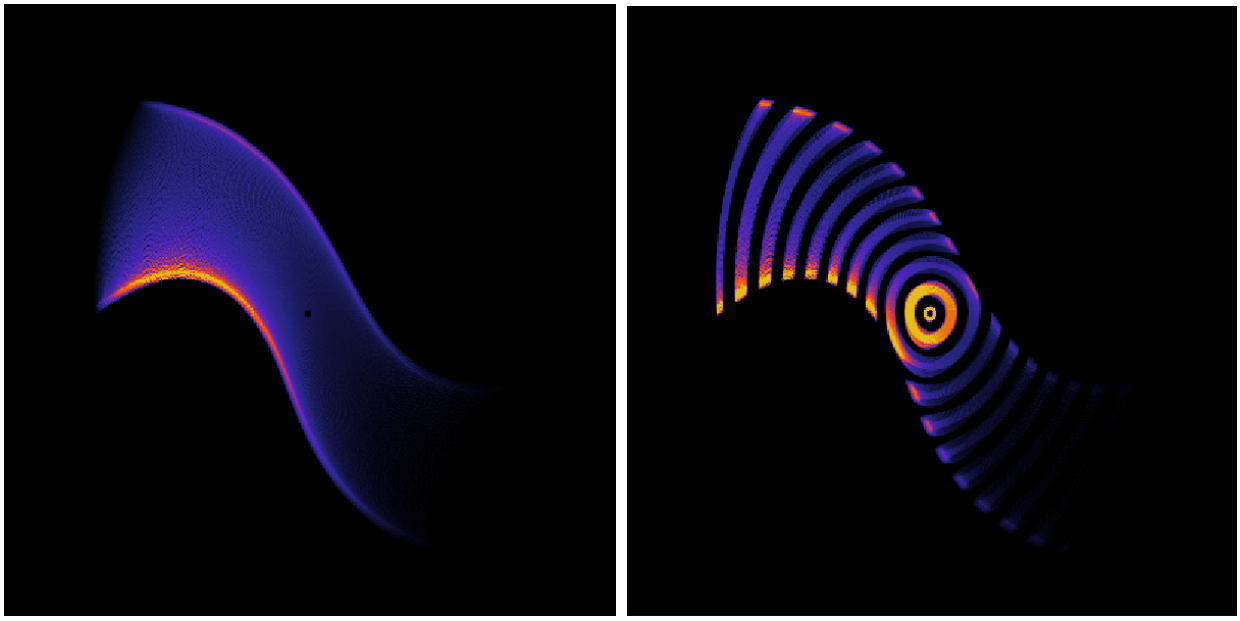

(a) (b)

Figure 5.9: (a) The reference SOFT image. (b) The same figure as (a), but with eleven radial bands of runaways highlighted. Each band has width $\Delta R = 1$ cm extending from $R = 68$-88 cm in steps of 2 cm. The detected intensity from runaways within each radial band is *normalized* to the maximum intensity from that band. Because runaways within the same band can produce non-circular features on either side of the central "ring," those features on the left (HFS) are brighter than their right (LFS) counterparts.

Refer back to figure 5.8b; it shows the toroidal and radial positions of runaway electrons which contribute synchrotron emission to the reference image in figure 5.9a. The intensity distribution of figure 5.8b indicates the actual intensity of synchrotron radiation *received by the midplane detector* from runaways at each location. Thus, figure 5.8b is *not* what an observer would

see when looking down on the tokamak. Instead, it shows the region of position space probed by the detector. In other words, there are runaways located at all positions within the plasma boundaries (solid white circles), but those in regions of zero emission (black) are not detectable. By comparing figures 5.8b and 5.9a, it can be inferred that the detector views an $\mathcal{S}$-like "tube" of runaways, with emission dominated by runaways on the HFS (with R_0 indicated by the dashed line in figure 5.8b). In addition, peak intensities near the edges of the $\mathcal{S}$ in the detected image (figure 5.9a) can be explained by line-integration effects as detector LOS pierce the so-called *surface-of-visibility* [3, 15]. Note that SOFT accounts for the inner wall, which can obstruct light, but reflections off the first wall are not yet implemented.

5.4.2 Cone model vs full angular distribution

Figure 5.10 compares reference images produced using the cone model approximation and full angular distribution calculation. Each figure is normalized to its own maximum intensity. The overall shape and intensity distribution is quite similar between the two images. The major difference is the fuzziness resulting from the full angular distribution, which slightly "spreads" out the radiation, as expected. Though not shown here, a distribution of pitch angles will also cause a similar effect; this is discussed further in chapter 7. The SOFT computation time required for the full angular distribution was almost a factor over 1000 longer than that needed for the cone model. Therefore, using the cone model is justified in most situations.

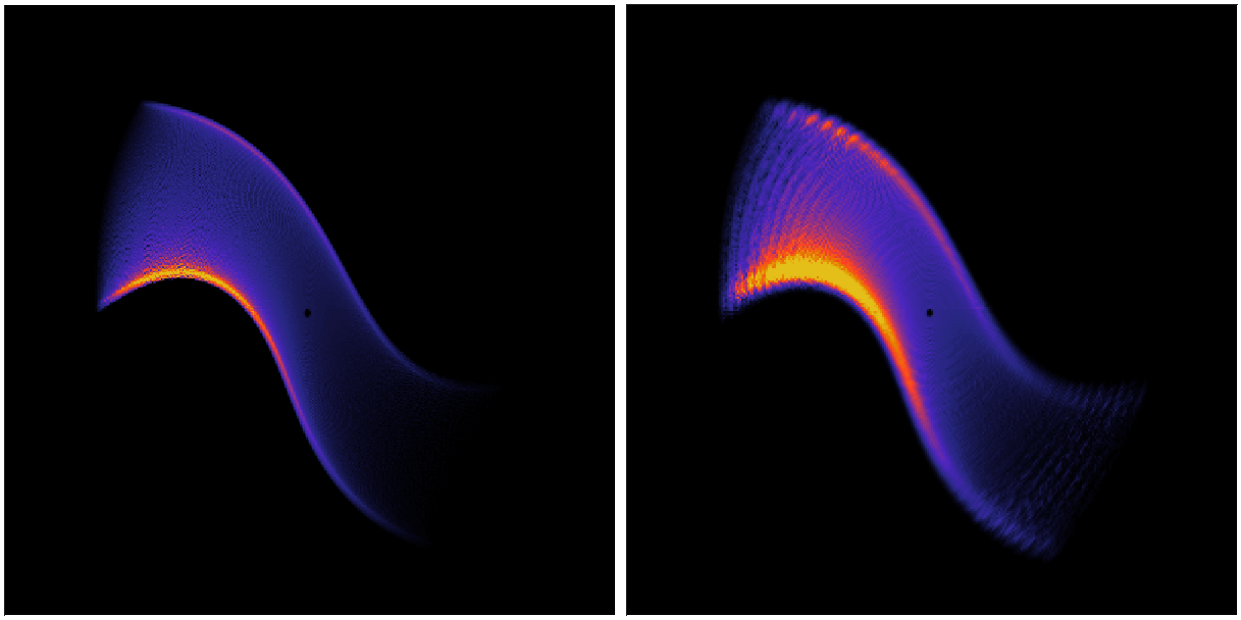

(a) Cone model. (b) Full angular distribution.

Figure 5.10: Reference images produced using (a) the cone model approximation (reference) and (b) the full angular distribution calculation. The intensity is normalized in each image.

5.4.3 Detector vertical position, Z

The vertical position of the detector was scanned, with resulting images shown in figure 5.11. Note that the LOS remains horizontal for each simulation. As the virtual detector is displaced downward (below the midplane), the synchrotron pattern moves upward, as expected. Recall that the runaway beam minor radius is 20 cm, so that the bottom-most position, Z = -20 cm, is really only viewing the bottom half of the runaway beam. Because the brightness peaks on the HFS, most light is visible from runaways in the bottom-left quadrant of the runaway beam. This leads to a distinct synchrotron intensity pattern which more closely resembles a parabola than a backward-$\mathcal{S}$. Having multiple cameras at different vertical positions could therefore help diagnose different regions of position space. The wide-view camera in C-Mod, which captured images of synchrotron emission, is also located significantly below the midplane, at Z = -22 cm, as discussed in chapter 4. Therefore, the experimental images analyzed in this thesis work are most similar to that in figure 5.11c.

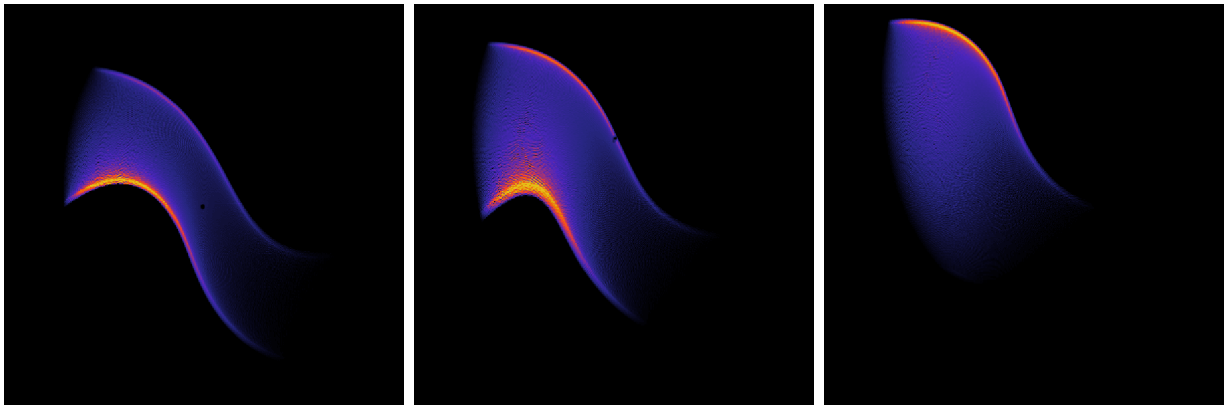

(a) Z = 0 cm (b) Z = -10 cm (c) Z = -20 cm

Figure 5.11: Synthetic synchrotron images resulting from a scan in detector vertical position: Z = (a) 0 (reference), (b) -10 cm, and (c) -20 cm. All images have the same color-scale, so they can be compared directly.

A scan in the virtual detector's major radial position was also performed, but the result was only a left-right shift of the synchrotron pattern without any other noticeable changes. Similarly, increasing/decreasing the detector opening angle only shrinks/grows the overall synchrotron spot size. The results of these scans are not included here.

5.4.4 Detector spectral range, λ

The spectral range of the virtual detector was also varied to simulate visible (λ = 500-1000 nm), near-infrared (λ = 1-1.5 μm), and infrared (λ = 2.5-3 μm) cameras. The resulting images are shown in figure 5.12. For these SOFT simulations, the spectral response function is treated as uniform over the given wavelength range. Note that all three images are plotted with the same color-scale; thus, the intensity distributions can all be compared directly. It is seen that the shape of the intensity distribution does not vary among the images, but the absolute intensity increases with λ. This indicates that the peak of the spectral power density is in the infrared instead of the visible, as predicted for parameters p/mc = 60, θ_{p} = 0.1 rad, and B_0 = 5.4 T in figure 3.2.

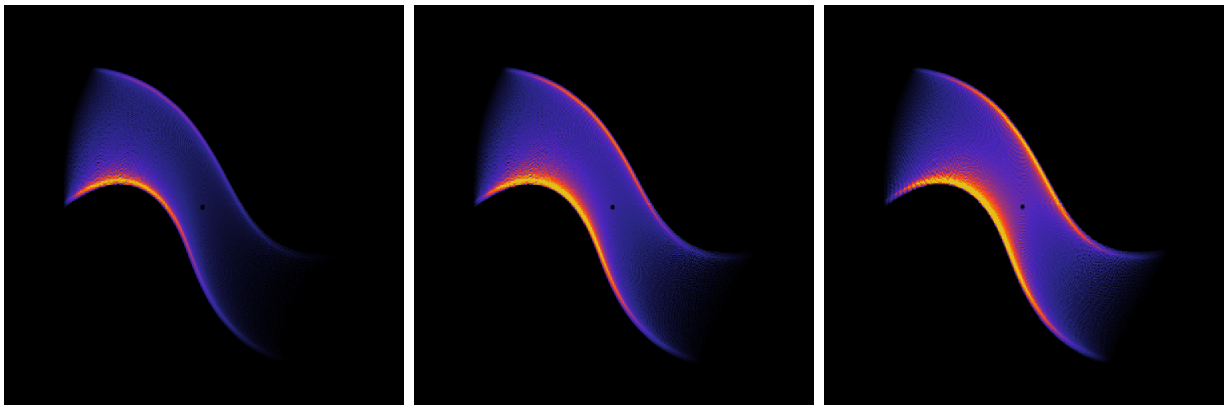

(a) λ = 500-1000 nm (b) λ = 1-1.5 μm (c) λ = 2.5-3 μm

Figure 5.12: Synthetic synchrotron images resulting from a scan over detector spectral ranges: λ = (a) 500-1000 nm (reference), (b) 1-1.5 μm, and (c) 2.5-3 μm. All images have the same color-scale, so they can be compared directly.

5.4.5 Runaway electron momentum (energy), p ($\mathcal{E}$)

Figure 5.13 shows the synthetic images resulting from a scan in runaway momentum, while keeping the pitch angle fixed at $\theta_{\mathrm{p}} = 0.1$ rad. As is seen, the shape of the synchrotron pattern does not change with energy; however, the intensity increases nonlinearly. The intensities of figures 5.13a and 5.13b are scaled by factors 10 and 5, respectively, in order to make them visible on the same color-scale as figure 5.13c. Unless the detector is absolutely-calibrated and the total density/number of runaways can be estimated, it is probably better to estimate the runaway energies from the synchrotron spectrum (see figure 5.12) rather than from the absolute intensity seen here. This could involve a camera measuring intensities at different wavelengths.

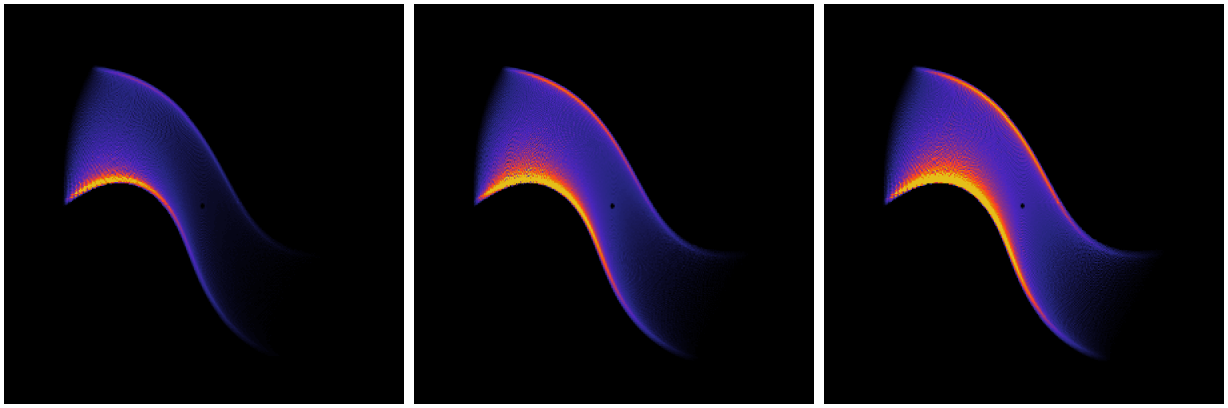

(a) $p/mc = 50$, scale $= 10$ (b) $p/mc = 60$, scale $= 5$ (c) $p/mc = 70$, scale $= 1$

Figure 5.13: Synthetic images resulting from a scan in momentum: $p/mc =$ (a) 50, (b) 60 (reference), and (c) 70. Each intensity distribution is scaled by a factor of (a) 10, (b) 5, and (c) 1 in order to be plotted on the same color-scale. Note that (a)-(c) correspond to energies of $\mathcal{E} \approx 25$, 30, and 35 MeV, respectively.

5.4.6 Runaway electron pitch angle, θ_p

Unlike the energy, changing the runaway pitch angle significantly alters the synchrotron spot shape. The synchrotron $\mathcal{S}$ is slim for small pitch angles, as seen in figure 5.14a, and broadens as θ_p increases. For $\theta_\mathrm{p} = 0.2$ rad, shown in figure 5.14c, the synchrotron spot has almost filled the entire detector FOV. Increasing θ_p beyond this essentially creates a blob-like shape. Note that the intensity also increases nonlinearly with θ_p, but each image is normalized to its peak intensity in order to highlight the changes in shape.

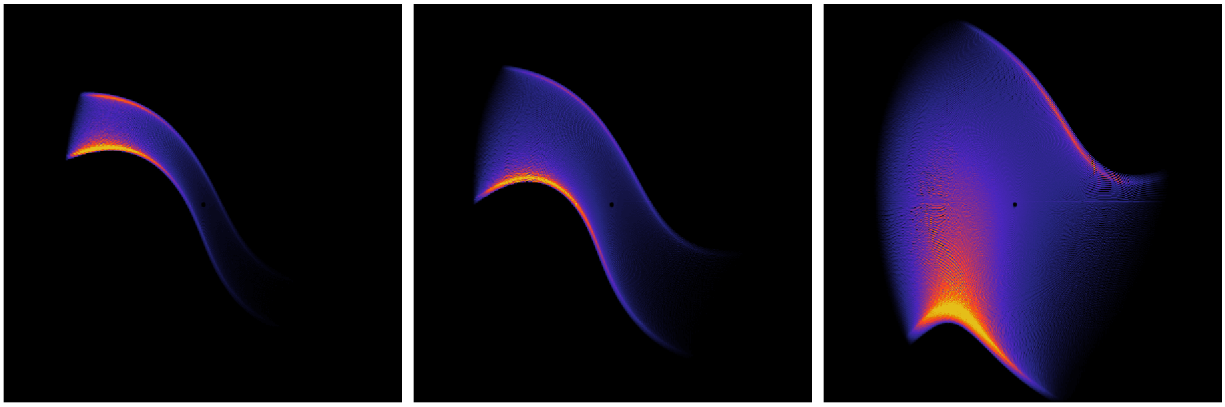

(a) $\theta_\mathrm{p} = 0.05$ rad (b) $\theta_\mathrm{p} = 0.10$ rad (c) $\theta_\mathrm{p} = 0.20$ rad

Figure 5.14: Synthetic images resulting from a scan in pitch angle: $\theta_\mathrm{p} =$ (a) 0.05 rad, (b) 0.1 rad (reference), and (c) 0.2 rad. Each image is normalized to its own maximum intensity. If the maximum intensity of (a) is scaled to be 1 (a.u.), then the maximum value of (b) is $\sim$54 and of (c) is $\sim$380.

5.4.7 Runaway electron density profile, n_r

Figure 5.15 shows the synthetic images resulting from three different runaway density profiles across the minor radius: uniform, linearly-decreasing (used in the reference image), and Gaussian of the form

$$n_\mathrm{r} \propto \exp\left[-\frac{1}{\sigma^2}\left(\frac{r}{a_\mathrm{r}}\right)^2\right] \tag{5.11}$$

with $a_\mathrm{r} = 20$ cm the runaway beam radius, and $\sigma = 1/3$ in this case. Each image is normalized to its own maximum intensity.

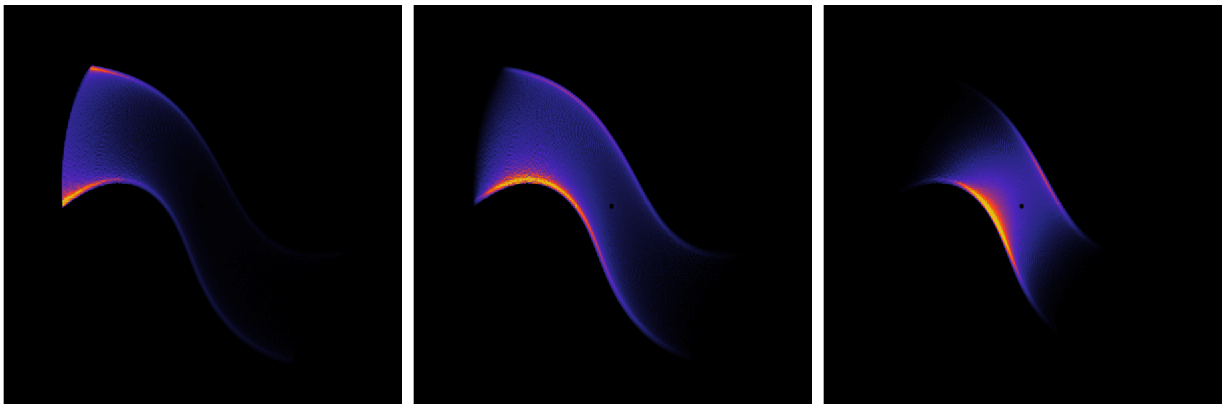

(a) Uniform. (b) Linear. (c) Gaussian ($\sigma = 1/3$).

Figure 5.15: Synthetic images resulting from three different runaway density profiles: (a) uniform, (b) linearly-decreasing from $r = 0$ to a_r ($R =$ 68-88 cm, reference), and (c) Gaussian with $\sigma = 1/3$, as described in the text. Each image is normalized to its own maximum intensity.

For the uniform profile, in figure 5.15a, the synchrotron emission detected is completely dominated by runaways at the beam edge on the HFS. A linearly-decreasing profile, in figure 5.15b, helps to even out the synchrotron intensity distribution. The highly centrally-peaked Gaussian profile, in figure 5.15c, emphasizes the central region of the runaway beam. As explored in chapter 7, experimental observations of non-saturated, full synchrotron shapes indicate that n_r must decrease with minor radius, or else only a sliver of light on the HFS would be seen. For the calculation of n_r in CODE, refer to appendix D.

5.4.8 Polarization measurements

Because synchrotron emission is polarized, a polarization filter could be placed in front of our virtual detector to capture images of horizontally and vertically-polarized light. The following synthetic images were created using the Stokes parameters calculated with SOFT (see appendix B for more details). From (B.6), the intensity of light passing through a polarization filter is

$$\mathcal{I}(\theta_0) = \frac{1}{2}\left[I + Q\cos(2\theta_0) + U\sin(2\theta_0)\right], \tag{5.12}$$

where θ_0 is the angle of the *transmission* axis with respect to the horizontal axis of the detector, in this case. The resulting horizontally and vertically-polarized images are shown in figures 5.16a and 5.16b, respectively. Both are plotted on the same color-scale, so they can be compared directly.

Note that (5.12) can be recast in a more familiar form using the intensity L and polarization angle $\theta_{\rm pol}$ of detected *linearly*-polarized light at each pixel. Since $Q = L\cos(\theta_{\rm pol})$ and $U = L\sin(\theta_{\rm pol})$, we can write

$$\mathcal{I}(\theta_0) = \frac{1}{2}(I - L) + L\cos^2(\theta_{\rm pol} - \theta_0). \tag{5.13}$$

The first term corresponds to light that is not linearly-polarized, with the factor of $1/2$ coming from an average over all angles, i.e. $\langle\cos^2(\cdot)\rangle = 1/2$. The second term is the expected contribution from linearly-polarized light.

Polarization angles are shown in figure 5.16c, where $\theta_{\rm pol} = 0°$ (grey) and $90°$ (black) indicate horizontal and vertical polarization, respectively. Interestingly, the edges of the backward-$\mathcal{S}$ shape are primarily horizontally-polarized, while the center of the $\mathcal{S}$ is vertically-polarized. As will be discussed further in chapter 8, this bifurcation in $\theta_{\rm pol}$ is highly sensitive to the runaway pitch angle distribution, magnetic topology, and detector geometry. Foreshadowing what is to come, note how there are two $90°$ transitions in $\theta_{\rm pol}$, from $\theta_{\rm pol} = 0°$ to $90°$ and then $\theta_{\rm pol} = 90°$ back to $0°$, as the detector LOS moves across the midplane of the image. This will be shown to be a unique property of runaway synchrotron emission.

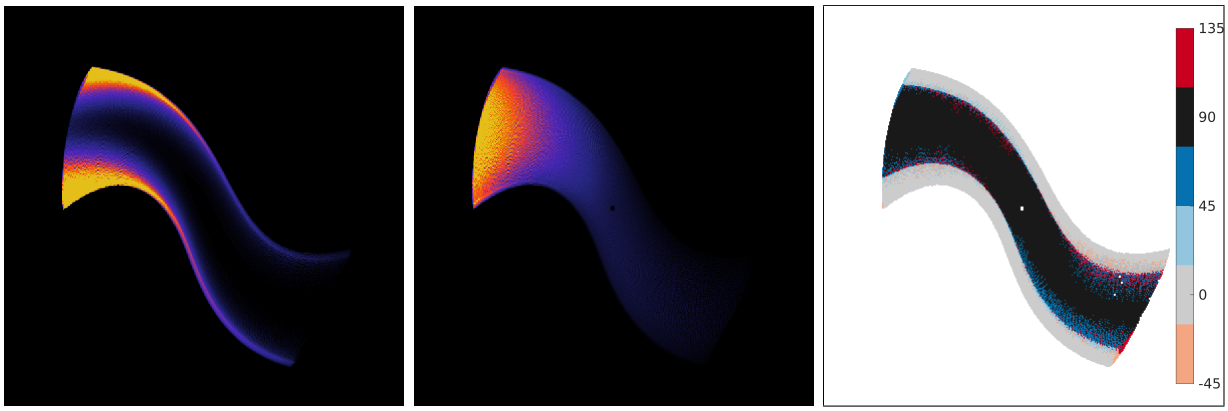

(a) Horizontally-polarized. (b) Vertically-polarized. (c) Polarization angle (°).

Figure 5.16: (a) Horizontally-polarized and (b) vertically-polarized light from the reference image—except here the runaway beam has a uniform runaway density profile—plotted with the same color-scale. (c) The polarization angle of light detected at each pixel, in degrees. The white region in (c) indicates zero detected synchrotron light, which is otherwise black in (a) and (b).

References—Chapter 5

[1] M. Landreman, A. Stahl, and T. Fülöp. Numerical calculation of the runaway electron distribution function and associated synchrotron emission. *Computer Physics Communications*, 185(3):847 – 855, 2014.

[2] A. Stahl, O. Embréus, G. Papp, M. Landreman, and T. Fülöp. Kinetic modelling of runaway electrons in dynamic scenarios. *Nuclear Fusion*, 56(11):112009, 2016.

[3] M. Hoppe, O. Embréus, R.A. Tinguely, R.S. Granetz, A. Stahl, and T. Fülöp. SOFT: a synthetic synchrotron diagnostic for runaway electrons. *Nuclear Fusion*, 58(2):026032, 2018. SOFT can be downloaded at https://github.com/hoppe93/SOFT, with documentation found at https://soft.readthedocs.io.

[4] W. Pauli. *Theory of Relativity*. Dover Books on Physics. Dover Publications, 1981.

[5] M.N. Rosenbluth and S.V. Putvinski. Theory for avalanche of runaway electrons in tokamaks. *Nuclear Fusion*, 37(10):1355, 1997.

[6] S.C. Chiu, M.N. Rosenbluth, R.W. Harvey, and V.S. Chan. Fokker-Planck simulations mylb of knock-on electron runaway avalanche and bursts in tokamaks. *Nuclear Fusion*, 38(11):1711, 1998.

[7] A. Stahl. *Momentum-space dynamics of runaway electrons in plasmas*. Chalmers University of Technology, 2017.

[8] C. Liu, E. Hirvijoki, G.-Y. Fu, D.P. Brennan, A. Bhattacharjee, and C. Paz-Soldan. Role of kinetic instability in runaway-electron avalanches and elevated critical electric fields. *Phys. Rev. Lett.*, 120:265001, 2018.

[9] C. Liu, L. Shi, E. Hirvijoki, D.P. Brennan, A. Bhattacharjee, C. Paz-Soldan, and M.E. Austin. The effects of kinetic instabilities on the electron cyclotron emission from runaway electrons. *Nuclear Fusion*, 58(9):096030, jul 2018.

[10] J.W. Connor and R.J. Hastie. Relativistic limitations on runaway electrons. *Nuclear Fusion*, 15(3):415, 1975.

[11] L.L. Lao, H. St. John, R.D. Stambaugh, A.G. Kellman, and W. Pfeiffer. Reconstruction of current profile parameters and plasma shapes in tokamaks. *Nuclear Fusion*, 25(11):1611, 1985.

[12] J. Schwinger. On the classical radiation of accelerated electrons. *Phys. Rev.*, 75:1912–1925, 1949.

[13] K.C. Westfold. The Polarization of Synchrotron Radiation. *The Astrophysical Journal*, 130:241, 1959.

[14] R.A. Tinguely, M. Hoppe, O. Embréus, R.S. Granetz, S. Scott, and R.T. Mumgaard. Experimental and synthetic measurements of polarized synchrotron emission from runaway electrons in Alcator C-Mod. 2019. Submitted to *Nuclear Fusion*.

[15] M. Hoppe, O. Embréus, C. Paz-Soldan, R.A. Moyer, and T. Fülöp. Interpretation of runaway electron synchrotron and bremsstrahlung images. *Nuclear Fusion*, 58(8):082001, 2018.

Chapter 6

Analysis of synchrotron spectra

As part of this thesis work, runaway electron experiments were performed during low density, diverted, flattop plasma discharges in C-Mod at three magnetic field strengths: $B_0 = 2.7$, 5.4, and 7.8 T, the last being the highest field to-date at which runaways have been generated and observed in any tokamak. Synchrotron radiation spectra were measured in the visible/near-infrared wavelength range ($\lambda \approx$ 300-1000 nm) by two absolutely-calibrated spectrometers viewing co- and counter-plasma current directions, as described in chapter 4 and shown in figure 6.1.

In this chapter, the test particle model and runaway growth rates from chapter 2 are implemented to predict momentum-space and density evolutions, respectively, of runaways on the magnetic axis and flux surfaces with $q = 1$, $3/2$, and 2. Drift orbits and subsequent loss of confinement are also incorporated into the evolution. These spatiotemporal results are then input into SOFT which reproduces experimentally-measured spectra. As will be discussed, for these discharges, it is inferred that (i) synchrotron radiation dominates over collisional friction as a power loss mechanism and (ii) runaway energies decrease as the magnetic field strength increases. These results are published in [1]. Additionally, the threshold electric field for runaway generation, deduced from these most recent runaway experiments, is compared to current theoretical predictions.

6.1 Measurements of synchrotron spectra at three magnetic field strengths

Recall that in C-Mod, multi-MeV runaways—i.e. those emitting *visible* synchrotron radiation—are generally not observed after disruptions of diverted plasmas, likely due to the fast stochasticization of magnetic flux surfaces [2, 3]. However, these runaways can be generated during flattop discharges of sufficiently low plasma density ($\bar{n}_e \sim 5{\times}10^{19}$ m^{-3}), sometimes with the aid of lower

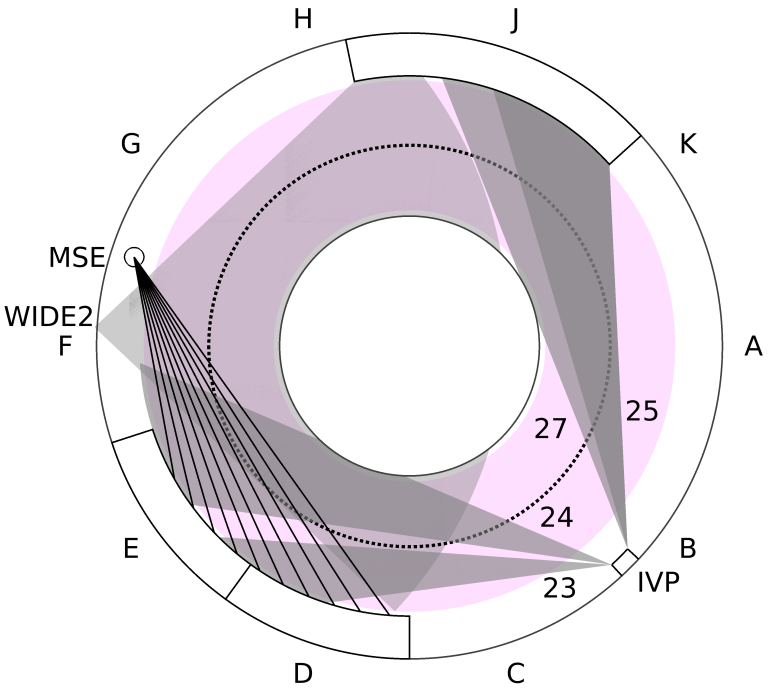

Figure 6.1: A top-down schematic of the tokamak midplane. The plasma is pink, with the major radius of the plasma axis dotted. The spectrometer views (CW: 23/24 and CCW: 25/27) are located on the In-Vessel Platform (IVP). Note that the field-of-view of IVP25 lies *within* that of IVP27. This is the same figure as figure 4.1, shown again here for reference.

hybrid (LH) seeding or short ramps in I_p ($\sim$200 kA/100 ms) to increase the loop voltage. This section explores the effects of varying toroidal magnetic field strength B on the evolution of flattop ("quiescent") runaways and their synchrotron radiation in C-Mod. Here, B is approximately *constant* throughout the time that runaways evolve; thus, discharges with similar runaway-relevant parameters are simply reproduced—to the best of our experimental abilities—with different, but constant B_0. In appendix C, the effects of *time-changing* B_0 on an already-formed runaway beam and its synchrotron radiation will be discussed. While the magnetic field was ramped from $B_0 = 5.4$-6.2 T in this discharge, the percent change in B_0 was not enough to measure significant changes in synchrotron spectra.

The test particle model (TPM) of momentum evolution from [4] and runaway density evolution from [5, 6]—both detailed in chapter 2—are coupled with SOFT—described in chapter 5—to produce synthetic spectra which are directly compared with experiment. For the first time, spatial effects are included in the runaway evolution and resulting spectra. As will be discussed,

good agreement is seen between experimental and predicted spectra, and it is shown that higher magnetic fields are *consistent* with greater synchrotron power loss and therefore lower expected runaway energies.

6.1.1 Experimental setup

To explore the impact of increased magnetic field on synchrotron power loss and runaway evolution, flattop runaways were generated at three time-independent magnetic field strengths in C-Mod: $B_0 = 2.7$, 5.4, and 7.8 T.[a] The experimental plasma parameters for the three discharges are shown in figure 6.2. For each discharge, n_e was decreased in time to achieve $E_0/E_\mathrm{C} \gtrsim 5$ on-axis. In addition, to encourage runaway production, the plasma current was ramped from $I_\mathrm{p} =$ 0.5-0.6 MA and 1.0-1.4 MA during the 2.7 and 7.8 T discharges, respectively, and LH current drive was used for a short time from $t =$ 0.74-0.76 s during the 2.7 T discharge. These three discharges were chosen for comparison due to their similar ratios of E_0/E_C on-axis; thus, they have similar runaway-driving forces. Low values of $\tau_\mathrm{rad}/\tau_\mathrm{coll} \sim$ 2-4 for the 5.4 and 7.8 T discharges indicate the potential for synchrotron power to surpass collisional friction as the dominant power loss mechanism.

Prior to 2015, several diagnostics were available for the study of runaways on C-Mod. Wide-view visible cameras—like the one discussed in chapter 4—allowed observation of runaway spatial evolution; however, the images would often be obscured by hard X-ray (HXR) "white-noise" or particulate build-up on camera windows. A radially-viewing, energy-resolved HXR camera with 32 chords measured HXR emission from runaway bremsstrahlung within the plasma for energies up to ∼240 keV. Unconfined runaways impacting the vessel wall also produced bremsstrahlung radiation in the form of HXRs and gammas; the latter generate photoneutrons through (γ,n) reactions. (See figure 6.2f-g). In addition, the Motional Stark Effect diagnostic was able to measure synchrotron radiation spectra in the visible wavelength range, but only over a narrow spectral range, with width $\Delta\lambda < 5$ nm.

As described in chapter 4, two visible spectrometers—see table 4.1 for specifications—were installed on Alcator C-Mod for better spectral measurements. Both clockwise (CW) and counter-clockwise (CCW) viewing directions allow (i) determination of the presence of runaways as synchrotron emission is only observed from one direction, (ii) synchrotron measurements for forward and reversed experimental configurations of B and I_p, and (iii) subtraction of background light. Refer to figure 6.1 for a top-down schematic view of the tokamak midplane with the CW and CCW fields-of-view (FOV) overlaying a typical C-Mod plasma. Spectrometer views In-Vessel Platform 24 and 27 were used exclusively for the following analysis. Note that the spectrometers

[a] To the author's knowledge, 7.8 T is the highest magnetic field strength at which runaways have been generated and observed in a tokamak, or at least at the publication date of [1].

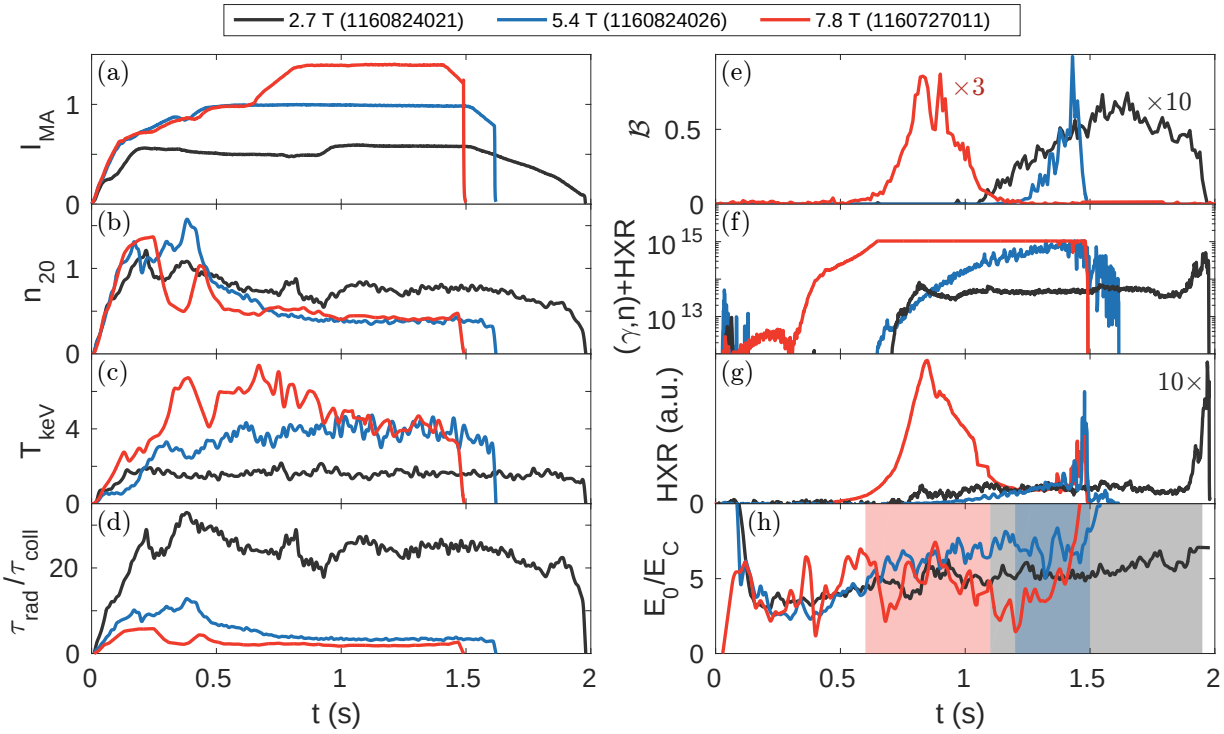

Figure 6.2: Parameters for three plasma discharges with time-independent $B_0 = 2.7$ T (black), 5.4 T (blue), and 7.8 T (red): (a) plasma current in MA, (b) central electron density in 10^{20} m^{-3}, (c) central electron temperature in keV, (d) ratio of the synchrotron radiation timescale to the collisional timescale—see (2.24), (e) measured synchrotron brightness at wavelength $\lambda = 850$ nm in μW/mm^2/sr/nm, (f) signal from HXR and photoneutrons in s^{-1}, (g) HXR signal, and (h) ratio of the electric field on-axis to the critical electric field [5]. The shaded regions in (h) highlight the time windows in (e) during which synchrotron radiation is observed. Note that in (e)-(h), some data have been scaled by the factors given.

do not view an entire plasma poloidal cross-section, and the CW FOV does not view a tangent point on the magnetic axis. Since highly relativistic electrons will experience outward radial drifts along their helical trajectories, these combined geometric effects must ultimately be considered when analyzing synchrotron data.

Raw synchrotron spectra (photon counts) and absolutely-calibrated brightness spectra (μW/mm^2/sr/nm) from the 7.8 T discharge are shown in figures 6.3a-b, respectively, with each solid curve representing one measurement in time and colors corresponding to the time trace in figure 6.3c. The low-signal grey line in figure 6.3a is the time-averaged background spectrum from the co-I_p (non-runaway) viewing spectrometer. The contrast between spectra clearly indicates a measurement of synchrotron radiation for the counter-I_p viewing system. The absolute calibration

of the spectrometers allows qualitative comparison of the measured brightnesses with theoretical power spectra $\mathrm{d}P/\mathrm{d}\lambda$ in the visible wavelength range, such as those shown in figure 3.2 in chapter 3. While deuterium Balmer peaks ($\lambda \approx 488$ and 658 nm) are visible in both the raw and absolute brightness spectra, the fiber absorption "dips" ($\lambda \approx 590$, 730, and 880 nm) are essentially removed by the absolute calibration. The time evolution of brightness amplitude can also yield information about runaway dynamics; figure 6.3c interestingly displays two peaks in time at $t \approx 0.8$ and 0.9 s, somewhat similar to the HXR signal (black), which occur approximately after the I_p-ramp shown in figure 6.2a.

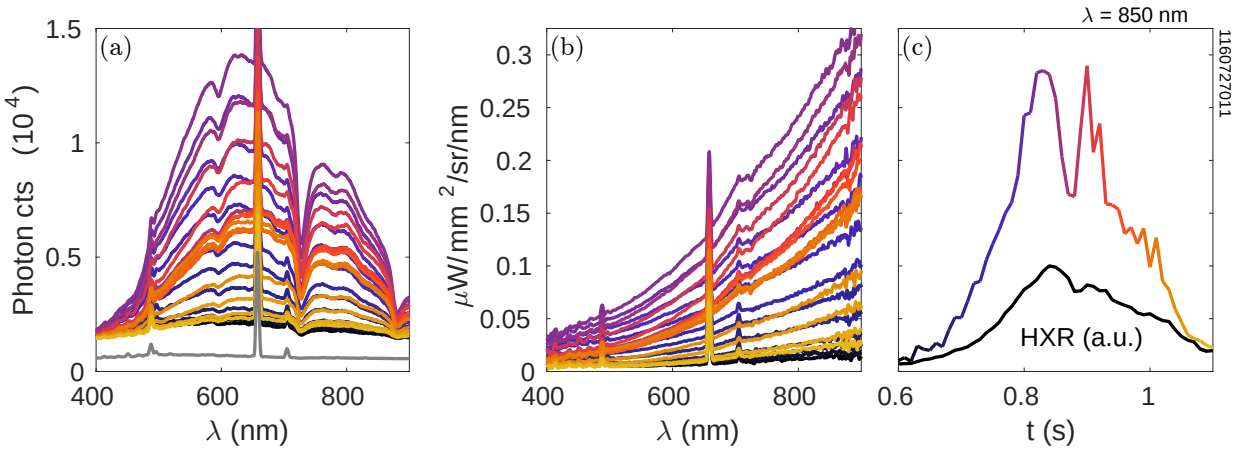

Figure 6.3: Synchrotron spectral data for the 7.8 T plasma discharge: (a) Raw photon count spectra from the CW spectrometer are plotted for times between $t = 0.6$-1.1 s at $\Delta t = 10$ ms intervals. The grey line is the time-averaged background spectrum from the opposite-direction-viewing (CCW) spectrometer. (b) Absolute brightness spectra corresponding to the same times (colors) as the photon count spectra. (c) Brightness at $\lambda = 850$ nm is plotted as a function of time with the same color-coding as spectra. The HXR signal (black, arbitrary units) from figure 6.2g is shown in (c) for comparison.

6.1.2 Approach

The analysis of synchrotron spectra is subtle; many factors contribute to the measured brightness, so careful interpretation of data is necessary. First attempts [7, 8] to determine runaway parameters from spectra assumed that mono-energetic (i.e. single-energy, single-pitch) distributions of runaways, concentrated in the plasma core, emitted synchrotron radiation directly into the spectrometer's FOV. For a highly-collimated spectrometer viewing the magnetic axis, such as that reported in [8], this approximation has some merit. However, for un-collimated spectrometers, like those used in this study, the situation is much more complicated: The runaway

population has a distribution of energies and pitches which evolves in time with changing plasma parameters. Furthermore, these momentum and density evolutions will vary on different flux surfaces as plasma parameters and magnetic field are spatially-dependent. The path of runaways along helical trajectories coupled with particle drifts can also bring runaways into and out of the spectrometer FOV. Solving the inverse problem, i.e. determining the spatiotemporal runaway population and momentum distribution functions from time-evolving spectra, is intractable for these volume-averaged spectral measurements. Instead, for this analysis, the forward problem is pursued by using a methodology similar to that used in [9–11]:

1. Flux-surface-averaged plasma parameters are obtained for the magnetic axis and surfaces with $q = 1$, $3/2$, and 2.
2. A TPM is implemented to evolve runaway momenta and densities on each surface.
3. Drift orbits are calculated, and runaways which lose confinement are removed from the population.
4. At each time step, the highest energy runaways on each surface, as predicted by the TPM, are assumed to contribute most to the synchrotron spectra.
5. The resulting evolutions of energy and density in time and space are input into SOFT to produce synthetic synchrotron spectra, which are then compared to experiment.

This approach differs from those employed previously in [10, 11] by (i) including spatial and drift orbit effects, (ii) *not* attempting to approximate the full runaway energy distribution, and (iii) utilizing SOFT. In [9], drifts and radial diffusion—the latter of which was not explored here—were used to compare TPM energies to those measured by gamma ray spectra resulting from unconfined runaways impacting plasma-facing components.

Regarding steps 1 and 2, the reader may wonder why runaway evolution is simulated only at four locations throughout the plasma. The reason for this is two-fold: First, these locations cover a large volume of the plasma, spanning the FOV of both spectrometers; thus, they should adequately capture the spatial variation of plasma parameters and thus resulting runaway generation and evolution. Second, because spectra are volume-integrated measurements with low (i.e. almost no) spatial resolution, there is no real motivation to use finer spatial resolution.

Furthermore, regarding steps 2-4, the reader may inquire as to why a TPM was used instead of CODE, which should give a fuller picture of the runaway distribution as discussed in chapter 5. Here, the reason is three-fold: First, some numerical difficulties arose for the high-B (7.8 T) case; however, CODE *is* compared to the TPM for $B_0 = 2.7$ T below. Second, as described in chapter 5, a TPM can capture the dynamics of the runaways which dominate the production (intensity) of synchrotron radiation. Finally, as this is a bulk measurement of the runaway beam, it is enough to know the approximate maximum energies, pitch angles, and (relative) densities,

and not concern ourselves with finer details of the phase space distribution, which would not be resolvable anyway.

6.1.3 Motivation

When runaways are generated during the flattop current of C-Mod discharges, little variation is seen in the loop voltage; thus, it is inferred that the current carried by runaways is small compared to the plasma current (i.e. $I_\mathrm{r} \ll I_\mathrm{p}$), making the total number of runaways, or runaway density n_r, difficult to estimate. Moreover, the amplitude of synchrotron emission is a poor indicator of n_r, as only those runaways with sufficient energy ($\mathcal{E} > 10$ MeV) will contribute to the visible spectra. Thus, in this analysis of synchrotron spectra, the effect of changing density is removed by normalizing the measured experimental brightness at one wavelength. The resulting normalized brightness spectra $\bar{\mathcal{B}}(\lambda, t)$ then only depend on the momenta and *relative* densities of runaways on different flux surfaces and their contributions to the total spectra. For this study, signal-to-noise and calibration factors limit the wavelength range of interest to $\lambda =$ 500-850 nm. (Refer to figure 6.3a.) A normalization wavelength $\lambda_0 = 675$ nm is chosen, away from the line radiation peaks and fiber absorption features.[b] The normalized brightness spectra are shown for several times in figure 6.4a. It is observed that the "slope" of the spectra increases in time, meaning that the relative fraction of synchrotron power emitted at longer wavelengths ($\lambda > \lambda_0$) is increasing compared to shorter wavelengths ($\lambda < \lambda_0$). This slope will be useful in determining the evolution of runaway energy.

The "traditional" approach of analyzing synchrotron spectra involves fitting experimental spectra using a single-particle, mono-energetic approximation, as in [8, 10, 11].[c] To demonstrate this, a scan in momentum space was performed from $p_\parallel/mc =$ 0-120 and $p_\perp/mc =$ 0-60 in increments of $\Delta p_\parallel/mc = 1$ and $\Delta p_\perp/mc = 0.5$. (Recall that $p/mc \approx 2\mathcal{E}_\mathrm{MeV}$ for electrons.) At each point, the power spectrum $\mathrm{d}P/\mathrm{d}\lambda$ was calculated, and the (normalized) synthetic brightness $\bar{\mathcal{B}}_\mathrm{syn}$ was estimated from (3.48), presented in chapter 3. Then the χ^2 degree-of-fit of $\bar{\mathcal{B}}_\mathrm{syn}$ to normalized experimental data $\bar{\mathcal{B}}_\mathrm{exp}$ was calculated as

$$\chi^2(t) = \sum_i \frac{\left[\bar{\mathcal{B}}_\mathrm{exp}(\lambda_i, t) - \bar{\mathcal{B}}_\mathrm{syn}(\lambda_i, t)\right]^2}{\bar{\mathcal{B}}_\mathrm{exp}(\lambda_i, t)}, \tag{6.1}$$

with the sum taken over each wavelength λ_i.

[b] Conveniently, $\lambda_0 = 675$ nm is halfway between 500 and 850 nm.

[c] In [8], the runaway pitch angle was estimated from camera images of the synchrotron spot size; unfortunately, camera images were not available for these particular C-Mod discharges. In [10, 11], a similar TPM was used to determine the pitch angle, and the best-fit energy was found to be consistent with that model.

Regions of $\chi^2 \leq 0.1$ are shown in figures 6.4b and 6.4c as functions of normalized parallel versus perpendicular momenta $(p_\parallel/mc, p_\perp/mc)$ and normalized total momenta versus pitch angle $(p/mc, \theta_\mathrm{p})$, respectively. As is seen, *there is no unique solution for this simple approach.* If we were to assume that all runaways had a constant pitch angle $\theta_\mathrm{p} = 0.1$ rad, this would imply a change in energy of $\mathcal{E} \sim 25$ to 20 MeV in time. As will be described in section 7.1.6, a TPM governed by the electric field, collisional friction, and synchrotron losses confines runaways to the region of momentum space inside the shaded box in figure 6.4b. In other words, experimental conditions and the equations of motion require that (the bulk of) runaway electrons have momenta with values $p_\parallel/mc \lesssim 43$ and $p_\perp/mc \lesssim 4$.

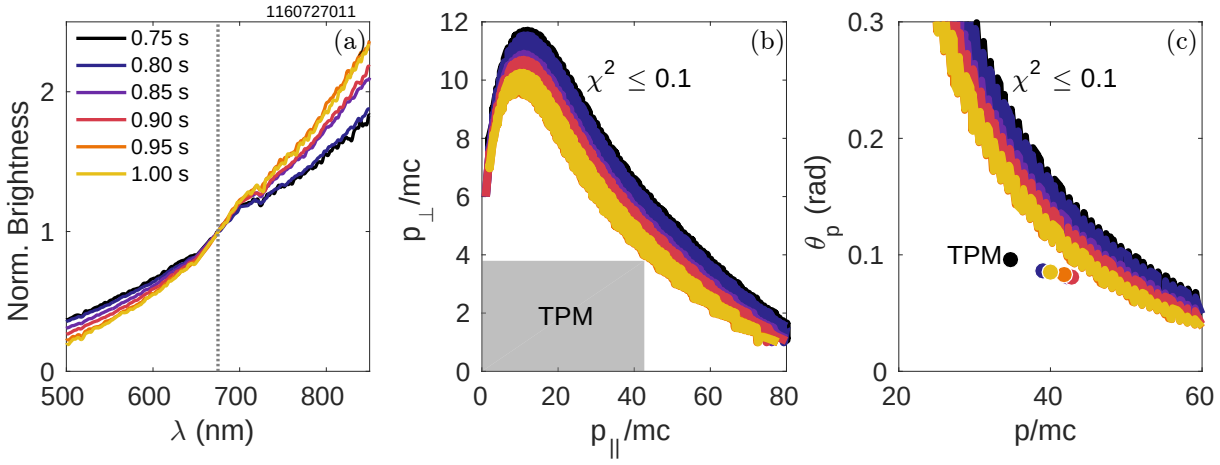

Figure 6.4: (a) Brightness data from figure 6.3a is normalized at $\lambda_0 = 675$ nm (dotted) for six times in $t = 0.75$-1.00 s. Regions of $\chi^2 \leq 0.1$ when fitting the experimental data in (a) to mono-energetic $\bar{\mathcal{B}}_\mathrm{syn}$ are shown for two representations of momentum space: (b) $p_\parallel/mc$ vs $p_\perp/c$ and (c) p/mc vs θ_p. A TPM using plasma parameters from the 7.8 T discharge predicts runaway momenta confined within the shaded box in (b) and *maximum* p/mc as indicated by dots in (c).

What is more, the time evolution of the maximum value of p/mc (and corresponding θ_p) from the same TPM are represented as dots in figure 6.4c. Runaway electrons with these energies and pitch angles live at the boundary of the box in figure 6.4b. While the TPM-predicted pitch angle is $\theta_\mathrm{p} \approx 0.08$-0.10 rad—not too far off from the previous assumption—the energies shown in figure 6.4c are lower than the fits suggest, and the time evolution (dark-to-light in colors) does not match. Thus, a more physically-motivated approach must be taken.

A *complete* analysis would require the full runaway phase space distribution function. However, as argued, because synchrotron emission is dominated by runaways localized in momentum space, a single-particle approximation is sufficient to reproduce synchrotron data. Figure 7.5a shows the normalized runaway momentum space distribution function $f(\boldsymbol{p})$ calculated with CODE [12, 13]—

refer to chapter 5—using experimental plasma parameters on-axis for the 2.7 T discharge. As expected, $f(\boldsymbol{p})$ is highly elongated parallel to the magnetic field, since electrons are primarily accelerated in that direction. As runaways are scattered to larger perpendicular momenta, they emit synchrotron radiation, lose energy, and repeat the cycle.

A convolution of f, $\mathrm{d}P/\mathrm{d}\lambda$, and Jacobian $p_\perp$ determines the region of momentum space in which most synchrotron power is radiated. This normalized convolution, evaluated at $\lambda = 800$ nm, is shown in figure 7.5b. At the time shown, the maximum emission results from runaways with average momenta $p_\parallel/mc \approx 81$ and $p_\perp/mc \approx 8$. (Recall from chapter 5 that the peak location is relatively insensitive to λ in the visible range.) The TPM predicts a single-particle on-axis momentum of $p_\parallel/mc \approx 76$ and $p_\perp/mc \approx 8$, indicated by the dot. Since parameter scans and iteration of the TPM were more feasible—i.e. less computationally-intensive—than the full kinetic solvers, a TPM was pursued in this analysis. Moreover, as will be described in section 6.1.7, spectra produced using the TPM match experimental data as well or even better than those generated using CODE.

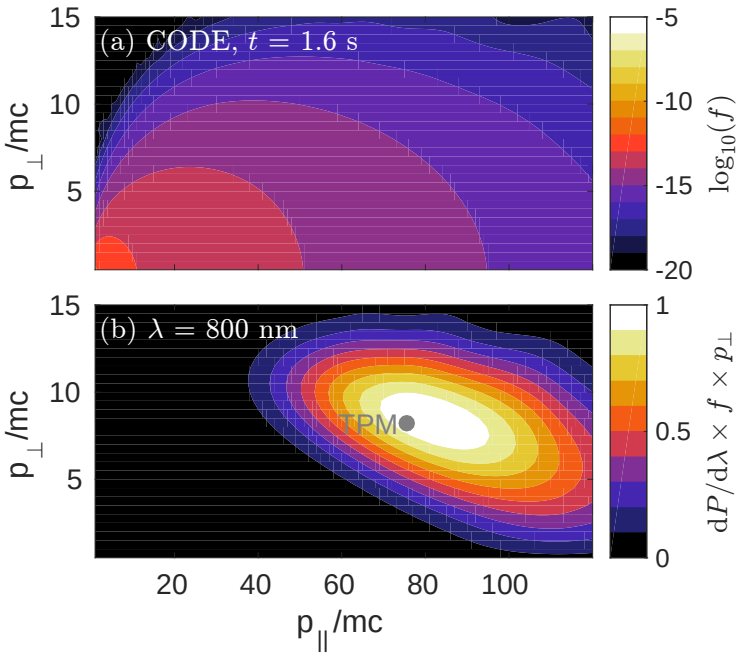

Figure 6.5: (a) The normalized momentum space distribution function $f(p_\parallel, p_\perp)$ generated by CODE for on-axis plasma parameters of the 2.7 T discharge at $t = 1.6$ s, and (b) the normalized convolution of spectral power density $\mathrm{d}P/\mathrm{d}\lambda$ at $\lambda = 800$ nm, f, and Jacobian $p_\perp$. The dot in (b) represents the TPM prediction of $p_\parallel/mc$ and $p_\perp/mc$ on-axis at time t.

6.1.4 Test particle model

The TPM used in this analysis is the same as that described in chapter 2 with parallel and total momenta evolutions described by (2.26) and (2.28), respectively [4]. In addition, the runaway density evolution given by (2.11)—with linear and exponential growth rates for Dreicer generation [5] and Rosenbluth-Putvinski avalanching [6]—can be used to predict the density of runaways on each surface, thereby constructing an ad hoc density profile and estimating relative contributions to the total synchrotron emission.

Because runaways can be generated at any time throughout the discharge, new TPM are initiated starting at $t = 60$ ms (corresponding to the first EFIT [14] time) and in $\Delta t = 10$ ms intervals. Example time-evolutions of $p_\parallel/mc$ for many initiation times are shown in figure 6.6. The early start time is motivated by spikes in HXR signals early in the three discharges (see figure 6.2f). Regardless of the time of initiation, most runaways generated during the first ∼0.5-1.0 s reach an approximately steady-state momentum by the time of observed synchrotron emission. In general, runaways initiated earliest in time gain the highest energies and densities; however, they can lose confinement, as described in the next section, and thus lower energy runaways generated at later times can become important (see figure 6.6). For simplicity, the initial momenta were chosen to be $p_{\parallel 0}/mc = 1$ (as done in [9]) and $p_{\perp 0}/mc = 0.001$, which are representative of an electron above the threshold velocity (along $\boldsymbol{B}$) to run away, but not yet highly relativistic. In addition, the initial density was simply chosen to be $n_0 = 1$ m^{-3}. For both momentum and density evolutions, the TPM is insensitive to initial conditions.

6.1.5 Spatial profiles and drifts

Since our spectrometers make volume-integrated measurements over significant cross-sections of the plasma (refer to figure 6.1), it is important to account for the energy and density evolutions of runaways on different flux surfaces, as well as the spatial variation of the magnetic field. The spatial profile of runaways is approximated by calculating the evolutions for four locations: the magnetic axis and on rational flux surfaces with $q = 1$, 3/2, and 2. Surface-averaged plasma parameters were input into the TPM: The q-profile and electric field $E = (\partial\psi_\mathrm{p}/\partial t)/(2\pi R)$ were determined from EFIT magnetic reconstructions [14], where ψ_p is the poloidal magnetic flux. Thomson scattering profiles of n_e and T_e on the outer midplane were used and assumed to be flux surface functions. Because B and E both decrease as $\sim 1/R$, particles on helical trajectories necessarily experience varying electric and magnetic fields; it was assumed that all runaways are passing particles with constant speeds ($\mathrm{v} \approx c$) to calculate the surface-averages. Due to stray synchrotron light overwhelming/contaminating the diagnostic measuring effective charge, values of Z_eff could not be accurately measured for these discharges. Therefore, a scan

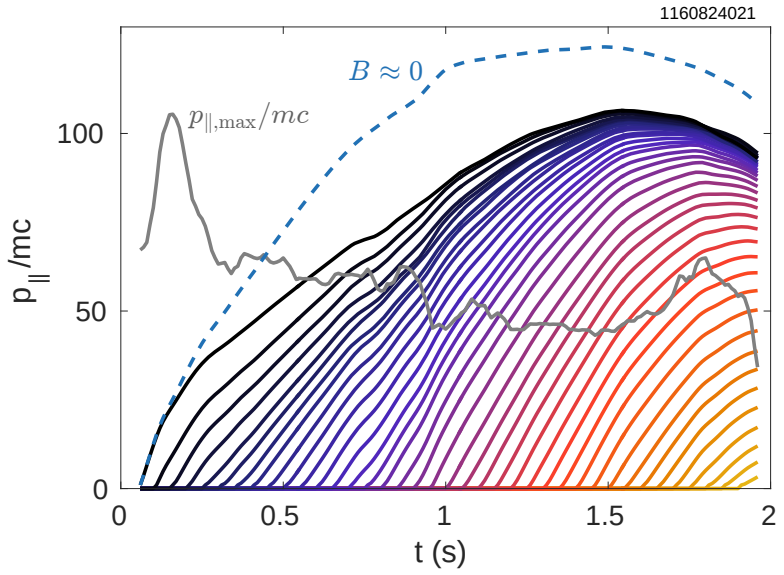

Figure 6.6: Time evolution of parallel momenta for particles initiated every $\Delta t = 50$ ms on the $q = 2$ surface for the 2.7 T discharge. The maximum parallel momenta are shown for runaway confinement ($p_{\parallel,\max}/mc$, grey) and when synchrotron radiation is neglected ($B = 10^{-4}$ T ≈ 0, dashed). ($Z_{\text{eff}} = 4$)

was performed from $Z_{\text{eff}} = 1$-4, which was also assumed to be constant in time and space in each TPM simulation. (Note that $Z_{\text{eff}} \sim 3$-4 is common for low density C-Mod discharges.) In this analysis, data are only shown for those values of Z_{eff} which best reproduced experimental results.

As derived in chapter 2, highly relativistic electrons can also experience large particle drifts in a toroidal magnetic field. Thus, runaways of sufficient energy can lose confinement, especially if they are generated on outer flux surfaces. Recall from (2.41), that the maximum parallel momentum for runaway confinement, in a plasma with a *parabolic* current profile, is given by

$$\frac{p_{\parallel,\max}}{mc} \approx 724\, I_{MA} \left(1 - \frac{r}{a}\right) \left[1 - \frac{1}{2}\left(\frac{r}{a}\right)^2\right] \tag{6.2}$$

where I_{MA} is I_{p} expressed in MA. This neglects other radial transport mechanisms, such as magnetic field perturbations.

An illustration of the TPM and drift orbit calculations is shown in figure 6.6. Here the TPM was simulated for plasma parameters on the surface $q = 2$ for the 2.7 T discharge. Each curve represents the momentum evolution, from (2.26), of a particle generated at a different time step within the discharge. If drift orbit losses are not considered, it can be seen that runaways produced in the first $\sim$1 s of the discharge reach a momentum space *attractor* at $p_\parallel/mc \approx 100$ around

$t = 1.5$ s; this is where the electric, friction, and synchrotron radiation reaction forces balance.

The importance of synchrotron power loss is highlighted by the dashed curve for which the magnetic field was artificially reduced to $B \approx 0$.[d] In the case that drifts and orbit losses are *not* considered, these runaways would reach a maximum energy of $p_\parallel/mc \approx 120$; that is $\Delta\mathcal{E} \approx 10$ MeV higher than particles subject to synchrotron power loss. The maximum allowable momentum beyond which runaways would drift out of the plasma is calculated from (6.2) and is shown by the grey line. This indicates that runaways on the surface $q = 2$ would lose confinement early in the shot, around $t = 0.6$ s, and therefore the maximum momentum expected is actually only $p_\parallel/mc \approx$ 50-60, or ∼25-30 MeV. Note that for plasmas with higher I_p and for runaways inside $q < 2$, the TPM-predicted energies are often much lower than the maximum allowable for confinement.

6.1.6 Spectrometer implementation in SOFT

The synthetic spectrometer capabilities of the SOFT code [15] were utilized in this work. Recall that inputs to SOFT include the magnetic geometry from EFIT; spectrometer specifications (e.g. position, orientation, viewing angle, and spectral response) provided in table 4.1; runaway momenta and pitch angles from the TPM (or momentum space distribution functions from CODE); and midplane major radial locations of the runaways. Because drift orbit effects are not yet fully implemented in SOFT, they are only utilized for the calculation of the *input* momenta and densities. The full angular distribution of synchrotron emission was used for the synchrotron power computation, although the simplified cone model—with opening half-angle θ_p and zero angular width—was found to work just as well.

In this analysis, separate SOFT simulations were performed for each flux surface q_i and time of interest. In each simulation, the same number of particles were distributed uniformly in a radial band of width $\Delta R = 1$ cm centered at the outer midplane major radius corresponding to the flux surface. The resulting spectra were scaled by the total number of runaways expected on each surface, calculated using the runaway density and cylindrical plasma approximation

$$N_\mathrm{r}(q_i, t) \approx n_\mathrm{r}(q_i, t) \times 2\pi R_0 \times 2\pi \left(R(q_i, t) - R_0\right) \Delta R. \tag{6.3}$$

The total brightness was then calculated as

$$\mathcal{B}_{\mathrm{SOFT,tot}}(t) = \sum_i N_\mathrm{r}(q_i, t)\, \mathcal{B}_{\mathrm{SOFT}}(q_i, t), \tag{6.4}$$

[d] Actually, a small value, $B = 10^{-4}$ T, was used since the numerical solver breaks for $B = 0$.

which was normalized at λ_0 and compared to experiment.

6.1.7 Experimental analyses

The following subsections detail the application of the aforementioned methodology to the three plasma discharges of interest with magnetic field strengths on-axis $B_0 = 2.7$, 5.4, and 7.8 T. The organization of each subsection is as follows: Plasma parameters n_e, T_e, E/E_C, and outer midplane major radial position R are shown for the magnetic axis and surfaces with $q = 1$, 3/2, and 2 as subplots (a)-(d), respectively, in figures 6.7, 6.9, and 6.11. In the same figures, TPM results of p/mc, θ_p, and n_r are shown in subplots (f)-(h), respectively, for each surface. Note that drift orbits are accounted for in the TPM calculation and are shown as dotted lines in subplot (d). The time evolution of experimentally-measured synchrotron brightness is shown in subplot (e) for qualitative comparisons with TPM parameters; vertical lines indicate the times at which synthetic spectra are produced with SOFT.

In figures 6.8, 6.10, and 6.12, synthetic SOFT spectra are compared to experimental spectra for the 2.7, 5.4, and 7.8 T discharges, respectively. In each figure, subplot (a) shows the experimentally-measured normalized brightness spectra. The synthetic spectra shown in the accompanying subplots (b) and (c) are calculated using (b) only on-axis TPM data input into $\mathcal{B}_\mathrm{syn}$ (3.48) and (c) TPM data from all surfaces input into SOFT. Subplot (d) is different for each discharge and figure. Finally, the χ^2 degree-of-fit is shown in figure 6.13 and discussed in section 6.1.8.

6.1.7a Synchrotron spectra measured at $B_0 = 2.7$ T

During the 2.7 T discharge, n_e was decreased in time (see figure 6.7a) and I_p was ramped from 0.5-0.6 MA over $t = 0.9$-1.0 s (see figure 6.2a) to encourage runaway generation. LH current drive was also used to help produce a seed population of non-thermal electrons, but was not modeled explicitly. The resulting increase in E/E_C due to the I_p ramp can be seen during this time interval in figure 6.7c, especially for the outer flux surfaces with $q = 3/2$ and 2. Higher values of E/E_C on the outer flux surfaces lead to higher predicted runaway momenta early in the plasma discharge, as seen in figure 6.7f. However, the resulting drift orbits, shown in figure 6.7d, approach the plasma boundary ($R \approx 0.9$ m), and runaways begin to lose confinement at $t \approx 0.6$ and 1.2 s, on the $q = 2$ and 3/2 surfaces, respectively; these are seen as decreases in energy and density in figures 6.7f-h. The former time, $t \approx 0.6$ s, is approximately the time at which photoneutron and HXR signals rise in figure 6.2f-g. While it is predicted that the highest energy runaways are on the $q = 3/2$ surface, the runaway density n_r there is much lower than on-axis. Thus, it is expected that runaways at the core will dominate the synchrotron spectra.

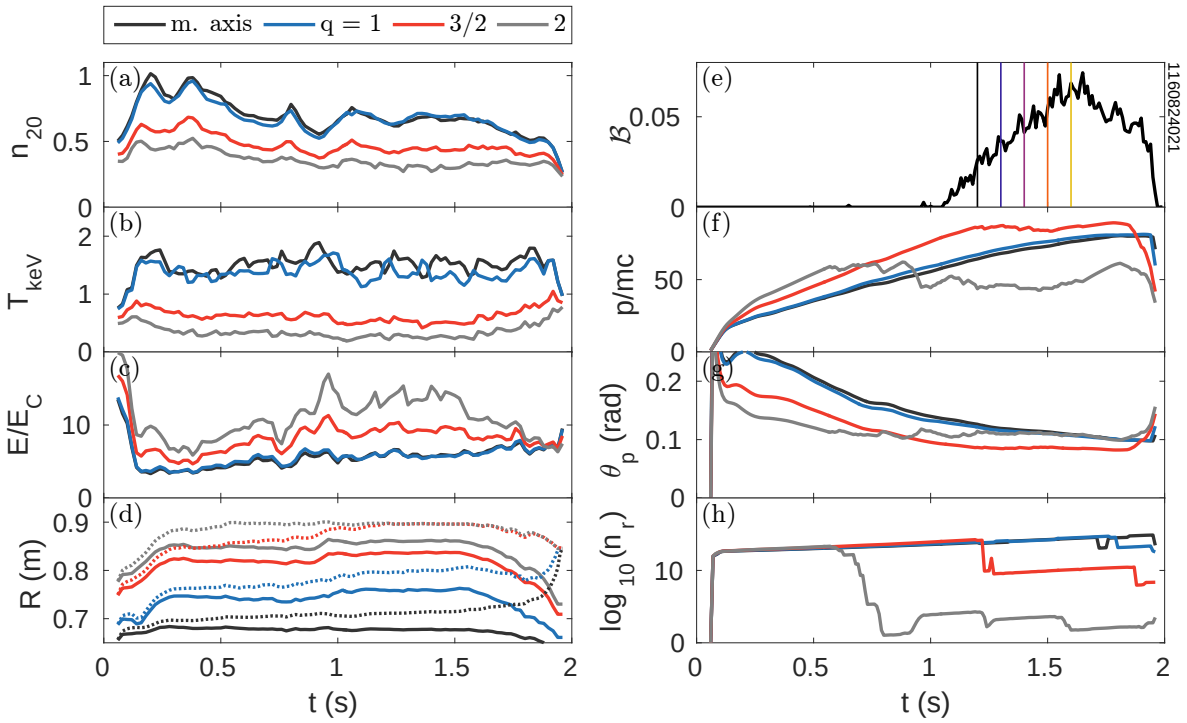

Figure 6.7: For the 2.7 T discharge, parameters on the magnetic axis and surfaces with $q = 1$, 3/2, and 2: (a) electron density in 10^{20} m^{-3}, (b) electron temperature in keV, (c) ratio of electric to critical fields, and (d) outer midplane major radius with (dotted) and without (solid) including drifts; (e) measured synchrotron brightness at $\lambda = 850$ nm (in μW/mm^2/sr/nm) with times of interest corresponding to figure 6.8 indicated as vertical lines; and TPM results for runaway (f) total normalized momentum, (g) pitch angle, and (h) density in m^{-3}. ($Z_{\text{eff}} = 4$)

Synchrotron emission was measured by the CCW spectrometer (see figure 6.1) for the 2.7 T discharge. The experimental normalized brightnesses at five times, as indicated in figure 6.7e, are compared to synthetic spectra in figure 6.8. Considering only on-axis runaways, and using the brightness formula for $\mathcal{B}$ (3.48), produces spectra similar to experiment, as seen in figure 6.8b. This is consistent with measured synchrotron emission dominated by runaways in the core, as expected. Combining TPM data from all surfaces and inputting it into SOFT produces synthetic spectra most similar to experiment, except at $t = 1.2$ s, as seen in figure 6.8c. This discrepancy is due to a significant contribution of synchrotron emission from high energy runaways on the $q = 3/2$ surface, before they lose confinement. However, at $t = 1.23$ s, slightly *after* the loss of these runaways on the $q = 3/2$ surface, the modeled spectra match experiment. This could indicate that runaways on the $q = 3/2$ surface are lost ~30 ms earlier than the TPM and drift orbit calculations predict, perhaps through an additional transport mechanism. Such an explanation

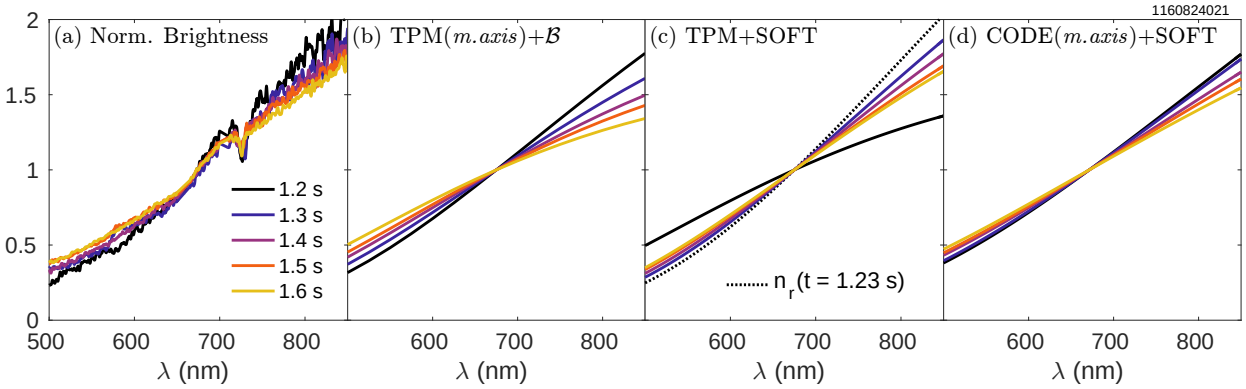

Figure 6.8: For five times during the 2.7 T discharge: comparisons of (a) experimental normalized brightness spectra to synthetic data from (b) on-axis TPM data input into $\mathcal{B}$ (3.48), (c) TPM data from all surfaces input into SOFT, and (d) the on-axis CODE distribution function input into SOFT. The dotted line in (c) uses runaway densities at $t = 1.23$ s. Note that the full angular distribution was used for SOFT in (b), while the cone model approximation was used in (d).

seems physically plausible. Finally, the full distribution function from CODE (see figure 7.5), using only on-axis plasma parameters, was input into SOFT to produce the synthetic spectra shown in figure 6.8d. As is seen, the TPM+SOFT synthetic spectra match the experimental spectra as well as the CODE+SOFT data, further motivating/validating the use of the TPM approximation.

In addition, note that drift orbits of ∼4 cm, shown in figure 6.7d, are predicted for runaways on the magnetic axis and $q = 1$ surface at the time of observed synchrotron emission. This implies that the trajectories of runaways "on-axis" are actually at the boundary of the CCW spectrometer FOV (refer to figure 6.1). The SOFT synthetic spectra in figure 6.8c-d do not include drift effects. However, since both inner surfaces would still be seen by the CCW spectrometer, even with drifts, the resulting synthetic spectra would likely be unchanged.

6.1.7b Synchrotron spectra measured at $B_0 = 5.4$ T

Similar to the 2.7 T discharge, the plasma density n_e was decreased in time during the 5.4 T discharge to encourage the growth of runaways (see figure 6.9a). The surface-averaged values of E/E_C are consistently higher on the $q = 3/2$ and 2 surfaces than near the center of the plasma, leading to higher energies predicted on outer surfaces by as much as ∼5-10 MeV. However, these runaway energies are lower than those predicted for the 2.7 T discharge, due to the increase in synchrotron power by a factor of $\sim(5.4/2.7)^2 = 4$. Additionally, the poloidal magnetic field resulting from the higher plasma current ($I_p = 1$ MA) is strong enough to confine runaways on each surface. An increase in n_r on inner surfaces is predicted at $t \approx 0.6$ s, about the time that

$E/E_C \geq 5$ and T_e increases in the core plasma. The runaway density profile n_r still peaks in the core, but the ratio of on-axis n_r to that at the $q = 2$ surface is only ∼100 in this discharge, which means that high energy runaways at the edge contribute more significantly to the total brightness.

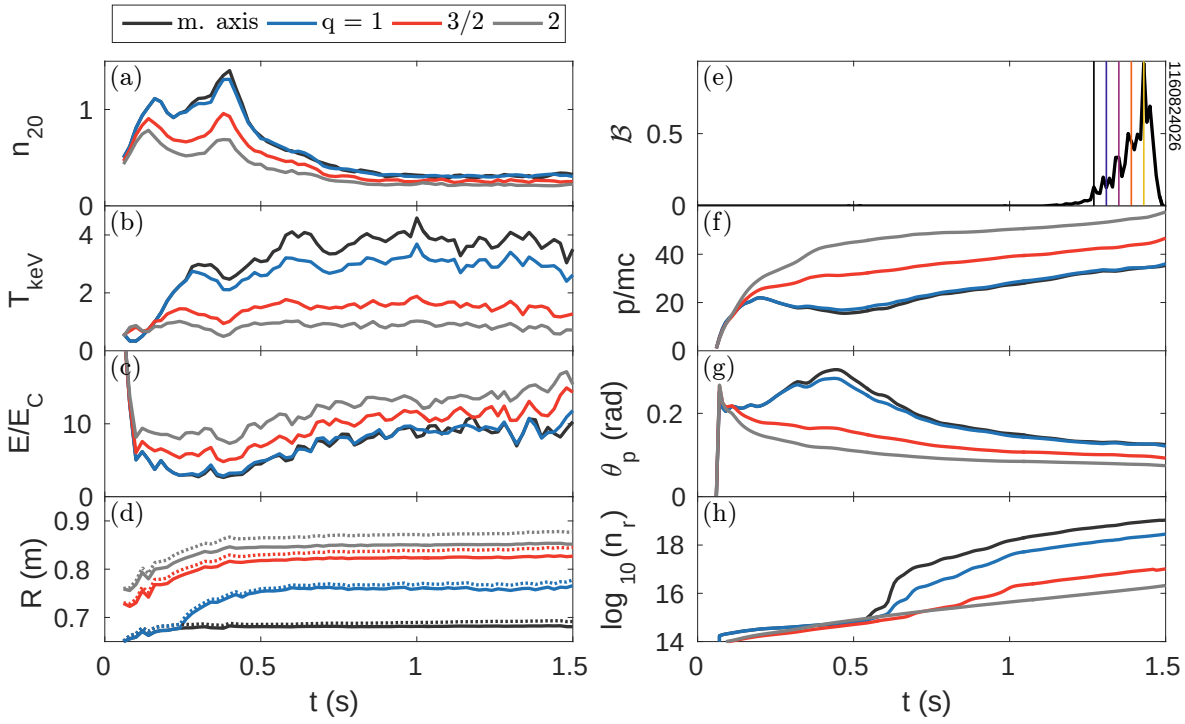

Figure 6.9: For the 5.4 T discharge, parameters on the magnetic axis and surfaces with $q = 1$, 3/2, and 2: (a) electron density in 10^{20} m^{-3}, (b) electron temperature in keV, (c) ratio of electric to critical fields, and (d) outer midplane major radius with (dotted) and without (solid) including drifts; (e) measured synchrotron brightness at $\lambda = 850$ nm (in μW/mm^2/sr/nm) with times of interest corresponding to figure 6.10 indicated as vertical lines; and TPM results for runaway (f) total normalized momentum, (g) pitch angle, and (h) density. ($Z_{\text{eff}} = 3.5$)

Synchrotron spectra were measured by the CCW spectrometer for this discharge. The experimental and synthetic normalized brightnesses are compared at five times in figure 6.10. While there is significant variation in the measured spectra plotted in figure 6.10a, almost none is predicted by the TPM results input into SOFT, as shown in subplot figure 6.10c. This is due to TPM data changing little over the times of interest, which is seen for energy, pitch angle, and density in figure 6.9f-h. Nevertheless, at this magnetic field, the brightness formula $\mathcal{B}$ is no longer able to reproduce experimental spectra, as seen in figure 6.10b. Note that the TPM+$\mathcal{B}$ model predicts far more emission at wavelengths $\lambda > 675$ nm compared to $\lambda < 675$ nm, and the time

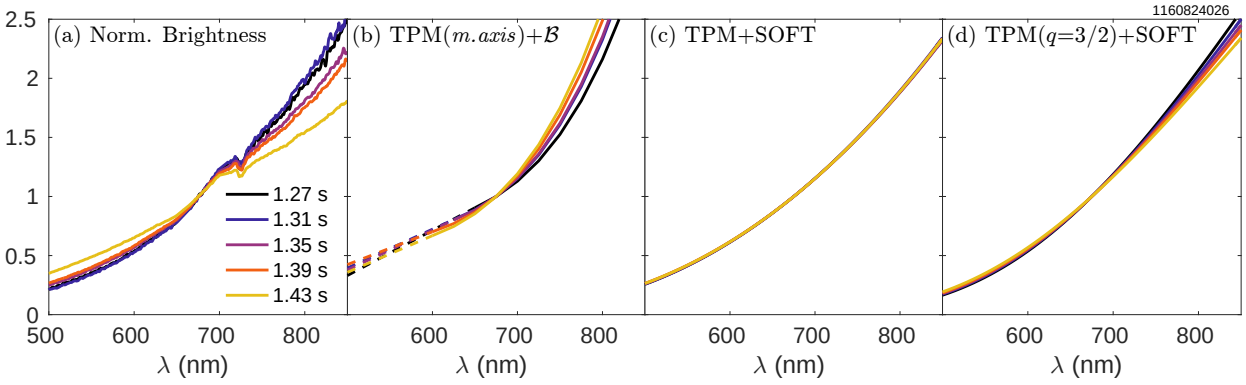

Figure 6.10: For five times during the 5.4 T discharge: comparisons of (a) experimental normalized brightness spectra to synthetic data from (b) TPM data only on-axis input into $\mathcal{B}$ (3.48), (c) TPM data from all surfaces input into SOFT, and (d) TPM data from only the $q = 3/2$ surface input into SOFT. The dashed lines in (b) are linear extrapolations of the spectral curves to wavelengths at which the oscillating integrand of $\mathrm{d}P/\mathrm{d}\lambda$ caused large errors.

evolution is opposite to that measured. The SOFT contribution from only the $q = 3/2$ surface is shown in figure 6.10d to highlight that this data better matches earlier times, while that in figure 6.10b is more similar to later times. A more precise prediction of the spatial density profile could be needed to best match experiment. Even so, SOFT better predicts the spectral shape and evolution than the traditional approach.

6.1.7c Synchrotron spectra measured at $B_0 = 7.8$ T

While the same procedure of decreasing the plasma density n_e was employed in the 7.8 T discharge, synchrotron radiation was only observed after the current ramp $I_\mathrm{p} = 1.0$-1.4 MA from $t = 0.6$-0.8 s. The resulting increase in E/E_C is most significant on the outer surfaces, at $q = 3/2$ and 2, as seen in figure 6.11c. The TPM-predicted energies peak at $t \approx 0.8$ s and then decay; this follows quite closely the evolution of synchrotron brightness in figure 6.11e. However, the sharp "dip" in experimental brightness around $t \approx 0.88$ s is not captured in the TPM. Instead, the start of a locked mode at this time likely causes increased transport of runaways which would otherwise be confined by the relatively high plasma current. Nonetheless, predicted synchrotron spectra are still similar to experimental spectra, even after this time, suggesting that the large amplitude MHD activity primarily affected the runaway *density* but not the *energy* distribution in this case. The predicted runaway densities, on different flux surfaces, are also much closer in magnitude than for the other discharges, differing by only a factor of $\sim$10 between the magnetic axis and at the $q = 2$ surface. Thus, for this discharge, we expect an even greater contribution

to the total synchrotron emission from high energy runaways on outer flux surfaces. Note also that n_r is predicted to continue increasing even after the decline in observed synchrotron emission at $t \approx 1.1$ s. This is consistent with HXR data, in figures 6.2f-g, up to the time of disruption; however, runaway energies are simply not high enough to produce significant visible synchrotron radiation during these later times.

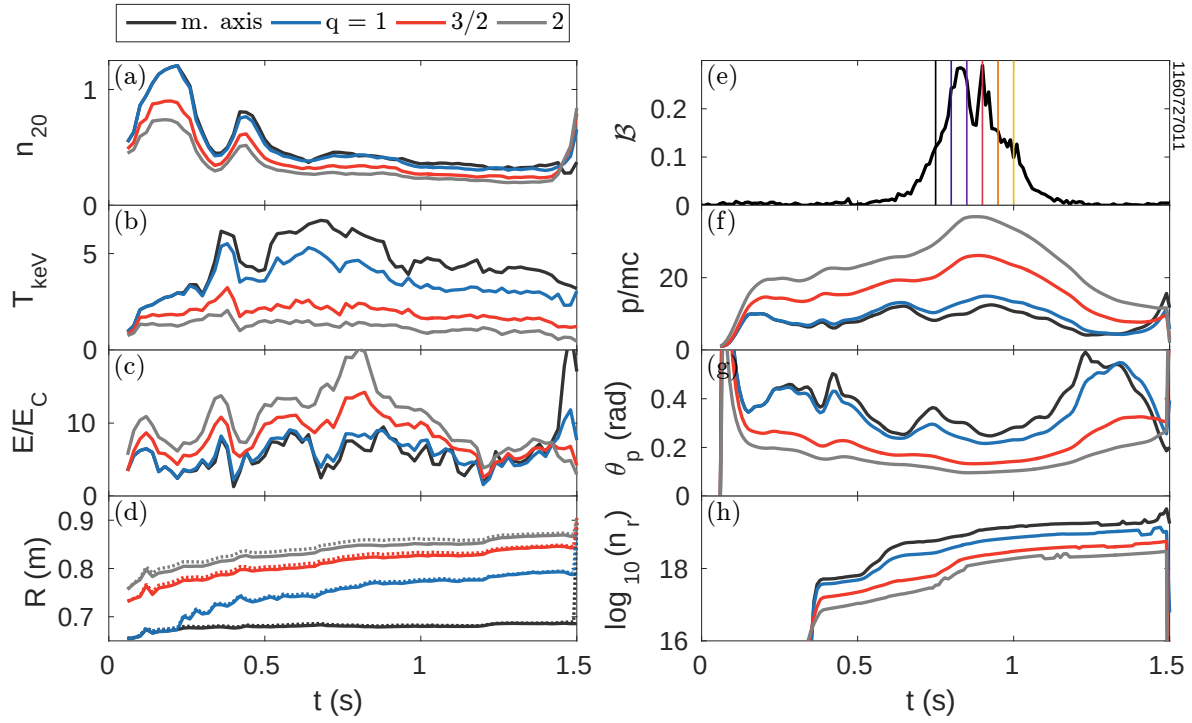

Figure 6.11: For the 7.8 T discharge, parameters on the magnetic axis and surfaces with $q = 1$, 3/2, and 2: (a) electron density in 10^{20} m^{-3}, (b) electron temperature in keV, (c) ratio of electric to critical fields, and (d) outer midplane major radius with (dotted) and without (solid) including drifts; (e) measured synchrotron brightness at $\lambda = 850$ nm (in μW/mm^2/sr/nm) with times of interest corresponding to figure 6.12 indicated as vertical lines; and TPM results for runaway (f) total normalized momentum, (g) pitch angle, and (h) density. ($Z_\mathrm{eff} = 4$)

The 7.8 T discharge was run in the reversed-magnetic-field configuration of C-Mod, i.e. I_p and B opposite to the directions in the 2.7 and 5.4 T discharges; therefore, synchrotron emission was measured by the *CW* spectrometer. The measured normalized brightnesses at six times are shown in figure 6.12a. Note that the spectral "slope" *increases* in time, opposite to the trends of the 2.7 and 5.4 T discharges. The synthetic spectra, produced using TPM data on the magnetic axis and the brightness formula $\mathcal{B}$ (3.48), are completely unlike experiment, as seen in figure 6.12b. One explanation for this large discrepancy is that an asymptotic expansion

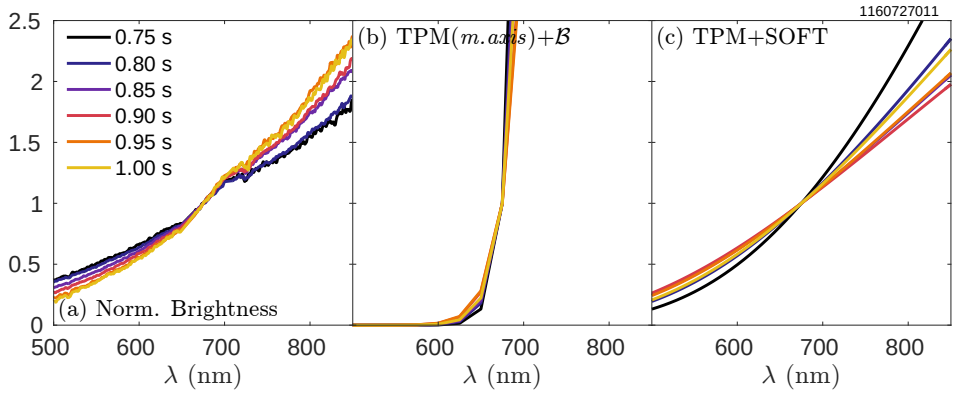

Figure 6.12: For six times during the 7.8 T discharge: comparisons of (a) experimental normalized brightness spectra to synthetic data from (b) on-axis TPM data input into $\mathcal{B}$ (3.48), and (c) TPM data from all surfaces input into SOFT. Note that in (b), equation (21) in [16] was used as a better approximation for $\mathrm{d}P/\mathrm{d}\lambda$.

of $\mathrm{d}P/\mathrm{d}\lambda$, given by equation (21) in [16], is used here to compute the spectra, as the full calculation becomes increasingly computationally-intensive for such low runaway energies. More importantly, as seen in figure 6.1, synchrotron emission from runaways on the magnetic axis is never directly viewed by the spectrometer, so emission from runaways on other flux surfaces *must* be considered.[e] Coupling the TPM with SOFT is better at matching experiment, as shown in figure 6.12c, but only for later times, $t = 0.85$-1.00 s. Earlier times, $t = 0.75$-0.80 s, have a trend that is opposite the experimental trend, and the time evolution of the "slope" is non-monotonic, unlike the measured data. Because all runaways should be well-confined by the high $I_\mathrm{p} = 1.4$ MA, this cannot be easily explained. Implementation of full drift orbit effects into SOFT is likely needed to best reproduce experimental spectra; future work could test this with SOFT2 [17].

6.1.8 Discussion

The χ^2 values comparing synthetic and experimental normalized brightnesses are shown in figure 6.13 for the three discharges. The traditional approach—i.e. assuming that synchrotron emission is dominated by on-axis runaways and using a simplified brightness formula (TPM+$\mathcal{B}$)—works well for the 2.7 T discharge, but becomes increasingly inaccurate for the higher field discharges. The agreement in the low B case is likely due to runaways at outer surfaces losing confinement (due to low I_p) so that emission was in fact dominated by runaways in the core. As higher magnetic fields lead to increased synchrotron radiation, lower energies are attained by runaways

[e] SOFT also determines zero contribution to the spectra from runaways on-axis, as expected.

and make the calculation of $\mathrm{d}P/\mathrm{d}\lambda$ and thus $\mathcal{B}$ less precise. A synthetic diagnostic like SOFT—which incorporates runaway momenta and spatial profiles, magnetic equilibria, and the detector geometry and spectral range—is required to reproduce experimental spectra.

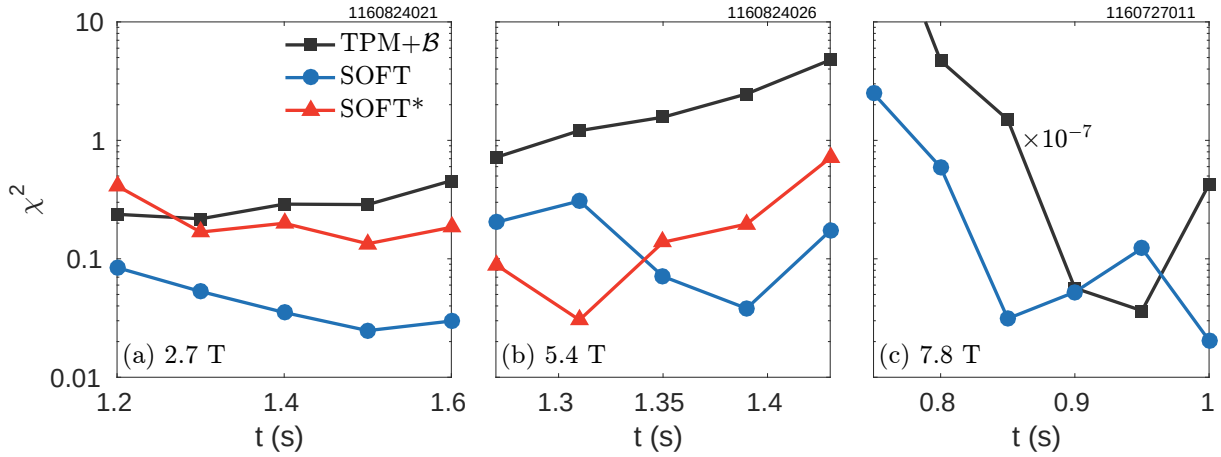

Figure 6.13: Time evolution of χ^2 values (log-scale) comparing experimental to synthetic spectra for the (a) 2.7, (b) 5.4, and (c) 7.8 T discharges. The SOFT (circles) and TPM+$\mathcal{B}$ (squares) correspond to subplots (b) and (c), respectively, of figures 6.8, 6.10, and 6.12. The SOFT* data (triangles) highlight additional SOFT simulations for comparison: Here, subplot (a) uses CODE distributions input into the SOFT cone model from figure 6.8d, and subplot (b) includes the TPM contribution from the $q = 3/2$ surface shown in figure 6.10d. In (a), $n_\mathrm{r}(t = 1.23\ \mathrm{s})$ was used for the SOFT data; in (c), the TPM+$\mathcal{B}$ curve has been scaled by the factor given.

In addition, the fact that experimental spectra were reproduced validates our methodology (see section 6.1.2), which incorporated both TPM energy and density evolutions as well as drift orbit effects on several flux surfaces throughout the plasma. The maximum energies attained by runaways during flattop I_p, as calculated by the TPM, are shown in figure 6.14 as a function of highest magnetic field experienced by the particle. Using a simple assumption of constant radiated synchrotron power, i.e. $p_\perp^2 B^2 \approx$ constant, a function of the form $\mathcal{E}_\mathrm{max} \propto 1/B$ is fit to all data, with constant of proportionality ~124 MeV/T. Therefore, we conclude that in C-Mod discharges with similar E/E_C values, experimental synchrotron spectral data are *consistent* with lower runaway energies attained at higher magnetic field strengths, as synchrotron radiation becomes a more important power loss mechanism. A similar result was inferred from HXR emission from runaways in DIII-D [18].

Moreover, note from figure 6.14 that, at higher magnetic field strengths, runaways on outer flux surfaces attained higher energies than those near the plasma core. This resulted from a combination of higher electric fields (due to $E \sim 1/R$ and diffusion time into the plasma), lower

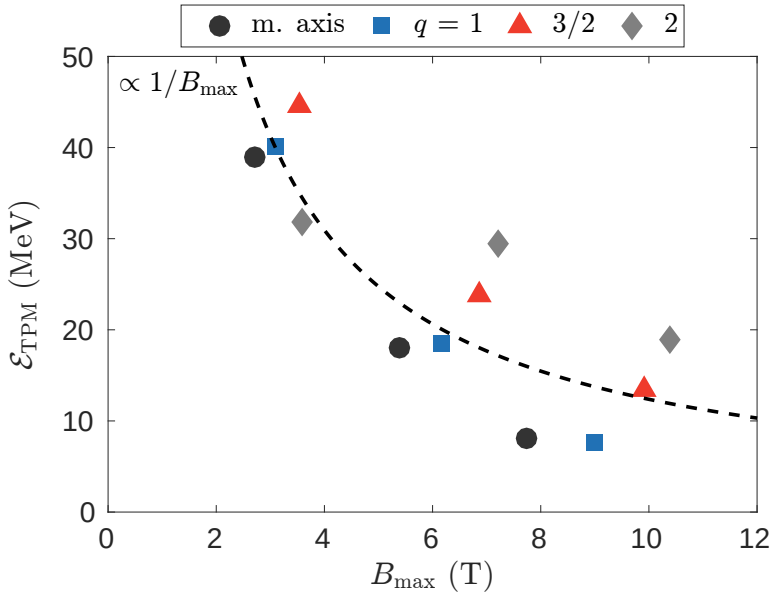

Figure 6.14: Maximum runaway energies in MeV, as predicted by the TPM, plotted as a function of highest magnetic field experienced for particles on the magnetic axis (circles) and surfaces with $q = 1$ (squares), 3/2 (triangles), and 2 (diamonds) for the $B_0 = 2.7$, 5.4, and 7.8 T discharges. A representative best-fit curve of the form $\mathcal{E}_{\mathrm{TPM}} \propto 1/B_{\max}$ is shown, with proportionality constant $\sim$124 MeV/T.

plasma densities at the edge, and increased confinement from larger I_{p} (which is allowed by higher B at a fixed edge safety factor q_{95}). While a greater number of runaways are usually generated near the magnetic axis due to higher temperatures, a full study of runaway energy and density evolution throughout the plasma is necessary for the prediction of runaway dynamics and the threat they pose to future tokamaks.

6.2 Threshold electric field

As described in chapter 2, there should exist a threshold electric field $E_{\rm thr}$ below which no runaway electrons can be generated in a plasma. This threshold effect has been tested experimentally in many tokamaks, and its value has been found to be a factor of at least ∼2-5 higher than predicted when assuming that collisional friction is the only damping mechanism [19, 20]. The discrepancy between theory and experiment implies that other damping mechanisms on runaway generation—like synchrotron emission, bremsstrahlung, or kinetic instabilities—can be significant compared to collisional friction. Recall from 2.24 that the relative importance of synchrotron radiation versus collisional friction is often given by the ratio of respective timescales $\hat{\tau}_{\rm rad} = \tau_{\rm rad}/\tau_{\rm coll} \approx 280\, n_{20}/B^2$, where n_{20} is electron density in units of 10^{20} m^{-3} and B is in Tesla. The operation of C-Mod at high magnetic field strengths allows exploration of $\hat{\tau}_{\rm rad} \approx$ 2-4, values much lower than for most tokamaks. The ratio of power lost per electron through synchrotron emission compared to frictional drag is given by $P_{\rm synch}/P_{\rm coll} \approx \left(p_\perp/mc\right)^2/\hat{\tau}_{\rm rad}$. As seen in the previous section, values of $p_\perp/mc \approx$ 3-8 are predicted in C-Mod, meaning that synchrotron power should dominate over collisional friction as a power loss mechanism.

An analysis of RE-producing C-Mod discharges prior to 2014 is presented in [20]. Since then, several runaway experiments have been performed on C-Mod for a range of magnetic field strengths, including those described in the previous section. It is of interest to study the effect of changing B on runaway generation and $E_{\rm thr}$. Since not all runaway discharges produce measurable synchrotron radiation, the threshold electric field is computed at the time when photoneutron and HXR signals increase above detector noise level, i.e. at the approximate onset of runaway generation. See, for example, the sharp increases of signal above 10^{12}/s in figure 6.2f. The ratios of the electric field to critical field ($E/E_{\rm C}$) at these times are shown in figure 6.15, for runaways generated during flattop $I_{\rm p}$, as a function of $1/\hat{\tau}_{\rm rad} = \tau_{\rm coll}/\tau_{\rm rad}$. This calculation of $E/E_{\rm C}$—refer to (2.8)—uses the line-averaged electron density $\bar{n}_e$, electric field approximation $E = V/2\pi R_0$, and Coulomb logarithm $\ln\Lambda = 15$ to represent "bulk" plasma parameters and to be consistent with previous studies. Here, $V = V_{\rm loop} - L\,{\rm d}I_{\rm p}/{\rm d}t$, where the inductance is $L \approx 1$ μH for these C-Mod conditions. Note that some discharges used LH current drive to encourage runaway growth, especially at low B, and are denoted by the open circles. These data indicate that the threshold field is ∼5 times higher than predicted by purely collisional theory, in agreement with previous experiments.

In recent years, several theoretical predictions of $E_{\rm thr}$ have gone beyond collisional friction to account for such effects as synchrotron radiation, impurities, and pitch angle scattering. In this study, three theories are compared to the experimental data shown in figure 6.15:

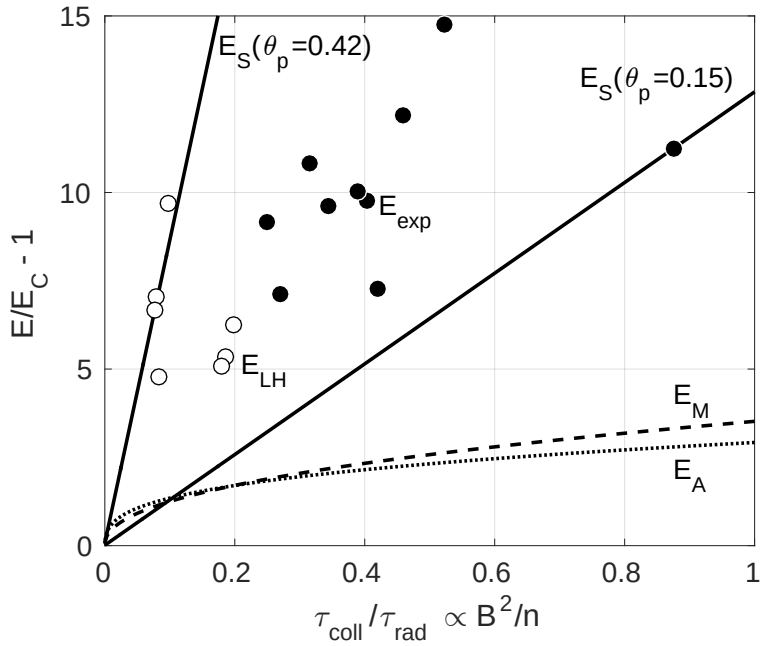

Figure 6.15: Ratios of the experimentally-measured threshold to critical electric field ($E/E_{\rm C}-1$) are plotted for experimental data and from theory. The threshold fields for runaway onset as measured in C-Mod experiments are shown as circles, with open circles representing those discharges using LH current drive. Theoretical predictions of the threshold field are $E_{\rm M}$ (dashed) from (6.5), $E_{\rm A}$ (dotted) from (6.6), and $E_{\rm S}$ (solid) from (6.7). For $E_{\rm S}$, which requires inputs of energy and pitch angle, values of $p/mc = 24$ ($\mathcal{E} \approx 12$ MeV) and $\theta_{\rm p} = 0.15$ rad and 0.42 rad were selected.

(i) In the FTU tokamak, the threshold field $E_{\rm M}$ required for runaway *suppression*—i.e. to make the growth rate negative—was empirically fit and is given by equation (3) of [19],

$$\frac{E_{\rm M}}{E_{\rm C}} \approx 1 + \frac{1.64 + 0.53\,Z_{\rm eff} - 0.015\,(Z_{\rm eff})^2}{(\hat{\tau}_{\rm rad})^{\delta}} \tag{6.5}$$

where $\delta = 0.45 \pm 0.03$. For this analysis, the effective charge $Z_{\rm eff} = 4$ was chosen as a representative value, and the mean value of $\delta \approx 0.45$ was used.

(ii) In [21], the threshold field $E_{\rm A}$ required to *sustain* runaways is derived from kinetic theory; equation (8) therein gives an analytical fit

$$\frac{E_{\rm A}}{E_{\rm C}} \approx 1 + \frac{Z_{\rm eff}+1}{(\hat{\tau}_{\rm rad})^{1/2}}\left[\frac{1}{8} + \frac{(Z_{\rm eff}+1)^2}{\hat{\tau}_{\rm rad}}\right]^{-1/6}. \tag{6.6}$$

However, note that (6.6) is only valid for $\hat{\tau}_{\rm rad} > 5$, or $\tau_{\rm coll}/\tau_{\rm rad} < 0.2$ in figure 6.15.

(iii) In equation (2) of [22], the effective critical field E_{S} required for a particle with momentum p and pitch angle θ_{p} to overcome collisional drag and the Abraham-Lorentz radiation reaction force [23] is given by

$$\frac{E_{\mathrm{S}}}{E_{\mathrm{C}}} = \sec\theta_{\mathrm{p}}\left[1+\sin^2\theta_{\mathrm{p}}\,\frac{1+(p/mc)^2}{\hat{\tau}_{\mathrm{rad}}}\right], \tag{6.7}$$

where the approximation $\beta = v/c \to 1$ (so $\gamma = (1-\beta^2)^{-1/2} \gg 1$) was used.

Equations (6.5)-(6.7) are plotted as functions of $1/\hat{\tau}_{\mathrm{rad}}$ in figure 6.15. As is seen, experimental data are several factors greater than E_{A} and E_{M}.[f] For E_{S} (6.7), a particle with energy $\mathcal{E} \approx$ 12 MeV ($p/mc = 24$) was chosen as an estimate for the energy at which photoneutrons would be produced. These occur when runaways impact the first wall, producing gamma rays of similar energy via thick-target bremmstrahlung; these gamma rays can then "eject" neutrons from the nuclei of wall materials, which are detected. Pitch angles of $\theta_{\mathrm{p}} = 0.15$ rad and 0.42 rad were also selected to bound the experimental data. As can be seen in figure 6.15, E_{S} provides the best prediction of the threshold electric field; however, a model which does not require a priori knowledge of the runaway population is necessary for predictions of the E_{thr} of future devices. This motivates a more careful study of the threshold electric field at low $\hat{\tau}_{\mathrm{rad}}$ (i.e. high B) values, as an unmitigated disruption in ITER or SPARC could have $\hat{\tau}_{\mathrm{rad}} < 10$. Furthermore, as discussed previously, spatial variation of n_{e}, T_{e}, and E lead to spatial variation of E/E_{C}; this obscures the physical meaning of a threshold field for the bulk plasma, and a more general treatment should be pursued.

[f] The subscript of each E is just the last initial of the first author of the respective publication.

References—Chapter 6

[1] R.A. Tinguely, R.S. Granetz, M. Hoppe, and O. Embréus. Measurements of runaway electron synchrotron spectra at high magnetic fields in Alcator C-Mod. *Nuclear Fusion*, 58(7):076019, 2018.

[2] E. Marmar, A. Bader, M. Bakhtiari, H. Barnard, W. Beck, I. Bespamyatnov, A. Binus, P. Bonoli, B. Bose, M. Bitter, I. Cziegler, G. Dekow, A. Dominguez, B. Duval, E. Edlund, D. Ernst, M. Ferrara, C. Fiore, T. Fredian, A. Graf, R. Granetz, M. Greenwald, O. Grulke, D. Gwinn, S. Harrison, R. Harvey, T.C. Hender, J. Hosea, K. Hill, N. Howard, D.F. Howell, A. Hubbard, J.W. Hughes, I. Hutchinson, A. Ince-Cushman, J. Irby, V. Izzo, A. Kanojia, C. Kessel, J.S. Ko, P. Koert, B. LaBombard, C. Lau, L. Lin, Y. Lin, B. Lipschultz, J. Liptac, Y. Ma, K. Marr, M. May, R. McDermott, O. Meneghini, D. Mikkelsen, R. Ochoukov, R. Parker, C.K. Phillips, P. Phillips, Y. Podpaly, M. Porkolab, M. Reinke, J. Rice, W. Rowan, S. Scott, A. Schmidt, J. Sears, S. Shiraiwa, A. Sips, N. Smick, J. Snipes, J. Stillerman, Y. Takase, D. Terry, J. Terry, N. Tsujii, E. Valeo, R. Vieira, G. Wallace, D. Whyte, J.R. Wilson, S. Wolfe, G. Wright, J. Wright, S. Wukitch, G. Wurden, P. Xu, K. Zhurovich, J. Zaks, and S. Zweben. Overview of the Alcator C-Mod research program. *Nuclear Fusion*, 49(10):104014, 2009.

[3] V.A. Izzo, E.M. Hollmann, A.N. James, J.H. Yu, D.A. Humphreys, L.L. Lao, P.B. Parks, P.E. Sieck, J.C. Wesley, R.S. Granetz, G.M. Olynyk, and D.G. Whyte. Runaway electron confinement modelling for rapid shutdown scenarios in DIII-D, Alcator C-Mod and ITER. *Nuclear Fusion*, 51(6):063032, 2011.

[4] J.R. Martín-Solís, J.D. Alvarez, R. Sánchez, and B. Esposito. Momentum-space structure of relativistic runaway electrons. *Physics of Plasmas*, 5(6):2370–2377, 1998.

[5] J.W. Connor and R.J. Hastie. Relativistic limitations on runaway electrons. *Nuclear Fusion*, 15(3):415, 1975.

[6] M.N. Rosenbluth and S.V. Putvinski. Theory for avalanche of runaway electrons in tokamaks. *Nuclear Fusion*, 37(10):1355, 1997.

[7] R. Jaspers, N.J. Lopes Cardozo, A.J.H. Donné, H.L.M. Widdershoven, and K.H. Finken. A synchrotron radiation diagnostic to observe relativistic runaway electrons in a tokamak plasma. *Review of Scientific Instruments*, 72(1):466–470, 2001.

[8] J.H. Yu, E.M. Hollmann, N. Commaux, N.W. Eidietis, D.A. Humphreys, A.N. James, T.C. Jernigan, and R.A. Moyer. Visible imaging and spectroscopy of disruption runaway electrons in DIII-D. *Physics of Plasmas*, 20(4):042113, 2013.

[9] B. Esposito, J.R. Martín-Solís, F.M. Poli, J.A. Mier, R. Sánchez, and L. Panaccione. Dynamics of high energy runaway electrons in the Frascati Tokamak Upgrade. *Physics of Plasmas*, 10(6):2350–2360, 2003.

[10] Z. Popovic, B. Esposito, J.R. Martín-Solís, W. Bin, P. Buratti, D. Carnevale, F. Causa, M. Gospodarczyk, D. Marocco, G. Ramogida, and M. Riva. On the measurement of the threshold electric field for runaway electron generation in the Frascati Tokamak Upgrade. *Physics of Plasmas*, 23(12):122501, 2016.

[11] B. Esposito, L. Boncagni, P. Buratti, D. Carnevale, F. Causa, M. Gospodarczyk, J.R. Martín-Solís, Z. Popovic, M. Agostini, G. Apruzzese, W. Bin, C. Cianfarani, R. De Angelis, G. Granucci, A. Grosso, G. Maddaluno, D. Marocco, V. Piergotti, A. Pensa, S. Podda, G. Pucella, G. Ramogida, G. Rocchi, M. Riva, A. Sibio, C. Sozzi, B. Tilia, O. Tudisco, M. Valisa, and FTU Team. Runaway electron generation and control. *Plasma Physics and Controlled Fusion*, 59(1):014044, 2017.

[12] M. Landreman, A. Stahl, and T. Fülöp. Numerical calculation of the runaway electron distribution function and associated synchrotron emission. *Computer Physics Communications*, 185(3):847 – 855, 2014.

[13] A. Stahl, O. Embréus, G. Papp, M. Landreman, and T. Fülöp. Kinetic modelling of runaway electrons in dynamic scenarios. *Nuclear Fusion*, 56(11):112009, 2016.

[14] L.L. Lao, H. St. John, R.D. Stambaugh, A.G. Kellman, and W. Pfeiffer. Reconstruction of current profile parameters and plasma shapes in tokamaks. *Nuclear Fusion*, 25(11):1611, 1985.

[15] M. Hoppe, O. Embréus, R.A. Tinguely, R.S. Granetz, A. Stahl, and T. Fülöp. SOFT: a synthetic synchrotron diagnostic for runaway electrons. *Nuclear Fusion*, 58(2):026032, 2018. SOFT can be downloaded at https://github.com/hoppe93/SOFT, with documentation found at https://soft.readthedocs.io.

[16] I.M. Pankratov. Analysis of the synchrotron radiation spectra of runaway electrons. *Plamsa Physics Reports*, 25(2):145–148, 1999.

[17] M. Hoppe *et al*. SOFT2 can be downloaded at https://github.com/hoppe93/SOFT2.

[18] C. Paz-Soldan, C.M. Cooper, P. Aleynikov, D.C. Pace, N.W. Eidietis, D.P. Brennan, R.S. Granetz, E.M. Hollmann, C. Liu, A. Lvovskiy, R.A. Moyer, and D. Shiraki. Spatiotemporal evolution of runaway electron momentum distributions in tokamaks. *Physical Review Letters*, 118:255002, 2017.

[19] J.R. Martín-Solís, R. Sánchez, and B. Esposito. Experimental observation of increased threshold electric field for runaway generation due to synchrotron radiation losses in the FTU tokamak. *Phys. Rev. Lett.*, 105:185002, 2010.

[20] R.S. Granetz, B. Esposito, J.H. Kim, R. Koslowski, M. Lehnen, J.R. Martín-Solís, C. Paz-Soldan, T. Rhee, J.C. Wesley, L. Zeng, and ITPA MHD Group. An ITPA joint experiment to study runaway electron generation and suppression. *Physics of Plasmas*, 21(7):072506, 2014.

[21] P. Aleynikov and B.N. Breizman. Theory of two threshold fields for relativistic runaway electrons. *Phys. Rev. Lett.*, 114:155001, 2015.

[22] A. Stahl, E. Hirvijoki, J. Decker, O. Embréus, and T. Fülöp. Effective critical electric field for runaway-electron generation. *Phys. Rev. Lett.*, 114:115002, 2015.

[23] W. Pauli. *Theory of Relativity*. Dover Books on Physics. Dover Publications, 1981.

Chapter 7

Analysis of synchrotron images

As discussed in chapter 3, one of the most interesting features of synchrotron radiation produced by runaway electrons is that the emission is primarily directed along each particle's velocity vector; thus, it is only seen from the counter-I_p direction, i.e. from one viewing direction. In chapter 6, this effect was observed by two spectrometers viewing opposite directions, as shown in figure 7.1. However, this is much more easily captured by a wide-view camera, also shown schematically in figure 7.1 and experimentally-verified in figure 7.2. While synchrotron spectra can provide insight into the energy distribution of runaways, camera images of synchrotron emission record the spatiotemporal evolution of runaways throughout the plasma. The analysis of these images is the focus of this chapter and is published in [1].

In section 7.1, the kinetic equation solver CODE—described in chapter 5—is used to predict the spatially-varying *momentum* space distribution of runaways in one C-Mod discharge, and the synthetic diagnostic SOFT—also described in chapter 5—is then used to infer their time-evolving radial density profile from synchrotron images. Interesting spatial structure in these images appears to be correlated with MHD activity, and the relationship between magnetic fluctuations and runaways is investigated in more detail in section 7.2. Finally, section 7.3 uses a statistical analysis of over one thousand camera images to explore the plasma conditions under which visible synchrotron radiation is emitted by runaways and detected in C-Mod.

7.1 Spatiotemporal evolution from images of synchrotron radiation

Table 7.1 gives an overview of previous studies in which runaways were diagnosed using synchrotron images. Here, experiments are discriminated by their runaway generation phase—during plasma start-up (S), flattop current I_p (F), or disruption (D)—and camera type—visible (V) or

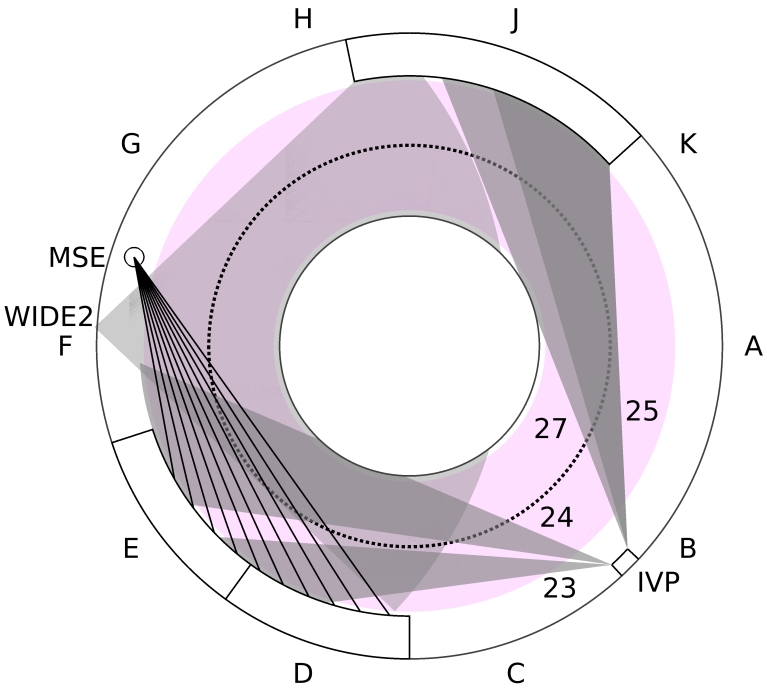

Figure 7.1: A top-down schematic of the tokamak midplane. The plasma is pink, with the major radius of the plasma axis dotted. The wide-view (WIDE2) camera views both CW and CCW directions. This is the same figure as figure 4.1, shown again here for reference.

infrared (IR). In addition, these studies analyzed synchrotron images in various ways. To indicate this, the "spatial dimensionality" is reported: In some studies, only 0D time evolutions of synchrotron intensity (e.g. the total number of photon counts within the detected image) were analyzed; in others, 1D radial profiles (e.g. vertical integrations of a horizontal camera "slit") were used, often to explore radial diffusion. Two-dimensional (2D) data have been used to study the spatial properties of the runaway beam: height and width, often related to the pitch angle; shape, like crescents or hollow rings; or feature-mapping from images to flux surfaces and drift orbits.[a] Some efforts have been made to go beyond the identification of spatial features and to analyze the synchrotron intensity *distribution* throughout the image; these are bolded in table 7.1.

[a]Note that many works which utilize 2D information also include 0D and 1D analyses.

Table 7.1: An overview of runaway synchrotron image analyses organized by device; runaway generation during start-up (S), plasma current flattop (F), or disruption (D) phases; visible (V) or infrared (IR) camera type; and highest "spatial dimensionality" of each analysis (as described in the text). **Bold** entries indicate analyses of the intensity distribution beyond just spatial features (e.g. width, shape, etc.).

Device	Generation	Camera type	Spatial dim.	References
Alcator C-Mod	F	V	**2D**	[1, 2]
COMPASS	F	IR	2D	[3]
DIII-D	F	V	0D	[4, 5]
			2D	[6]
			2D	[7]
	D	V+IR	2D	[8]
		V		[9]
EAST	S+F	V	2D	[10, 11]
	F			[12]
FTU	F	V+IR	0D	[13]
HL-2A	D	V	2D	[14]
HT-7	F	IR	2D	[15]
J-TEXT	F+D	IR	2D	[16]
KSTAR	S	IR	2D	[17]
TEXTOR	D	IR	0D	[18]
			1D	[19]
			2D	[20]
	F	IR	0D	[21]
			1D	[22, 23]
			2D	[24–26]

This section describes the analysis of 2D camera images of visible synchrotron emission from runaways generated during the flattop phase of low density, diverted C-Mod plasma discharges. The work presented here has been published in [1]. Novel to this analysis—compared to most in table 7.1—is the combination of the following: (i) Experimentally-measured spatial profiles of plasma parameters are used to simulate (with CODE) the time evolution of the runaway momentum space distribution *throughout* the plasma, while past studies typically only calculated single particle momenta from plasma parameters at the magnetic axis. (ii) SOFT is used to model the synchrotron intensity pattern detected by a camera (see chapter 5), given experimentally-measured magnetic and detector geometries, while most previous works do not account for these

necessary geometric effects. (iii) Comparisons of the full 2D intensity distributions of synthetic and experimental images allow diagnosis of the time-evolving runaway density profile n_{r}; only recently have other synchrotron image analyses moved beyond spatial feature identification.

A similar methodology was also used in chapter 6 to study the time evolution and magnetic field dependence of runaway synchrotron *spectra*. However, for that analysis, spectral measurements were volume-integrated within each spectrometer's field-of-view, providing less spatial information than an imaging camera. Consequently, a test particle approach for runaway density and momentum evolution was sufficient to match experimental spectral measurements. As will be discussed in section 7.1.6, the full momentum space distribution is required to adequately reproduce experimental synchrotron images.

7.1.1 Experiment and setup

As described in chapter 4, a wide-angle visible/near-IR camera, with wavelength range $\lambda \approx$ 400-900 nm, is used for general monitoring of the vacuum vessel during the plasma discharge. The camera is located $\sim$21 cm below the midplane with a near-radially-inward view, capturing images at (approximately) 60 frames per second. (Refer to table 4.3 for additional camera specifications.) Because the peak of the synchrotron power spectrum shifts toward shorter wavelengths with increasing magnetic field strength (assuming fixed runaway energy and pitch angle), synchrotron radiation can be measured by the camera in the visible-NIR wavelength range for C-Mod's typical operational space, $B_0 \approx$ 2-8 T. An example of raw camera data is shown in figure 7.2a. The camera measures intensity only (i.e. greyscale, not in color), so no spectral information is obtained. All other figures in this chapter are false-colored to better highlight the intensity distribution.

The "annulus" of light at the bottom of figure 7.2a comes from the divertor, or exhaust system of the tokamak. The two brightest "rings," one with a slightly smaller radius than the other, show the locations of the divertor "strike points," i.e. where the plasma comes into contact with the vacuum vessel first wall. This visible-NIR light results from two physical effects: First and foremost, the plasma near the wall is cold enough such that atomic excitation and recombination occur, producing visible line-radiation. This same process creates the narrow spectral peaks noted in chapter 6 and seen in figure 6.3. Second, the heat flux convected and conducted to the metal wall will cause some materials to "glow red." The latter is likely of lesser importance than the former since the plasma discharge is only $\sim$2 seconds long. Above the divertor region, we see that visible light dominates on the right side of the image, indicating that this is in fact synchrotron emission from runaways traveling in the counter-I_{p} direction. The white speckles on the image are the result of HXR radiation impacting the camera. Recall that the camera auto-gain is turned off; while this means that sometimes pixel saturation occurs, it also allows frame-by-frame comparisons of pixel intensity.

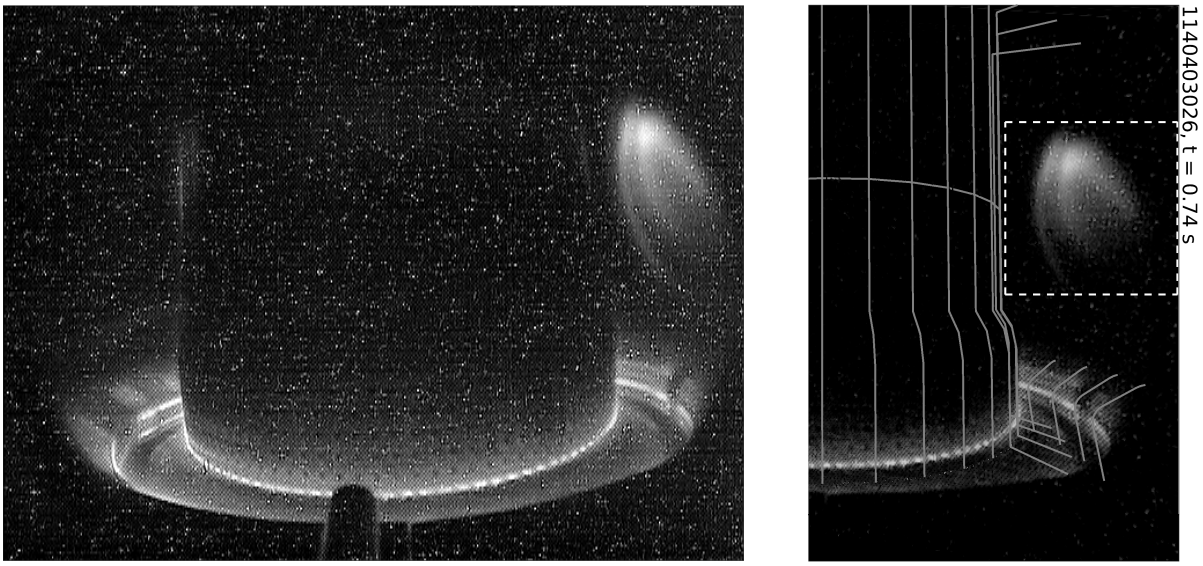

Figure 7.2: The (a) original camera image and (b) right half of the corrected image after distortion-correction, vertical-alignment, background-subtraction, and HXR-removal (described in the text). A 2D projection of the 3D vacuum vessel geometry overlays the image. Intensity data within the dashed box are analyzed. (t = 0.74 s)

A fish-eye lens on the camera causes barrel distortion of the images. Therefore, an in-vessel calibration was performed to map raw pixel data to a rectilinear detector plane; details of this procedure can be found in chapter 4. However, an absolute calibration, mapping pixel intensity to Watts, was not performed. The right half of the corrected image is shown in figure 7.2b. Note how the vertical extent of the distortion-corrected synchrotron spot has been shortened significantly. This emphasizes the importance of camera calibration before synchrotron image processing and analysis.

Background visible plasma emission, averaged from the co-I_{p} direction (left side of figure 7.2a), has been subtracted in figure 7.2b. Most HXR speckles have been "filtered out" by finding pixels with intensities several times higher than the average of their immediate neighbors. A 2D projection of the 3D vacuum vessel geometry overlays the corrected image and matches reflected light features quite well. Vertical positions of the midplane ($Z = 0$) and lower inboard divertor "notch" ($Z \approx$ -48 cm) are also indicated in figure 7.2b. Because the camera is below the midplane, the synchrotron spot has a unique parabolic shape, different from the crescents, ellipses, and hollow rings seen in other tokamaks. This matches expectations based on the vertical scan performed for SOFT synthetic images in chapter 5 and seen in figure 5.11.

The dashed box outlines the subset of pixels (150 $\times$ 150) within which synchrotron emission is primarily observed; this region will be the focus of the following analyses.

Plasma parameters for the flattop runaway discharge of interest are shown in figure 7.3e. Camera images of the synchrotron spot (within the 150 $\times$ 150 pixel box of figure 7.2b) are shown at four times, indicated by the vertical dashed lines in figure 7.3e-f: $t = 0.44$, 0.74, 1.04, and 1.34 s. Initially, the plasma density n decreases in time, thereby reducing collisional friction and encouraging runaway growth. (This is similar to the procedure used to generate runaways in the discharges analyzed in chapter 6.) The measured synchrotron intensity, summed within each frame, is brightest at $t \approx 0.4$ s, as seen in figure 7.3f; in fact, the synchrotron emission actually saturates part of the camera image, as seen in figure 7.3a.

At $t \approx 0.7$ s, the plasma rotation slows as a locked mode begins. This is determined (empirically) by both a partial reduction of sawteeth in the temperature T evolution, as well as magnetic fluctuations $\widetilde{B}$ measured by Mirnov coils within the first wall. These magnetic fluctuations actually correspond to a high frequency ($\sim$40-60 kHz) signal which is found to be correlated with locked modes in C-Mod; they will be discussed further in the section 7.2. There is a reduction in total synchrotron intensity at this time, and the synchrotron spot develops interesting spatial structure: As seen in figure 7.3b, there appear to be three "legs" to the synchrotron spot, with distinct "inner" and "outer" legs on the high-field (left) side of the image. During the period of $\widetilde{B}$ fluctuations from $t \approx$ 0.7-1.0 s, measured HXR and photoneutron signals also increase, indicating the loss of runaways to the first wall.

At $t = 1$ s, the plasma density is increased in order to suppress runaway growth. In response, the synchrotron spot decreases both in intensity and size, as seen in figure 7.3c. Around the same time, sawteeth in T disappear, suggesting a fully-locked plasma. The amplitude of $\widetilde{B}$ fluctuations increases as the runaway beam continues to decrease in size and intensity (see figure 7.3d). Finally, at the end of the discharge, during the I_p ramp-down, there is a sudden flash of synchrotron light and "white noise" in the image, corresponding to spikes in HXR signals and indicating the final loss of runaway confinement.

Poloidal flux contours, as calculated by EFIT [27], are shown for one time, $t = 0.74$ s, in figure 7.4. Note that this is the same as figure 1.4 and is at the same time as the camera image in figure 7.2. Specifically highlighted are the magnetic axis, rational flux surfaces with $q = 1$, 4/3, 3/2, 2, and 3, as well as the last closed flux surface. It is important to note that all discharges analyzed in this chapter were elongated and diverted. In addition, the magnetic flux was reconstructed in EFIT by constraining (only) the on-axis safety factor q_axis; that is, a bound was set around $q_\mathrm{axis} \approx 1$ due to observations of sawtoothing. Similar C-Mod plasma discharges, from different experimental runs, were able to perform more accurate magnetic reconstructions

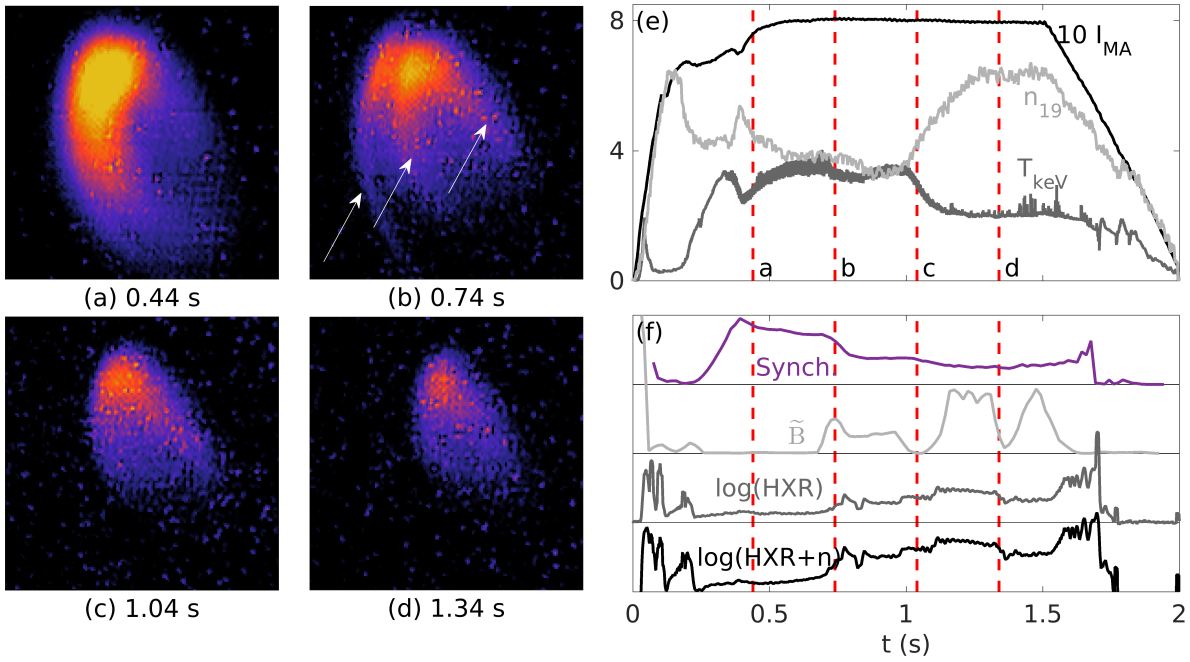

Figure 7.3: Corrected experimental images (false-colored) at four times: $t =$ (a) 0.44 s, (b) 0.74 s, (c) 1.04 s, and (d) 1.34 s. The observed synchrotron spot "legs" are indicated by the arrows in (b). Plasma parameters in (e) are the plasma current in MA (multiplied by a factor of 10), line-integrated density in 10^{19} m^{-3}, and central temperature in keV; in (f) are signals (a.u.) of summed synchrotron intensity in each frame (purple), locked-mode proxy $\widetilde{B}$, HXR radiation, and HXR+photoneutrons, each with a different vertical axis offset. Times (a)-(d) are marked by vertical dashed lines in (e)-(f).

using data from the Motional Stark Effect (MSE) diagnostic operating in its normal capacity.[b] The MSE-constrained q-profiles closely match those used in this work, thus improving confidence in the validity the following analyses.

7.1.2 Spatiotemporal evolution

A wealth of information relating to the spatiotemporal evolution of the runaway phase space distribution is encoded synchrotron images. In this section, a detailed analysis of one C-Mod discharge (1140403026) is performed to infer the evolution of the radial density profile of the runaway population. As discussed previously in chapter 5, solving the *inverse* problem—i.e. determining the 3D (or higher dimensional) position and momentum space distribution of runaways

[b] Actually, the MSE measurements of polarized synchrotron radiation from this same discharge are the focus of the next chapter, chapter 8.

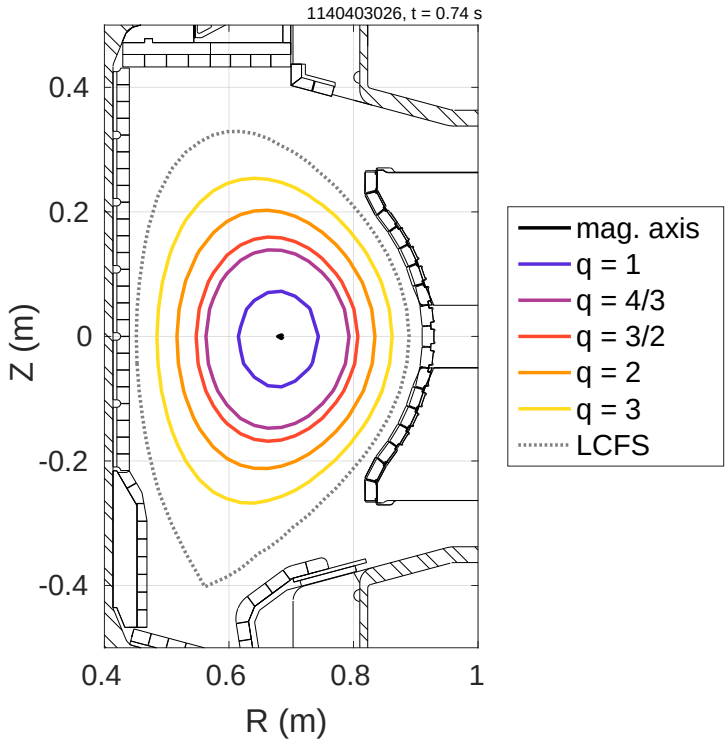

Figure 7.4: Overlaying a poloidal cross-section of the C-Mod vacuum vessel are poloidal flux contours from EFIT [27]: the magnetic axis (black dot), rational surfaces $q = 1$, $4/3$, $3/2$, 2, and 3 (solid), and the last closed flux surface (LCFS, dotted). This figure is the same as figure 1.4, re-plotted here for convenience. ($q_{95} \approx 4.5$, $t = 0.74$ s)

from a 2D camera image—is currently intractable. First, it is unlikely that there is a "unique enough" solution; that is, the range of possible solutions is too large to be useful, especially within experimental uncertainties. (Refer to the discussion of chapter 6 and figure 6.4.) Second, the computational resources required are expensive. Conversely, there is an opportunity to solve the *forward* problem: Given 3D spatial distributions of all plasma parameters (e.g. E, n, T, B, etc.), one could solve the equations of motion for all electrons, calculate their synchrotron emission, and model its detection by a camera. Such a 6D solver—including the synthetic camera diagnostic—has been developed [28, 29]; however, these simulations are computationally-intensive, requiring hundreds of thousands of CPU-hours. Instead, a much more computationally-feasible, multi-step approach is adopted here to partly solve both the forward and inverse problems, meeting in the middle. The methodology is as follows:

(I) Flux-surface-averaged plasma parameters are obtained from experimental measurements for the magnetic axis and rational flux surfaces with $q = 1$, $4/3$, $3/2$, 2, and 3.

(II) For each surface, the runaway momentum space distribution function is evolved using the kinetic solver CODE [30, 31], which is described in further detail in chapter 5. An ad hoc, piecewise, radial phase space distribution, normalized to the local runaway density, is constructed

$$F(R,\boldsymbol{p}) = \begin{cases} F_{\text{axis}}(\boldsymbol{p}), & R \in \left[R_0, (R_0+R_1)/2\right) \\ F_{q_m}(\boldsymbol{p}), & R \in \left[(R_{m-1}+R_m)/2, (R_m+R_{m+1})/2\right) \\ F_3(\boldsymbol{p}), & R \in \left[(R_2+R_3)/2, R_0+a\right] \end{cases}, \tag{7.1}$$

where R is the major radial coordinate, $\boldsymbol{p} = (p_\parallel, p_\perp)$ is the 2D momentum vector, and $q_m = \{1, 4/3, 3/2, 2\}$ are the inner flux surfaces. Note that all F_{q_m} and R_m are also functions of time, but t is dropped for convenience.

(III) This phase space distribution, $F(R,\boldsymbol{p})$ from (7.1), is input into the synthetic diagnostic SOFT [2]—refer to chapter 5 for more details—along with the magnetic field and detector geometry to generate a Green's function $\hat{G}_{ij}(R)$ describing the *partial* image produced by the distribution function localized at radius R, as in equation (9) of [2]. Here, i and j refer to the 2D pixel coordinates within the image.

(IV) For an array of radial positions R_k, $\hat{G}_{ij}(R_k)$ is used as a set of basis functions, such that the final 2D image in the detector plane can be calculated as

$$I_{ij} = \sum_k C(R_k)\,\hat{G}_{ij}(R_k)\,\Delta R_k, \tag{7.2}$$

where ΔR_k is the radial step, and $C(R_k)$ can be calculated to produce the best fit between I_{ij} and the experimental image.

The runaway density profile $n_\text{r}(R)$ can be related to coefficients $C(R_k)$ using $F(R,\boldsymbol{p})$, which is normalized to the local runaway density as given by equation (9) of [30]

$$F(\boldsymbol{p}) = \frac{\pi^{3/2}\, m^3\, v_\text{ref}^3}{n_\text{ref}} f(\boldsymbol{p}). \tag{7.3}$$

Here, m is the electron mass, v_ref is a reference electron thermal velocity, n_ref is a reference electron density, and $\int f(\boldsymbol{p})\,\mathrm{d}\boldsymbol{p} = n$ is the total plasma density; thus, $F(\boldsymbol{p})$ is *unitless*. The reference parameters are usually taken as the initial electron thermal velocity and density (at

$t = 0$) when running CODE, but that is inconsequential here. Thus, analagous to (7.1), the *unnormalized* ad hoc profile is given by

$$f(R, \boldsymbol{p}) = \frac{n_{\mathrm{ref}}(R)}{\pi^{3/2}\, m^3\, v_{\mathrm{ref}}^3(R)} F(R, \boldsymbol{p}), \tag{7.4}$$

which has the typical units $\mathrm{s}^3/\mathrm{kg}^3/\mathrm{m}^6$. Here, $n_{\mathrm{ref}}(R)$ and $v_{\mathrm{ref}}(R)$ are also piecewise functions like $F(R, \boldsymbol{p})$. CODE also calculates a total runaway density n_{CODE} (with units $1/\mathrm{m}^3$), like that plotted in figure 7.5d. In this work, the Green's function $\hat{G}_{ij}(R)$, from (7.2), was calculated using normalized $F(R, \boldsymbol{p})$ instead of $f(R, \boldsymbol{p})$. Therefore, the fitted runaway density profile is calculated by scaling $n_{\mathrm{CODE}}(R)$ by the computed coefficients $C(R)$ and the appropriate normalization factor, i.e.

$$n_{\mathrm{r}}(R) = \frac{\pi^{3/2}\, m^3\, v_{\mathrm{ref}}^3(R)}{n_{\mathrm{ref}}(R)} n_{\mathrm{CODE}}(R)\, C(R). \tag{7.5}$$

Again, $C(R)$ are the best-fit coefficients of (7.2). Note that all quantities that vary with R also vary in time, but t has been dropped for clarity. For a full derivation of (7.5) and further discussion, see appendix D.

7.1.3 Momentum space simulations using CODE

The kinetic Fokker-Planck solver CODE was used in this analysis to evolve runaway momenta on each flux surface. As described in chapter 5, inputs to CODE are time evolutions of the electric field E, electron density n and temperature T, and effective charge Z_{eff}; the toroidal magnetic field B is also input, but must be time-*independent*. In these experiments, a measurement of Z_{eff} was unavailable as visible synchrotron light dominated the diagnostic measurement; thus, $Z_{\mathrm{eff}} = 4$ (a value consistent with previous measurements during low density C-Mod discharges) was assumed and taken to be constant in time and space. The other parameters vary throughout the plasma: n and T radial profiles were measured via Thomson scattering; E and q profiles were determined using EFIT [27]; and the toroidal magnetic field was approximated as $B = B_0 R_0 / R$. The Chiu-Harvey knock-on collision model [32]—described in chapter 2—was used for avalanche generation. All CODE simulations described here required ∼300 CPU-hours in total.

This analysis considers runaway generation and evolution at six locations throughout the plasma: the magnetic axis and flux surfaces with $q = 1$, 4/3, 3/2, 2, and 3. These were chosen because they are approximately equally-spaced radially (see figure 7.4) and, as rational surfaces, could potentially exhibit interesting MHD-related behavior. Additionally, as will be described, all measurable synchrotron activity is found to occur within $q \leq 3$, so analyses at higher q are not necessary. Both n and T are assumed to be flux functions, but E and B were flux-surface

averaged.

The ratios of the electric field to the critical field E/E_{C} [33], from (2.8), and to the Dreicer field E/E_{D} [34, 35], from (2.7), are shown for each location of interest in figures 7.5a-b. Notice how E/E_{C} increases radially from the magnetic axis to the plasma edge; this is primarily due to the decreasing n profile, but can also be affected by the radial dependence $E \propto 1/R$ and finite diffusion time as $\partial E/\partial t$ propagates into the plasma. From this, the runaway average energy $\mathcal{E}$ is expected to increase from the core to edge. Conversely, the values of E/E_{D} are higher in the plasma center than at the boundary, due to the centrally-peaked T profile. Thus, the runaway density n_{r} is expected to be highest in the core because a larger population of thermal electrons available to run away exists there. Figures 7.5c-d confirm these expectations: CODE predicts higher $\mathcal{E}$ on the $q = 3$ surface compared to on-axis, whereas n_{r} is estimated to be approximately two orders of magnitude larger in the core than at the edge.

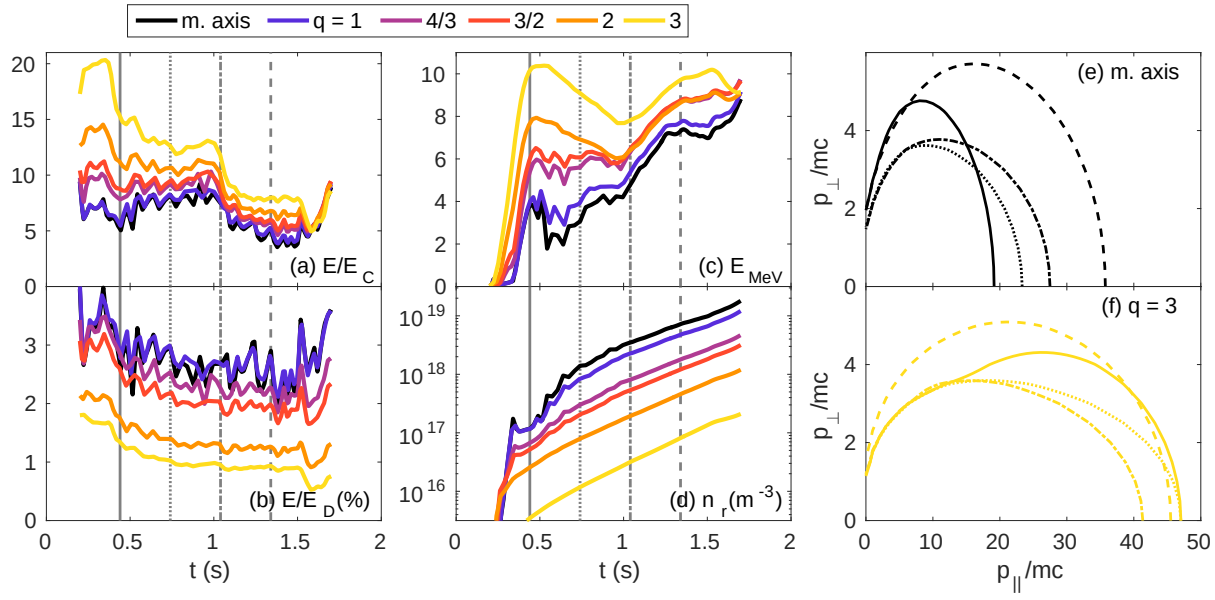

Figure 7.5: Experimentally-measured ratios (a) E/E_{C} and (b) E/E_{D} (%) are provided as inputs to CODE for six radial positions: the magnetic axis and rational flux surfaces with $q = 1$, 4/3, 3/2, 2, and 3. CODE outputs the predicted (c) average runaway energy in MeV and (d) runaway density in m^{-3}. Contours of CODE momentum space distribution functions are shown for the (e) magnetic axis and (f) $q = 3$ flux surface for four times, marked as vertical lines in (a)-(d): $t = 0.44$ s (solid), 0.74 s (dotted), 1.04 S (dot-dashed), and 1.34 s (dashed). Note that the value of each contour is (arbitrarily) chosen to be $\log_{10}(F) =$ -15/4, where F is normalized. The color scheme is the same as that in figure 7.4. ($B_0 = 5.4$ T, $Z_{\mathrm{eff}} = 4$)

The time evolution of $\mathcal{E}$ in figure 7.5c illustrates the complicated interplay of time-changing plasma parameters and runaway dynamics. First, it is important to note that $\mathcal{E}$ is the *average* energy of the high energy runaway region in momentum space, *not* the maximum runaway energy. Second, a finite time is required for runaways to respond to changes in E/E_{C} or E/E_{D}, meaning that $\mathcal{E}(t)$ will exhibit some time delay. In figure 7.5c, $\mathcal{E}$ increases rapidly during the I_{p} ramp-up, but levels off or decreases as E/E_{C} drops, even for values of $E/E_{\mathrm{C}} \sim$ 7-14. When the bulk plasma density increases at $t \approx 1$ s, E/E_{C} decreases to ∼5-10, but $\mathcal{E}$ rises, due to both $E/E_{\mathrm{C}} > 5$ and increased pitch angle scattering from higher collisionality.

The complex evolution can also be seen from the contours of the normalized momentum space distribution function at the magnetic axis and $q = 3$ surface in figures 7.5e-f. The four times of interest are $t = 0.44$ s (solid), 0.74 s (dotted), 1.04 s (dot-dashed), and 1.34 s (dashed). At the magnetic axis, the distribution function F_{axis} initially has a broad pitch angle distribution ($p_\perp/p_\parallel \approx 0.5$), which then elongates along $p_\parallel$ as runaways are accelerated in the direction of the magnetic field. From $t =$ 1.04-1.34 s, F_{axis} grows in both $p_\parallel$ and $p_\perp$ with increased pitch angle scattering due to the higher collisionality. For comparison, the distribution function F_3, at the $q = 3$ surface, has high energies at early times due to high E/E_{C} values, before decreasing in $p_\parallel$ and $p_\perp$. Similar to F_{axis}, F_3 spreads in $p_\perp$ later in time. While these are contours of the distribution function *normalized* at each time, the density of runaways is actually predicted to increase exponentially from secondary avalanching, as seen in figure 7.5d.

7.1.4 Synthetic images using SOFT

To best reproduce experimental synchrotron images, the synthetic diagnostic SOFT [2]—refer to chapter 5—was used for its synthetic camera capabilities. Recall that SOFT takes as inputs (i) the magnetic topology—assumed to be axisymmetric—obtained from EFIT [27], (ii) detector specifications including geometry and spectral range (refer to table 4.3), and (iii) a runaway phase space distribution $F(R, \boldsymbol{p})$. The use of a synthetic diagnostic, like SOFT, is of utmost importance in the analysis of synchrotron images (and other measurements) as synchrotron radiation *emitted* is not always *detected*.

The full spectral and angular calculation of synchrotron emission is available in SOFT. However, recall from chapter 3 that the angular spread of synchrotron emission is quite small ($\sim 1/\gamma$, where γ is the relativistic factor); therefore, the "cone" model—where radiation is only emitted along the runaway direction of motion—serves as an adequate approximation of the full *angular* formulation, as discussed in chapter 5 and [1, 2, 7, 36]. Additionally, the cone model significantly reduces computation time, which for all SOFT simulations used in this work was ∼3700 CPU-hours in total. SOFT is based on a zeroth-order guiding center formulation, meaning that drift orbits and associated effects have not been accounted for in this study. Using (2.39), the radial

drift of a 20 MeV runaway in a plasma with parabolic current density profile and $I_\mathrm{p} = 800$ kA is $r_\mathrm{d} \leq 3$ cm. This is small but non-negligible for image analysis and should be investigated in future work.

A powerful feature of SOFT utilized in this work is its ability to calculate the Green's function $\hat{G}_{ij}(R)$ which accounts for the momentum space distribution function as well as magnetic and detector geometries. (Again, i and j are the 2D pixel coordinates.) This function can be integrated with a radial density profile $n_\mathrm{r}(R)$, as described in step (IV) of section 7.1.2, to produce the final synchrotron image. Moreover, using $\hat{G}_{ij}(R)$, it is possible to identify the contribution of runaways on a particular flux surface to the final image, simply by using a delta function at the flux surface location, i.e. $\delta(R - R_q)$. To highlight the contributions from runaways near the magnetic axis and around flux surfaces with $q = 1$, 4/3, 3/2, 2, and 3, step functions of width ΔR 4 mm (i.e. $\Delta R/a \approx 2\%$) centered on each surface were used instead of delta functions. For each surface, a closed contour at a level of 50% maximum intensity, as predicted by SOFT, indicates the region of the image within which most of the synchrotron emission from runaways on that surface will be detected. These contours are shown in figures 7.6a-c overlaying the experimental images from figures 7.3a-c. As seen in each subplot, the contour grows in size and moves from right-to-left with increasing q-value (and R).

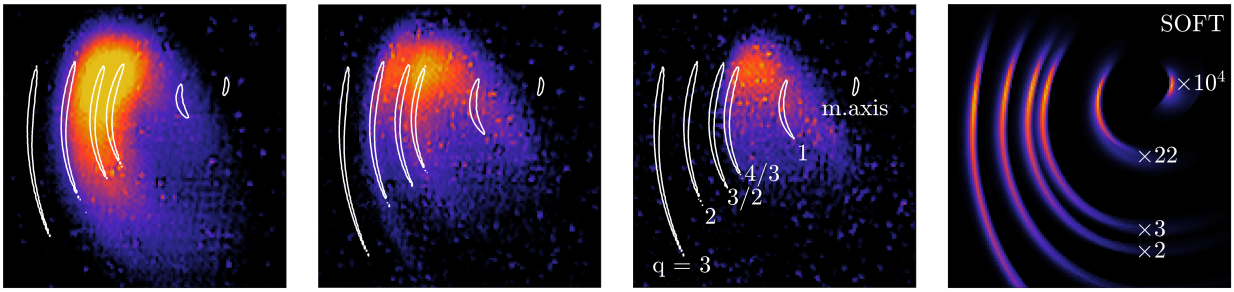

(a) 0.44 s (b) 0.74 s (c) 1.04 s (d) 1.04 s

Figure 7.6: (a)-(c) Closed contours (white) of 50% SOFT-predicted synchrotron emission, from the magnetic axis and rational flux surfaces with $q = 1$, 4/3, 3/2, 2, and 3, overlay experimental images from figures 7.3a-c. (d) The full SOFT-predicted emission of each contour in (c) is shown, along with scaling factors required to plot all surfaces on the same color-scale. Note that the q-value increases from right-to-left in each subplot and is labeled in (c).

Even before considering the full intensity distribution predicted by SOFT, some spatial information can be gleaned from these images. Note how, in figure 7.6a, the synchrotron spot shape matches the curvature of the SOFT contours quite well. In fact, the observed synchrotron spot is almost completely confined within the $q \approx 2$ surface. This does not necessarily imply that runaways exist only within $q \leq 2$; rather, runaways at $q \geq 2$ could have too low energies (e.g.

$\lesssim$ 10 MeV) and/or densities to be detected by the camera. Figure 7.6b shows the experimental image with interesting spatial structure at time $t = 0.74$ s. Recall from figure 7.3 that, at $t \approx 0.7$ s, increased MHD activity is observed at the onset of a locked mode. From figure 7.6b, it is clearly seen that the locations of the $q = 3/2$ and $q = 2$ surfaces match the inner and outer "legs," respectively, on the left side of the image. Since locked modes are usually associated with $\mathrm{m/n} = 2/1$ tearing modes, the camera is likely capturing the radial transport of runaways out of the plasma by an island at the rational $q = 2$ surface. At $t = 1.04$ s, the synchrotron spot shrinks within the $q \approx 4/3$ surface. This reduction in size could be due to (i) decreasing energies of runaways located at $q \gtrsim 4/3$ caused by the increasing plasma density and/or (ii) increased radial diffusion due to the locked mode.

Figure 7.6d is distinct from figures 7.6a-c; here, the full SOFT-predicted synchrotron intensity distribution is shown for each SOFT contour in subplot 7.6c. (Compare to figure 5.9 and 5.11c.) The factors given next to the contours are the scalings required to plot the intensities of synchrotron emission from runaways at magnetic axis and on surfaces with $q = 1$, $4/3$, and $3/2$ on the same color-scale as the $q = 2$ and $q = 3$ surfaces. The outermost surfaces are brightest due to the $\geq B^3$ scaling of synchrotron power spectra in the tokamak magnetic geometry.[c] Geometric factors also affect the synchrotron radiation detected. Because the camera is far below the midplane, runaways close to the magnetic axis and with small pitch angles—which would otherwise dominate synchrotron emission in this scenario—are not seen. The small contributions seen from runaways at the magnetic axis in figure 7.6d come from particles with larger pitch angles, which are far fewer in number.

[c] Refer to section 7.1.4 for an explanation of this scaling.

7.1.5 Fit and reproduction of experimental images

As seen in figure 7.6, contributions from different flux surfaces to the final synchrotron image are almost non-overlapping. This is a consequence of the interplay between the high directionality of synchrotron emission and magnetic and detector geometries. Thus, one approach to reproduce the experimental images is to use $\hat{G}_{ij}(R_k)$ as a set of basis functions for discrete radial positions R_k; then, coefficients $C(R_k)$ from (7.2) can be determined such that the resulting image I_{ij} best matches experimental data. Finally, the runaway density profile $n_\mathrm{r}(R)$ can be related to $C(R)$ through $F(R, \boldsymbol{p})$, as detailed in 7.1.2. The motivation for this fitting procedure is that while CODE has been used to construct a cylindrical plasma via $F(R, \boldsymbol{p})$, spatial dynamics—such as drifts, diffusion, and trapping—are not captured. Therefore, fitting a density profile is actually *required* to provide useful spatial information about runaway density evolution from the synchrotron images.

Note that equation (7.2) can be written as a matrix equation: Although the image I_{ij} is visualized in 2D, it can be represented as a 1D vector $\mathbf{I}$ with $(i \times j)$ elements. Similarly, the coefficients, $C(R_k)$, also make up a 1D vector $\mathbf{C}$ of length k, for the k discrete values of R used in the SOFT simulations. Then, the Green's function $\hat{G}_{ij}$ can be rearranged into a 2D matrix $\hat{\mathbf{G}}$ with dimensions $(i \times j) \times k$, so that

$$\mathbf{I} = \hat{\mathbf{G}}\,\mathbf{C}, \tag{7.6}$$

where $\Delta R =$ constant from (7.2) has been absorbed into $\hat{\mathbf{G}}$. While the SOFT simulations were performed with runaways at 200 radial positions, the output data were down-sampled into $k = 100$ radial bins to counteract over-fitting and best match pixel resolution. The best-fit coefficients were calculated using a linear least-squares solver subject to the constraint $\mathbf{C} \geq 0$, i.e. requiring non-negative contributions of synchrotron emission. In this analysis, values of $C(R) = 0$ occurred in regions of low measured intensity near the plasma core and edge. This makes sense at the boundary of the synchrotron spot since we expect the runaway radial profile to decay with R. However, values of $C(R) = 0$ in the plasma center—where high runaway densities are expected—simply indicate our ignorance of the runaway population there due to the camera's vertical offset.

Fitted images are shown for four times in figures 7.7e-f, corresponding to the experimental images in figures 7.7a-d (reproduced from figures 7.3a-d). Note that each SOFT image is smoothed over a 5 × 5 pixel window (∼0.1% of the image area) to remove unphysical sharp edges resulting from the piecewise structure of $F(R, \boldsymbol{p})$. For $t = 0.44$ s, the fitted SOFT image does not match experiment well. This is likely because I_p and the magnetic geometry are still evolving at this time. The simulated CODE momentum space distributions also have large pitch angles at this time, causing more overlap in the contributions of adjacent flux surfaces to the final image. What is more, the experimental image is saturated. For these reasons, a good fit

of SOFT to the experimental image at $t = 0.44$ s is difficult. The fitted images of later times, however, are more similar to experiment. As seen in figure 7.7b, the spatial structure of the inner and outer legs can be reproduced by SOFT. The location of peak intensity and intensity gradients are also quite similar. Note that the vertical position of the synthetic image is slightly lower than that in experiment; a likely reason for this is calibration error, but the difference is only ≤ 10 pixels, which is small compared to the full size of the camera image (640×480 pixels). The fitted SOFT images for the later times, $t = 1.04$ and 1.34 s in figures 7.7c-d, also match experiment quite well, showing the decrease in both synchrotron spot size and intensity.

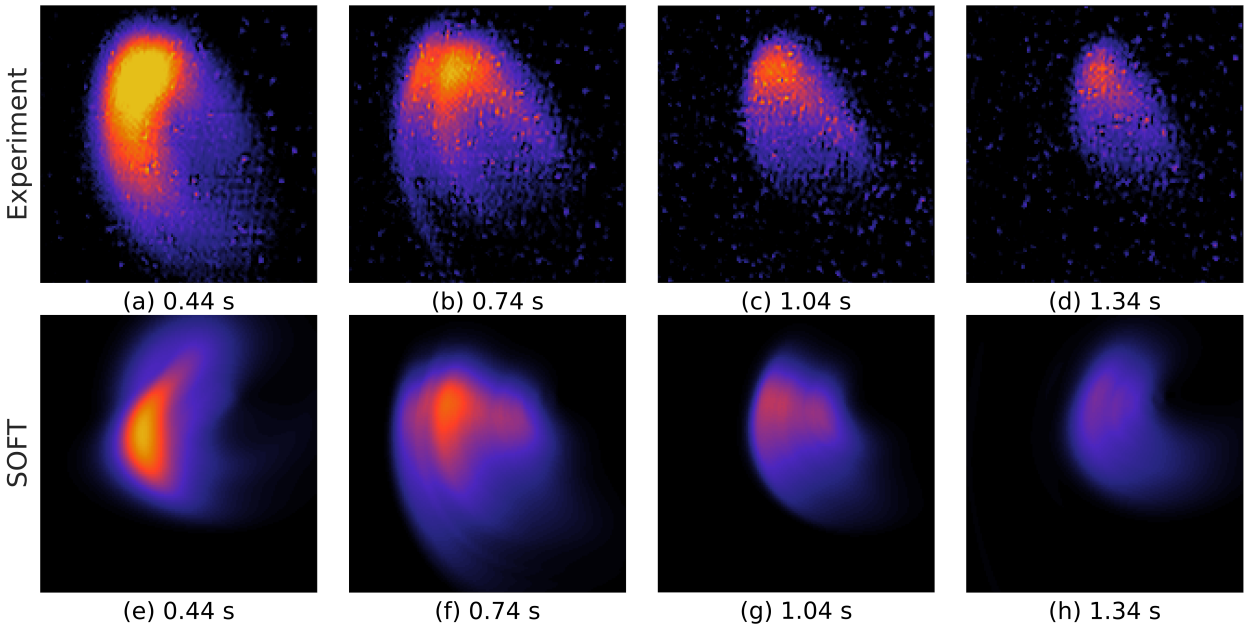

Figure 7.7: Best-fit SOFT reproductions of the experimental images in (a)-(d) are shown in (e)-(h). Note that (a)-(d) are reproduced from figures 7.3a-d.

As mentioned previously, modeling efforts are currently underway to solve the runaway forward problem, i.e. to predict the 6D runaway phase space distribution from known plasma parameters. If the runaway densities as calculated by CODE are used for the density profile, instead of the fitted profile, the resulting SOFT image at $t = 0.74$ s would be that shown in figure 7.8a. Here, the two bright features correspond to the regions around the $q = 2$ and $q = 3$ surfaces. Specifically, the discontinuity in intensity occurs due to the piecewise nature of $F(R, \boldsymbol{p})$ and the uniform density throughout each radial interval assumed here. Even though the runaway densities are predicted to be $\sim$100$\times$ lower in the region near the plasma edge compared to on-axis, geometric effects and increasing synchrotron power with magnetic field lead to CODE-predicted emission dominating near the edge. This synthetic image clearly does not match experiment, further motivating the

fitting procedure employed in this work.

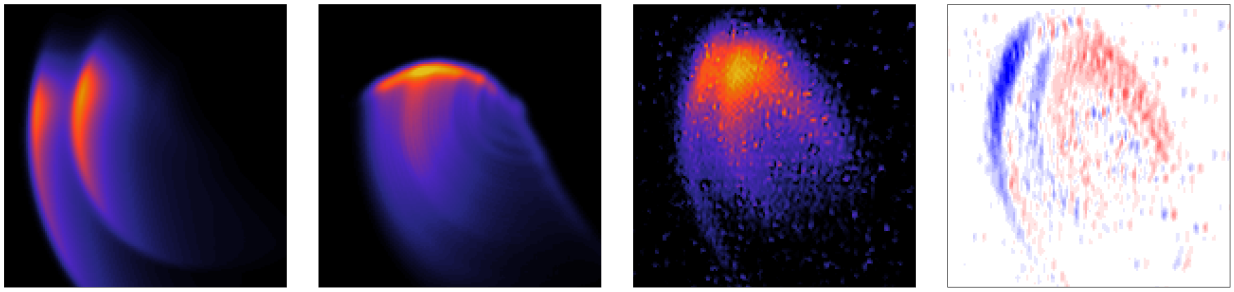

(a) No fit (b) TPM (c) Exp, 0.74 s (d) Edge Detection

Figure 7.8: (a) SOFT image resulting from no experimental fitting, but instead with only the CODE-predicted radial density profile (see figure 7.5d). (b) Best-fit SOFT reproduction using a test particle model (TPM) of momentum space evolution, as described in section 7.1.6 and chapters 2 and 6. (c) Experimental image from figure 7.3b reproduced for comparison. (d) Edge detection [37] applied to (c), with blue/red colors corresponding to positive/negative horizontal gradients of pixel intensity, as described in section 7.1.7. ($t = 0.74$ s)

7.1.6 Application of a test particle model

In previous analyses, test particle models (TPMs) of runaway evolution were used to estimate runaway energies and pitch angles for comparison with experimental synchrotron images [8–12, 15, 16, 24, 25]. In the current analysis, the TPM from [38] and described in chapter 2 was applied and found to be insufficient in capturing all spatial features of the experimental intensity distributions. As detailed in chapter 2, a coupled system of differential equations describes the trajectory of a test runaway in momentum space, governed by time-evolving plasma parameters. These trajectories (delta functions in momentum space) were calculated for 40 equally-spaced flux surfaces throughout the plasma, resulting in radial profiles of runaway energy and pitch angle. Following a similar fitting procedure as that described in section 7.1.5, the best-fit TPM+SOFT image for $t = 0.74$ s is shown in figure 7.8b. The fitted TPM image is still able to match the horizontal width of the synchrotron spot, and the intensity distribution is similar to experiment, e.g. the parabolic shape and approximate location of maximum intensity. However, the vertical extent of the synchrotron spot is not reproduced by the TPM (compare to figure 7.8c). This is because there is no pitch angle distribution, leading to a sharp intensity gradient at the top of the image. Thus, it is concluded that the full momentum space distribution is needed to reproduce the smooth intensity gradients at the edges of the synchrotron spot.

7.1.7 Edge detection

The full analysis of spatial intensity distributions within synchrotron images can be time-consuming and computationally-expensive. Yet useful spatial information can still be obtained from SOFT without knowing the full momentum space evolution. Specifically, spatial structure in the synchrotron image can be mapped to flux surfaces in the plasma, assuming that most observed runaways have small pitch angles (e.g. $p_\perp/p_\parallel \leq 0.2$). To demonstrate this, the Sobel operator [37] for edge detection was applied to the experimental data. The basic idea is that the Sobel operator approximates the gradient of pixel intensity within the image. Here, the *horizontal* gradient operator was used to identify *vertical* edges in the images, via the 3×3 matrix

$$\mathbf{S} = \begin{bmatrix} -1 & 0 & 1 \\ -2 & 0 & 2 \\ -1 & 0 & 1 \end{bmatrix}, \tag{7.7}$$

which is simple and efficient in implementation. Note that this matrix can be rotated to calculate the vertical gradient or have signs flipped to switch gradient directions.

The edge detection algorithm works as follows: Consider a pixel at location (i, j) in an image, as well as its neighboring pixels. A subset of the total image is the 3×3 matrix surrounding (i, j)

$$\widetilde{\mathbf{I}}_{\mathbf{ij}} = \begin{bmatrix} I_{i-1,j-1} & I_{i,j-1} & I_{i+1,j-1} \\ I_{i-1,j} & I_{i,j} & I_{i+1,j} \\ I_{i-1,j+1} & I_{i,j+1} & I_{i+1,j+1} \end{bmatrix} \tag{7.8}$$

From (7.7) and (7.8), the resulting "gradient image" $\mathbf{I'_{ij}}$ used for edge detection is evaluated by (i) element-wise multiplication of $\mathbf{S}$ and $\widetilde{\mathbf{I}}_{\mathbf{ij}}$ and (ii) summation over all (nine) elements. Explicitly, the value of the Sobel horizontal gradient at pixel location (i, j) is

$$I'_{ij} = -I_{i-1,j-1} + I_{i+1,j-1} - 2I_{i-1,j} + 2I_{i+1,j} - I_{i-1,j+1} + I_{i+1,j+1} \, . \tag{7.9}$$

Note that this calculation cannot be performed at the edges of the image.

The resulting horizontal gradient of pixel intensity in the experimental image is shown in figure 7.8d for one time, $t = 0.74$ s. The blue/red colormap corresponds to the amplitude of positive/negative gradients of pixel intensity in the horizontal direction from left-to-right. Thus, the left edge of the synchrotron spot is blue, and right edge is red. By setting a threshold value of the gradient, the edges can be detected, and the pixel locations can be mapped to flux surfaces using SOFT. Notice that in the frame shown, there are two blue regions, indicating that there is

a more complicated spatial structure. These are the inner and outer legs of the synchrotron spot. The white region (zero slope) between blue and red (positive and negative slopes, respectively) were used to identify the spatiotemporal evolution of these legs, which will be described in the next section.

7.1.8 Best-fit runaway density profile

The resulting best-fit runaway density profile is plotted versus time and normalized minor radius r/a in figure 7.9a, with one time, $t = 0.74$ s, highlighted in figure 7.10. Only times during flattop I_p are shown as the fitting procedure did not reproduce experimental images before $t \approx 0.5$ s (see figure 7.7a). In addition, the spatial range only spans $r/a \sim 0.2$-1.0, since little synchrotron emission is visible from runaways near the magnetic axis by a camera displaced so far below the midplane; this makes interpretation of results for $r/a \lesssim 0.2$ difficult (or impossible). (For reference, the $q = 1$ surface is located at $r/a \approx 0.3$.) The time resolution of this analysis is $\Delta t = 100$ ms, limited primarily by the long computation times of SOFT simulations of each time-slice. While the radial resolution of the SOFT simulations is $\Delta r/a \approx 0.01$, caution should be used when interpreting fine spatial features. Note also that the colormap of $\log_{10}(n_\mathrm{r})$ has arbitrary units since no absolute calibration of the camera was performed. It follows that the density threshold for detection cannot be inferred from this analysis; here, the scale spans 8 orders of magnitude, which adequately portrays the spatiotemporal evolution while also highlighting interesting spatial features.

As seen in figures 7.9a and 7.10, the radial profile is peaked in the core and decays toward the plasma edge. In figure 7.9a, at the start of the flattop, the observed runaway beam is confined within $r/a \leq 0.75$. Then, at $t \approx 0.7$ s, the n_r profile spreads outward toward the $q = 2$ surface, corresponding to the start of MHD activity (shown again in figure 7.9b) and spatial structure observed at that time. Figure 7.10 shows the radial profile for $t = 0.74$ s. Note that the profile decreases (approximately) monotonically; i.e. there is no significant "bump" in n_r near the $q = 2$ surface ($r/a \approx 0.7$). There are, however, several "steps" around $r/a \approx 0.4$, 0.55, and 0.65, which are caused by the piecewise momentum space distribution in (7.1). Beyond $r/a \approx 0.75$, n_r drops off steeply. This is in contrast with the runaway density profile predicted by CODE, also shown in figure 7.10, which is broader in radial extent and predicts much higher densities at $q = 3$ than inferred. For times after $t \approx 0.74$ s, the density n_r shrinks in size and amplitude, as seen in figure 7.9a. This is consistent with the runaway population being suppressed by the increasing bulk plasma density.

Overlaying the contour plot of figure 7.9a is the time-evolving location of the $q = 2$ surface, as well as features determined from edge detection: the synchrotron spot boundary and legs (see section 7.1.7). The boundary matches the shape of the density profile quite well. The low

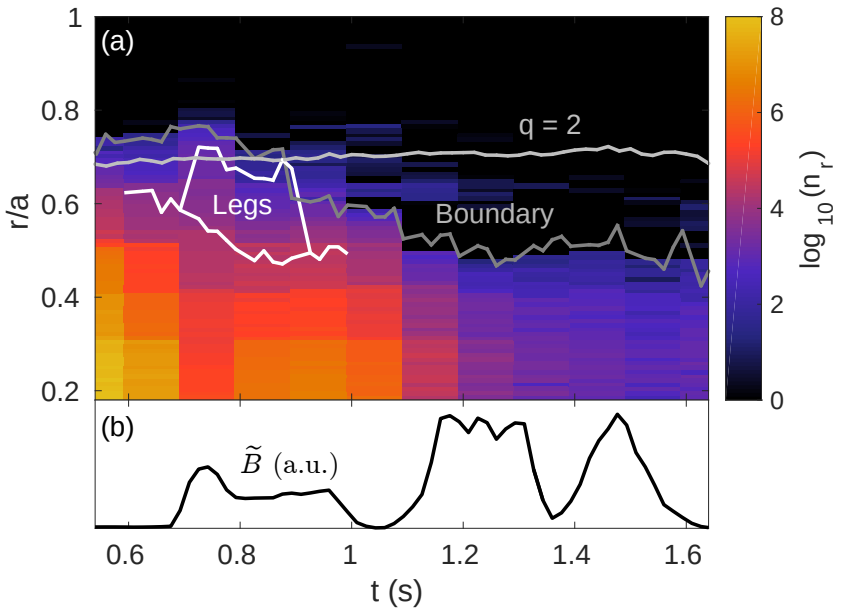

Figure 7.9: (a) Contour plot of best-fit runaway density $\log_{10}(n_{\rm r})$ (a.u.) versus time and normalized minor radius r/a. The positions of the boundary and legs determined from edge detection, as well as the $q = 2$ surface, (each labeled) overlay the radial profile. Time and radial resolutions are $\Delta t \approx 100$ ms and $\Delta r/a \approx 0.01$, respectively. (b) Reproduction of the magnetic fluctuation signal (a.u.) from figure 7.3e.

density "bumps" outside this boundary are likely due to mis-identification of some HXRs—with low enough intensity to be missed by the data filtering technique—as synchrotron light. The inner and outer legs (where the white lines diverge) form at the same time that magnetic fluctuations and a locked mode are observed, as seen in figure 7.9b. From $t \approx$ 0.7-0.9 s, the inner leg follows the density contour $\log_{10}(n_{\rm r}) \approx 5$ in figure 7.9a, while the outer leg moves to the region near the $q \approx 2$ surface. At $t \approx 0.9$ s, the two legs recombine as the $\widetilde{B}$ signal decreases.

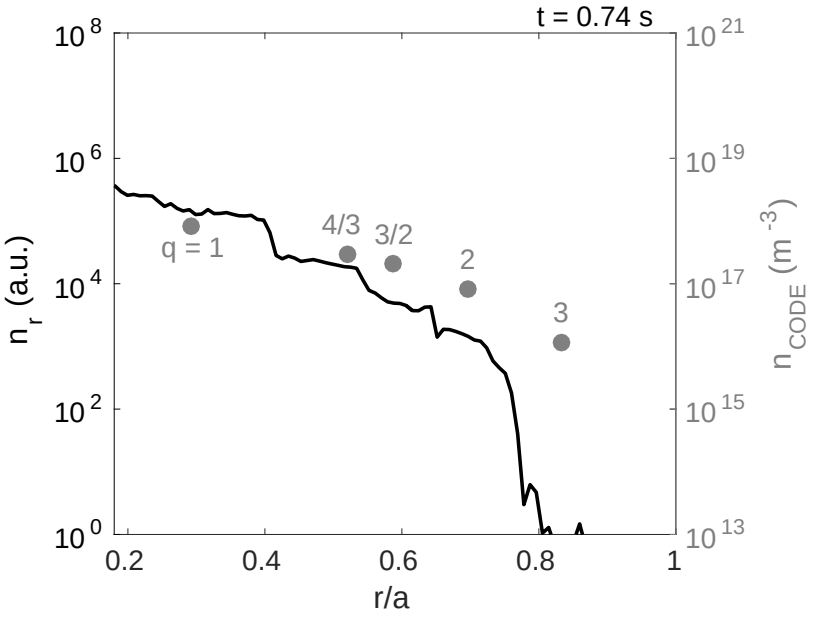

Figure 7.10: (Left axis) The fitted $n_{\rm r}$ radial profile (solid) at one time $t = 0.74$ s, plotted on the same radial and logarithmic scales as figure 7.9a. (Right axis) The CODE-predicted runaway densities $n_{\rm CODE}$ (dots) for the surfaces in figure 7.5d, also at time $t = 0.74$ s and spanning 8 orders of magnitude.

7.2 Magnetic fluctuations and interactions with runaways

As mentioned, Mirnov coils located in the first wall measured high frequency (∼40-60 kHz) fluctuations $\widetilde{B}$ correlated in time with an observed locked mode (see figure 7.3). Indications of this locked mode include the decreasing amplitude of $T_{\rm e}$ sawtooth crashes around $t \approx 0.7$ s and then the almost complete disappearance of sawteeth around $t \approx 1.1$ s. It is likely that $\widetilde{B}$ is associated with the MHD activity causing or resulting from the locked mode. This section explores further the interactions of magnetic fluctuations and runaways, speculating about the origin of $\widetilde{B}$ and looking at its correlation with HXR signals.

7.2.1 Magnetic fluctuations, locked modes, and REs

Figure 7.11 shows a spectrogram of magnetic fluctuations in the range $f = 0$-100 kHz over the duration of C-Mod discharge 1140403026; also seen is the time evolution of the central electron temperature $T_{\rm e}$ as measured from electron cyclotron emission (ECE). At $t \approx 0.7$ s, a high frequency $\widetilde{B}$ signal appears at $f \sim 50$ kHz. At the same time, the $T_{\rm e}$ sawteeth reduce in

amplitude; this is more easily seen in the zoom-in of figure 7.12. Around $t \approx 1$ s, the $\widetilde{B}$ signal disappears, but then reappears again at $t \approx 1.1$ s. The reason for this is unclear, although some interesting spikes in the ECE T_e signal are observed in the interval $t = 1.0$–1.1 s. These spikes could be signs of non-thermal ECE emission from runaways [39]. From $t = 1.1$ s on, the sawteeth almost completely go away; this is seen most clearly in figure 7.13. The fluctuations continue until $t \approx 1.6$ s, when runaways are finally suppressed.

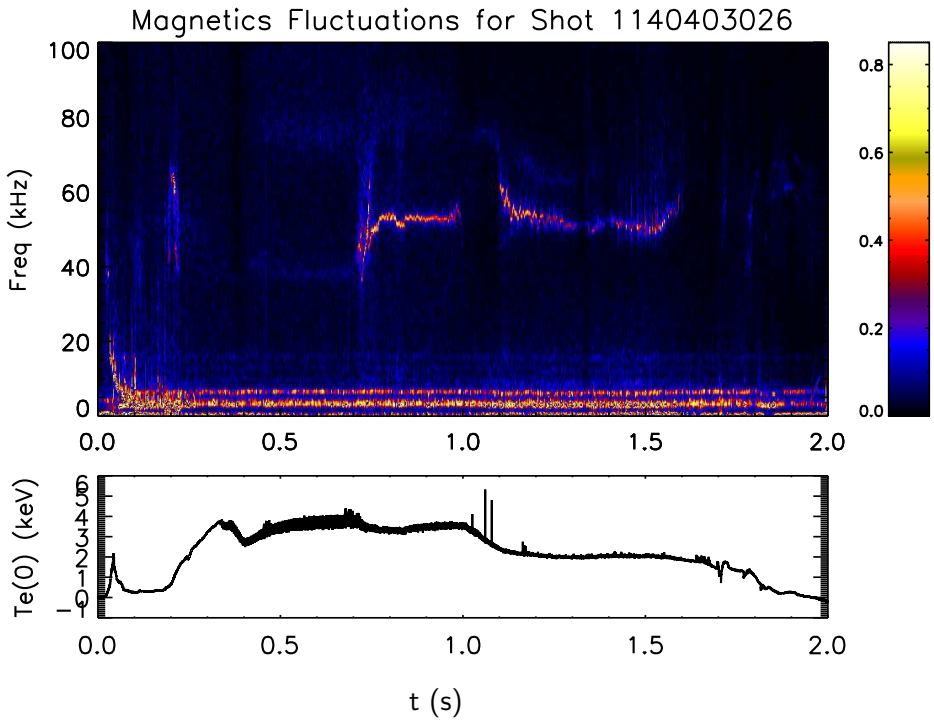

Figure 7.11: *Top*: A spectrogram of magnetic fluctuations measured by Mirnov coil BP14_GHK near the midplane on the low field side. *Bottom*: Central electron temperature measurement in keV.

On Alcator C-Mod, this ∼50 kHz magnetic fluctuation is experimentally observed to be correlated with locked modes; specifically, $\widetilde{B}$ is seen when T_e sawteeth disappear. It is not clear why such a high frequency signal would be measured if the plasma's rotation should be slowing and ultimately stopping. Other experiments have also reported observation of high frequency fluctuations during mode-locking. For instance, in FTU [40], a ∼50 kHz signal has been measured at the same time as an $\mathrm{m/n} = 2/1$ tearing mode, which eventually causes the plasma to lock. In [40], it is assumed that the high-f signal is actually a beta-induced Alfvén Eigenmode (BAE),

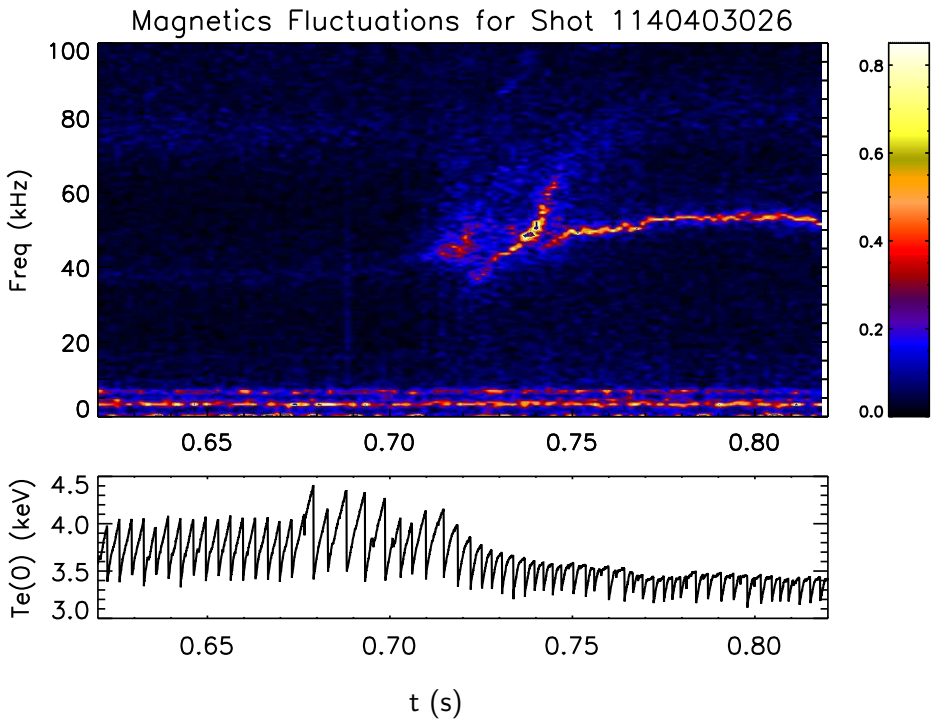

Figure 7.12: The same as figure 7.11, but with the time range limited to $t = 0.62$-0.82 s. Full sawtooth crashes are clearly seen in the T_e signal for $t \lesssim 0.72$ s; they reduce in amplitude (i.e. become partial sawteeth) for $t \gtrsim 0.72$ s.

which has a frequency bounded by [41]

$$f_{\mathrm{BAE}} \leq \frac{1}{2\pi R_0}\sqrt{\frac{2T_\mathrm{i}}{m_\mathrm{i}}\left(\frac{7}{4}+\frac{T_\mathrm{e}}{T_\mathrm{i}}\right)}, \tag{7.10}$$

where R_0 is the major radius, and T_i and m_i are the ion temperature and mass, respectively. For C-Mod, with $R_0 = 0.68$ m and $T_\mathrm{e} \approx 3$ keV, an assumption of $T_\mathrm{i} \approx T_\mathrm{e}$ gives $f_{\mathrm{BAE}} \leq 200$ kHz. Thus, the magnetic fluctuations measured in experiment *could* be BAEs.

In general, it is found that this high-f $\widetilde{B}$ signal is *not* correlated with measurements of runaways on C-Mod; that is, there are many discharges with runaways but without the ~50 kHz $\widetilde{B}$ signal. In J-TEXT, however, BAEs in the range 20-45 kHz were observed during runaway discharges [42]. This study concluded that BAEs could only be excited when *both* an $\mathrm{m/n} = 2/1$ tearing mode and large enough runaway populations were present.

7.2.2 Correlation of magnetic and HXR fluctuations

The spectrogram of figure 7.11 can be studied in more detail to determine whether a correlation exists between observed magnetic fluctuations and runaway dynamics. Here, the hard X-ray (HXR) and photoneutron[d] (n) signals (also shown in figure 7.3f) are used as indicators of runaway confinement loss, as both are produced through bremsstrahlung radiation when runaways impact the first wall. Figure 7.13 shows the same spectrogram as figure 7.11, but with the time and frequency ranges restricted to $t =$ 1.0-1.7 s and $f =$ 40-80 kHz, respectively. Here, it can be seen more clearly that when the $\widetilde{B}$ signal begins at $t \approx$ 1.1 s, the T_{e} sawteeth go away. At the same time, there is a rise in HXR and HXR+n signals that lasts until $t \approx$ 1.35 s. One interpretation of this is that these magnetic fluctuations lead to increased transport of runaways out of the plasma, as discussed in chapter 2, thereby producing HXRs and photoneutrons. Conversely, a population of high energy runaways could also *excite* magnetic fluctuations via kinetic instabilities; then perhaps both the HXR+n and $\widetilde{B}$ signals are just indicators that runaways are present.

One interesting feature of the spectrogram in figure 7.13 is the "oscillation" observed in fluctuation frequency and amplitude. For instance, in the range $t \approx$ 1.1-1.3 s, the peak $\widetilde{B}$ frequency and amplitude (indicated by the colormap) clearly rise and fall. Similarly, an oscillation is seen in the HXR signal at the same time. Estimations of these oscillation frequencies, made by comparing the times between successive maxima, are $f_{\widetilde{B}} \approx$ 53 Hz and $f_{\mathrm{HXR}} \approx$ 56 Hz for the interval $t =$ 1.1-1.2 s. Thus, MHD activity and runaway transport do seem to be correlated during this time range.

Later in time, starting at $t \approx$ 1.5 s, the HXR signals start to increase and oscillate rapidly. It is inferred that runaways are losing confinement in apparent successive bursts. This is likely caused in part by the ramp-down in plasma current as the decreasing poloidal magnetic field is no longer able to confine the highest energy runaways. However, it is not clear what causes these oscillatory "crashes." The Mirnov coils also measure "bursty" fluctuations during this period, indicated by the broadband $\widetilde{B}$ streaks in the spectrogram. Again, measuring the periods of successive peaks in both $\widetilde{B}$ and HXR signals gives approximate frequencies of $f_{\widetilde{B}} \approx$ 210 Hz and $f_{\mathrm{HXR}} \approx$ 222 Hz for $t \approx$ 1.53 s. It is not clear if there is a correlation or anti-correlation; nevertheless, there certainly appears to be a connection between MHD activity and runaway dynamics.

[d] Recall, from chapter 6, that a photoneutron is a neutron ejected from a wall material following an interaction with a runaway-produced gamma ray.

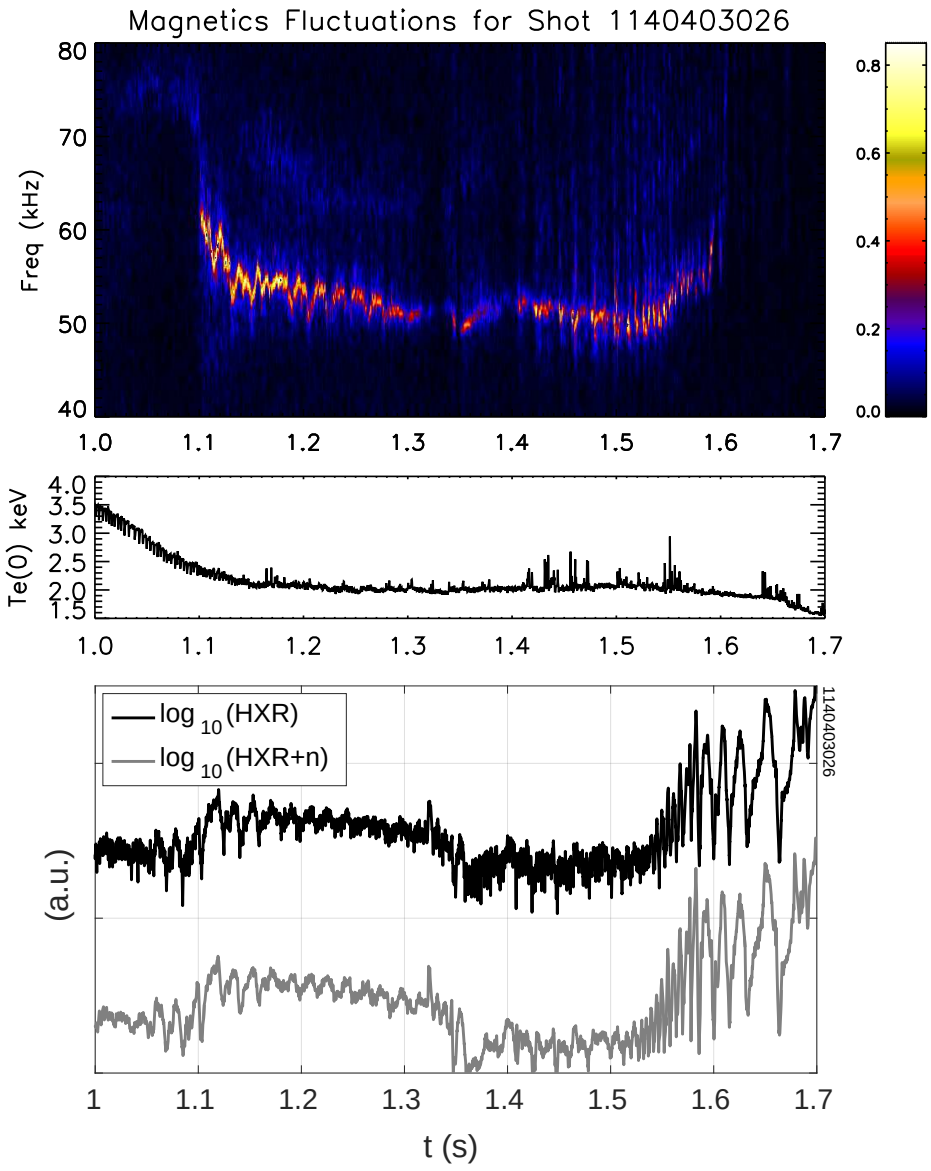

Figure 7.13: Top and middle: Same as figure 7.11, but with time and frequency ranges restricted to $t = 1.0$-1.7 s and $f = 40$-80 kHz, respectively. Bottom: HXR and photoneutron signals (a.u.). The HXR-only signal is offset vertically (shifted upward) compared to the HXR+n signal, in order to show both signals clearly. Otherwise, they almost overlap exactly.

7.3 Aggregate analysis of synchrotron images

The original purpose of these C-Mod runaway experiments, from which images of synchrotron emission were obtained, was to evaluate the critical electric field for runaway generation and suppression. These results are reported in [43] and furthered in chapter 6 for discharges with spectral measurements of synchrotron radiation. However, in those analyses, periods of runaway growth and decay were deduced from HXR signals, not synchrotron emission, since low energy runaways ($\lesssim$ 10 MeV) do not radiate significantly in the visible wavelength range and therefore would not be detected by a visible camera. Here, the analysis of [43] is extended to investigate the plasma conditions under which visible synchrotron emission was or was not observed. Many plasma discharges were reproduced throughout C-Mod experimental run day 1140403[e], varying such parameters as plasma density to produce runaways. In total, 23 discharges provided useful data for this aggregate analysis, which focuses on the flattop I_p phase ($t \approx$ 0.5-1.5 s). Since the camera captures images at ∼60 fps, there are ∼1400 total time-slices, and synchrotron radiation was detected over the background plasma light and HXR speckles during ∼25% of these times. At each time, the following RE-relevant parameters were evaluated:

a. the electric field on-axis, calculated as $E_0 = V_\mathrm{loop}/2\pi R_0$, using the external loop voltage measurement while $I_\mathrm{p} \approx$ constant,
b. the theoretical Connor-Hastie threshold electric field E_C [33] from (2.8),
c. the Dreicer electric field E_D [34, 35] from (2.7),
d. the characteristic synchrotron radiation timescale τ_rad from (2.22), and
e. the runaway collisional timescale τ_coll from (2.23).

In these calculations, the Coloumb logarithm $\ln\Lambda = 15$ was assumed. As described in chapter 2, three ratios of these parameters are (most) important: The first, $E_0/E_\mathrm{C} \propto V_\mathrm{loop}/n$, gives insight into the competition between the driving electric force and collisional friction on runaways. The second, $E_0/E_\mathrm{D} \propto V_\mathrm{loop}\,T/n$, indicates the population of thermal electrons available to accelerate/diffuse into the runaway regime. The third, $\tau_\mathrm{rad}/\tau_\mathrm{coll} \propto n/B^2$, compares the roles of synchrotron radiation damping and collisional drag on runaways.

Histograms in figure 7.14 show the percentage of times during which synchrotron emission was (red) or was not (black) observed, binned for each ratio of interest. Error bars are calculated as $\sqrt{N_\mathrm{bin}}/N_\mathrm{tot}$, where N_bin is the number of counts in each bin, and N_tot is the sum of counts in all bins. When synchrotron emission is observed, the distributions of E_0/E_C and E_0/E_D are shifted toward higher values (see figures 7.14a-b), whereas the distribution of $\tau_\mathrm{rad}/\tau_\mathrm{coll}$ is slightly skewed toward lower values (see figure 7.14c). This matches expectations: higher E_0/E_C and

[e]That means 3 April 2014.

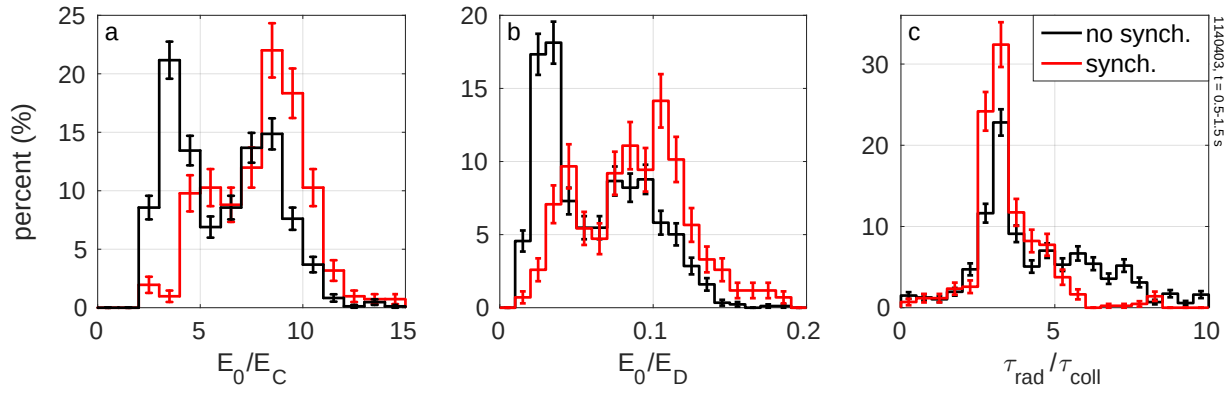

Figure 7.14: Histograms (with statistical error bars) of measured ratios of (a) on-axis to Connor-Hastie threshold electric fields $E_0/E_{\rm C}$ [33], from (2.8); (b) on-axis to Dreicer electric fields $E_0/E_{\rm D}$ [34, 35], from (2.7); and (c) characteristic radiation to collisional timescales $\tau_{\rm rad}/\tau_{\rm coll}$, from (2.24), for flattop data when synchrotron radiation was (red) and was not (black) observed. Note the different vertical axis limits. (t = 0.5-1.5 s)

$E_0/E_{\rm D}$ values lead to higher runaway energies and densities; lower $\tau_{\rm rad}/\tau_{\rm coll}$ values, on the other hand, indicate more power lost—and detected—from synchrotron emission relative to that from collisions.

It is important to note several subtleties associated with this analysis, especially since there is significant overlap in the histograms. First, spatial variation of runaway parameters has been neglected, i.e. only bulk plasma parameters were used. In addition, runaways dynamically evolve in energy and number, so the runaway population at any time is always affected by plasma parameters from earlier times. While time evolution has not been considered here, this analysis of aggregate data, collected at ∼60 Hz, still provides a general physical picture of the conditions under which runaways will or will not produce detectable synchrotron emission at visible wavelengths in C-Mod. Due to the slow variation of plasma parameters during flattop $I_{\rm p}$, multiple data points within the flattop period can help counteract noise and improve statistics. Even then, the energy confinement time is ∼20-30 ms, similar to the time between camera frames, ∼17 ms; therefore, the plasma can evolve and equilibrate on a timescale similar to that used for data collection.

References—Chapter 7

[1] R.A. Tinguely, R.S. Granetz, M. Hoppe, and O. Embréus. Spatiotemporal evolution of runaway electrons from synchrotron images in Alcator C-Mod. *Plasma Physics and Controlled Fusion*, 60(12):124001, 2018.

[2] M. Hoppe, O. Embréus, R.A. Tinguely, R.S. Granetz, A. Stahl, and T. Fülöp. SOFT: a synthetic synchrotron diagnostic for runaway electrons. *Nuclear Fusion*, 58(2):026032, 2018. SOFT can be downloaded at https://github.com/hoppe93/SOFT, with documentation found at https://soft.readthedocs.io.

[3] M. Vlainic, P. Vondracek, J. Mlynar, V. Weinzettl, O. Ficker, M. Varavin, R. Paprok, M. Imrisek, J. Havlicek, R. Panek, J.-M. Noterdaeme, and the COMPASS Team. Synchrotron radiation from runaway electrons in COMPASS tokamak. *42nd European Physical Society Conference on Plasma Physics*, (P4.108), 2015.

[4] C. Paz-Soldan, C.M. Cooper, P. Aleynikov, D.C. Pace, N.W. Eidietis, D.P. Brennan, R.S. Granetz, E.M. Hollmann, C. Liu, A. Lvovskiy, R.A. Moyer, and D. Shiraki. Spatiotemporal evolution of runaway electron momentum distributions in tokamaks. *Physical Review Letters*, 118:255002, 2017.

[5] C. Paz-Soldan, C.M. Cooper, P. Aleynikov, N.W. Eidietis, A. Lvovskiy, D.C. Pace, D.P. Brennan, E.M. Hollmann, C. Liu, R.A. Moyer, and D. Shiraki. Resolving runaway electron distributions in space, time, and energy. *Physics of Plasmas*, 25(5):056105, 2018.

[6] C. Paz-Soldan, N.W. Eidietis, R.S. Granetz, E.M. Hollmann, R.A. Moyer, J.C. Wesley, J. Zhang, M.E. Austin, N.A. Crocker, A. Wingen, and Y. Zhu. Growth and decay of runaway electrons above the critical electric field under quiescent conditions. *Physics of Plasmas*, 21(2):022514, 2014.

[7] M. Hoppe, O. Embréus, C. Paz-Soldan, R.A. Moyer, and T. Fülöp. Interpretation of runaway electron synchrotron and bremsstrahlung images. *Nuclear Fusion*, 58(8):082001, 2018.

[8] E.M. Hollmann, P.B. Parks, N. Commaux, N.W. Eidietis, R.A. Moyer, D. Shiraki, M.E. Austin, C.J. Lasnier, C. Paz-Soldan, and D.L. Rudakov. Measurement of runaway electron energy distribution function during high-Z gas injection into runaway electron plateaus in DIII-D. *Physics of Plasmas*, 22(5):056108, 2015.

[9] J.H. Yu, E.M. Hollmann, N. Commaux, N.W. Eidietis, D.A. Humphreys, A.N. James, T.C. Jernigan, and R.A. Moyer. Visible imaging and spectroscopy of disruption runaway electrons in DIII-D. *Physics of Plasmas*, 20(4):042113, 2013.

[10] R.J. Zhou, L.Q. Hu, E.Z. Li, M. Xu, G.Q. Zhong, L.Q. Xu, S.Y. Lin, J.Z. Zhang, and the EAST Team. Investigation of ring-like runaway electron beams in the EAST tokamak. *Plasma Physics and Controlled Fusion*, 55(5):055006, 2013.

[11] R.J. Zhou, I.M. Pankratov, L.Q. Hu, M. Xu, and J.H. Yang. Synchrotron radiation spectra and synchrotron radiation spot shape of runaway electrons in Experimental Advanced Superconducting Tokamak. *Physics of Plasmas*, 21(6):063302, 2014.

[12] Y. Shi, J. Fu, J. Li, Y. Yang, F. Wang, Y. Li, W. Zhang, B. Wan, and Z. Chen. Observation of runaway electron beams by visible color camera in the Experimental Advanced

Superconducting Tokamak. *Review of Scientific Instruments*, 81(3):033506, 2010.

[13] B. Esposito, L. Boncagni, P. Buratti, D. Carnevale, F. Causa, M. Gospodarczyk, J.R. Martín-Solís, Z. Popovic, M. Agostini, G. Apruzzese, W. Bin, C. Cianfarani, R. De Angelis, G. Granucci, A. Grosso, G. Maddaluno, D. Marocco, V. Piergotti, A. Pensa, S. Podda, G. Pucella, G. Ramogida, G. Rocchi, M. Riva, A. Sibio, C. Sozzi, B. Tilia, O. Tudisco, M. Valisa, and FTU Team. Runaway electron generation and control. *Plasma Physics and Controlled Fusion*, 59(1):014044, 2017.

[14] Y.P. Zhang, Y. Liu, G.L. Yuan, M. Isobe, Z.Y. Chen, J. Cheng, X.Q. Ji, X.M. Song, J.W. Yang, X.Y. Song, X. Li, W. Deng, Y.G. Li, Y. Xu, T.F. Sun, X.T. Ding, L.W. Yan, Q.W. Yang, X.R. Duan, and Y. Liu. Observation of the generation and evolution of long-lived runaway electron beams during major disruptions in the HuanLiuqi-2A tokamak. *Physics of Plasmas*, 19(3):032510, 2012.

[15] Z.Y. Chen, B.N. Wan, S.Y. Lin, Y.J. Shi, L.Q. Hu, X.Z. Gong, H. Lin, and M. Asif. Measurement of the runaway electrons in the HT-7 tokamak. *Review of Scientific Instruments*, 77(1):013502, 2006.

[16] R.H. Tong, Z.Y. Chen, M. Zhang, D.W. Huang, W. Yan, and G. Zhuang. Observation of runaway electrons by infrared camera in J-TEXT. *Review of Scientific Instruments*, 87(11):11E113, 2016.

[17] A.C. England, Z.Y. Chen, D.C. Seo, J. Chung, Y.S. Leev, J.W. Yoo, W.C. Kim, Y.S. Bae, Y.M. Jeonv, J.G. Kwak, M. Kwon, and the KSTAR Team. Runaway electron suppression by ECRH and RMP in KSTAR. *Plasma Science and Technology*, 15(2):119, 2013.

[18] S.A. Bozhenkov, M. Lehnen, K.H. Finken, M.W. Jakubowski, R.C. Wolf, R. Jaspers, M. Kantor, O.V. Marchuk, E. Uzgel, G. Van Wassenhove, O. Zimmermann, D. Reiter, and the TEXTOR team. Generation and suppression of runaway electrons in disruption mitigation experiments in TEXTOR. *Plasma Physics and Controlled Fusion*, 50(10):105007, 2008.

[19] K. Wongrach, K.H. Finken, S.S. Abdullaev, R. Koslowski, O. Willi, L. Zeng, and the TEXTOR Team. Measurement of synchrotron radiation from runaway electrons during the TEXTOR tokamak disruptions. *Nuclear Fusion*, 54(4):043011, 2014.

[20] K. Wongrach, K.H. Finken, S.S. Abdullaev, O. Willi, L. Zeng, Y. Xu, and the TEXTOR Team. Runaway electron studies in TEXTOR. *Nuclear Fusion*, 55(5):053008, 2015.

[21] I. Entrop, N.J. Lopes Cardozo, R. Jaspers, and K.H. Finken. Scale size of magnetic turbulence in tokamaks probed with 30-MeV electrons. *Physical Review Letters*, 84:3606–3609, 2000.

[22] I. Entrop, N.J. Lopes Cardozo, R. Jaspers, and K.H. Finken. Diffusion of runaway electrons in TEXTOR-94. *Plasma Physics and Controlled Fusion*, 40(8):1513, 1998.

[23] T. Kudyakov, S.S. Abdullaev, S.A. Bozhenkov, K.H. Finken, M.W. Jakubowski, M. Lehnen, G. Sewell, O. Willi, Y. Xu, and the TEXTOR team. Influence of B_t on the magnetic turbulence and on the runaway transport in low-density discharges. *Nuclear Fusion*, 52(2):023025, 2012.

[24] K.H. Finken, J.G. Watkins, D. Rusbüldt, W.J. Corbett, K.H. Dippel, D.M. Goebel, and R.A. Moyer. Observation of infrared synchrotron radiation from tokamak runaway electrons in TEXTOR. *Nuclear Fusion*, 30(5):859, 1990.

[25] R. Jaspers, N.J. Lopes Cardozo, K.H. Finken, B.C. Schokker, G. Mank, G. Fuchs, and F.C. Schüller. Islands of runaway electrons in the TEXTOR tokamak and relation to transport in a stochastic field. *Physical Review Letters*, 72:4093–4096, 1994.

[26] I. Entrop, R. Jaspers, N.J. Lopes Cardozo, and K.H. Finken. Runaway snakes in TEXTOR-94. *Plasma Physics and Controlled Fusion*, 41(3):377, 1999.

[27] L.L. Lao, H. St. John, R.D. Stambaugh, A.G. Kellman, and W. Pfeiffer. Reconstruction of current profile parameters and plasma shapes in tokamaks. *Nuclear Fusion*, 25(11):1611, 1985.

[28] L. Carbajal and D. del Castillo-Negrete. On the synchrotron emission in kinetic simulations of runaway electrons in magnetic confinement fusion plasmas. *Plasma Physics and Controlled Fusion*, 59(12):124001, 2017.

[29] L. Carbajal, D. del Castillo-Negrete, D. Spong, S. Seal, and L. Baylor. Space dependent, full orbit effects on runaway electron dynamics in tokamak plasmas. *Physics of Plasmas*, 24(4):042512, 2017.

[30] M. Landreman, A. Stahl, and T. Fülöp. Numerical calculation of the runaway electron distribution function and associated synchrotron emission. *Computer Physics Communications*, 185(3):847 – 855, 2014.

[31] A. Stahl, O. Embréus, G. Papp, M. Landreman, and T. Fülöp. Kinetic modelling of runaway electrons in dynamic scenarios. *Nuclear Fusion*, 56(11):112009, 2016.

[32] S.C. Chiu, M.N. Rosenbluth, R.W. Harvey, and V.S. Chan. Fokker-Planck simulations mylb of knock-on electron runaway avalanche and bursts in tokamaks. *Nuclear Fusion*, 38(11):1711, 1998.

[33] J.W. Connor and R.J. Hastie. Relativistic limitations on runaway electrons. *Nuclear Fusion*, 15(3):415, 1975.

[34] H. Dreicer. Electron and ion runaway in a fully ionized gas. I. *Physical Review*, 115:238–249, 1959.

[35] H. Dreicer. Electron and ion runaway in a fully ionized gas. II. *Physical Review*, 117:329–342, 1960.

[36] R.A. Tinguely, R.S. Granetz, M. Hoppe, and O. Embréus. Measurements of runaway electron synchrotron spectra at high magnetic fields in Alcator C-Mod. *Nuclear Fusion*, 58(7):076019, 2018.

[37] I. Sobel and G. Feldman. A 3×3 isotropic gradient operator for image processing, 1968. Presented at the Stanford Artificial Intelligence Project.

[38] J.R. Martín-Solís, J.D. Alvarez, R. Sánchez, and B. Esposito. Momentum-space structure of relativistic runaway electrons. *Physics of Plasmas*, 5(6):2370–2377, 1998.

[39] C. Liu, L. Shi, E. Hirvijoki, D.P. Brennan, A. Bhattacharjee, C. Paz-Soldan, and M.E. Austin. The effects of kinetic instabilities on the electron cyclotron emission from runaway electrons. *Nuclear Fusion*, 58(9):096030, jul 2018.

[40] B. Angelini, S.V. Annibaldi, M.L. Apicella, G. Apruzzese, E. Barbato, A. Bertocchi, F. Bombarda, C. Bourdelle, A. Bruschi, P. Buratti, G. Calabrò, A. Cardinali, L. Carraro, C. Castaldo, C. Centioli, R. Cesario, S. Cirant, V. Cocilovo, F. Crisanti, R. De Angelis, M. De Benedetti, F. De Marco, B. Esposito, D. Frigione, L. Gabellieri, F. Gandini, L. Garzotti, E. Giovannozzi,

C. Gormezano, F. Gravanti, G. Granucci, G.T. Hoang, F. Iannone, H. Kroegler, E. Lazzaro, M. Leigheb, G. Maddaluno, G. Maffia, M. Marinucci, D. Marocco, J.R. Martin-Solis, F. Martini, M. Mattioli, G. Mazzitelli, C. Mazzotta, F. Mirizzi, G. Monari, S. Nowak, F. Orsitto, D. Pacella, L. Panaccione, M. Panella, P. Papitto, V. Pericoli-Ridolfini, L. Pieroni, S. Podda, M.E. Puiatti, G. Ravera, G. Regnoli, G.B. Righetti, F. Romanelli, M. Romanelli, F. Santini, M. Sassi, A. Saviliev, P. Scarin, A. Simonetto, P. Smeulders, E. Sternini, C. Sozzi, N. Tartoni, D. Terranova, B. Tilia, A.A. Tuccillo, O. Tudisco, M. Valisa, V. Vershkov, V. Vitale, G. Vlad, and F. Zonca. Overview of the FTU results. *Nuclear Fusion*, 45(10):S227, 2005.

[41] F. Zonca, L. Chen, and R.A. Santoro. Kinetic theory of low-frequency Alfvén modes in tokamaks. *Plasma Physics and Controlled Fusion*, 38(11):2011, 1996.

[42] L. Liu, J. He, Q. Hu, and G. Zhuang. Observation of beta-induced Alfvén eigenmode in J-TEXT tokamak. *Plasma Physics and Controlled Fusion*, 57(6):065007, 2015.

[43] R.S. Granetz, B. Esposito, J.H. Kim, R. Koslowski, M. Lehnen, J.R. Martín-Solís, C. Paz-Soldan, T. Rhee, J.C. Wesley, L. Zeng, and ITPA MHD Group. An ITPA joint experiment to study runaway electron generation and suppression. *Physics of Plasmas*, 21(7):072506, 2014.

This page intentionally left blank

Chapter 8

Analysis of polarized synchrotron radiation

As discussed in chapter 3, the classical polarization of electromagnetic radiation emitted by a charged particle is known to be mostly parallel to the particle's acceleration, or instantaneous radius of curvature in the case of gyro-motion. The derivation of the polarization of *synchrotron* radiation, presented in chapter 3, followed Westfold's 1959 calculation [1], which was originally motivated by experimental observations of highly polarized light coming from the Crab Nebula [2, 3]. The most promising hypothesis at the time [4] suggested that ultra-relativistic electrons moving in a magnetic field were the source of this polarized light emitted from astrophysical plasmas.

This chapter describes the first analysis of experimentally-measured polarized synchrotron radiation from runaway electrons in *tokamak plasmas*; the resulting work has been submitted for publication in *Nuclear Fusion* [5]. The first theoretical analyses of polarization properties and synthetic measurements of synchrotron radiation in a tokamak were performed by Sobolev [6], who suggested that polarization information could be used to diagnose runaway beams. As will be discussed, polarization measurements of synchrotron emission can provide insight into the distribution of runaway pitch angles θ_p. Thus, synchrotron polarization can help better constrain kinetic models of runaway evolution and investigate mechanisms of pitch angle scattering, such as wave-particle instabilities [7, 8] and interactions with injected high-Z ions [9, 10]. Ultimately, understanding these runaway dynamics and power loss mechanisms—such as radiated synchrotron power which increases with pitch angle, $P_\mathrm{synch} \propto \sin^2\theta_\mathrm{p}$—can inform runaway avoidance and mitigation strategies for future devices like ITER [11] and SPARC [12].

The outline of the rest of the chapter is as follows: Section 8.1 discusses experimental measurements of polarized synchrotron emission made using the Motional Stark Effect diagnostic, shown schematically in figures 8.1 and 8.2 and detailed in chapter 4. A heuristic model of polarized synchrotron radiation is presented in section 8.2, and SOFT is used to interrogate the phase space distribution of runaways in section 8.3. Then, synthetic and experimental polarization measurements from one discharge are compared in section 8.4. The analyses of sections 8.1-8.3 only consider data from times when lower hybrid current drive (LHCD) is disengaged; section 8.5, however, expands on these to investigate the effect of LHCD on synchrotron polarization measurements. Finally, in section 8.6, we explore the use of polarized synchrotron light as a diagnostic of the runaway current density profile.

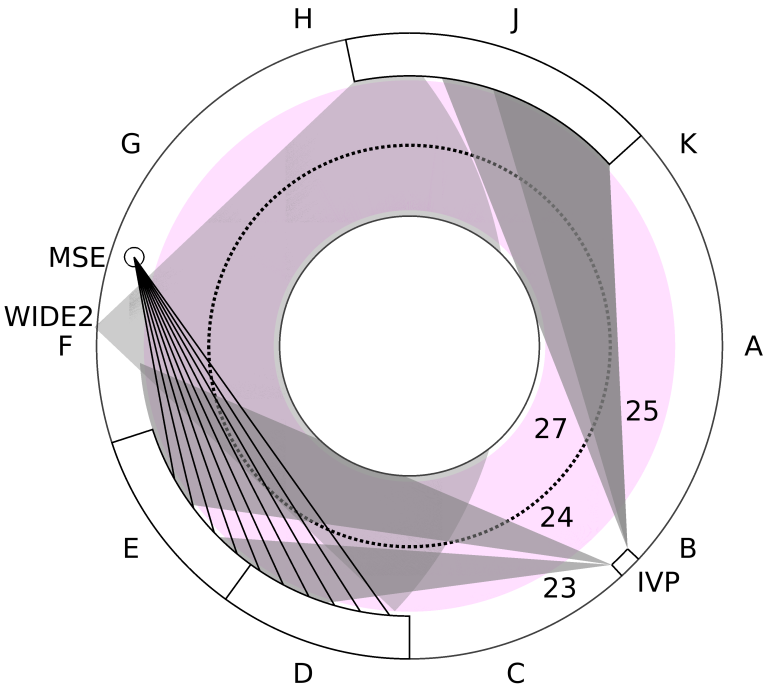

Figure 8.1: A top-down schematic of the tokamak midplane. The plasma is pink, with the major radius of the magnetic axis dotted. The MSE diagnostic has ten CCW views; here, only the lines-of-sight are shown. This figure is the same as figure 4.1. Refer to figure 8.2 for the full fields-of-view.

8.1 Measurements of polarized synchrotron emission from runaway electrons

For these polarization analyses, runaways were purposefully generated during the flattop plasma current of low-density, Ohmic, elongated and diverted discharges in C-Mod. Time traces of one sample discharge, explored in further detail in section 8.4, are shown in figure 8.9a. Note that this is the *same* discharge as that studied in chapter 7. It is convenient that we acquired both images and polarization information of the synchrotron radiation produced during that discharge. We will use the runaway density profile, inferred from images in chapter 7, later in this section. In addition, the analysis was simplified since the CODE simulations could be re-used.

As discussed in chapter 4, polarization information of synchrotron radiation is gathered by the ten-channel Motional Stark Effect (MSE) diagnostic [13] which accepts light within a narrow wavelength band, $\Delta\lambda \approx 0.8$ nm, centered at $\lambda \approx 660$ nm in the visible range. During routine tokamak operation, the MSE system serves a completely separate diagnostic purpose, measuring a different source of polarized light: line radiation resulting from electron transitions between Stark-shifted atomic (hydrogen) energy levels. This measurement requires neutral atoms within an injected diagnostic neutral hydrogen beam (DNB). The field-of-view (FOV) of each MSE channel is small (see figure 8.2), with a total opening angle of $2\alpha \approx 1.7°$; this means that each channel's measurement of emission from the DNB is radially-localized. The polarization angle $\theta_{\rm pol}$[a] of the detected isotropic emission indicates the pitch of the local magnetic field $\tan\theta_B = B_{\rm p}/B_{\rm t}$, where $B_{\rm p}$ and $B_{\rm t}$ are the local poloidal and toroidal fields, respectively. The DNB was not in use during any of the runaway experiments reported in this chapter; therefore, the detected signal was dominated by synchrotron emission. In addition, the only times considered in this section are those when LHCD was disengaged. Data from times when LHCD was in use are explored in section 8.5.

A top-down schematic of the MSE diagnostic and its ten fields-of-view is depicted in figures 8.1 and 8.2. (Refer back to tables 4.5 and 4.6 for a list of detector and geometric specifications.) Although each channel makes a volume-integrated measurement within its FOV, the tangency major radius, or impact parameter $R_{\rm tan}$, is used to identify the major radius at which each line-of-sight (LOS) is orthogonal to the local major radial vector $\hat{R}$. The tangency *minor* radius is then defined as $r_{\rm tan} = R_{\rm tan} - R_0$ and falls in the range $r_{\rm tan} \in [-a, a]$. See figure 8.3a for the values of the *normalized* tangency radius $r_{\rm tan}/a$ of each channel and figure 8.4a for an illustration. When runaway pitch angles $\theta_{\rm p}$ are smaller than the local magnetic pitch angle θ_B (discussed further in section 8.2), it is expected that most detected synchrotron emission will come from runaways

[a] Not to be confused with the *poloidal* angle.

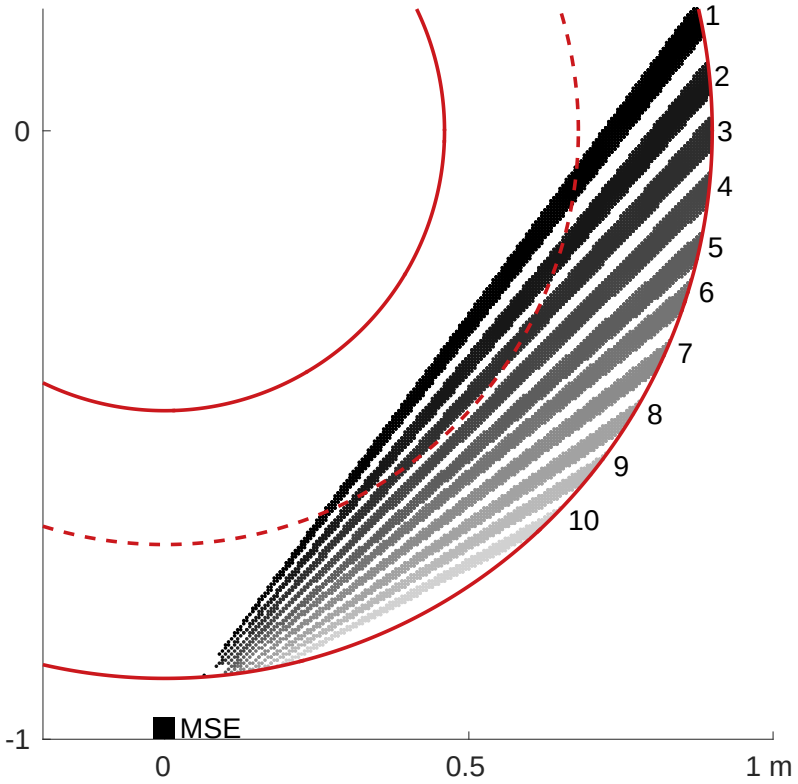

Figure 8.2: A top-down schematic of the ten-channel MSE diagnostic (black box) and its ten fields-of-view. The plasma boundary (solid) and magnetic axis (dotted) are overlaid. This is the same figure as figure 4.11b. Compare to figure 8.1.

located near $R_{\tan}$. Note also that the MSE diagnostic is situated slightly above the midplane; therefore, all channels have a small downward-viewing orientation, i.e. an inclination $\delta \approx$ -3°, to intersect the midplane trajectory of the DNB.

The MSE system measures a spatial profile of synchrotron polarization information. Each channel records the total intensity of detected light I, intensity of linearly-polarized light L, and linear polarization angle $\theta_{\rm pol}$. Because the absolute value of sensitivity varies between channels, it is most useful to consider the *degree* of linear polarization, or rather the *fraction* of detected light that is linearly-polarized: $\mathrm{f}_{\rm pol} = L/I \in$ [0,1]. These polarization fraction measurements are calibrated, with estimated uncertainties of ∼10%. The polarization angle measurement has a lower uncertainty, less than a degree. Experimental measurements of $\theta_{\rm pol}$ and $\mathrm{f}_{\rm pol}$, and their comparisons with synthetic models, will be the focus of this chapter, although qualitative trends of L will be explored for one discharge in section 8.4.

In total, polarization data of runaway synchrotron emission were collected from 28 plasma discharges at over one-thousand time points. Plasma parameters for these discharges span line-averaged electron densities $\bar{n}_e \approx$ 0.2-1.0 $\times$ 10^{20} m^{-3}, central electron temperatures $T_{e0} \approx$ 1-5 keV, plasma currents $I_p \approx$ 0.4-1.0 kA, and on-axis magnetic field strengths $B_0 \approx$ 2-6 T. Ranges of RE-relevant parameters include the ratios of the electric to critical field [14] from (2.8), $E/E_C \approx$ 3-15, and collisional to synchrotron radiation timescales, from (2.24), $\tau_{coll}/\tau_{rad} > 0.1$. As discussed in chapter 2, these indicate the relative strengths of the electric force and radiation damping to collisional friction, respectively.

Histograms of measured θ_{pol} and f_{pol} are shown in figures 8.3a and 8.3b, respectively. The distributions of θ_{pol} are well-localized for most channels, and an interesting spatial trend is observed: At the innermost radius (channel 1, $r_{tan}/a =$ -0.4), a polarization angle measurement of $\theta_{pol} \approx 0°$ indicates *horizontally*-polarized synchrotron light.[b] For channels 2-5 ($|r_{tan}/a| \leq 0.23$, near the plasma center), measurements of $\theta_{pol} \approx 90°$ indicate *vertical* polarization of the detected synchrotron radiation. Beyond $r_{tan}/a \geq 0.35$ (channels 6-9), the polarization angle flips back to $\theta_{pol} \approx 0°$. The outermost radius (channel 10, $r_{tan}/a = 0.83$) shows a more evenly-distributed range of measured θ_{pol}, possibly due to a lack of (synchrotron-emitting) runaways at the plasma edge. This 90° transition in space was predicted by Sobolev [6] and is explained more intuitively in the next section, section 8.2. Also, note that only a range of $\theta_{pol} \in$ [-45°, 135°) is considered because there is a 180° degeneracy in θ_{pol}.

Compared to θ_{pol}, experimental measurements of f_{pol} do not exhibit as clear a spatial trend. Still, there are some features to note in figure 8.3b: A peak in f_{pol} ($\sim$0.6) is often observed on channel 4 which has a FOV near the magnetic axis ($r_{tan}/a = 0.08$). There are also instances of $f_{pol} \approx$ 0.6-0.7 near the plasma edge (channels 9-10, $r_{tan}/a \geq 0.73$), but these may not always be dominated by synchrotron light. Interestingly, values of $f_{pol} \geq 0.7$ are not seen. One plausible explanation for this is that light from the plasma and/or reflections from C-Mod's metal wall are contributing to the fraction of emission which is *not* linearly polarized. While this could mean that up to 30% of the detected light is not synchrotron emission, the good agreement seen in the comparisons of synthetic and experimental θ_{pol} signals—discussed in section 8.4—indicates that any extra light is likely mostly unpolarized. If the background light is instead negligible compared to synchrotron radiation, this would imply that the polarization fraction of the observed synchrotron emission is truly $f_{pol} \leq 0.7$, which is achievable according to the analysis in section 8.4.

[b] Recall that this convention of measuring θ_{pol} upward from the midplane is *opposite* that normally used for MSE measurements on C-Mod, where θ_{pol} is instead measured downward from the vertical axis.

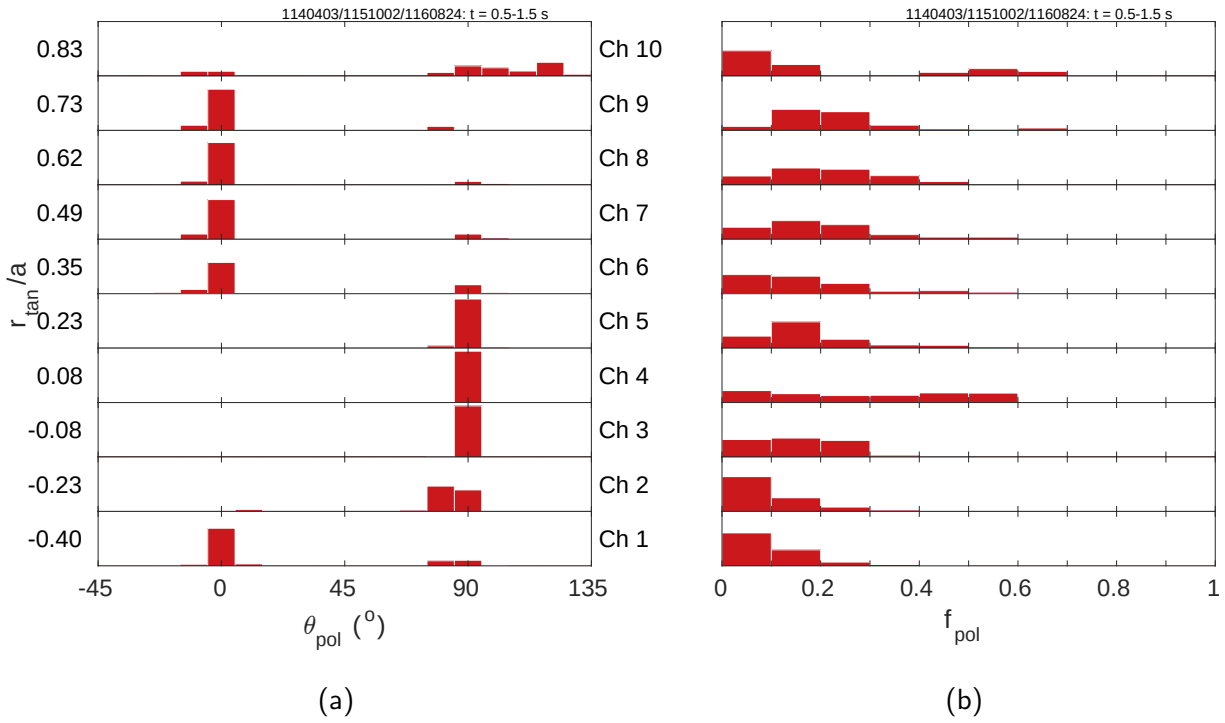

(a) (b)

Figure 8.3: Histograms of polarization (a) angle $\theta_{\rm pol}$ and (b) fraction $\rm f_{pol}$ for each channel, denoted by the normalized tangency radius $r_{\rm tan}/a$. Bin widths are $\Delta\theta_{\rm pol} = 10^\circ$ and $\Delta \rm f_{pol} = 0.1$. For each channel, the vertical axis spans 0 to 1, and all bar heights (probabilities) sum to 1. Data are from 28 discharges and over 1000 time-slices during the plasma current flattop (t = 0.5-1.5 s).

Furthermore, note in figure 8.3b that the *mean* $\rm f_{pol}$ values of channels 7-9 ($r_{\rm tan}/a \in$ [0.49, 0.73]) are higher than the those for channels 6 and 10 ($r_{\rm tan}/a$ = 0.35 and 0.83). This spatial "bump" of mean $\rm f_{pol}$ values for $r_{\rm tan}/a \in$ [0.23, 0.83] (channels 5-10) means there is usually a local minimum in $\rm f_{pol}$ around $r_{\rm tan}/a \approx$ 0.23-0.35. This is a slightly non-intuitive result since we might expect the intensity of (linearly-polarized) light to increase from the plasma edge to the center.

8.2 A heuristic "cone" model of polarized synchrotron light

In the guiding-center picture (schematically represented in figures 8.4a and 8.4b), a runaway electron travels *anti-parallel*[c] to $\boldsymbol{B}$, emitting a "cone" of synchrotron radiation in its forward direction with an opening half-angle equal to the runaway pitch angle $\theta_{\rm p}$. Once again, the pitch angle is defined by $\tan\theta_{\rm p} = v_\perp/v_\parallel$, where $v_\parallel$ and $v_\perp$ are the components of the runaway velocity $\boldsymbol{v}$ parallel and perpendicular to $-\boldsymbol{B}$, respectively. Of course, this synchrotron radiation is only *observed* if the cone (or, equivalently, $\boldsymbol{v}$) is directed within a detector's FOV toward the detector's aperture.

On the plasma midplane, the pitch of $\boldsymbol{B}$ is simply given by $\tan\theta_B = B_{\rm p}/B_{\rm t}$. In tokamaks, $B_{\rm t}$ is sufficiently larger than $B_{\rm p}$ (typically $B_{\rm t}/B_{\rm p} \approx 10$), so that $\boldsymbol{B}$ is approximately horizontal. In fact, for realistic safety factor profiles—e.g. $q(0) \approx 1$ and $q_{95} > 3$—the magnetic field pitch angle is $|\theta_B| \leq 0.2$ rad. Therefore, in order for a detector to measure *horizontally*-polarized synchrotron emission (i.e. $\theta_{\rm pol} \approx 0°$), it must view the "top" or "bottom" of the emission cone. That is, $\boldsymbol{v}$ should lie in the *vertical* plane so that $\boldsymbol{E}$ is horizontal, since $\boldsymbol{E}$ is approximately proportional to the Lorentz acceleration $\boldsymbol{v}\times\boldsymbol{B}$. Conversely, to observe *vertically*-polarized light (i.e. $\theta_{\rm pol} \approx 90°$), a detector should view the "sides" of the synchrotron cone, when $\boldsymbol{v}$ lies in the *horizontal* plane. As an aside, note here that synchrotron light directed along the side(s) of the emission cone is actually radiated by a runaway electron located at the top/bottom of its gyro-orbit, and vice versa. This reality is often forgotten when neglecting gyro-motion in the guiding center picture.

The clear spatial trends in the data of figures 8.3a and 8.3b—$\theta_{\rm pol}$, in particular—indicate a strong dependence of the experimental measurements on geometry. To give the reader a better intuition for *why* a 90° transition is observed across the plasma, consider a detector situated on the midplane with a tangency radius $R_{\rm tan} < R_0$, inclination $\delta < 0$, and opening half-angle $\alpha \ll 1$. Imagine a midplane cross-section of the plasma and detector view, as shown in figure 8.4a. For $\boldsymbol{B}$ and $I_{\rm p}$ in the CCW direction (as viewed downward from above), runaways will travel in the CW direction, and the poloidal magnetic field will point upward (out of the page) for $R_{\rm tan} < R_0$. In this simplistic model, the detector will receive synchrotron light from runaways at all $R \geq R_{\rm tan}$, with the observable $\theta_{\rm p}$ increasing as R increases. For small α and δ, radiation from runaways with $\theta_{\rm p} > \theta_B$ (corresponding to runaways at $R > R_{\rm tan}$) will be primarily *vertically*-polarized. That is, the velocity $\boldsymbol{v}$ of these runaways must lie approximately in the midplane for light to reach the detector, and only the "sides" of the cone can be observed.

[c] In Alcator C-Mod, the plasma current and toroidal magnetic field are usually *parallel*, so that a strong electric field drives runaways in the direction *anti-parallel* to $\boldsymbol{B}$.

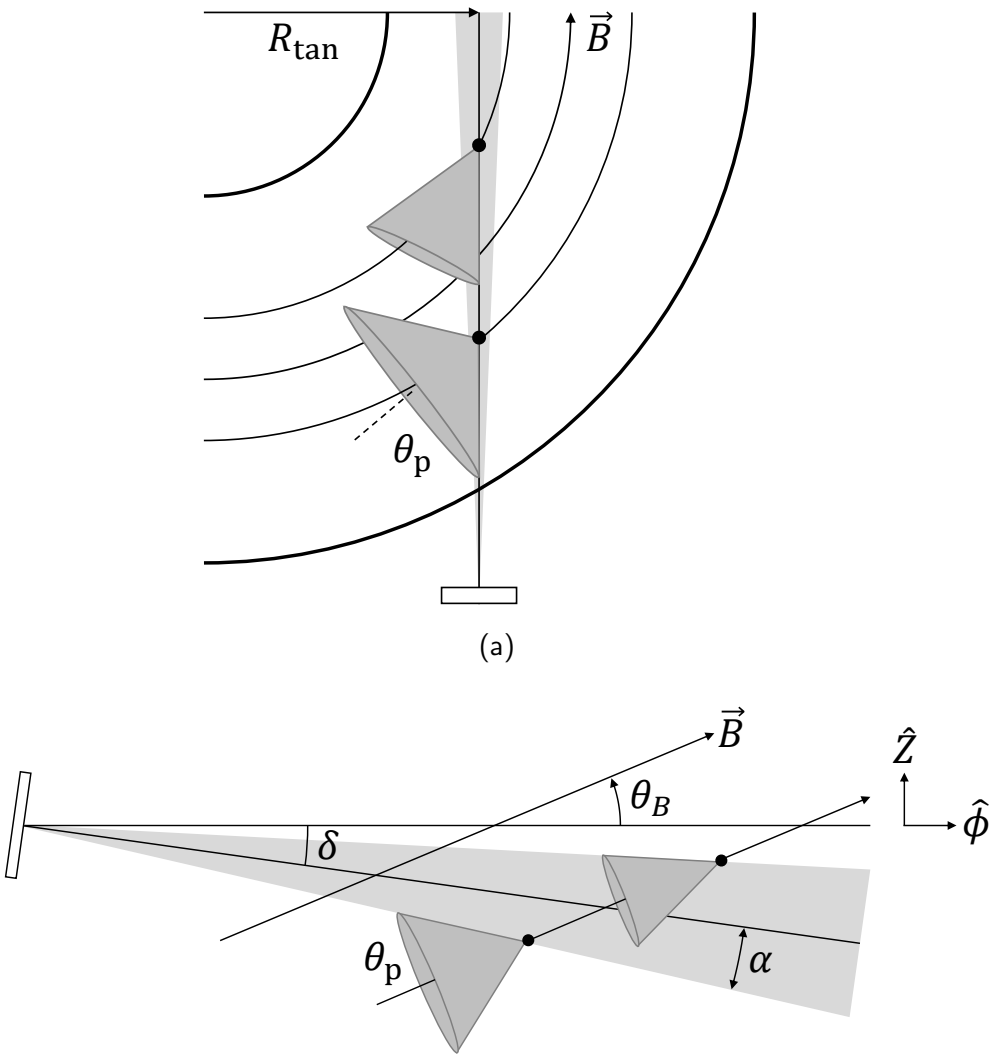

Figure 8.4: (a) A horizontal cross-section: A detector (bottom), with line-of-sight tangency radius $R_{\tan}$, views two runaways (black dots) moving in approximately circular orbits with different pitch angles $\theta_{\rm p}$ at two radii. (b) A vertical cross-section: A detector (left), with inclination $\delta < 0$ and opening half-angle $\alpha > 0$, views runaways with pitch angles $\theta_{\rm p,min} = |\theta_B - \delta| - \alpha$ (upper) and $\theta_{\rm p,max} = |\theta_B - \delta| + \alpha$ (lower) in a magnetic field $\boldsymbol{B}$ with local pitch $\tan\theta_B > 0$. The vertical axis is $\hat{Z}$, and *local* toroidal vector is $\hat{\phi}$. (Not to-scale.)

However, for runaways located close to $R_{\tan}$ with $\theta_{\rm p} \approx \theta_B$, the local magnetic field pitch must be taken into account. A vertical cross-section near $R_{\tan}$ is shown in figure 8.4b. The range of runaway pitch angles for which the detector will measure synchrotron light is bounded by $\theta_{\rm p,min} \leq \theta_{\rm p} \leq \theta_{\rm p,max}$, where

$$\theta_{\rm p,min}^{\rm p,max} = \max\left(|\theta_B - \delta| \pm \alpha,\, 0\right). \tag{8.1}$$

Here, the superscript and subscript correspond to the $\pm$ sign. Both θ_B and δ are measured positively CCW from $\hat{\phi}$ toward $\hat{Z}$ (see figure 8.4b), and both $\alpha \geq 0$ and $\theta_{\rm p} \geq 0$ are assumed non-negative. Since α and δ are small, we assume that θ_B varies little over the finite radial and vertical extent of the detector's FOV. Thus, we expect that *horizontally*-polarized light is *only* measurable for $\theta_{\rm p} \in [\theta_{\rm p,min}, \theta_{\rm p,max}]$. This implies that the 90° transition in $\theta_{\rm pol}$ measurements (horizontal to vertical) should be observed as a runaway's pitch angle increases past the threshold $\theta_{\rm p} \approx \theta_{\rm p,max}$. Additionally, for runaways with $\theta_{\rm p} \approx \theta_{\rm p,max}$, we hypothesize that a mix of light with many polarizations will lead to low values of $\rm f_{pol}$ since the total radiation from many particles will be effectively unpolarized. Finally, we expect that a detector should see almost no synchrotron radiation from runaways with pitch angles $\theta_{\rm p} < \theta_{\rm p,min}$ simply because they are not emitting light into the detector's FOV.

The radial profile of $\theta_{\rm p} \in [\theta_{\rm p,min}, \theta_{\rm p,max}]$ for a sample magnetic geometry from EFIT is shown as the bounded region in figure 8.7a; these are the pitch angles within which a measurement of $\theta_{\rm pol} \approx 0°$ is expected. As will be discussed further in section 8.3, this simple model shows good agreement when compared to synthetic data from SOFT. Notably, measurements of $\theta_{\rm pol} \approx 90°$ are more probable close to the magnetic axis where θ_B is small, and the minimum runaway pitch angle at which synchrotron emission is detected increases with increasing $r_{\tan}/a$.

It is important to note that these and following calculations require knowledge of the magnetic field geometry. For runaway populations carrying a significant fraction of the plasma current, like runaway plateaus after disruptions in some tokamaks [15–17], the interpretation of synchrotron polarization data, specifically, would become more difficult and convoluted. The challenges and opportunities associated with this will be discussed further in section 8.6. However, in C-Mod, almost no variation in the externally-applied loop voltage is observed during flattop runaway discharges as synchrotron emission increases in time; therefore, the runaway current is inferred to be negligible compared to the total plasma current, and a magnetic reconstruction, like EFIT, is considered to be an accurate approximation of the real magnetic topology.

8.3 Probing phase space with SOFT

Similar to the analysis of synchrotron images in chapter 7, we utilize SOFT's calculation of Green's functions for the analysis of polarized synchrotron emission. Recall that these Green's functions are essentially *detector response functions* which, when integrated with a runaway phase space distribution, give the expected synthetic signal. These response functions account for the detector geometry and spectral range, as well as the magnetic field. (Refer to chapter 5 for a description of SOFT and to appendix B for details of the modeling and implementation of polarized synchrotron radiation in SOFT.) Here, the Green's functions are calculated for the Stokes parameters—see chapters 3 and 5—from which our quantities of interest L, θ_{pol}, and $\mathrm{f}_{\mathrm{pol}}$ can be computed.

Unlike the Green's functions $\hat{G}_{ij}(R)$ used to invert the runaway density profile from synchrotron images in chapter 7, the Green's functions used here are functions of position *and* momentum space, i.e. $\hat{G}(R, p, \theta_{\mathrm{p}})$. The functional dependencies of $\hat{G}$ on radius R, total momentum p, and pitch angle θ_{p} allow us to better constrain the runaway population in position and momentum space when comparing synthetic and experimental measurements. In other words, they allow us isolate the contribution of an individual electron, with initial position R, momentum p, and pitch angle θ_{p}, to the final polarization measurement. In the end, we will be most interested in the θ_{p}-dependency of $\hat{G}$.

For this analysis, a response function was computed for each channel (and each time of interest) using parameters in tables 4.5 and 4.6, magnetic geometries from EFIT, and a phase space spanning $r/a \in$ [0, 1], $p/mc \in$ [0, 100] (i.e. energies extending up to approximately 50 MeV), and $\theta_{\mathrm{p}} \in$ [0, 0.3] rad. Note that the *size* of each SOFT Green's function (matrix) grows with added dimensions, increased resolution, and the number of quantities of interest (4 for Stokes parameters). Nevertheless, these were computationally-feasible for the MSE system and this analysis because each LOS is represented by only *one* pixel, whereas a camera image often has over 10^4 pixels.

Figure 8.5 shows the intensity $\langle \hat{I} \rangle$ of light *detected* by each channel (and averaged over momentum space) versus radius for runaways populated across the entire plasma. Note how each channel's measurements are radially-localized, as expected, approximately at the appropriate $r_{\tan}/a$, indicated as a black vertical line for each channel. Recall that in SOFT, runaways are "initiated" on the outer midplane ($R \geq R_0$) and then follow magnetic field lines. Therefore, while some channels only "see" runaways on the high field side ($R < R_0$), the Green's function records their starting positions on the low field side. This is the case for channels 1-3 (see figure 8.2), so their SOFT-measured synthetic intensities have been mirrored over the magnetic axis in figure 8.5, shown in grey. There is significant overlap in radial distributions of detected intensity between adjacent channels, and some pairs of channels even view almost the same

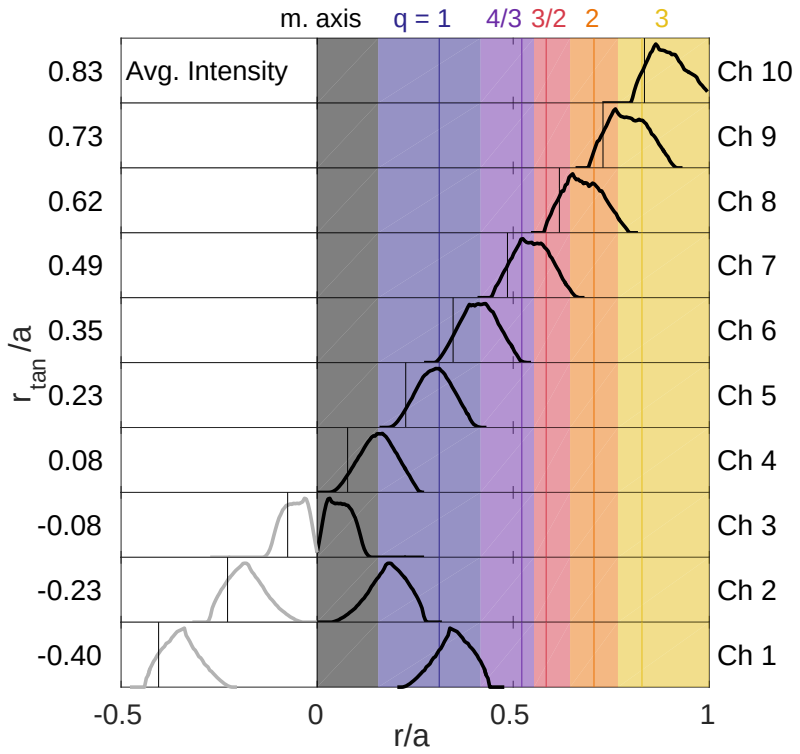

Figure 8.5: Synthetic intensity measurements of each MSE channel modeled in SOFT, averaged with a uniform distribution over momentum space, as a function of normalized minor radius (i.e. initial runaway position). The experimentally-determined normalized tangency radius is indicated by a vertical black line for each channel (labeled at left). Note that channels 1-3 have data reflected over $r/a = 0$ (in grey). The locations of the magnetic axis and flux surfaces with $q = 1$, 4/3, 3/2, 2, and 3 are shown as solid vertical lines; shaded regions, extending halfway between adjacent surfaces, are used in step (iii) of the methodology of section 8.4.

radial band of runaways. For instance, channels 1 and 2 are sensitive to the same runaways as channels 5 and 4, respectively. Thus, an opportunity exists to interrogate different parts of the *same* runaway phase space distribution by comparing data among multiple channels.

Sample response functions of $\hat{\theta}_{\mathrm{pol}}$ and $\hat{\mathrm{f}}_{\mathrm{pol}}$ are plotted over momentum space for channel 2 (r_{tan}/a = -0.23) in figures 8.6a and 8.6b, respectively. These have already been integrated over position space using the runaway density profile inferred from images of synchrotron emission (see chapter 7). In any case, the final results are fairly insensitive to the runaway density profile shape. The interpretation of these response functions is that a single runaway electron with a given momentum and pitch angle—i.e. a delta function in momentum space—would produce synchrotron emission resulting in the shown measurement of θ_{pol} or $\mathrm{f}_{\mathrm{pol}}$. The grey areas in both

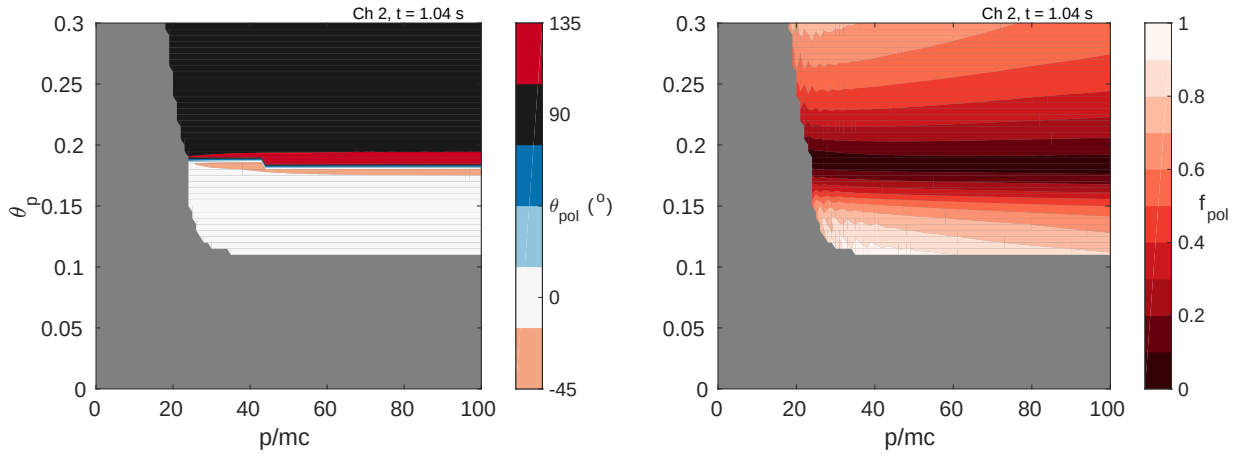

Figure 8.6: Detector response functions, from SOFT, of the polarization (a) angle θ_{pol} and (b) fraction $\mathrm{f}_{\mathrm{pol}}$ versus normalized (total) momentum p/mc and pitch angle θ_{p}, for MSE channel 2 at time $t = 1.04$ s. Grey regions indicate practically-undetectable regions of phase space.

plots indicate the regions in which little-to-no signal[d] is detected by channel 2. Therefore, this specific channel geometry limits the diagnosis of runaways to those with momenta $p/mc > 20$ and pitch angles $\theta_{\mathrm{p}} > 0.11$ rad.

It is clear from figure 8.6a that measurements of $\theta_{\mathrm{pol}} = 0°$ or $90°$ are most common, and the phase space is bifurcated at a critical pitch angle $\theta_{\mathrm{p,crit}} \approx 0.185$ rad. This implies that if channel 2 records a measurement of $\theta_{\mathrm{pol}} \approx 90°$, then a significant fraction of the runaway population must have pitch angles $\theta_{\mathrm{p}} > \theta_{\mathrm{p,crit}}$. Conversely, measuring $\theta_{\mathrm{pol}} \approx 0°$ implies that the bulk of the runaway distribution function is confined within $\theta_{\mathrm{p}} < \theta_{\mathrm{p,crit}}$. An improved localization of runaways in momentum space can be obtained by using both $\hat{\theta}_{\mathrm{pol}}$ and $\hat{\mathrm{f}}_{\mathrm{pol}}$ data. In figure 8.6b, the minimum of $\hat{\mathrm{f}}_{\mathrm{pol}}$ occurs near $\theta_{\mathrm{p,crit}}$ and increases as $|\theta_{\mathrm{p}} - \theta_{\mathrm{p,crit}}|$ increases, as expected from the heuristic argument presented in section 8.2. Thus, for example, experimental measurements of $\theta_{\mathrm{pol}} \approx 90°$ and $\mathrm{f}_{\mathrm{pol}} \approx 0.5$ would indicate that the detected synchrotron light is dominated by runaways with pitch angles $\theta_{\mathrm{p}} \approx 0.25$ rad.

As seen in figures 8.6a and 8.6b, synthetic measurements are relatively insensitive to the runaway momentum p/mc. As mentioned, they are also insensitive to the runaway density profile n_{r} (see figures 7.9 and 7.10) for two main reasons: (i) measurements are dominated by runaways within narrow radial bands (see figure 8.5) over which significant variations in n_{r} are not expected, and (ii) both θ_{pol} and $\mathrm{f}_{\mathrm{pol}}$ are independent of the emission amplitude. Therefore, a cross-section

[d]Specifically, the cutoff for SOFT data was (arbitrarily) chosen to be $L/\max(L) \leq 10^{-8}$ for all channels and times. The final results are insensitive to this choice.

of $\hat{G}(R, p, \theta_\mathrm{p})$, at one momentum and summed over each channel's radial range, provides a reference or "look-up" plot of a synchrotron polarization measurement versus channel r_tan/a and runaway pitch angle θ_p. These are shown for θ_pol and f_pol in the contour plots in figures 8.7a and 8.7b, respectively, as well as the line plots in figure 8.8.

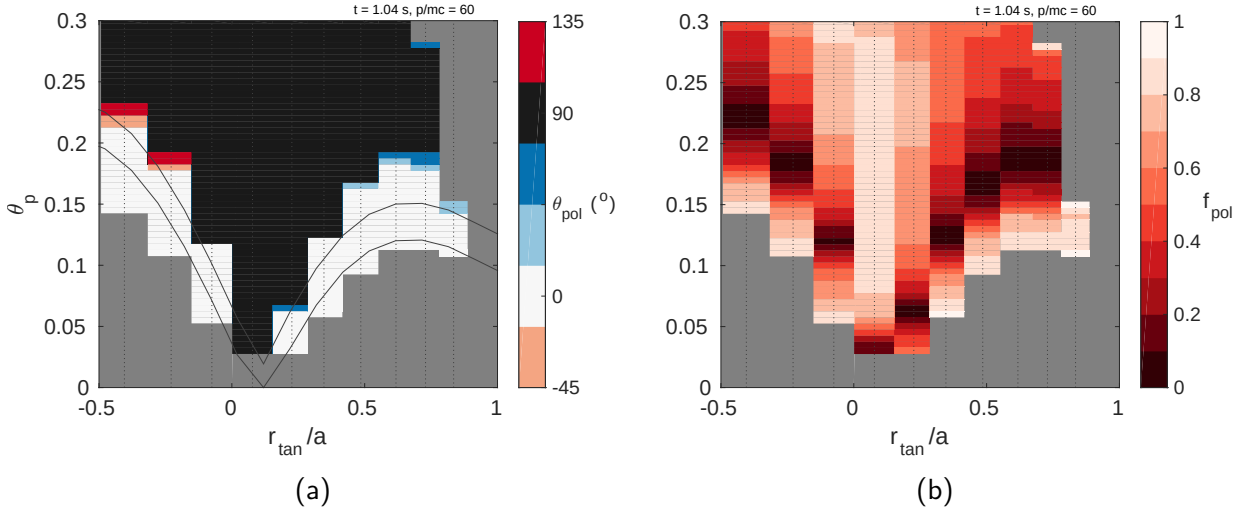

Figure 8.7: SOFT-predicted polarization (a) angle θ_pol and (b) fraction f_pol versus normalized tangency radius r_tan/a of the MSE channels (vertical dotted lines) and runaway pitch angle θ_p, for $t = 1.04$ s and $p/mc = 60$. The bounded region in (a) corresponds to the region of expected $\theta_\mathrm{pol} \approx 0°$ from the heuristic argument presented in section 8.2, i.e. $\theta_\mathrm{p,min} \leq \theta_\mathrm{p} \leq \theta_\mathrm{p,max}$. See figure 8.8 for line plots of θ_pol and f_pol for channels 1, 3, 5, 7, and 9.

In figure 8.7a, note that only a narrow band of $\theta_\mathrm{pol} \approx 0°$ (white) is expected; it follows a similar spatial pattern as that predicted by the heuristic model in section 8.2, with bounds of $\theta_\mathrm{p,min}$ (lower) and $\theta_\mathrm{p,max}$ (upper) overlaying the data. The differences between heuristic argument and simulation here are likely due to the more realistic 3D detector geometry implemented in SOFT, as well as the discrete radial resolution. The complementary reference plot for f_pol is shown in figure 8.7b, where it is again seen that the minimum in f_pol always occurs at the 90° transition location seen in figure 8.7a. The same data in figures 8.7a and 8.7b are also shown in figure 8.8 for only channels 1, 3, 5, 7, and 9; these plots are simply to help the reader better visualize the spatial (between-channel) variations of the 90° transition in θ_pol and the minimum in f_pol.

Comparing these plots to C-Mod experimental data can help identify the pitch angles of runaways which dominate the synchrotron emission measurement. However, not all channels provide useful information. For example, channel 4 ($r_\mathrm{tan}/a = 0.08$) should *always* measure a polarization angle of $\theta_\mathrm{pol} \approx 90°$, which is confirmed by experiment as seen in figure 8.3a. In addition, the f_pol measurement from channel 4 should be maximal for typical runaway pitch

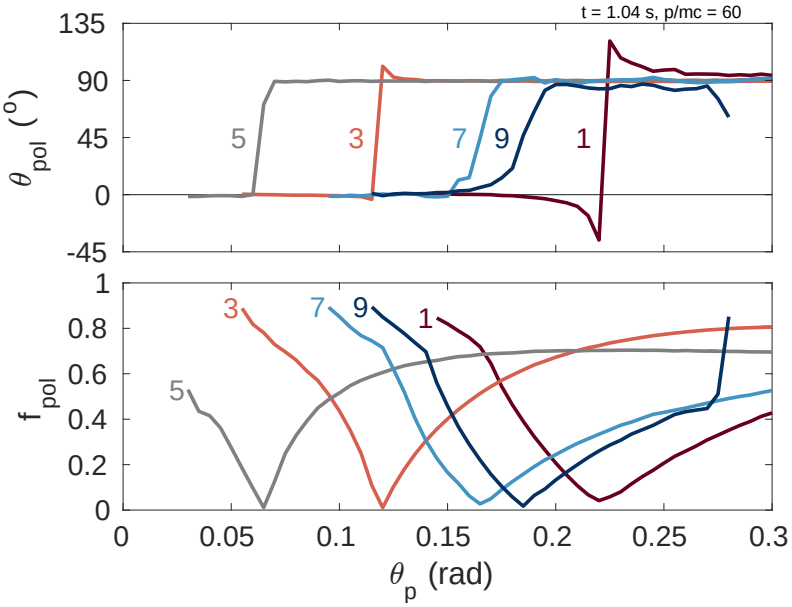

Figure 8.8: Trends in SOFT-predicted polarization (top) angle θ_{pol} and (bottom) fraction $\mathrm{f}_{\mathrm{pol}}$ versus runaway pitch angle θ_{p} for channels 1, 3, 5, 7, and 9 (labeled). The data for these line plots correspond to the *same* data in the contour plots of figures 8.7a and 8.7b, re-plotted here for clarity.

angles $\theta_{\mathrm{p}} > 0.05$ rad; this is also seen in the experimental trends of figure 8.3b. Values of $\mathrm{f}_{\mathrm{pol}} \leq 0.6$ could help constrain the pitch angle to $\theta_{\mathrm{p}} \approx 0.5$ rad; however, it is difficult to make a quantitative comparison in this situation since background/reflected light is not yet included in SOFT. Finally, note that data in figures 8.7a and 8.7b are not perfectly symmetric about the magnetic axis; therefore, the seemingly conflicting measurements between channels which "see" runaways on the same flux surface (approximately $\pm r_{\tan}/a$) are actually the result of each channel investigating a different region of phase space.

8.4 Comparisons of experimental and synthetic data

In this section, the spatiotemporal evolution of polarized synchrotron emission is explored in detail for Alcator C-Mod discharge 1140403026. Note again that this is the same discharge for which images of synchrotron light were analyzed in chapter 7. Time traces of several plasma parameters are shown in figure 8.9a. In this experiment, runaways were generated during the flattop portion of the plasma current (I_{MA}) by decreasing the plasma density (n_{20}) and hence collisional friction. The intensity of linearly-polarized synchrotron emission L_{MSE}, shown for all channels in figure 8.9b, starts rising at $t \approx 0.4$ s. Recall that there is not a reliable absolute

calibration of L_{MSE} among the channels; relative errors of 30-40% are expected. However, there are certainly similar temporal trends, especially in groups of channels: 1-5, 6-7, and 8-10.

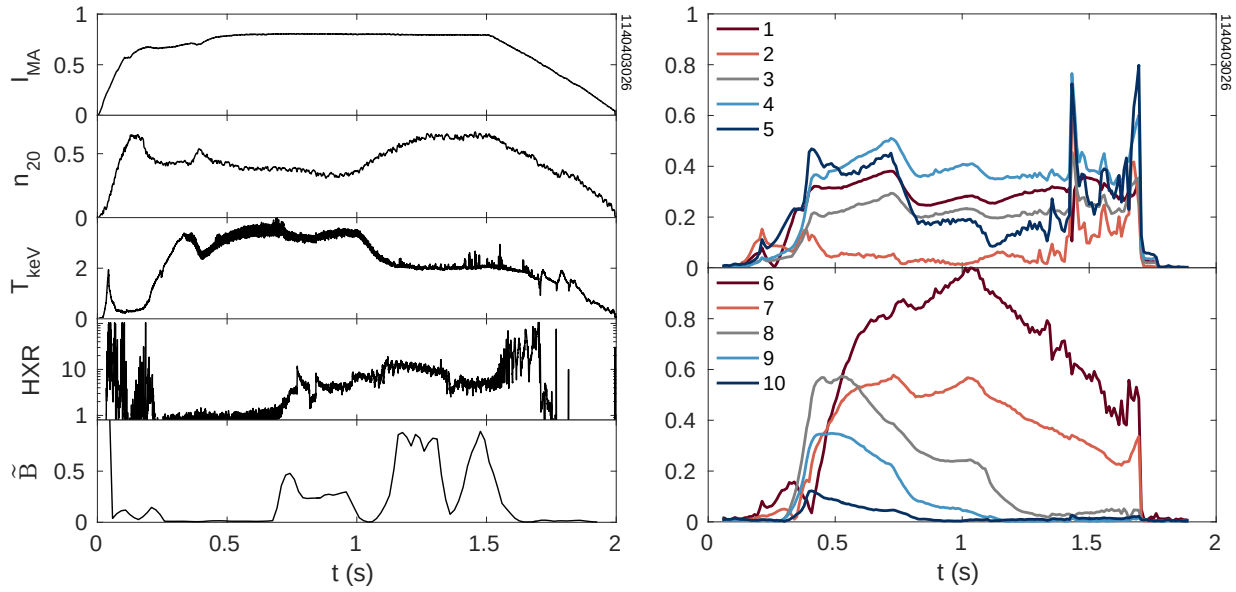

(a) Plasma parameters. (b) L_{MSE} (a.u.).

Figure 8.9: (a) From top to bottom: the plasma current (MA), line-averaged electron density (10^{20} m^{-3}), central electron temperature (keV), HXR signal (a.u.), and locked mode indicator (a.u.) are shown for an Alcator C-Mod plasma discharge. (b) The intensity of linearly-polarized light (a.u.) from MSE channels 1-5 (top) and 6-10 (bottom), all normalized to the maximum of channel 6. Compare to figure 7.3.

As seen in figure 8.9a, the hard x-ray (HXR) signal increases at $t \approx 0.7$ s; this is around the same time that a locked mode begins, indicated by a reduction in the sawtooth amplitude of plasma electron temperature (T_{keV}) and an increase in magnetic fluctuations ($\widetilde{B}$). This likely indicates the expulsion of runaways from the plasma due to MHD activity, leading to thick-target bremsstrahlung radiation from the first wall. In figure 8.9b, dips in the intensity (L_{MSE}) are also observed across all channels at this time. At $t = 1$ s, the density is increased to suppress runaways, and L_{MSE} starts to decrease, in particular for channels 6-10; these are viewing the runaway beam edge as it shrinks in size. Sharp spikes in both HXR and L_{MSE} signals—especially across channels 1-5—begin at $t \approx 1.5$ s, around the time of the final burst of MHD activity and ramp-down in plasma current and density. Both the synchrotron emission and HXR signals then disappear at $t \approx 1.7$ s.

Experimental measurements of θ_{pol} and $\mathrm{f}_{\mathrm{pol}}$ are shown in figures 8.10a and 8.10b, respectively, for all channels and times. Here, the time and spatial resolutions are $\Delta t \sim 1$ ms and $\Delta r_{\mathrm{tan}}/a \sim$ 0.1-0.2. In this analysis, we focus on the flattop portion of the discharge ($t \approx$ 0.5-1.6 s) when plasma parameters are relatively stable. First consider the θ_{pol} data: Spatially, the 90° transition occurs in the range $r_{\mathrm{tan}}/a =$ -0.4 to -0.08 (channel 1 to 3) and $r_{\mathrm{tan}}/a =$ 0.23 to 0.35 (channel 5 to 6). Temporally, the most interesting θ_{pol} evolution is at $r_{\mathrm{tan}}/a =$ -0.23 (channel 2) which experiences 90° transitions from $\theta_{\mathrm{pol}} =$ 90° to 0° at $t \approx$ 0.7 s and then back from $\theta_{\mathrm{pol}} =$ 0° to 90° around $t \approx$ 1.2-1.4 s. From our reference plot, figure 8.7a, this implies that the dominant pitch angle of runaways located within the channel 2 FOV decreases below $\theta_{\mathrm{p,crit}} =$ 0.185 rad for $t \approx$ 0.7-1.4 s.

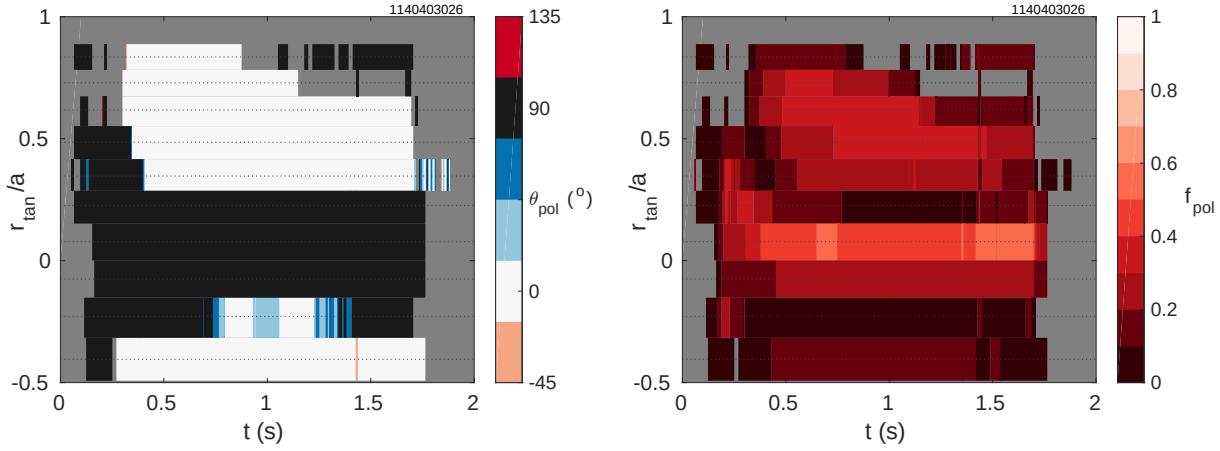

(a) (b)

Figure 8.10: Experimentally-measured polarization (a) angle θ_{pol} and (b) fraction $\mathrm{f}_{\mathrm{pol}}$ from one Alcator C-Mod discharge, versus time and normalized tangency radius of the MSE channels (horizontal dotted lines). Time and spatial resolutions are $\Delta t \sim 1$ ms and $\Delta r_{\mathrm{tan}}/a \sim$ 0.1-0.2. Grey regions indicate signal below the noise floor, i.e. $L_{\mathrm{MSE}} \leq 10^{-3}$.

Regarding experimental $\mathrm{f}_{\mathrm{pol}}$ measurements, shown in figure 8.10b, a maximum value of $\mathrm{f}_{\mathrm{pol}} \approx 0.6$ is observed near the magnetic axis (channel 4), as expected. Note how the non-monotonic feature (i.e. the "bump") in $\mathrm{f}_{\mathrm{pol}}$ values at outer radii decreases in radial extent as the runaway beam contracts in size. This shrinking is confirmed by the synchrotron images analyzed in chapter 7.

Synthetic (SOFT) signals of θ_{pol} and $\mathrm{f}_{\mathrm{pol}}$ are shown in figures 8.12a and 8.12b, respectively. They were produced using the the same methodology as in chapter 7. It is repeated here for clarity:

(i) Spatial profiles of experimental plasma parameters, like electron density and temperature from Thomson scattering and electric and magnetic fields from EFIT, were calculated for six locations throughout the plasma: at the magnetic axis and on rational flux surfaces with $q = 1$, 4/3, 3/2, 2, and 3. A constant $Z_{\rm eff} = 4$ was assumed.

(ii) For each location, these parameters were input into CODE to solve for the time-evolving electron momentum space distribution function. See figure 8.11a for a sample time-slice, and refer to chapter 5 for more information on CODE.

(iii) The runaway *phase* space distribution (i.e. in momentum and position space) was "stitched" together via a piecewise interpolation of the six momentum space distribution functions, with steps halfway between each flux surface as illustrated by the shaded regions in figure 8.5 and given explicitly in (7.1) in chapter 7.

(iv) The density profile $n_{\rm r}$ was inferred for the range $r/a \approx$ 0.2-1 from experimental images of the synchrotron emission, as described in chapter 7, and a Gaussian fit was used to extrapolate to $r/a = 0$. In general, it is observed that the SOFT synthetic modeling of measurements is *not* sensitive to the precise shape of the $n_{\rm r}(R)$. Nonetheless, the experimentally-fit profiles were used for completeness.

(v) The entire phase space distribution was multiplied with the SOFT response functions (and Jacobian) for times $t =$ 0.54-1.64 s, with time step $\Delta t = 100$ ms limited by computation time.[e] Integration over phase space then gives the synthetic SOFT+CODE results for $\theta_{\rm pol}$ and $\mathrm{f}_{\rm pol}$, shown in figures 8.12a and 8.12b, respectively.

Figure 8.11b shows the convolution of the CODE distribution function in figure 8.11a with the detected intensity response function $\hat{I}$ of channel 3 ($r_{\rm tan}/a =$ -0.08). This highlights the region of momentum space ($p/mc \approx 40$ and $\theta_{\rm p} \approx 0.16$ rad, in this case) which dominates the detected synchrotron measurement and determines the synthetic measurements of $\theta_{\rm pol}$ and $\mathrm{f}_{\rm pol}$ shown in figures 8.12a and 8.12b, respectively.

There are a few major takeaways when comparing experimental data in figure 8.10 with SOFT+CODE predictions in figure 8.12. First, it is somewhat difficult to compare $\mathrm{f}_{\rm pol}$ data quantitatively. Although the experimental $\mathrm{f}_{\rm pol}$ measurements were calibrated, SOFT does not account for the effect of background plasma light or reflections, which would decrease $\mathrm{f}_{\rm pol}$ and would be expected to have both spatial and temporal dependencies. However, there is relatively good *qualitative* agreement between experimental and synthetic spatial profiles. Both have maximum $\mathrm{f}_{\rm pol}$ values near the magnetic axis ($r_{\rm tan}/a = 0.08$, channel 4), with minima on either side of this peak. In general, it is observed that *increasing* runaway pitch angles, e.g. through increased pitch angle scattering, gives a better match of the synthetic signals to the experimental measurements.

[e] This is the same time step as that used in the analysis of chapter 7.

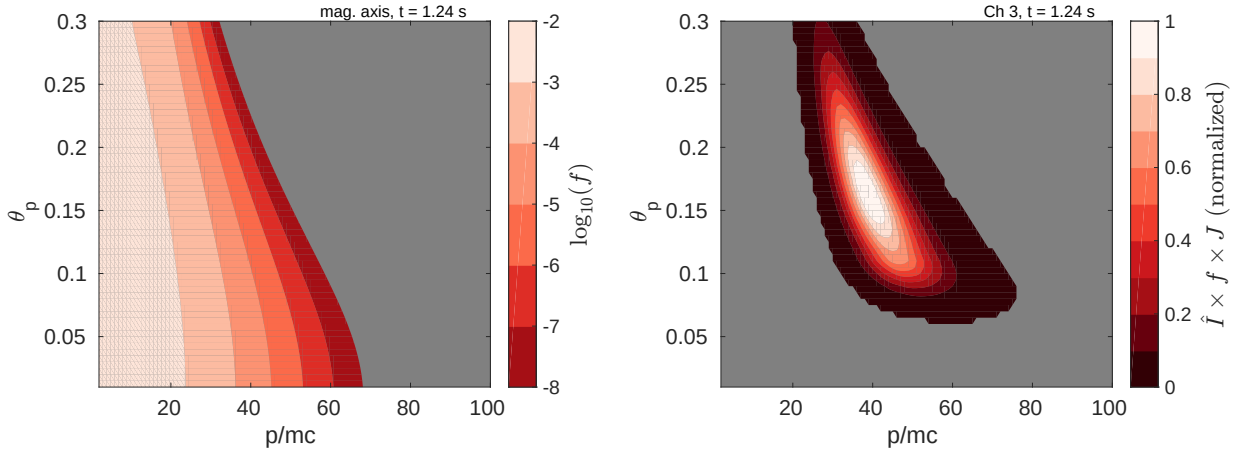

(a) (b)

Figure 8.11: (a) A momentum space distribution function $f(p, \theta_p)$ (log scale) calculated by CODE for plasma parameters at the magnetic axis. (b) The normalized convolution of f, the detector response function $\hat{I}(p, \theta_p)$ for channel 3, and Jacobian $J = p^2 \sin\theta_p$. The location of peak detected emission is $p/mc \approx 40$ and $\theta_p \approx 0.16$ rad.

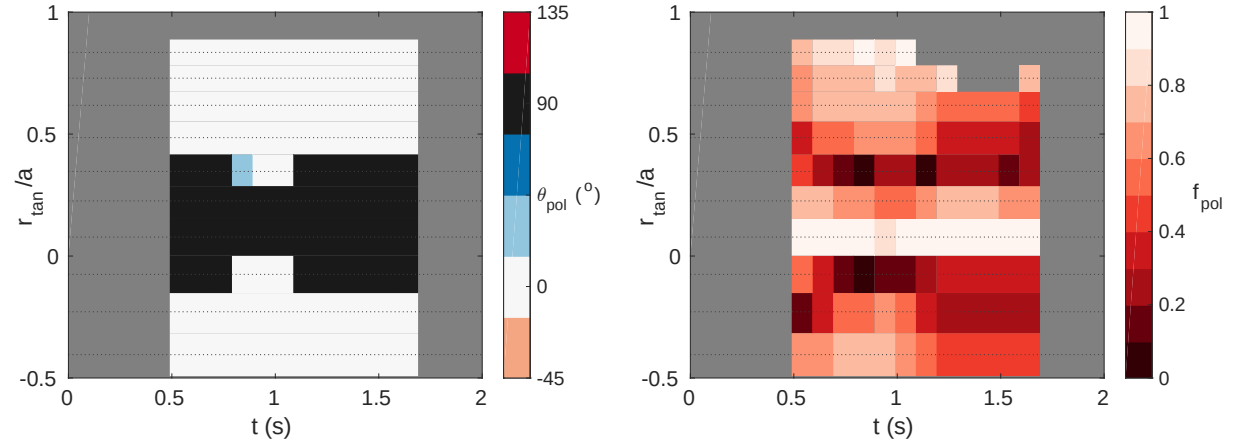

(a) (b)

Figure 8.12: SOFT+CODE-predicted polarization (a) angle θ_{pol} and (b) fraction f_{pol} for the Alcator C-Mod discharge of interest, versus time and normalized tangency radius of the MSE channels (horizontal dotted lines). Time and spatial resolutions are $\Delta t = 100$ ms and $\Delta r_{tan}/a \sim 0.1$-$0.2$. Compare to figure 8.10a and 8.10b.

Second, consider channel 3 ($r_{\tan}/a$ = -0.08). In experiment, $\theta_{\rm pol} \approx 90^\circ$ is observed for *all* times (see figure 8.10a); however, from SOFT+CODE, $\theta_{\rm pol} \approx 0^\circ$ is predicted for t = 0.64-0.84 s (see figure 8.12a). As seen in figure 8.5, channel 3 only "sees" runaways near the magnetic axis, with a momentum space distribution modeled in CODE using plasma parameters from the magnetic axis. Consulting our look-up plot, figure 8.7a, experimental $\theta_{\rm pol}$ data indicate that a significant fraction of runaways must maintain $\theta_{\rm p} \geq 0.12$ rad for all times. This is achieved by the distribution function, from CODE, at time t = 1.24 s shown in figure 8.11a; there, emission is dominated by runaways with $\theta_{\rm p} \approx 0.16$ rad, as seen in figure 8.11b. However, the CODE-calculated pitch angle distribution falls below the threshold $\theta_{\rm p} = 0.12$ rad for t = 0.64-0.84 s, which does not match experiment.

Conversely, for channel 6 ($r_{\tan}/a = 0.35$), experimental values of $\theta_{\rm pol} = 0^\circ$ are observed during the flattop current ($t > 0.5$ s), but SOFT+CODE predicts 90° transitions at $t \approx 0.64$ and 0.84 s, similar to those predicted for channel 3. As seen in figure 8.5, channel 6 views runaways in a radial range overlapping the momentum space distributions of runaways on flux surfaces with q = 1 and 4/3. From the look-up plot, figure 8.7a, the bulk of the *observed* runaway population must have pitch angles $\theta_{\rm p} < 0.12$ rad for all flattop times in order for measurements of $\theta_{\rm pol} = 0^\circ$ to be made. Therefore, the actual runaway pitch angle distribution is inferred to be *narrower* for runaways in the radial range $q \approx$ 1-4/3 compared to that predicted by CODE for times $t \approx$ 0.5-0.7 s and 1.1-1.7 s.

Finally, consider once again channel 2 ($r_{\tan}/a$ = -0.23), for which an interesting time-evolution in experimental $\theta_{\rm pol}$ measurements is observed in figure 8.10a. SOFT+CODE, however, predicts that $\theta_{\rm pol} = 0^\circ$ for *all* times (see figure 8.12a). As seen in figure 8.5, channel 2 views the radial range including the momentum space distributions of runaways at the magnetic axis and on the q = 1 flux surface. Referencing figure 8.7a, it is seen that the runaway pitch angle distribution from CODE should *broaden* (past the threshold $\theta_{\rm p} > 0.185$ rad) for times $t \approx$ 0.5-0.7 s and $\sim$1.3-1.7 s in order to improve agreement between synthetic and experimental data. In other words, the actual runaway pitch angle distribution is inferred to be *broader* than that predicted by CODE for those times. Note also from figure 8.5 that channel 4 ($r_{\tan}/a$ = -0.08) views the same runaway phase space distribution as channel 2. However, as previously mentioned, channel 4 provides little additional information, and SOFT+CODE synthetic data for channel 4 are consistent with experiment for all times.

To summarize, the runaway pitch angle distribution is inferred from experiment to be *broader* than that predicted by CODE in the radial region between the magnetic axis and $q \approx 1$ surface, but *narrower* between the $q \approx 1$ and 4/3 surfaces, for some times throughout the plasma discharge. It is not clear which physical mechanisms would cause an *increase* of $\theta_{\rm p}$ between the magnetic axis and the $q \approx 1$ surface, but a *decrease* of $\theta_{\rm p}$ in the region $q \approx$ 1-4/3. One possible explanation is

the interaction of the sawtooth instability with runaways within and near the so-called "inversion radius" at $q = 1$. The timing of the partial reduction in T_e sawteeth at the onset of the locked mode ($t \approx 0.7$ s) and complete suppression of sawteeth ($t \approx 1.1$ s) correlates with the above times. This suggests that some of the differences between experimental and synthetic measurements are due to CODE not accounting for spatial dynamics, such as radial transport. Note that while radial transport of runaways near the $q = 2$ surface was inferred from synchrotron images (see chapter 7), runaway dynamics within $q < 1$ were not observable; they are captured here.

In general, it is seen that the synthetic and experimental θ_pol data match well for most channels and times. The observation that a *broader* CODE-predicted runaway pitch angle distribution would improve agreement between synthetic and experimental f_pol data indicates that additional pitch angle scattering mechanisms may not be captured in this model. The uniform $Z_\mathrm{eff} = 4$ profile is assumed from previous experience with low density C-Mod discharges, but was not directly measured for this discharge. An increase in Z_eff could cause the inferred increase in pitch angle scattering. So, too, could the magnetic fluctuations related to the locked mode or perhaps another RE-induced kinetic instability, as discussed in chapter 2. Because pitch angle scattering *increases* as particle energies *decrease*, an unaccounted power loss mechanism might also explain the results. These mechanisms could be isolated and better diagnosed in future experiments.

8.5 Measurements of polarized synchrotron light during lower hybrid current drive

Lower hybrid current drive (LHCD) was enabled for a few short time intervals during the 28 runaway discharges mentioned in section 8.1 (see figure 8.3). Sometimes LHCD was used to encourage runaway growth through the creation of a "seed" population, while at other times it was just turned on near the end of the discharge. As stated, the analyses of section 8.1 do *not* include data from times when LHCD was on. The purpose of this section is to explore the effect of LHCD on polarized synchrotron emission by considering the data recorded during these times when LHCD was active. These measurements of polarization angle $\theta_{\rm pol}$ and fraction $\mathrm{f}_{\rm pol}$ are shown in the histograms of figures 8.13a and 8.13b, respectively. Note that there are only $\sim$50-100 data points (time-slices) for each channel, so the uncertainties here ($\sim$10-15%) are much larger than those for the data in figure 8.3. The $\mathrm{f}_{\rm pol}$ data in figure 8.13b look very similar to those in figure 8.3b: A peak of $\mathrm{f}_{\rm pol} \approx 0.7$ is measured by channel 4, and there is also the bump-like feature in the data of channels 6-10.

The polarization angle $\theta_{\rm pol}$ data, however, is starkly different for the cases with and without LHCD. (Compare figures 8.13a and 8.3a.) When LHCD is on, there is no 90° transition in $\theta_{\rm pol}$ observed; all channels measure $\theta_{\rm pol} \approx 90°$. Referring to our "look-up" plot (figure 8.7a), these data *could* indicate that a significant fraction of the runaways observed by channels 1 and 6-10 have sufficiently large pitch angles $\theta_{\rm p}$, although it is not clear why LHCD would broaden the runaway pitch angle distribution. LH waves usually damp on *non-relativistic* energetic electrons with speeds $\sim$3-10 times higher than the electron thermal velocity (e.g. with energies $\sim$10-100 keV), "pushing" them in the direction *parallel* to the magnetic field. Perhaps this fast electron population somehow evolves into a relativistic electron population with higher pitch angles than in a no-LHCD scenario, but a possible physical mechanism has not yet been identified.

Another reason why only vertically-polarized synchrotron light is measured—which the author finds more likely than that previously stated—could be the following: LHCD seeds runaway electrons, but does not affect their pitch angles; instead, LH waves alter the plasma current profile $J_{\rm p}(r)$ (as intended), changing the poloidal magnetic field geometry $B_{\rm p}(r)$ and thus also the polarization of synchrotron radiation. Recall from the discussions of section 8.1 that the polarization of synchrotron radiation is highly dependent on both the runaway pitch angle $\theta_{\rm p}$ *and* the local magnetic field pitch angle θ_B. In this scenario, the LH-driven, non-thermal electrons would perform two roles: First, they would seed and feed the runaway population, but the runaway distribution would otherwise evolve similarly to a non-LH-seeded one. Second, the fast electrons would locally increase the current density $J_{\rm p}(r)$, changing $B_{\rm p}(r)$ enough such that the observed polarization $\boldsymbol{E} \propto \boldsymbol{v} \times \boldsymbol{B}$ is mostly vertical. See [18] for one study of LHCD experiments on

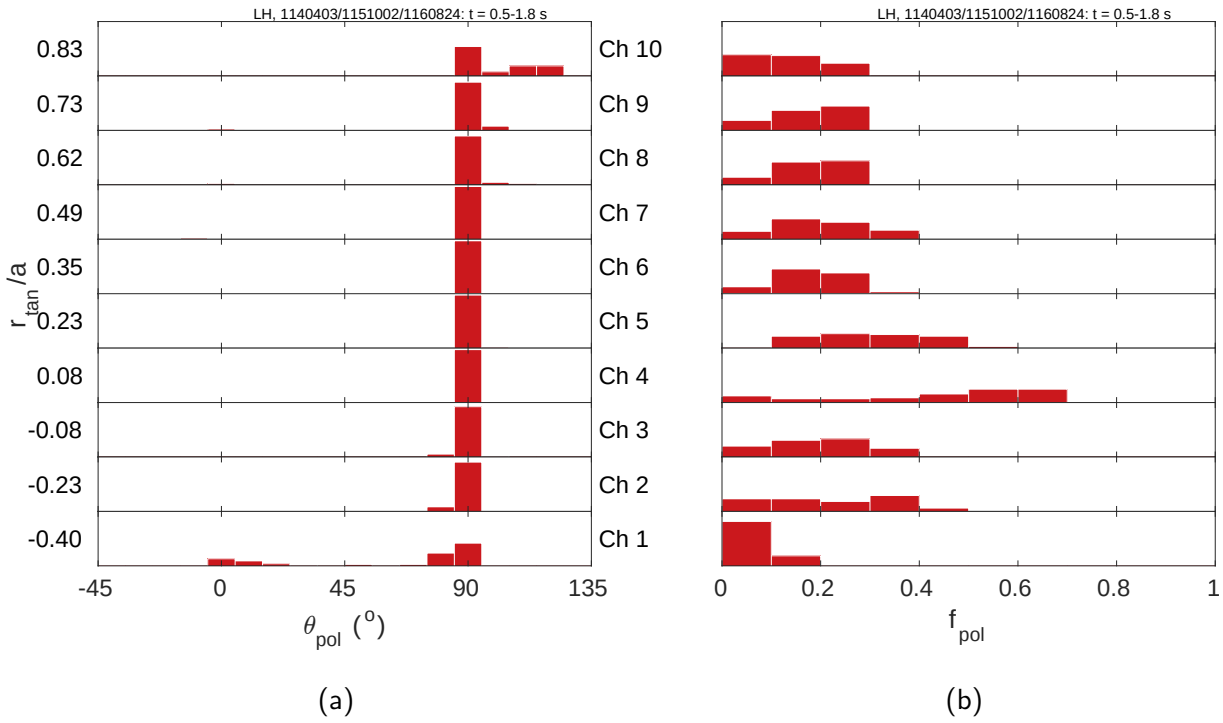

(a) (b)

Figure 8.13: Histograms of polarization (a) angle $\theta_{\rm pol}$ and (b) fraction $\rm f_{pol}$ for each channel, denoted by the normalized tangency radius $r_{\rm tan}/a$. These data were taken at times when lower hybrid (LH) current drive was *on*. Bin widths are $\Delta\theta_{\rm pol} = 10^\circ$ and $\Delta \rm f_{pol} = 0.1$. For each channel, the vertical axis spans 0 to 1, and all bar heights (probabilities) sum to 1. Data are from 28 discharges, but from only 50-100 total time-slices within t = 0.5-1.8 s. Compare to figure 8.3.

Alcator C-Mod and comparisons with theory and simulations.

It would be difficult—maybe impossible—to disentangle the two effects of LHCD changing $\theta_{\rm p}$ and/or θ_B. However, this intriguing observation opens up the opportunity to probe the local magnetic field (and current density) using synchrotron emission from runaways, as explored in the next section.

8.6 Current density profile of a runaway electron beam

Up until now, the current I_r carried by runaways has been neglected in our analyses. As argued in chapter 5, the approximation $I_\mathrm{r} \ll I_\mathrm{p}$ holds for runaways generated during the flattop portion of low-density, Ohmic discharges in C-Mod. For clarity, the physics is re-explained here: In a tokamak, an externally-applied loop voltage V_loop is required to drive the plasma current I_p, in the absence of other current drive mechanisms (e.g. neutral beam injection, electron cyclotron current drive, etc.). Runaway electrons, if generated, also carry a current approximately proportional to their number N_r,

$$I_\mathrm{r} \approx \frac{ecN_\mathrm{r}}{2\pi R_0}, \tag{8.2}$$

where all runaways are assumed to travel at speed $v = c$. Therefore, there is the potential[f] for a sufficiently large population of runaways to carry a current equal to the intended (programmed) plasma current. Then, since runaways experience so few collisions, $V_\mathrm{loop} \to 0$ as it is no longer required to drive current. In C-Mod, little-to-no variation in V_loop is seen in the presence of runaways, confirming that $I_\mathrm{r} \ll I_\mathrm{p}$. Fortunately, this means that EFIT reconstructions of the magnetic field are adequate when studying runaway dynamics (and for use as SOFT inputs).

It is of interest to explore how the analysis changes for $I_\mathrm{r} \sim I_\mathrm{p}$, which can be the case for post-disruption runaway beams and plateaus observed in other tokamaks. As discussed in section 8.5, the effect of changing the local current density (and poloidal magnetic field) may have already been observed in polarization measurements of runaway synchrotron radiation during lower hybrid current drive in C-Mod.

As a first investigation into how the runaway current density profile $J_\mathrm{r}(r)$ could be diagnosed using synchrotron radiation data, four current density profiles were modeled and are shown in figure 8.14a. A cylindrical plasma with C-Mod-like parameters ($R_0 = 68$ cm, $a = 22$ cm) was assumed, with a *total* current $I_\mathrm{tot} = I_\mathrm{p} + I_\mathrm{r} = 800$ kA. The *plasma* current profile $J_\mathrm{p}(r)$ was assumed to be parabolic. (See (2.35)-(2.38) for calculations of $J_\mathrm{p}(r)$ and $B_\mathrm{p}(r)$ for polynomial degree $\mathrm{n} = 2$.) The runaway *number* density n_r was taken to be exponentially-decaying with minor radius

$$n_\mathrm{r}(r) \propto \exp\left(-\frac{r}{\Delta r}\right), \tag{8.3}$$

where $\Delta r = 2$ cm ($\Delta r/a \approx 0.1$) was estimated from the experimentally-inferred n_r profiles from chapter 7. Here, an exponential form was chosen for simplicity, although this means that $J_\mathrm{r}(r)$ is not smooth (i.e. $\mathrm{d}J_\mathrm{r}/\mathrm{d}r \neq 0$) at $r = 0$ or $r = a$, which is unphysical. However, the effect on

[f] Pun intended.

the final results is expected to be inconsequential. The runaway current density is given by

$$J_{\mathrm{r}}(r) \approx ecn_{\mathrm{r}}(r), \tag{8.4}$$

and the total current density is $J_{\mathrm{tot}} = J_{\mathrm{p}} + J_{\mathrm{r}}$, satisfying

$$I_{\mathrm{tot}} = \int_0^{2\pi} \int_0^a J_{\mathrm{tot}}\, r\, \mathrm{d}r\, \mathrm{d}\theta. \tag{8.5}$$

The ratio $I_{\mathrm{r}}/I_{\mathrm{tot}}$ takes the values 0, 1/8, 1/4, and 1/2, as labeled in figure 8.14a. The poloidal magnetic field $B_{\mathrm{p}}(r)$ was calculated from Ampere's law for each case, and a toroidal field $B_{\mathrm{t}}(R) = B_0 R_0/R$ was assumed, using $B_0 = 5.4$ T, C-Mod's field on-axis. These four magnetic geometries were then input into SOFT.

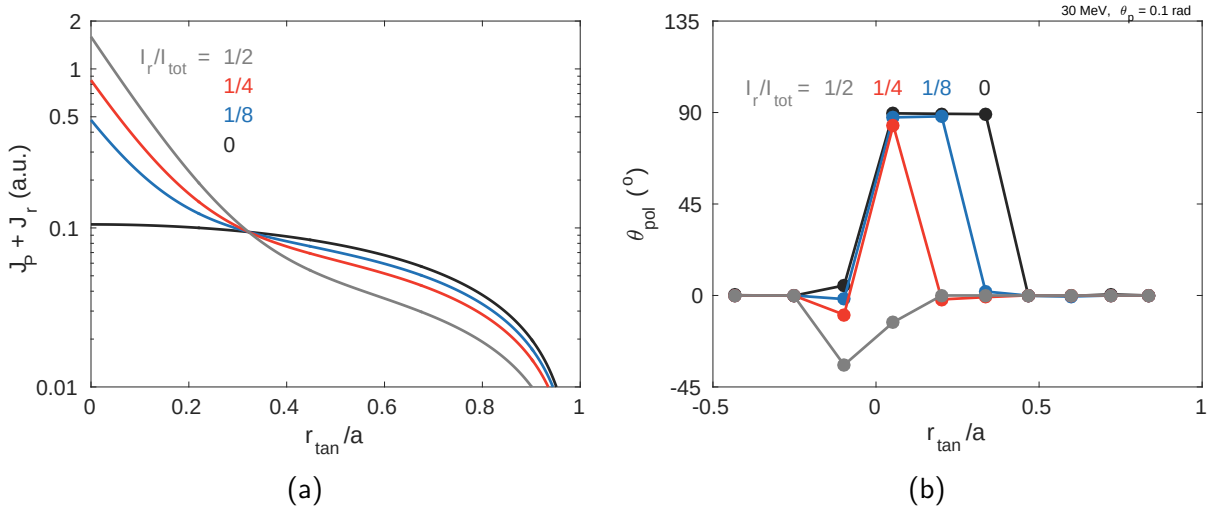

Figure 8.14: (a) Modeled *total* (plasma + runaway) current density profiles, $J_{\mathrm{tot}} = J_{\mathrm{p}} + J_{\mathrm{r}}$, and (b) SOFT-predicted polarization angle θ_{pol} measurements, versus normalized radius r/a, for four ratios of $I_{\mathrm{r}}/I_{\mathrm{tot}}$: 0 (black), 1/8 (blue), 1/4 (red), and 1/2 (grey). Note the logarithmic vertical axis in (a). All runaways were modeled with energies $\mathcal{E} = 30$ MeV and pitch angles $\theta_{\mathrm{p}} = 0.1$ rad in (b).

The same detector setup as that of the MSE system, described in chapter 4 and section 8.1, was used here. All runaways were given the same energy $\mathcal{E} = 30$ MeV and pitch angle $\theta_{\mathrm{p}} = 0.1$ rad. This is representative of the localized region of momentum space which often dominates the synchrotron emission measurement, as discussed in chapter 5. The runaway density profile input into SOFT is just that in (8.3) with the appropriate scaling factor.

The resulting synthetic measurements of the polarization angle $\theta_{\rm pol}$ of synchrotron radiation are shown in figure 8.14b. For negligible runaway current ($I_{\rm r}/I_{\rm tot} = 0$), the characteristic 90° transitions in $\theta_{\rm pol}$ are seen between channels 3-4 ($r_{\rm tan}/a \approx 0$) and channels 6-7 ($r_{\rm tan}/a \approx 0.4$). Recall from section 8.1 that horizontal and vertical polarizations (i.e. $\theta_{\rm pol} \approx 0°$ and 90°) are expected when $\theta_{\rm p} \lesssim \theta_B$ and $\theta_{\rm p} \gg \theta_B$, respectively. For the case of $I_{\rm r}/I_{\rm tot} = 0$, this means that the local magnetic pitch angles observed by channels 4-6 are $\theta_B \lesssim \theta_{\rm p} = 0.1$ rad. (This is similar to the trend seen in figure 8.7a.) As $I_{\rm r}/I_{\rm tot}$ increases to $1/8$ and then $1/4$, the current profile becomes more peaked in the plasma center, as seen in figure 8.14a. This results in the poloidal field (and magnetic pitch angle) decreasing throughout the plasma. Thus, the region of the plasma with magnetic pitch angles $\theta_B \gtrsim 0.1$ rad shrinks; we can actually identify those locations based on the switch from $\theta_{\rm pol} = 90°$ to 0°. Finally, the 90° transition completely disappears for large enough runaway currents, e.g. $I_{\rm r}/I_{\rm tot} = 1/2$, when $\theta_B \lesssim 0.1$ rad across the minor radius. An interesting feature of $\theta_{\rm pol} < 0°$ does appear near the magnetic axis, possibly due to the highly-peaked current density profile. Note that for this modified current profile, almost all polarization angle measurements are $\theta_{\rm pol} \approx 0°$, which is opposite to the $\theta_{\rm pol}$ data measured during LHCD shown in figure 8.13a. This difference could be due to LHCD driving current off-axis, while this analysis increased the current density on-axis.

While this analysis excitingly suggests that the current density profile of runaways could be diagnosed using their own polarized synchrotron radiation, the problem of inverting/inferring the runaway phase space distribution from these measurements could actually become *more* difficult and convoluted. Because a sufficiently large runaway population would produce a magnetic field comparable to that of the background plasma, the magnetic geometry could no longer be treated as known, as was done in the previous analyses. Solving this problem would likely require an iterative process; for example: The base case could assume that the true magnetic geometry is that calculated from a reconstruction algorithm, like EFIT. Then, the runaway phase space distribution could be forward-modeled using a kinetic solver, like CODE, and/or partially-inverted from a synthetic diagnostic, like SOFT. From the predicted/inferred runaway density profile, the total current density could be calculated and the magnetic geometry updated. The analysis could then be performed again, comparing experimental and synthetic measurements until a good level of agreement is reached.

References—Chapter 8

[1] K.C. Westfold. The Polarization of Synchrotron Radiation. *The Astrophysical Journal*, 130:241, 1959.

[2] M.A. Vashakidze. On the degree of polarization of the radiation of nearby extragalactic nebulae and of the Crab Nebula. *Astronomical Circular of the USSR*, 147(11), 1954.

[3] V.A. Dombrovsky. On the nature of the radiation from the Crab Nebula. *Proceedings of the USSR Academy of Sciences*, 94:1021, 1954.

[4] I.S. Shklovskii. On the nature of the luminescence of the Crab Nebula. 90(983):1900–1975, 1953.

[5] R.A. Tinguely, M. Hoppe, O. Embréus, R.S. Granetz, S. Scott, and R.T. Mumgaard. Experimental and synthetic measurements of polarized synchrotron emission from runaway electrons in Alcator C-Mod. 2019. Submitted to *Nuclear Fusion*.

[6] Ya.M. Sobolev. Polarization of synchrotron radiation from relativistic electrons moving within toroidal magnetic fields. *Problems of Atomic Science and Technology*, 4(86):108–111, 2013.

[7] D.A. Spong, W.W. Heidbrink, C. Paz-Soldan, X.D. Du, K.E. Thome, M.A. Van Zeeland, C. Collins, A. Lvovskiy, R.A. Moyer, M.E. Austin, D.P. Brennan, C. Liu, E.F. Jaeger, and C. Lau. First direct observation of runaway-electron-driven Whistler waves in tokamaks. *Phys. Rev. Lett.*, 120:155002, 2018.

[8] C. Liu, E. Hirvijoki, G.-Y. Fu, D.P. Brennan, A. Bhattacharjee, and C. Paz-Soldan. Role of kinetic instability in runaway-electron avalanches and elevated critical electric fields. *Phys. Rev. Lett.*, 120:265001, 2018.

[9] L. Hesslow, O. Embréus, A. Stahl, T. C. DuBois, G. Papp, S. L. Newton, and T. Fülöp. Effect of partially screened nuclei on fast-electron dynamics. *Phys. Rev. Lett.*, 118:255001, 2017.

[10] L. Hesslow, O. Embréus, G.J. Wilkie, G. Papp, and T. Fülöp. Effect of partially ionized impurities and radiation on the effective critical electric field for runaway generation. *Plasma Physics and Controlled Fusion*, 60(7):074010, 2018.

[11] M. Lehnen, S.S. Abdullaev, G. Arnoux, S.A. Bozhenkov, M.W. Jakubowski, R. Jaspers, V.V. Plyusnin, V. Riccardo, and U. Samm. Runaway generation during disruptions in JET and TEXTOR. *Journal of Nuclear Materials*, 390-391:740 – 746, 2009. Proceedings of the 18th International Conference on Plasma-Surface Interactions in Controlled Fusion Device.

[12] M. Greenwald, D.G. Whyte, P. Bonoli, Z.S. Hartwig, J. Irby, B. LaBombard, E. Marmar, J. Minervini, M. Takayasu, J. Terry, R. Vieira, A.E. White, S. Wukitch, D. Brunner, R.T. Mumgaard, and B.N. Sorbom. The high-field path to practical fusion energy, 2018. https://doi.org/10.7910/DVN/OYYBNU.

[13] R.T. Mumgaard, S.D. Scott, and M. Khoury. A ten sightline multi-spectral line-polarization MSE system for Alcator C-Mod. *Review of Scientific Instruments*, 87, 2016. https://doi.org/10.1063/1.4959793.

[14] J.W. Connor and R.J. Hastie. Relativistic limitations on runaway electrons. *Nuclear Fusion*, 15(3):415, 1975.

[15] V.V. Plyusnin, V. Riccardo, R. Jaspers, B. Alper, V.G. Kiptily, J. Mlynar, S. Popovichev, E. de La Luna, F. Andersson, and JET EFDA contributors. Study of runaway electron generation during major disruptions in JET. *Nuclear Fusion*, 46(2):277, 2006.

[16] J.R. Martín-Solís, B. Esposito, R. Sánchez, F.M. Poli, and L. Panaccione. Enhanced production of runaway electrons during a disruptive termination of discharges heated with lower hybrid power in the Frascati Tokamak Upgrade. *Phys. Rev. Lett.*, 97:165002, 2006.

[17] V.V. Plyusnin, C. Reux, V.G. Kiptily, G. Pautasso, J. Decker, G. Papp, A. Kallenbach, V. Weinzettl, J. Mlynar, S. Coda, V. Riccardo, P. Lomas, S. Jachmich, A.E. Shevelev, B. Alper, E. Khilkevitch, Y. Martin, R. Dux, C. Fuchs, B. Duval, M. Brix, G. Tardini, M. Maraschek, W. Treutterer, L. Giannone, A. Mlynek, O. Ficker, P. Martin, S. Gerasimov, S. Potzel, R. Paprok, P. J. McCarthy, M. Imrisek, A. Boboc, K. Lackner, A. Fernandes, J. Havlicek, L. Giacomelli, M. Vlainic, M. Nocente, U. Kruezi, COMPASS team, TCV team, ASDEX-Upgrade team, EUROFusion MST1 Team, and JET contributors. Comparison of runaway electron generation parameters in small, medium-sized and large tokamaks—a survey of experiments in COMPASS, TCV, ASDEX-Upgrade and JET. *Nuclear Fusion*, 58(1):016014, 2018.

[18] P.T. Bonoli, J. Ko, R. Parker, A.E. Schmidt, G. Wallace, J.C. Wright, C.L. Fiore, A.E. Hubbard, J. Irby, E. Marmar, M. Porkolab, D. Terry, S.M. Wolfe, S.J. Wukitch, J.R. Wilson, S. Scott, E. Valeo, C.K. Phillips, and R.W. Harvey. Lower hybrid current drive experiments on Alcator C-Mod: Comparison with theory and simulation. *Physics of Plasmas*, 15(5):056117, 2008.

This page intentionally left blank

Chapter 9

Conclusions and future work

9.1 Contributions to the field

As a result of this thesis work, the author has become an expert in the analysis of visible synchrotron radiation emitted by relativistic runaway electrons in tokamak plasmas. Specifically, the analyses of synchrotron radiation spectra, polarization, and images have lead to greater understanding of the energy, pitch angle, and spatial distributions of runaways, respectively. The analysis techniques developed and utilized in this thesis are applicable to future fusion devices, which—like Alcator C-Mod—will have the potential to measure visible synchrotron radiation due to their high magnetic fields; e.g. ITER ($\sim$5 T), SPARC ($\sim$12 T), and ARC ($\sim$9 T). The major contributions of this thesis work to the field of runaway electron physics are briefly summarized below in chronological order. Further details are provided in section 9.2.

I. In collaboration with the Plasma Theory group at Chalmers University in Sweden, the author provided the first experimental validation of the state-of-the-art synthetic diagnostic SOFT, described in chapter 5. The author of this thesis was the third author of the publication introducing SOFT [1] and wrote section 4.1 therein.

II. The author performed the most complete analysis to-date of spectral measurements of synchrotron radiation from runaways, as described in chapter 6. It was shown that both spatial information of the runaway population and a proper synthetic diagnostic (SOFT) were/are required to reproduce and explain experimental data. The agreement of synthetic and experimental spectra is consistent with the physical picture that, all else constant, runaway electron energies *decrease* as the magnetic field *increases* in a tokamak. This work resulted in a first-author publication [2] in *Nuclear Fusion*.

III. The most detailed analysis to-date of images of runaway synchrotron emission was performed by the author and described in chapter 7. Spatiotemporal dynamics of the runaway

electron population were identified from the distribution of pixel intensities. Increased radial transport of runaways located on the $q = 2$ flux surface was inferred from the images using SOFT. Additionally, the time-evolving runaway density profile was inverted from the images. The culmination of this work was a first-author publication [3] in *Plasma Physics and Controlled Fusion*.

IV. The first experimental analysis of polarized synchrotron emission from runaways in a tokamak plasma was presented in chapter 8. A physically-intuitive explanation was provided for the 90° transitions in polarization angle observed in experimental data. Importantly, it was shown that polarization measurements can directly probe the pitch angle distribution of runaways. Discrepancies between synthetic (SOFT) and experimental data indicated that the sawtooth instability may influence the pitch angle scattering of runaways near the $q = 1$ surface. This work has been submitted for publication in *Nuclear Fusion* [4], with the author of this thesis as the first author.

The author has presented this thesis work at several conferences, including the annual meetings of the American Physical Society Division of Plasma Physics, the European Physical Society Conference on Plasma Physics, and Runaway Electron Meetings. During his graduate career, the author has also published several other fusion-related journal articles, both as the first author [5–7] and as a co-author [8–12].

9.2 Summary of work

The sections below summarize the analyses, results, and conclusions of this thesis. In particular, they focus on the "substantive" chapters 6, 7, and 8.

9.2.1 On the spectra of synchrotron radiation

As described in chapter 6, runaway electron experiments were performed at high magnetic fields during low-density, Ohmic, elongated and diverted discharges in Alcator C-Mod. The threshold electric field required for runaway generation was deduced from HXR and photo-neutron measurements from 17 plasma discharges and compared to recent theoretical predictions [13–15]. The effective critical field was found to be a factor of $\sim$5 higher than that predicted by purely collisional theory [16] and $\sim$3 times higher than estimates incorporating knowledge of bulk plasma parameters, i.e. electric field, electron density, effective charge, and magnetic field [13, 15]. A priori knowledge of the approximate runaway energies and pitch angles allowed a better prediction of the threshold field [14], but this will likely not be possible for future fusion devices. Therefore,

further work must be done to predict the threshold electric field for runaway onset, particularly for high magnetic field scenarios.

Absolutely-calibrated visible spectrometers, described in chapter 4, were installed on C-Mod to measure runaway synchrotron radiation spectra. In particular, the spectra were studied from three plasma discharges with similar electric-to-friction force ratios E_0/E_C [16] but varying magnetic field strengths, $B_0 = 2.7$, 5.4, and 7.8 T. A test particle model (TPM) of runaway momentum evolution [17], as well as primary (linear) [16] and knock-on (exponential) [18] runaway electron density growth rates, were used to estimate runaway dynamics at the magnetic axis and on flux surfaces with safety factors $q = 1$, 3/2, and 2. Drift orbits and loss of confinement [19] were also included in the calculations. The synthetic diagnostic SOFT [1] was used to produce synthetic spectra, including contributions from runaways located throughout the plasma, for given magnetic geometries and spectrometer specifications. It was found that experimental spectra could be best reproduced when incorporating the spatiotemporal results of the TPM into SOFT, especially at high magnetic fields. Simplified calculations of the expected spectral radiance, like those used in [20–23], could lead to unphysical interpretations of runaway energies. The major takeaway from this analysis was the following: Experimental spectra were consistent with runaway energies' decreasing when the toroidal magnetic field was increased, likely due to more power being lost through synchrotron radiation. This motivates further exploration of high field fusion devices for which high energy runaways could be of lesser concern (see appendix A).

9.2.2 On the images of synchrotron radiation

In chapter 7, runaways were also studied during the flattop plasma current phase of low density, diverted plasma discharges in C-Mod. Images of synchrotron emission were captured by a visible wide-angle camera viewing both co- and counter-I_p directions inside the tokamak. An in-vessel calibration, detailed in chapter 4, was performed to correct for image distortion, thereby allowing the diagnosis of "in-flight" runaway spatiotemporal evolution. A statistical analysis of aggregate data from 23 runaway-producing discharges (>1000 camera images) explored the plasma parameter space for regions in which runaway synchrotron radiation either was or was not detected by the visible camera. Compared to the times when synchrotron emission was *not* observed, visible synchrotron emission *was* observed for (i) higher values of the ratio of on-axis to critical electric fields E_0/E_C [16], (ii) higher values of the ratio of on-axis to Dreicer electric fields E_0/E_D [24, 25], and (iii) lower values of the ratio of radiation to collisional timescales $\tau_\mathrm{rad}/\tau_\mathrm{coll}$. This matches theoretical predictions: Higher E_0/E_C and E_0/E_D lead to higher runaway energies and larger runaway growth rates, thus increasing the likelihood of detection of visible synchrotron light. In addition, low $\tau_\mathrm{rad}/\tau_\mathrm{coll}$ values (<10) typically indicate that synchrotron radiation is dominating over collisional friction as a power loss mechanism.

For one discharge, the spatiotemporal evolution of runaways was explored in detail through the analysis of synchrotron image evolution. Both a TPM [17] and the kinetic solver CODE [26, 27] were used to simulate runaway dynamics in momentum space at several positions throughout the plasma: the magnetic axis and on rational flux surfaces with $q = 1$, $4/3$, $3/2$, 2, and 3. The resulting distributions of energy and pitch angle were input into SOFT, from which a Green's function allowed identification of contributions from each flux surface to the final synthetic image. Thus, edges detected [28] in the experimental images were mapped to the flux surface "boundary" of the synchrotron spot; this time-evolving boundary was observed to decrease in size with increases in both plasma density and MHD activity. In addition, an interesting spatial feature was measured at the onset of a locked mode; a third "leg" of the synchrotron spot was found to be located approximately at the rational surface with $q = 2$. Such spatial structure could indicate that runaways were trapped in an $\mathrm{m/n} = 2/1$ island and expelled from the plasma due to increased radial transport.

Moving beyond the identification of spatial features only, the experimental synchrotron intensity *distribution* within the images was also investigated. Due to the non-overlapping nature of SOFT-predicted emission from runaways on different flux surfaces, the Green's function approach was used to give a set of basis functions, from which a synthetic image could be constructed. In this way, the SOFT synthetic synchrotron images were fit to experiment, producing a runaway density profile evolution. Fitted synthetic images were found to match experiment well during the flattop I_p phase, but those during the I_p ramp-up did not. In addition, it was seen that the TPM could not reproduce all spatial features of experimental images; therefore, the full momentum space distributions from CODE were needed for a complete analysis. Such a procedure as that adopted in this analysis could be used to study the spatiotemporal dynamics of runaways in other current tokamaks and to make predictions for future devices and designs.

9.2.3 On the polarization of synchrotron radiation

Chapter 8 presented the first experimental analysis of polarized synchrotron emission from runaways in a tokamak plasma and showed that polarization information can be used as a novel diagnostic of the runaway pitch angle distribution. Once again, these runaway experiments were performed during low density, Ohmic, diverted plasma discharges in C-Mod. Significant levels of visible synchrotron radiation were detected by the ten-channel Motional Stark Effect (MSE) diagnostic, described in chapter 4, which measured spatial profiles of the intensity L and fraction $\mathrm{f_{pol}}$ of detected light which was linearly-polarized, as well as the polarization angle θ_pol. Data from 28 plasma discharges ($>$1000 time points), during which synchrotron-producing runaways were generated, indicated that measurements of θ_pol and $\mathrm{f_{pol}}$ are strongly dependent on the detector and magnetic geometries.

An interesting spatial feature, a 90° transition in $\theta_{\rm pol}$ first predicted by Sobolev [29], was also observed in experimental data. This trend was intuitively explained by the "cone model" of runaway synchrotron emission: Because the radiated electric field $\boldsymbol{E}$ is approximately proportional to the Lorentz acceleration $\sim \boldsymbol{v} \times \boldsymbol{B}$, horizontal or vertical polarization of synchrotron radiation is observed when the detector "sees" the top/bottom or sides, respectively, of the emission cone. Thus, a critical runaway pitch angle $\theta_{\rm p,crit}$, at which the 90° transition occurs, was calculated from the detector inclination and field-of-view opening angle, as well as local magnetic field pitch. Green's functions from SOFT confirmed the existence of $\theta_{\rm p,crit}$, at which the polarization fraction $\rm f_{pol}$ was also expected and confirmed to be minimal. From the Green's functions, powerful "look-up" plots were created from which experimental values of $\theta_{\rm pol}$ or $\rm f_{pol}$ could be used to constrain the pitch angle $\theta_{\rm p}$ of the runaways which dominate the synchrotron radiation measurement.

The spatiotemporal evolutions of L, $\theta_{\rm pol}$, and $\rm f_{pol}$ signals were explored in detail for one C-Mod discharge (actually the same as that examined in chapter 7). Like the analysis of chapter 7, experimentally-measured plasma parameters were input into CODE to calculate the momentum space distribution of runaways located at the magnetic axis and on flux surfaces with $q = 1$, 4/3, 3/2, 2, and 3. These were input into SOFT to compute synthetic signals which could then be compared to experiment. In general, synthetic $\theta_{\rm pol}$ measurements from SOFT were found to match experimental values for most channels and times. Disagreements were found in channels viewing runaways near the magnetic axis and surfaces with $q = 1$ and 4/3. When compared to the predicted runaway pitch angle distribution from CODE, it was inferred that the actual runaway pitch angle distribution was (i) dominated by *larger* pitch angles for runaways located within $q \leq 1$, but (ii) dominated by *smaller* pitch angles for runaways approximately between surfaces with $q = 1$ and 4/3, possibly indicating an interaction of the sawtooth instability and/or locked mode with runaways that was not captured by CODE. Moreover, it was seen more generally that *increasing* runaway pitch angles could give better agreement between synthetic and experimental $\rm f_{pol}$ measurements; therefore, additional pitch angle scattering mechanisms, e.g. from kinetic instabilities, may need to be incorporated in future analyses.

9.3 Opportunities for future work

Below are some opportunities for future work, listed in no particular order. Some require expertise or knowledge beyond the (current) level of the author; others would require more time than the author had or has available.

9.3.1 Kinetic simulations: non-linear and phase space evolutions

In chapter 6, a test-particle model (TPM) of runaway dynamics in momentum space—i.e. a delta function $n_\mathrm{r}\delta(\boldsymbol{p})$—was found to be sufficient when comparing experimental and synthetic synchrotron spectra. In chapter 7, it was seen that the full momentum space distribution $f(p_\parallel, p_\perp)$, calculated with the linearized kinetic equation solver CODE, was required to reproduce experimental images of synchrotron radiation. Additionally, an analysis of polarized synchrotron emission, presented in chapter 8, demonstrated the interrogation of the distribution of pitch angles θ_p in the runaway momentum space distribution function $f(p, \theta_\mathrm{p})$. For each of these analyses, *some* spatial effects were incorporated by considering runaways at different locations throughout the plasma; specifically at the magnetic axis and on a subset of the rational flux surfaces with $q = 1$, 4/3, 3/2, 2, and 3. However, as discussed in each chapter, the *lack* of an integrated model of momentum and position space evolutions required the author to *infer* spatial effects not included in the TPM or CODE, like drift orbits or radial transport due to MHD activity. This motivates the use of codes which solve the kinetic equation in *phase* space to see if spatiotemporal dynamics are adequately captured.

One candidate is the code LUKE[a] [30–32], which solves the 3D linearized, bounce-averaged drift kinetic equation for the phase space distribution function $f(\psi_\mathrm{p}, p, \theta_\mathrm{p})$. Here, ψ_p is the poloidal magnetic flux which can be mapped to the minor radius r. The bounce-average is an average over poloidal angle; specifically, "bounce" refers to particles which are *trapped* between two poloidal angles due to conservation of magnetic moment μ. Furthermore, assuming axisymmetry and averaging over the gyro-angle allow the reduction of a 6D phase space to three dimensions. It would be interesting to run LUKE for the plasma discharges analyzed in this thesis and then compare the output phase space distribution to the ad hoc, step-wise distribution functions stitched together from CODE as done in chapters 7 and 8. The radial density profile n_r should also be calculated by LUKE, but it is unclear (to the author) if or how magnetic fluctuations (from MHD activity) could be included.[b] Such a runaway density profile could be compared to those inverted from synchrotron images.

[a] LUKE stands for something like *Lower-Upper factorized solutions of the drift Kinetic Equation*.

[b] Actually, the effect of magnetic perturbations on runaway radial transport has been explored with another 3D kinetic equation solver called CQL3D [33]. This could be a candidate besides LUKE.

A step up from LUKE—both in dimensionality and computation time—is the *Kinetic Orbit Runaway electrons Code* (KORC) [34, 35], which simulates the evolution of the entire 6D phase space distribution function $f(\boldsymbol{r}, \boldsymbol{p}) = f(r, \theta, \phi, p_r, p_\theta, p_\phi)$ using a Monte-Carlo approach. These simulations are computationally-expensive, requiring hundreds of thousands of CPU-hours. Oftentimes, the simulated time, i.e. the physical time interval simulated, is ony on the order of a few microseconds. Nevertheless, KORC is able to capture all physics which can be added to the equations of motion. Interesting finite Larmor radius effects have been observed, including *collisionless* pitch angle scattering [36, 37]. This effect could play a role in the increased pitch angle scattering inferred from polarization measurements of synchrotron radiation in chapter 8.

The *NOn-linear Relativistic Solver for Electrons* (NORSE) [38] does *not* include spatial effects in its calculation of the 2D momentum space distribution function $f(p, \theta_\mathrm{p})$. However, NORSE is an improvement upon CODE[c] and LUKE because NORSE solves the fully *non-linear* kinetic equation and can thus handle scenarios when the density of runaways becomes comparable to the plasma density. NORSE was not needed for the analysis of runaways in this thesis since $I_\mathrm{r} \ll I_\mathrm{p}$ is inferred in C-Mod, at least during flattop phases of discharges without lower hybrid current drive. However, NORSE may be necessary for simulating post-disruption runaway beams which carry $I_\mathrm{r} \sim I_\mathrm{p}$ (see chapter 8). Furthermore, NORSE's capabilities allow modeling of electron "slide-away," when *all* electrons accelerate to relativistic speeds (i.e. when the electric field is comparable to the Dreicer field E_D [24, 25]). In the past, this has sometimes occurred during plasma start-up in tokamaks. Hopefully, it will not happen in any future tokamaks, but nonetheless is a fascinating plasma phenomenon.

9.3.2 New and improved diagnostics: an imaging spectropolarimeter and SOFT2

Unfortunately, there was never a runaway experiment in C-Mod during which measurements of synchrotron spectra, images, and polarization information were obtained simultaneously. Nevertheless, both images and polarization measurements were recorded for one discharge (1140403026). These data were analyzed in chapters 7 and 8, and the runaway density profile inferred from the images was used in the analysis of polarization data. Having all three sets of data could allow us to better constrain the runaway phase space distribution. Recently, the *Runaway Electron Imaging and Spectrometry* (REIS) diagnostic was developed at FTU [23] and collects both images and spectra of synchrotron radiation. The REIS system is compact and portable, allowing measurements on other devices, like ASDEX-U, TCV, and COMPASS.[d] Here, the author proposes

[c] Both CODE and NORSE were written by the same person, A. Stahl.

[d] These experiments are recent, in progress, or upcoming; the author is unaware of related publications.

an improved and novel diagnostic: an imaging spectropolarimeter (ISP) which would passively measure 2D images of polarized synchrotron emission at multiple wavelengths.

Passive imaging polarimetry has become a common technique for remote sensing [39]. One common ISP design uses dichroic mirrors to split light based on wavelength, with specialized, commercially-available cameras measuring the polarization information of the images. This method requires only as many cameras as wavelengths of interest. Considering the synchrotron spectral measurements of chapter 6, only two cameras would be needed to measure the *slope* of the visible spectra; however, three could be useful to estimate the curvature. In fact, three would be required if the peak of emission would shift into the detector spectral range; this could result from a combination of high runaway energies, runaway pitch angles, and magnetic fields. (See figure 3.2.) Construction of this ISP would require filters to select wavelength ranges not including visible line radiation, which could otherwise overwhelm and/or contaminate the signal. Absolute calibration of pixel intensity could also help determine the total runaway density.

The ISP system could even be optimized using a synthetic diagnostic such as SOFT. Green's functions $\hat{G}(R, p, \theta_{\mathrm{p}})$ could be produced for a range of detector positions, orientations, fields-of-view, spectral ranges, etc.[e] Then, the setup which provides the best interrogation of the phase space distribution could be constructed. SOFT2 [40] would be appropriate for the analysis due to its increased functionality and improved computational efficiency. For the data analysis itself, SOFT2 now includes first-order drift-orbit effects; these were speculated to be important in the interpretation of synchrotron spectra from chapter 6, but were not included in the analyses of images and polarization measurements of chapters 7 and 8. SOFT2 can be downloaded at https://github.com/hoppe93/SOFT2.

9.3.3 Machine learning methods for runaway electron studies

Finally, the author would like to mention some work in progress. As noted in chapters 6-8, inverting the runaway phase space distribution from synchrotron radiation data is difficult (and can be ill-defined when inferring 3D functions from 1D or 2D data). Machine learning algorithms may facilitate this process, especially when dealing with large parameter spaces like the SOFT Green's functions discussed in the previous section. The *Validation via Iterative Training of Active Learning Surrogates* (VITALS) [41] framework is currently being used to determine the runaway phase space distribution $f(R, p_{\perp}, p_{\parallel})$ which produces synthetic images best matching the experimental images of synchrotron radiation presented in chapter 7. VITALS employs optimized genetic algorithms to scan a parameter space, calculating the fit of synthetic and experimental

[e] Warning: These Green's functions can get quite large. Consider a phase space discretization of 200 radial points and 100 points in both $p_{\parallel}$ and $p_{\perp}$; a Green's function for the 4 Stokes parameters measured by a 200×200 pixel camera at 3 wavelengths would require almost 8 TB of storage.

images at each point. This parameter space includes features of the phase space distribution f; for instance, there could be N dimensions associated with the amplitudes of N nodes of the runaway density profile. A surrogate model then approximates the function mapping points in parameter space to the fitting figure-of-merit; if a local minimum is located, the process is repeated for a smaller region of parameter space surrounding the minimum. If VITALS converges, it outputs a vector parameterizing f which best reproduces the experimental data. It can be envisioned how multiple sets of data—i.e. images, spectra, and polarization measurements—could be used in this way to better constrain the runaway distribution function.

References—Chapter 9

[1] M. Hoppe, O. Embréus, R.A. Tinguely, R.S. Granetz, A. Stahl, and T. Fülöp. SOFT: a synthetic synchrotron diagnostic for runaway electrons. *Nuclear Fusion*, 58(2):026032, 2018. SOFT can be downloaded at https://github.com/hoppe93/SOFT, with documentation found at https://soft.readthedocs.io.

[2] R.A. Tinguely, R.S. Granetz, M. Hoppe, and O. Embréus. Measurements of runaway electron synchrotron spectra at high magnetic fields in Alcator C-Mod. *Nuclear Fusion*, 58(7):076019, 2018.

[3] R.A. Tinguely, R.S. Granetz, M. Hoppe, and O. Embréus. Spatiotemporal evolution of runaway electrons from synchrotron images in Alcator C-Mod. *Plasma Physics and Controlled Fusion*, 60(12):124001, 2018.

[4] R.A. Tinguely, M. Hoppe, O. Embréus, R.S. Granetz, S. Scott, and R.T. Mumgaard. Experimental and synthetic measurements of polarized synchrotron emission from runaway electrons in Alcator C-Mod. 2019. Submitted to *Nuclear Fusion*.

[5] R.A. Tinguely, R.S. Granetz, A. Berg, A.Q. Kuang, D. Brunner, and B. LaBombard. High-resolution disruption halo current measurements using Langmuir probes in Alcator C-Mod. *Nuclear Fusion*, 58(1):016005, 2017.

[6] R.A. Tinguely, A. Rosenthal, R. Simpson, S.B. Ballinger, A.J. Creely, S. Frank, A.Q. Kuang, B.L. Linehan, W. McCarthy, L.M. Milanese, K.J. Montes, T. Mouratidis, J.F. Picard, P. Rodriguez-Fernandez, A.J. Sandberg, F. Sciortino, E.A. Tolman, M. Zhou, B.N. Sorbom, Z.S. Hartwig, and A.E. White. Neutron diagnostics for the physics of a high-field, compact, $q \geq 1$ tokamak.

[7] R.A. Tinguely, K.J. Montes, C. Rea, R. Sweeney, and R.S. Granetz. An application of survival analysis to disruption prediction via Random Forests. 2019. Submitted to *Plasma Physics and Controlled Fusion*.

[8] A.Q. Kuang, N.M. Cao, A.J. Creely, C.A. Dennett, J. Hecla, B. LaBombard, R.A. Tinguely, E.A. Tolman, H. Hoffman, M. Major, J. Ruiz Ruiz, D. Brunner, P. Grover, C. Laughman, B.N. Sorbom, and D.G. Whyte. Conceptual design study for heat exhaust management in the ARC fusion pilot plant. *Fusion Engineering and Design*, 137:221 – 242, 2018.

[9] C. Rea, R.S. Granetz, K. Montes, R.A. Tinguely, N. Eidietis, J.M. Hanson, and B. Sammuli. Disruption prediction investigations using machine learning tools on DIII-D and Alcator C-Mod. *Plasma Physics and Controlled Fusion*, 60(8):084004, 2018.

[10] C. Rea, K.J. Montes, R.S. Granetz, R.A. Tinguely, K. Ericksson, et al. A real-time machine learning-based disruption predictor on DIII-D. 2018. Submitted to *Nuclear Fusion*.

[11] K.J. Montes, C. Rea, R.S. Granetz, R.A. Tinguely, N. Eidietis, O.M. Meneghini, D.L. Chen, B. Shen, B.J. Xiao, K. Erickson, and M.D. Boyer. Machine learning for disruption warning on Alcator C-Mod, DIII-D, and EAST tokamaks. 2018. Submitted to *Nuclear Fusion*.

[12] M.L. Reinke, S. Scott, R.S. Granetz, J.W. Hughes, S.G. Baek, S. Shiraiwa, R.A. Tinguely, S. Wukitch, and the Alcator C-Mod Team. Avoidance of impurity-induced current quench using lower hybrid current drive. 2019. Accepted for publication in *Nuclear Fusion*.

[13] J.R. Martín-Solís, R. Sánchez, and B. Esposito. Experimental observation of increased threshold electric field for runaway generation due to synchrotron radiation losses in the FTU tokamak. *Phys. Rev. Lett.*, 105:185002, 2010.

[14] A. Stahl, E. Hirvijoki, J. Decker, O. Embréus, and T. Fülöp. Effective critical electric field for runaway-electron generation. *Phys. Rev. Lett.*, 114:115002, 2015.

[15] P. Aleynikov and B.N. Breizman. Theory of two threshold fields for relativistic runaway electrons. *Phys. Rev. Lett.*, 114:155001, 2015.

[16] J.W. Connor and R.J. Hastie. Relativistic limitations on runaway electrons. *Nuclear Fusion*, 15(3):415, 1975.

[17] J.R. Martín-Solís, J.D. Alvarez, R. Sánchez, and B. Esposito. Momentum-space structure of relativistic runaway electrons. *Physics of Plasmas*, 5(6):2370–2377, 1998.

[18] M.N. Rosenbluth and S.V. Putvinski. Theory for avalanche of runaway electrons in tokamaks. *Nuclear Fusion*, 37(10):1355, 1997.

[19] H. Knoepfel and D.A. Spong. Runaway electrons in toroidal discharges. *Nuclear Fusion*, 19(6):785, 1979.

[20] R. Jaspers, N.J. Lopes Cardozo, A.J.H. Donné, H.L.M. Widdershoven, and K.H. Finken. A synchrotron radiation diagnostic to observe relativistic runaway electrons in a tokamak plasma. *Review of Scientific Instruments*, 72(1):466–470, 2001.

[21] J.H. Yu, E.M. Hollmann, N. Commaux, N.W. Eidietis, D.A. Humphreys, A.N. James, T.C. Jernigan, and R.A. Moyer. Visible imaging and spectroscopy of disruption runaway electrons in DIII-D. *Physics of Plasmas*, 20(4):042113, 2013.

[22] Z. Popovic, B. Esposito, J.R. Martín-Solís, W. Bin, P. Buratti, D. Carnevale, F. Causa, M. Gospodarczyk, D. Marocco, G. Ramogida, and M. Riva. On the measurement of the threshold electric field for runaway electron generation in the Frascati Tokamak Upgrade. *Physics of Plasmas*, 23(12):122501, 2016.

[23] B. Esposito, L. Boncagni, P. Buratti, D. Carnevale, F. Causa, M. Gospodarczyk, J.R. Martín-Solís, Z. Popovic, M. Agostini, G. Apruzzese, W. Bin, C. Cianfarani, R. De Angelis, G. Granucci, A. Grosso, G. Maddaluno, D. Marocco, V. Piergotti, A. Pensa, S. Podda, G. Pucella, G. Ramogida, G. Rocchi, M. Riva, A. Sibio, C. Sozzi, B. Tilia, O. Tudisco, M. Valisa, and FTU Team. Runaway electron generation and control. *Plasma Physics and Controlled Fusion*, 59(1):014044, 2017.

[24] H. Dreicer. Electron and ion runaway in a fully ionized gas. I. *Physical Review*, 115:238–249, 1959.

[25] H. Dreicer. Electron and ion runaway in a fully ionized gas. II. *Physical Review*, 117:329–342, 1960.

[26] M. Landreman, A. Stahl, and T. Fülöp. Numerical calculation of the runaway electron distribution function and associated synchrotron emission. *Computer Physics Communications*, 185(3):847 – 855, 2014.

[27] A. Stahl, O. Embréus, G. Papp, M. Landreman, and T. Fülöp. Kinetic modelling of runaway electrons in dynamic scenarios. *Nuclear Fusion*, 56(11):112009, 2016.

[28] I. Sobel and G. Feldman. A 3×3 isotropic gradient operator for image processing, 1968. Presented at the Stanford Artificial Intelligence Project.

[29] Ya.M. Sobolev. Polarization of synchrotron radiation from relativistic electrons moving within toroidal magnetic fields. *Problems of Atomic Science and Technology*, 4(86):108–111, 2013.

[30] Y. Peysson, J. Decker, and R.W. Harvey. Advanced 3-D Electron Fokker-Planck Transport Calculations. In *AIP Conference Proceedings*, volume 694, pages 495–498. AIP, 2003.

[31] J. Decker and Y. Peysson. DKE: A fast numerical solver for the 3D drift kinetic equation. *Euratom-CEA Report No. EUR-CEA-FC-1736*, 2004.

[32] E. Nilsson, J. Decker, Y. Peysson, R.S. Granetz, F. Saint-Laurent, and M. Vlainic. Kinetic modelling of runaway electron avalanches in tokamak plasmas. *Plasma Physics and Controlled Fusion*, 57(9):095006, 2015.

[33] R.W. Harvey, V.S. Chan, S.C. Chiu, T.E. Evans, M.N. Rosenbluth, and D.G. Whyte. Runaway electron production in DIII-D killer pellet experiments, calculated with the CQL3D/KPRAD model. *Physics of Plasmas*, 7(11):4590–4599, 2000.

[34] L. Carbajal and D. del Castillo-Negrete. On the synchrotron emission in kinetic simulations of runaway electrons in magnetic confinement fusion plasmas. *Plasma Physics and Controlled Fusion*, 59(12):124001, 2017.

[35] L. Carbajal, D. del Castillo-Negrete, D. Spong, S. Seal, and L. Baylor. Space dependent, full orbit effects on runaway electron dynamics in tokamak plasmas. *Physics of Plasmas*, 24(4):042512, 2017.

[36] J. Liu, Y. Wang, and H. Qin. Collisionless pitch-angle scattering of runaway electrons. *Nuclear Fusion*, 56(6):064002, may 2016.

[37] C. Liu, H. Qin, E. Hirvijoki, Y. Wang, and J. Liu. Conservative magnetic moment of runaway electrons and collisionless pitch-angle scattering. *Nuclear Fusion*, 58(10):106018, aug 2018.

[38] A. Stahl, M. Landreman, O. Embréus, and T. Fülöp. NORSE: A solver for the relativistic nonlinear Fokker–Planck equation for electrons in a homogeneous plasma. *Computer Physics Communications*, 212:269 – 279, 2017.

[39] J.S. Tyo, D.L. Goldstein, D.B. Chenault, and J. Shaw. Review of passive imaging polarimetry for remote sensing applications. *Applied Optics*, 45:5453–69, 2006.

[40] M. Hoppe *et al*. SOFT2 can be downloaded at https://github.com/hoppe93/SOFT2.

[41] P. Rodriguez-Fernandez, A.E. White, A.J. Creely, M.J. Greenwald, N.T. Howard, F. Sciortino, and J.C. Wright. VITALS: A Surrogate-Based Optimization Framework for the Accelerated Validation of Plasma Transport Codes. *Fusion Science and Technology*, 74(1-2):65–76, 2018.

Appendix A

Post-disruption runaways: scalings with B and R

In this section, we do some back-of-the-envelope calculations of *post-disruption* runaway parameters, like individual particle energy, total runaway beam energy/current, etc. It is of interest to see how these quantities scale with toroidal magnetic field B and machine size, denoted by the major radius R (where the subscript 0 is suppressed). In this way, we can semi-quantitatively compare the compact, high-field tokamak approach (e.g. SPARC, ARC) to the large, normal-field approach (e.g. ITER, DEMO). The general aim is to minimize both the energy *per runaway electron* as well as *total* energy of the runaway population. The former affects runaway penetration depth into materials; for instance, according to [115, 131], the penetration depths of 12.5 MeV runaways into beryllium, carbon, and tungsten are 2.5, 2.0, and 0.15 mm, respectively. Higher energies would likely lead to deeper penetration, which could reach cooling channels or electronics. The threat of total runaway beam energy dissipation is more likely melting of plasma-facing components. For example, in JET it was estimated that the first wall heat flux from a runaway strike (all with energies of 12.5 MeV) reached $\sim$400 MW/m^2, leading to a wall temperature increase of over 300 K [115].

For the purposes of this section, energies per particle will be assigned the variable ε, while $\mathcal{E}$ will be used for total energies of the entire runaway population/beam. The quantities of interest, their scalings with B and R, and a comparison of ITER to SPARC are summarized in table A.1 at the end of this section.

A.1 Assumptions

Below is a list of assumptions made for the following analyses. Much theoretical work has been done to predict post-disruption runaway evolution and its impact on the tokamak. These consider the runaway seed population, post-thermal-quench plasma temperature, toroidal magnetic ripple, and more. Here, the point is not to dive into details, but to provide a physically-motivated and plausible picture of runaway parameter scalings with field.[a] Therefore, the following are assumed to simplify equations and investigate solely the B and R dependencies:

(i) The aspect ratio $A = R/a$ is assumed to be constant for all tokamaks. For current experiments, $A \approx 3$. This means $a \propto R$.

(ii) The edge safety factor $q_{95} \approx q_a = B_\mathrm{t} a / B_\mathrm{p}(a) R$ is assumed to be constant for all plasmas. Note that there exists an empirical lower bound of $q_{95} \gtrsim 3$ to avoid disruptions. This neglects advanced tokamak scenarios.

(iii) Runaways are assumed to travel at $v = c$. For highly relativistic runaways (with energies $\gtrsim$10 MeV), this is a good approximation.

A.2 Considering total energy conversion

The poloidal magnetic field at the plasma edge $B_\mathrm{p}(a)$ can be related to the plasma current I_p by Ampere's law

$$B_\mathrm{p}(a) \propto \frac{\mu_0 I_\mathrm{p}}{2\pi a}, \tag{A.1}$$

where the proportionality indicates that shaping factors (like elongation) are not explicit. Therefore, $B_\mathrm{p}(a) \propto I_\mathrm{p}/R$, using assumption (i). The edge safety factor then satisfies

$$q_a \propto \frac{B}{R}\frac{2\pi a^2}{I_\mathrm{p}} \propto \frac{BR}{I_\mathrm{p}}. \tag{A.2}$$

Assumption (ii) implies $I_\mathrm{p} \propto BR$. Note here that this could be relaxed, since decreasing I_p increases q_a and actually makes plasma operation *safer*, i.e. lowers the chance of disruption. However, I_p is also usually maximized in order to improve confinement and performance.

As described in section 2.1, the runaway density n_r can grow exponentially through knock-on avalanching, taking the form

$$\Gamma_\mathrm{exp} = \frac{1}{n_\mathrm{r}}\frac{\mathrm{d}n_\mathrm{r}}{\mathrm{d}t} \propto I_\mathrm{p} \propto BR. \tag{A.3}$$

[a] Also, the author is not a theorist.

This implies that the rate of exponential runaway growth scales the same with B as with R.

The total magnetic energy carried by the plasma is

$$W_{\mathrm{mag}} = \frac{1}{2} L I_{\mathrm{p}}^2, \tag{A.4}$$

where $L \approx \mu_0 R$ is the plasma inductance. Therefore, the magnetic energy scales as $W_{\mathrm{mag}} \propto B^2 R^3$, which can be thought of as the energy density of the magnetic field B^2 multiplied by the volume R^3. Obviously, the worst-case scenario for post-disruption runaways is if all plasma magnetic energy is transferred to the runaway beam. Then, the maximum total energy of the runaway beam would be

$$\mathcal{E}_{\mathrm{max}} \propto B^2 R^3. \tag{A.5}$$

While this scales favorably with neither B nor R—i.e. it would be best to minimize both—doubling B is better than doubling R. For a comparison of values for ITER and SPARC, see table A.1.

It is also important to consider the final impact of runaways on the vacuum vessel if they lose confinement. In many experiments, damage from runaways is quite localized (for instance to a few tiles on one limiter, as shown in figure 1.6), but advanced mitigation strategies which introduce 3D magnetic perturbations could create stochastic fields which "spread" unconfined/lost runaways over the entire first wall [47]. If the first wall surface area is $S \approx 2\pi R \times 2\pi a \propto R^2$, the runaway energy flux is bounded below by

$$\Phi_{\mathrm{r}} \geq \frac{\mathcal{E}_{\mathrm{max}}}{S} \propto B^2 R. \tag{A.6}$$

In this case, doubling B is *worse* than doubling R.

We now consider the runaway energy *per particle*, which determines the penetration depth of runaways into materials (e.g. puncturing a cooling channel), as well as the upper bound energy of bremsstrahlung radiation (e.g. gammas produced on runaway wall impact)[b]. Assuming all runaways travel at the speed of light, by assumption (iii), the number of runaways N_{r} needed to sustain the plasma current (i.e. $I_{\mathrm{r}} = I_{\mathrm{p}}$ in the worst-case scenario) is given by

$$I_{\mathrm{p}} = I_{\mathrm{r}} = \frac{ecN_{\mathrm{r}}}{2\pi R}, \tag{A.7}$$

Therefore, $N_{\mathrm{r}} \propto BR^2$. Again, doubling B is better than doubling R. The *average* runaway

[b] This actually occurred due to runaway slide-away during one plasma start-up in the WEST tokamak. Localized gamma radiation, resulting from runaways impacting the first wall, heated the nearest superconducting toroidal field coil enough to quench it.

energy in this scenario of total current conversion is

$$\varepsilon_{\max} = \frac{\mathcal{E}_{\max}}{N_{\mathrm{r}}} \propto BR, \tag{A.8}$$

which is the same relationship found in [46]. Remember that this is the *worst-case* scenario. While many experiments have observed partial or even full conversion of I_{p} into I_{r}, there are many power loss mechanisms, including collisions, radiation, and kinetic instabilities which we have not yet taken into account.

A.3 Considering synchrotron power loss

During a disruption, it is the rapid decay of I_{p} which induces a large enough electric field to accelerate runaways. However, this E-field only exists during the time of the current quench (CQ); thus, runaways have only a finite amount of time to gain energy. Moreover, they are subject to other power loss mechanisms. Runaways will experience collisional friction with the background plasma, but the drag force is often negligible compared to the driving electric force during a disruption, i.e. $E/E_{\mathrm{C}} \gg 1$. For tokamaks with strong enough B, synchrotron radiation can dominate as a power loss mechanism, following the usual relation

$$P_{\mathrm{synch}} \propto p_{\perp}^2 B^2. \tag{A.9}$$

Therefore, power balance gives

$$P_{\mathrm{tot}} = P_{\mathrm{elec}} - P_{\mathrm{coll}} - P_{\mathrm{synch}} \approx eEc - \alpha p_{\perp}^2 B^2. \tag{A.10}$$

Here, P_{coll} was neglected, and α is a constant which is explicit in (2.21). The driving electric field can be written

$$E \approx \frac{V_{\mathrm{loop}}}{2\pi R} = \frac{L}{2\pi R}\frac{\Delta I_{\mathrm{p}}}{\Delta t}, \tag{A.11}$$

where $L \propto R$ is again the plasma inductance.

The pitch angle of a runaway electron is such that $p_{\perp} = p\sin\theta_{\mathrm{p}}$. Note that θ_{p} can change in time and with B (by conservation of magnetic moment), but the bulk of the runaway population usually has $\theta_{\mathrm{p}} \leq 0.3$ rad. Furthermore, we are interested in the extreme scenario in which runaways reach the maximum energy limited by synchrotron emission, i.e. $P_{\mathrm{elec}} = P_{\mathrm{synch}}$. Then,

$$p^2 B^2 \propto \frac{I_{\mathrm{p}}}{\Delta t}, \tag{A.12}$$

where it is assumed that *all* of I_p decays in time Δt. Both in experiments and simulations, it has been observed that $\Delta t \propto R^\mathrm{m}$, where m is a positive integer. For instance, in the database study of [132], the minimum CQ time was found empirically to be $\Delta t/S \geq 1.7$ ms/m^2, where $S \propto \pi a^2$ is the plasma cross-sectional area. Thus, $\mathrm{m} = 2$ implies that the CQ is a diffusive process. In another study [76], runaway test particles were tracked as they followed magnetic field lines (some closed, others stochastic) during a disruption simulated in NIMROD [133]. The characteristic runaway confinement time was found to scale as $\Delta t \propto R^3$. While a runaway confinement time is not necessarily the same as the current decay time, runaways cannot carry current if they are no longer confined, so it is an upper bound. The parameter m is left free in the following analyses.

Rearranging (A.12) and substituting the scalings for I_p and Δt, the maximum runaway energy per particle when accounting for synchrotron power loss is

$$\varepsilon_\mathrm{synch} \approx pc \propto B^{-1/2} R^{(1-\mathrm{m})/2}. \tag{A.13}$$

For $\mathrm{m} \geq 2$, this calculation implies that it is favorable to maximize *both* B and R to reduce the maximum energy per particle. Once again, conservatively assuming that all of I_p is converted into I_r, the *total* runaway beam energy, when including synchrotron emission, is

$$\mathcal{E}_\mathrm{synch} = \varepsilon_\mathrm{synch} \times N_\mathrm{r} \propto B^{1/2} R^{(5-\mathrm{m})/2}. \tag{A.14}$$

Thus, for $\mathrm{m} = 2$ or 3, the total runaway beam energy scales with R at *most* as favorably as with B. For completeness, the energy flux over the entire first wall is

$$\Phi_\mathrm{r,synch} \geq \frac{\mathcal{E}_\mathrm{synch}}{S} \propto B^{1/2} R^{(1-\mathrm{m})/2}, \tag{A.15}$$

which scales more favorably with R than B.

A.4 Other considerations

In reality, designing a fusion reactor is a complex optimization problem. Perhaps the most important consideration is maximizing fusion power, which scales as

$$P_\mathrm{fus} \propto \beta^2 B^4 R^3, \tag{A.16}$$

where the plasma β is the ratio of thermal to magnetic pressure, and the latter goes like the magnetic energy density B^2. Assuming constant β, which has its own empirical limit, P_fus scales more favorably with B than R. This is, of course, a strong motivation for the high-field, compact

(HFC) approach.

However, economics also drives design, since the electricity produced must ultimately be affordable. It is reasonable that cost scales with the volume ($\sim R^3$), but how about with B? This analysis is outside the scope of this thesis work; however, note that if we construct an ad hoc relation

$$\text{Cost} \propto B^j R^3, \tag{A.17}$$

only $j \leq 3$ is required for a HFC tokamak to be competitive economically.

A.5 Summary

This section investigated how post-disruption runaway parameters scale with toroidal magnetic field B and major radius R. A summary of the parameters of interest, their scalings, and the ratio of values between ITER and SPARC are given in table A.1 below. The primary assumptions made were (i) that all tokamaks have constant aspect ratios and (ii) that all plasmas have the same edge safety factor. From these, it was derived that the runaway avalanching rate scales as $\Gamma_{\rm exp} \propto BR$. To estimate individual and total runaway energies, two simple scenarios were considered; in both, the pre-disruption plasma current $I_{\rm p}$ was assumed to be totally converted into runaway current $I_{\rm r}$. In the first worst-case scenario, the pre-disruption magnetic energy was totally converted into runaway energy. For this case, the energies of a single runaway and full runaway beam scale as BR and B^2R^3, respectively.

Table A.1: A summary of post-disruption runaway parameters calculated in this section, and the ratio of values for ITER-to-SPARC. The toroidal magnetic field and major radius from table 1.2 are used: For ITER, $B = 5.3$ T and $R = 6.2$ m. For SPARC, $B = 12$ T and $R \approx 1.7$ m. Value pairs correspond to $\mathrm{m} = 2, 3$ respectively.

Parameter	Scaling	ITER/SPARC	Equation
$P_{\rm fus}$	B^4R^3	1.8	(A.16)
$\Gamma_{\rm exp}$	BR	1.6	(A.3)
$N_{\rm r}$	BR^2	5.9	(A.7)
$\varepsilon_{\rm max}$	BR	1.6	(A.8)
$\mathcal{E}_{\rm max}$	B^2R^3	9.5	(A.5)
$\Phi_{\rm r}$	B^2R	0.7	(A.6)
$\varepsilon_{\rm synch}$	$B^{-1/2}R^{(1-\mathrm{m})/2}$	0.8, 0.4	(A.13)
$\mathcal{E}_{\rm synch}$	$B^{1/2}R^{(5-\mathrm{m})/2}$	4.6, 2.4	(A.14)
$\Phi_{\rm r,synch}$	$B^{1/2}R^{(1-\mathrm{m})/2}$	0.3, 0.2	(A.15)

In the second more realistic case, the runaways were assumed to reach an energy at which the electric force balances the synchrotron radiation reaction force. Here, it was found that the energies of a single runaway and full runaway beam scale as $(BR)^{-1/2}$ and $B^{1/2}R^{3/2}$, respectively, when using the multi-tokamak empirical scaling of the current quench time, $\Delta t \propto R^2$ (i.e. $\mathrm{m} = 2$).

These results indicate that increasing B is *as favorable as or more favorable than* increasing R when trying to minimize runaway energies and currents. However, this is not always the case with runaway energy fluxes to the first wall. It should be noted that this energy flux scaling relied on the assumption that runaways impact the wall uniformly, which is not always seen in experiment and may not be achievable in future devices.

When comparing two upcoming machines, ITER and SPARC, it appears that ITER will have the worse runaway problem: the growth rate, number, and total energies of runaways are all higher for ITER compared to SPARC. On the other hand, individual runaway energies and fluxes to the first wall may be lower in ITER than SPARC. In the end, these results suggest that the threat of high energy runaways and runaway beams is reduced for some high-field, compact tokamaks.

This page intentionally left blank

Appendix B

Modeling polarized synchrotron radiation and synthetic measurements in SOFT

This section describes the modeling of polarized synchrotron light and accompanying synthetic diagnostic simulations in SOFT. This is needed not only to understand the trends seen in experimental data, but also to validate theoretical models of runaway phase space evolution, which should reproduce experimental results. First, the polarization of synchrotron emission and Stokes parameters are briefly re-introduced in section B.1. Section B.2 then describes the implementation of a synthetic polarimeter in SOFT. Finally, section B.3 puts the pieces together, detailing the synthetic Stokes vector calculation for synchrotron radiation from a given runaway phase space distribution. This work has been submitted for publication in *Nuclear Fusion* [23]. The author of this thesis would like to acknowledge M. Hoppe and O. Embréus, the creators of SOFT, who performed these derivations and actually did the coding.

B.1 Polarization of synchrotron emission

For a single runaway electron, it is often simplest to decompose the synchrotron radiation electric field vector as done in [134]

$$\boldsymbol{E} = \hat{e}_\perp E_\perp + i\hat{e}_\parallel E_\parallel. \tag{B.1}$$

Here, $\hat{e}_\parallel$ is a unit vector in the direction of acceleration, pointing (mostly) toward the magnetic field line for a runaway in gyro-motion, and $\hat{e}_\perp = \hat{n} \times \hat{e}_\parallel$, where $\hat{n}$ is a unit vector directed from the electron toward the observer. Recall that for synchrotron radiation, the acceleration vector is determined by the Lorentz force, meaning that $\hat{e}_\parallel \propto \boldsymbol{v} \times \boldsymbol{B}$, with $\boldsymbol{v}$ denoting the electron velocity and $\boldsymbol{B}$ the local magnetic field vector. It can be shown that for highly relativistic electrons, $E_\parallel \gg E_\perp$, so that the radiation is mainly linearly-polarized in the $\hat{e}_\parallel$ direction [135].

As discussed in chapter 3, a convenient—and complete—way of expressing the polarization of electromagnetic radiation is using the four Stokes parameters [136], now written in the *particle-dependent* basis $(\hat{e}_\parallel, \hat{e}_\perp)$

$$I = |E_\perp|^2 + |E_\parallel|^2, \tag{B.2}$$
$$Q = |E_\perp|^2 - |E_\parallel|^2, \tag{B.3}$$
$$U = 2\mathrm{Re}\left(E_\perp E_\parallel^*\right), \tag{B.4}$$
$$V = -2\mathrm{Im}\left(E_\perp E_\parallel^*\right). \tag{B.5}$$

Once again, the asterisk $(^*)$ denotes the complex-conjugate. Our observables are straightforwardly calculated from the Stokes parameters: I is just the total intensity. The intensity of *linearly*-polarized light is $L = \sqrt{Q^2 + U^2}$, and the degree of linear polarization is $\mathrm{f_{pol}} = \mathrm{f_{lin}} = L/I$. The degree of *circular* polarization is given by $\mathrm{f_{circ}} = V/I$, although synchrotron emission from highly relativistic electrons is *not* expected to have significant circular polarization [137]. Finally, the polarization angle, measured from $\hat{e}_\perp$ toward $\hat{e}_\parallel$ in this case, is $2\theta_{\mathrm{pol}} = \arctan(U/Q)$.

Recall that the "total" Stokes parameters of radiation produced by an ensemble of particles, with many different radiation fields $\boldsymbol{E}$, can be determined simply by a linear combination of individual Stokes *vectors* $[I, Q, U, V]$. However, this assumes that all Stokes vectors are measured in the same basis. This is *not* the case for the formulation of the Stokes parameters in (B.2)-(B.5); therefore, we must transform each $\boldsymbol{E}$ from the particle frame to the laboratory frame, as discussed in the next section.

B.2 Modeling a polarimeter in SOFT

Since the purpose of SOFT is to simulate the signals reported by synchrotron radiation diagnostics, the definitions of the Stokes parameters in SOFT must correspond to those used by a diagnostic. For example, the definitions (B.2)-(B.5) in section B.1 use a *radiation-local* coordinate system, whereas a diagnostic will measure the radiation in a fixed coordinate system that is independent of the propagation direction of the radiation. Thus, a realistic polarimeter must be modeled in SOFT.

A simple model for a polarization-measuring diagnostic can be obtained starting from the idealized setup shown in figure B.1: A polarizer, or polarized filter, is placed at point A' between an emitter at A and an observer at A''. As shown in [138], if the polarizer consists of just a linear polarization filter with its transmission axis $\hat{t}$ rotated about the $\hat{z}$-axis by an angle Υ from the

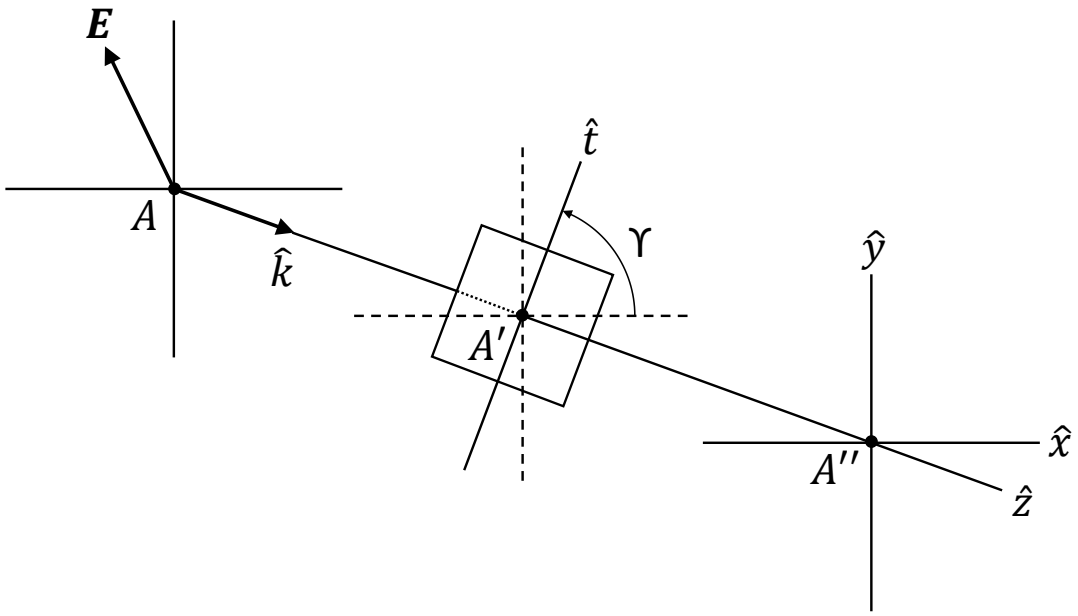

Figure B.1: Illustration of an idealized setup for measuring the four Stokes parameters. Polarized radiation $\boldsymbol{E}$ emitted at A along $\hat{k} = \hat{z}$ is incident on the linear polarization filter with transmission axis $\hat{t}$ at A'. By rotating the polarization filter between $\Upsilon = 0$, $\pi/4$, and $\pi/2$, we can solve for I, Q, and U from the measured intensity at A''. To also obtain V, we introduce a phase-shift between the electric field components by putting a quarter-wave plate in front of the linear polarizer.

horizontal, then the spectral radiance at A'' is given by

$$\mathcal{I}(\Upsilon) = \frac{1}{2}\left[I + Q\cos(2\Upsilon) + U\sin(2\Upsilon)\right]. \tag{B.6}$$

If a quarter-wave plate[a] is placed in front of the linear polarizer, so that the relative phase of the electric field components is shifted, the spectral radiance measured at A'' is then

$$\mathcal{I}_{\lambda/4}(\Upsilon) = \frac{1}{2}\left[I + Q\cos(2\Upsilon) + V\sin(2\Upsilon)\right]. \tag{B.7}$$

[a]A quarter-wave plate is usually a birefringent crystal with a polarization-dependent refractive index N. For orthogonal "fast" and "slow" axes, light polarized in the direction of the fast axis travels with a faster phase velocity ($v = c/N$) than light polarized along the slow axis.

Thus, by measuring the spectral radiance at A'' with the linear polarizer rotated to $\Upsilon = 0$, $\pi/4$, and $\pi/2$, as well as at $\Upsilon = \pi/4$ with the quarter-wave plate, we can solve for the Stokes parameters of the radiation field $\boldsymbol{E}$:

$$I = \mathcal{I}(0) + \mathcal{I}(\pi/2), \tag{B.8}$$

$$Q = \mathcal{I}(0) - \mathcal{I}(\pi/2), \tag{B.9}$$

$$U = 2\mathcal{I}(\pi/4) - \mathcal{I}(0) - \mathcal{I}(\pi/2), \tag{B.10}$$

$$V = 2\mathcal{I}_{\lambda/4}(\pi/4) - \mathcal{I}(0) - \mathcal{I}(\pi/2). \tag{B.11}$$

In SOFT, equations (B.8)-(B.11) are taken as the definitions of the Stokes parameters. In the idealized setup of figure B.1, where radiation is incident on the polarizer perpendicularly, these definitions correspond to the usual definitions (B.2)-(B.5) in section B.1. However, when radiation is incident on the polarizer along $\hat{k} \neq \hat{z}$, the relations (B.8)-(B.11) become approximate, with errors of order $1 - (\hat{k} \cdot \hat{z})^2$. Since the angle between $\hat{k}$ and $\hat{z}$ is always less than the detector FOV opening half-angle α, the error is less than $\sin^2 \alpha$. For the Motional Stark Effect (MSE) diagnostic, described in chapter 4 and used for synchrotron polarization measurements in chapter 8, each channel has $\alpha \approx 0.9°$, meaning that the error is small, on the order of $\sim 10^{-4}$. Thus, (B.8)-(B.11) are good approximations of the Stokes parameters for the analysis of polarization measurements made by the MSE system.

Since electrons can be located anywhere in the tokamak, the direction of propagation $\hat{k}$ of the radiation and polarizer surface normal ($\hat{z}$ in this case) are usually *not* parallel; this must be taken into account when modeling the linear polarizer. In general, the spectral radiance is equal to

$$\mathcal{I}(\Upsilon) = \epsilon_0 c |\boldsymbol{E}_{\text{in}}|^2 = \epsilon_0 c |\mathbf{T}(\Upsilon)\boldsymbol{E}|^2, \tag{B.12}$$

where $\boldsymbol{E}_{\text{in}}$ is the electric field vector incident *on the detector*, and the operator $\mathbf{T}(\Upsilon)$ describes the action of the polarizer on the emitted field $\boldsymbol{E}$. In the case when the polarizer consists of both a linear polarization filter and a quarter-wave plate, we can write $\mathbf{T}$ as the product between two matrices describing the action of each element, i.e. $\mathbf{T}(\Upsilon) = \mathbf{T}_{\lambda/4}\mathbf{T}_{\text{p}}(\Upsilon)$, where $\mathbf{T}_{\text{p}}$ describes the action of the linear polarizer and $\mathbf{T}_{\lambda/4}$ the action of the quarter-wave plate. If the quarter-wave plate is oriented with its fast axis[a] along $\hat{x}$ (and thus slow axis along $\hat{y}$), $\mathbf{T}_{\lambda/4}$ can be written in dyadic notation as

$$\mathbf{T}_{\lambda/4} = \hat{x}\,\hat{x} + \hat{y}\,\hat{y}\; e^{-i\pi/2} + \hat{z}\,\hat{z}\,. \tag{B.13}$$

For the linear polarization filter, represented by $\mathbf{T}_\mathrm{p}$, SOFT uses the model presented in [139], which describes the action of a linear polarization filter on obliquely incident radiation. The model assumes that the filter absorbs radiation along its absorption axis $\hat{a}$, which is perpendicular to the transmission axis $\hat{t}$, so that in the setup of figure B.1 the absorption axis becomes

$$\hat{a}(\Upsilon) = \hat{y}\,\cos\Upsilon - \hat{x}\,\sin\Upsilon. \tag{B.14}$$

When the radiation is not incident on the filter perpendicularly as in figure B.1, i.e. when $\hat{k} \neq \hat{z}$, radiation is instead assumed as absorbed along an *effective* absorption axis $\hat{a}_\mathrm{eff}$,[b] which is the projection of $\hat{a}$ onto the plane of the polarized radiation

$$\hat{a}_\mathrm{eff}(\Upsilon) = \frac{\hat{a} - \hat{k}(\hat{a}\cdot\hat{k})}{\sqrt{1-(\hat{a}\cdot\hat{k})^2}}, \tag{B.15}$$

where the denominator preserves the normalization. Using $\hat{a}_\mathrm{eff}$, the matrix $\mathbf{T}_\mathrm{p}$ for the linear polarizer can be written

$$\mathbf{T}_\mathrm{p}(\Upsilon) = \mathsf{I} - \hat{a}_\mathrm{eff}\hat{a}_\mathrm{eff}, \tag{B.16}$$

with I denoting the identity matrix. Hence, the measured spectral radiances are

$$\mathcal{I}(\Upsilon) = \epsilon_0 c|\boldsymbol{E} - \hat{a}_\mathrm{eff}\,(\hat{a}_\mathrm{eff}\cdot\boldsymbol{E})\,|^2, \tag{B.17}$$

$$\mathcal{I}_{\lambda/4}(\Upsilon) = \epsilon_0 c|\mathbf{T}_{\lambda/4}\boldsymbol{E} - \hat{a}_\mathrm{eff}\left[\hat{a}_\mathrm{eff}\cdot\left(\mathbf{T}_{\lambda/4}\boldsymbol{E}\right)\right]|^2, \tag{B.18}$$

without and with the quarter-wave plate, respectively.

[b] Check out that alliteration!

B.3 Synchrotron Stokes vector from a phase space distribution

So far, we have only considered the radiation field from one runaway electron. Here, we detail the Stokes vector calculation of synchrotron radiation from an entire phase space distribution $f(\boldsymbol{r}, \boldsymbol{p})$ of runaways. The procedure is as follows:

i. At each point $(\boldsymbol{r}, \boldsymbol{p})$ in (a discretized) phase space, the radiated electric field $\boldsymbol{E}$ is calculated. Actually, SOFT calculates a vector-potential-like quantity $\boldsymbol{A} = X\boldsymbol{E}$, as done in [134], where X is the distance between the emitting electron and detector—see (5.5). In the end, the calculation is similar to (3.29).

ii. For each $\boldsymbol{E}$, the spectral radiances, from (B.17) and (B.18), are calculated for different polarization states $\Upsilon = 0$, $\pi/4$, and $\pi/2$. The polarizer-action matrices $\mathbf{T}_{\mathrm{p}}$ and $\mathbf{T}_{\lambda/4}$ are also determined by the detector geometry.

iii. The Stokes vector for each $\boldsymbol{E}$ is calculated from the spectral radiances via (B.2)-(B.5). These are all now in the fixed detector basis.

iv. The power per unit solid angle Ω per unit wavelength λ can be related to the spectral radiance by

$$\frac{\mathrm{d}^2 P(\Upsilon)}{\mathrm{d}\Omega \mathrm{d}\lambda} = X^2 \mathcal{I}(\Upsilon). \tag{B.19}$$

This is the angular/spectral power density "contained" in each polarization state. Note that in the actual SOFT calculation, the X^2 term naturally comes from $|\boldsymbol{A}|^2 = X^2 |\boldsymbol{E}|^2$.

v. Because the total Stokes vector is just the sum of all individual Stokes vectors, this amounts to integration of the Stokes parameters over the phase space distribution function $f(\boldsymbol{r}, \boldsymbol{p})$. Thus, (B.19) is substituted into (5.5); integrations are performed for $\Upsilon = 0$, $\pi/4$, and $\pi/2$; and the appropriate arithmetic from (B.2)-(B.5) is carried out to obtain the total Stokes parameters.

Appendix C

Synchrotron radiation produced by runaways in a time-dependent B-field

For one C-Mod discharge (1160824028)[a], synchrotron emission was measured from runaways while the magnetic field was ramped from $B_0 =$ 5.4-6.2 T over ∼600 ms. While hopes were high, the impact of the B-field ramp on synchrotron spectral measurements was relatively minor and practically unmeasureable. Nevertheless, this experiment was an important attempt to reproduce the results obtained in the DIII-D tokamak [81], so it is included for completeness. The following sections will detail the experimental parameters, test-particle model (TPM) dynamics of runaways, inferences made from synchrotron spectra, and comparisons with the similar experiment performed at DIII-D.

C.1 Experimental data

The bulk plasma parameters and those for specific flux surfaces (the magnetic axis and surfaces with $q = 1$, 3/2, and 2) are shown in figure C.1. As is seen in figure C.1b, the plasma density decreases during the current flattop in order to increase the electric force relative to collisional drag; the ratio E/E_C increases above 10 for times $t >$ 0.5 s. The HXR signal becomes detectable at $t \approx$ 0.7 s, while synchrotron emission increases at $t \approx$ 1.0 s, as seen in figure C.1f. This is consistent with energies increasing from the (hundreds of) keV to MeV range from $t \approx$ 0.7-1.0 s. However, the parameter of most interest in this discharge is the toroidal magnetic field, which increases (approximately) linearly in time from $B_0 =$ 5.4-6.2 T over $t \approx$ 1-1.6 s. This was done to determine the effect of increasing B_0 on flattop runaways.

[a]This discharge ended with runaways impacting a limiter, producing the shower of molten metal seen in figure 1.6.

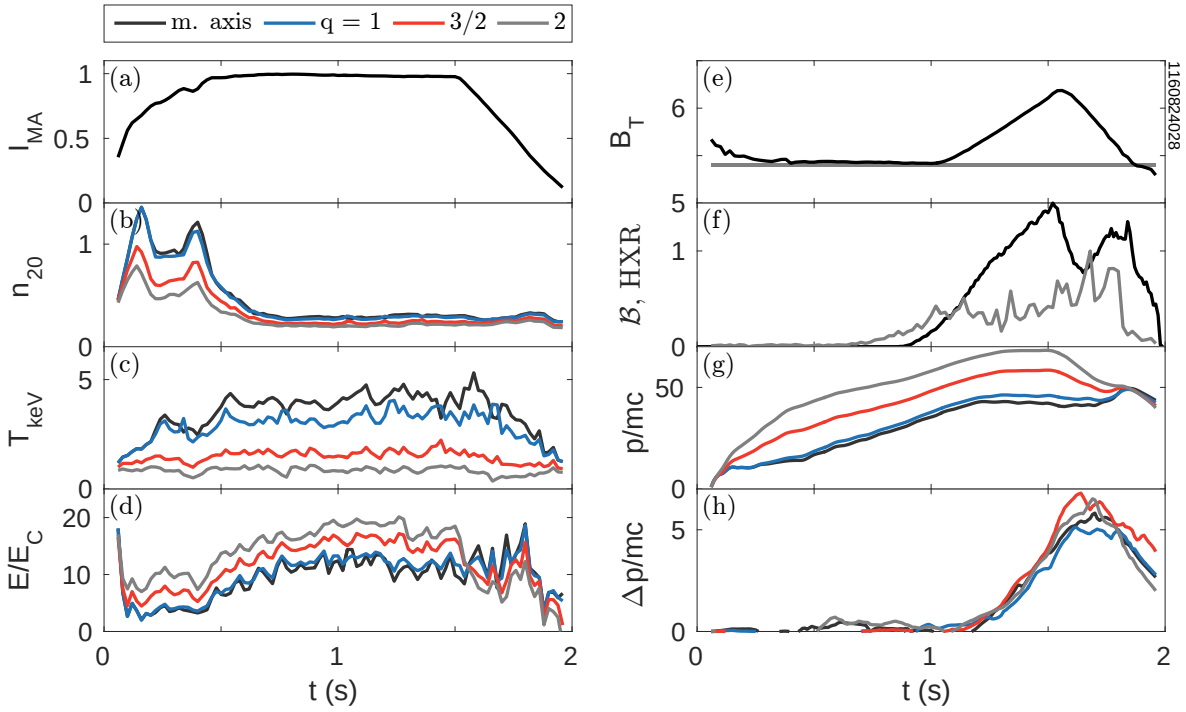

Figure C.1: Plasma parameters at the magnetic axis and flux surfaces with $q = 1$, 3/2, and 2 for Alcator C-Mod discharge 1160824028: (a) plasma current in MA, (b) electron density in 10^{20} m^{-3}, (c) electron temperature in keV, (d) ratios of electric to critical field, (e) toroidal magnetic field on axis (black) and $B_0 = 5.4$ T (grey), (f) synchrotron brightness measured at $\lambda = 850$ nm (black, a.u.) and HXR signal (grey, a.u.), (g) normalized total momentum, and (h) the estimated *change* in momentum if B_0 was instead held constant, as shown in (e).

C.2 Test-particle model dynamics

A TPM of runaway momenta and density is used (as done for the discharges in chapter 6) to estimate runaway dynamics in both real space (at the magnetic axis and flux surfaces with $q = 1$, 3/2, and 2) and in time. For this analysis, the effect of increasing B_0 on the predicted runaway momentum was investigated. Therefore, two TPMs were run: the first including the ramp in B_0, and the second with a constant $B_0 = 5.4$ T. The resulting p/mc of the former (B ramp) case is shown in figure C.1g. As is seen, p/mc is predicted to be highest on outer flux surfaces since the density is lower and electric field is higher. Note that the momenta flatten at $t \approx 1.3$ s, midway through the ramp in B_0. Here the maximum energies range from $\mathcal{E} \approx$ 25-35 MeV (for an assumed $Z_{\text{eff}} = 4$).

Figure C.1h shows the normalized momenta *gained* in the case when B_0 is held constant (shown as the grey line in figure C.1e). Runaways at the magnetic axis and on the three flux surfaces show almost identical trends: During the B_0 ramp, runaways are predicted to lose up to $\sim$3.5 MeV ($\Delta p/mc \approx 7$) compared to the case when there is no change in B_0. This is expected since synchrotron power scales as $P_{\text{synch}} \propto B^2$.

C.3 Experimental synchrotron spectra

As discussed previously, the time evolution of synchrotron spectra—specifically the spectral shape—can provide information about runaway dynamics, including energy and density. Consider the brightness evolution depicted in figure C.1f: The brightness increases in time while B_0 increases and begins to decrease at $t \approx 1.5$ s, the same time as both I_{p} and B_0 ramp down. It is likely that this decrease in synchrotron brightness is due to the loss of particles as the current—and thus confining poloidal magnetic field—decays. For both the outer surfaces, at $q = 3/2$ and 2, the predicted p/mc also decrease at this time, from $t \approx$ 1.5-1.65 s. Surprisingly, at $t \approx 1.65$ s, there is another sudden increase in observed synchrotron brightness, peaking at $t \approx 1.8$ s. Around this time, a resurgence in E/E_{C} is measured, especially on inner flux surfaces, which results in a slight increase in runaway momenta.

The synchrotron spectral shape can also reveal information about the energy distribution of runaways. The experimental brightness, normalized at $\lambda = 650$ nm, is shown in figure C.2a at nine times from $t =$ 1.1-1.9 s with $\Delta t = 100$ ms intervals. In figure C.2b, the "slope" of figure C.2a is simply calculated as the difference in normalized brightness between $\lambda =$ 500 and 850 nm. Recall that for fixed B_0, higher energy runaways will produce spectra with lower slopes as a larger fraction of synchrotron radiation is emitted at short wavelengths compared to long wavelengths (see figure 3.2). Similarly, for fixed p/mc, increasing B_0 causes the emission to shift

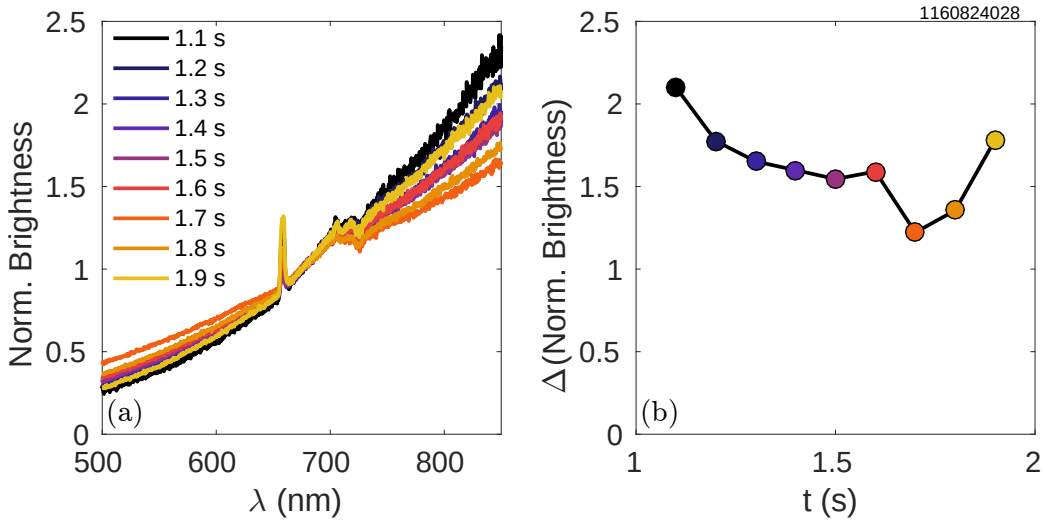

Figure C.2: (a) Normalized synchrotron brightness spectra from t = 1.1-1.9 s in intervals of Δt = 100 ms. (b) The *difference* of normalized brightness values at λ = 500 and 850 nm, i.e. $\bar{\mathcal{B}}$(850 nm) − $\bar{\mathcal{B}}$(500 nm); this is representative of the approximate linear slope of the spectrum at each time. Note the Balmer lines and absorption features in (a) at $\lambda \approx$ 658 and 720 nm, respectively, have not been removed.

toward shorter wavelengths, thus also lowering the slope. In time, the measured slope decreases during the time of the B-field ramp ($t \approx$ 1-1.5 s), decreases sharply from t = 1.6-1.7 s, and then increases from t = 1.7-1.9 s. The self-similarity of spectra—i.e. non-changing slope—from t = 1.3-1.6 s likely indicates that as B_0 increases, the runaway energy decreases accordingly to keep the spectral shape the same. The sudden drop in slope at t = 1.7 s could be related to a sharp increase in p/mc due to an increase in E/E_{C}, even though B_0 is decreasing at this time.

C.4 Comparison with DIII-D experiments

While the normalized spectra provide some qualitative information of runaway dynamics, it is difficult to determine the true change in energy from experimental data alone. This is, in part, due to the only slight change in expected synchrotron emission when the change in runaway energy is less than 3.5 MeV, which is <20% of the total runaway energy. However, this should have been expected as the percentage increase in synchrotron power loss was quite small: An increase from B_0 = 5.4-6.2 T increases P_{synch} by only ∼32%.

In experiments similar to this performed on the DIII-D tokamak [81], several plasma parameters were varied independently to measure their effects on quiescent (flattop) runaways. A scan in

B_0 was performed: In one case, B_0 was increased from $\sim$1.5 to 1.9 T; for another, B_0 was *decreased* from $\sim$1.5 to 1 T. Data from the DIII-D Gamma Ray Imager indicated shifts in the runaway energy spectrum opposite to the change in magnetic field, i.e. decreasing energy with increasing field, and vice-versa. However, for DIII-D, the absolute magnitude of toroidal field is much lower than C-Mod's; thus, the increase and decrease of B_0 in those experiments result in percent changes of the radiated power by approximately $\pm$50-60%, which is *twice* that of Alcator C-Mod. Then, the changes in runaway energy were more significant and could be more easily observed.

This page intentionally left blank

Appendix D

Calculation of the runaway density n_r from CODE

This section details the calculation of the runaway density profile n_r inferred from images of synchrotron radiation (see chapter 7). Recall from (7.2) that a synthetic 2D image can be computed in SOFT [20] as

$$I_{ij} = \sum_k C(R_k)\, \hat{G}_{ij}(R_k)\, \Delta R_k, \tag{D.1}$$

where I_{ij} is the intensity measured at each pixel coordinate (i, j), $\hat{G}_{ij}(R)$ is the Green's function computed from SOFT, $C(R)$ are experimentally-fit coefficients, and R_k are the major radial positions representing the discretization of position space, with step size ΔR_k.

Equation (D.1) is really just a discrete form of the integral over the major radius in (5.9). The integration over momentum space was already performed in SOFT, i.e.

$$\hat{G}_{ij}(R) = \int \mathrm{d}\boldsymbol{p}\, f(R, \boldsymbol{p})\, \hat{G}_{ij}(R, \boldsymbol{p}). \tag{D.2}$$

where $f(R, \boldsymbol{p})$ is an electron phase space distribution satisfying

$$n_\mathrm{e}(R) = \int f(R, \boldsymbol{p})\, \mathrm{d}\boldsymbol{p}, \tag{D.3}$$

which is the electron density profile. Recall from chapter 5 that SOFT assumes toroidal symmetry and follows guiding centers; thus, $f(R, \boldsymbol{p})$ is three-dimensional: one real space (radial) dimension and two momentum space dimensions, parallel and perpendicular to the magnetic field.

Imagine that the electron distribution function is known. Then, the Green's function $\hat{G}_{ij}(R)$ could be calculated from (D.2) and input into (D.1) to produce a synthetic image I_{ij}. Because

SOFT should reproduce reality, this would imply that all coefficients $C(R) = 1$, in this case. Thus, C is unitless, and $\hat{G}_{ij}$ will have units of W/m, assuming the pixel intensities are measured in Watts. If, for instance, we want to produce an image with the same setup but twice the number of runaways, we could set $C(R) = 2$ in (D.1).

As described in chapter 5, the kinetic equation solver CODE [36, 37] is used in this thesis to calculate the runaway electron distribution function given experimental plasma parameters. One of the inputs of CODE is the plasma electron density n_e, and one of CODE's outputs is the *fraction* f_r of runaways

$$f_\mathrm{r}(R,t) = \frac{n_\mathrm{CODE}(R,t)}{n_\mathrm{e}(R,t)}. \tag{D.4}$$

Here, n_CODE is the density of electrons in the "runaway regime," defined as the region of momentum space with total momentum $p > p_\mathrm{c}$, where

$$\frac{p_\mathrm{c}}{mc} = \frac{1}{\sqrt{E/E_\mathrm{C} - 1}}. \tag{D.5}$$

Here, E is the electric field (input into CODE), and E_C is the Connor-Hastie threshold field [27]. Note that for typical values of $E/E_\mathrm{C} \approx$ 5-10 during the flattop current of C-Mod discharges, $p_\mathrm{c}/mc \approx$ 0.3-0.5. Because thermal electrons in the bulk Maxwellian have far smaller momenta, i.e. $p_\mathrm{th} \ll p_\mathrm{c}$, we expect that slight variations in $E/E_\mathrm{C} \sim O(10)$ will not change the computed value of n_CODE by much.[a] Therefore, at any one time t, it is assumed that the runaway density profile can be calculated

$$n_\mathrm{r}(R) = C(R) \times n_\mathrm{CODE}(R). \tag{D.6}$$

As discussed in chapter 7, the output distribution function $F(\boldsymbol{p})$ from CODE is unitless, with normalization

$$F(\boldsymbol{p}) = \frac{\pi^{3/2}\, m^3\, v_\mathrm{ref}^3}{n_\mathrm{ref}} f(\boldsymbol{p}). \tag{D.7}$$

Here, m is the electron rest mass, v_ref is a reference electron thermal velocity, and n_ref is a reference electron density; the latter two are usually taken to be the electron thermal velocity and density at the start of the simulation. (See [36] for more details of CODE calculations.) Note that while $f(\boldsymbol{p}) = f(p_\parallel, p_\perp)$ is two dimensional, the differential element includes the third momentum space dimension; that is, $\mathrm{d}\boldsymbol{p} = 2\pi p_\perp \mathrm{d}p_\parallel \mathrm{d}p_\perp$, where an integration over gyro-angle has already been taken. Therefore, the units of $f(\boldsymbol{p})$ are $\mathrm{s}^3/(\mathrm{kg}^3\ \mathrm{m}^6)$.

[a] However, $p_\mathrm{th} \sim p_\mathrm{c}$ when the electric field approaches the Dreicer field, i.e. $E \sim E_\mathrm{D} \sim 100 E_\mathrm{C}$ [25, 26]. In this case, n_CODE would likely be large enough such that the linearization of the CODE calculation would no longer be appropriate, and a code like NORSE [128] would need to be used—see chapter 9.

In the analysis of synchrotron images of chapter 7, CODE simulations were run for plasma parameters at six locations throughout the plasma: at the magnetic axis and on rational flux surfaces with $q = 1$, 4/3, 3/2, 2, and 3. A *normalized* phase space distribution function $F(R, \boldsymbol{p})$ was then "stitched" together between the different locations, as given in (7.1). In this formulation, there are also profiles $n_{\rm ref}(R)$ and $v_{\rm ref}(R)$. A Green's function $\hat{G}'_{ij}$ (note the prime) was created with the *normalized* $F(R, \boldsymbol{p})$,

$$\hat{G}'_{ij}(R) = \int \mathrm{d}\boldsymbol{p}\, F(R, \boldsymbol{p}) \times (\cdots), \tag{D.8}$$

where the last term, $(\cdots)$, represents the geometric factors and spectral power density components of the SOFT calculation in (5.5). Substituting (D.7) into (D.8) gives

$$\hat{G}'_{ij}(R) = \frac{\pi^{3/2}\, m^3\, v_{\rm ref}^3(R)}{n_{\rm ref}(R)} \int \mathrm{d}\boldsymbol{p}\, f(R, \boldsymbol{p}) \times (\cdots) \tag{D.9}$$

$$= \frac{\pi^{3/2}\, m^3\, v_{\rm ref}^3(R)}{n_{\rm ref}(R)} \hat{G}_{ij}(R). \tag{D.10}$$

Thus, we have a relationship between the Green's functions computed with the normalized and true distribution functions from CODE.

In this section's notation, the synthetic image can also be calculated

$$I_{ij} = \sum_k C'(R_k)\, \hat{G}'_{ij}(R_k)\, \Delta R_k. \tag{D.11}$$

This is actually how the analysis was performed in chapter 7. Equations (D.1) and (D.11) must produce the same final image; they are both being compared to the same experimental image, after all. Thus, the coefficients can be related by

$$C(R) = \frac{\pi^{3/2}\, m^3\, v_{\rm ref}^3(R)}{n_{\rm ref}(R)} C'(R). \tag{D.12}$$

Plugging this result into (D.6) yields

$$n_{\rm r}(R) = \frac{\pi^{3/2}\, m^3\, v_{\rm ref}^3(R)}{n_{\rm ref}(R)} n_{\rm CODE}(R) C'(R). \tag{D.13}$$

The reader will note that this is only different from (7.5) by the change of notation $C \leftrightarrow C'$. In fact, the coefficients $C(R)$ and Green's function $\hat{G}_{ij}(R)$ of chapter 7 are what we call $C'(R)$ and $\hat{G}'_{ij}(R)$, respectively, in this section, so we have achieved the desired result.

This page intentionally left blank

List of Figures

List of Tables

References

[1] A. Jay, D.R. Reidmiller, C.W. Avery, D. Barrie, B.J. DeAngelo, A. Dave, M. Dzaugis, M. Kolian, K.L.M. Lewis, K. Reeves, , and D. Winner. Overview. Impacts, Risks, and Adaptation in the United States: Fourth National Climate Assessment, Volume II. *U.S. Global Change Research Program, Washington, DC, USA*, 2018.

[2] D.J. Wuebbles, D.W. Fahey, K.A. Hibbard, B. DeAngelo, S. Doherty, K. Hayhoe, R. Horton, J.P. Kossin, P.C. Taylor, A.M. Waple, and C.P. Weaver. Executive summary. Climate Science Special Report: Fourth National Climate Assessment, Volume I. *U.S. Global Change Research Program, Washington, DC, USA*, pages 12–34, 2017.

[3] National Academies of Sciences, Engineering, and Medicine. *Final Report of the Committee on a Strategic Plan for U.S. Burning Plasma Research*. The National Academies Press, 2018.

[4] US Energy Information Administration. Massachusetts Net Electricity Generation by Source, Nov. 2018. https://www.eia.gov/state/?sid=MA#tabs-4. Accessed: 2019-02-22.

[5] J.P. Freidberg. *Plasma Physics and Fusion Energy*. Cambridge University Press, 2008.

[6] File:hd.6d.768 (13471576805).jpg. https://commons.wikimedia.org/wiki/File:HD.6D.768_(13471576805).jpg#file. Accessed: 2019-02-13.

[7] File:alcator c-mod tokamak engineering diagram.jpg. https://commons.wikimedia.org/wiki/File:Alcator_C-Mod_tokamak_engineering_diagram.jpg. Accessed: 2019-02-13.

[8] M. Shimada, D.J. Campbell, V. Mukhovatov, M. Fujiwara, N. Kirneva, K. Lackner, M. Nagami, V.D. Pustovitov, N. Uckan, J. Wesley, N. Asakura, A.E. Costley, A.J.H. Donné, E.J. Doyle, A. Fasoli, C. Gormezano, Y. Gribov, O. Gruber, T.C. Hender, W. Houlberg, S. Ide, Y. Kamada, A. Leonard, B. Lipschultz, A. Loarte, K. Miyamoto, V. Mukhovatov, T.H. Osborne, A. Polevoi, and A.C.C. Sips. Chapter 1: Overview and summary. *Nuclear Fusion*, 47(6):S1–S17, 2007.

[9] M. Greenwald, D.G. Whyte, P. Bonoli, Z.S. Hartwig, J. Irby, B. LaBombard, E. Marmar, J. Minervini, M. Takayasu, J. Terry, R. Vieira, A.E. White, S. Wukitch, D. Brunner, R.T. Mumgaard, and B.N. Sorbom. The high-field path to practical fusion energy, 2018. https://doi.org/10.7910/DVN/OYYBNU.

[10] B.N. Sorbom, J. Ball, T.R. Palmer, F.J. Mangiarotti, J.M. Sierchio, P. Bonoli, C. Kasten, D.A. Sutherland, H.S. Barnard, C.B. Haakonsen, J. Goh, C. Sung, and D.G. Whyte. ARC: A compact, high-field, fusion nuclear science facility and demonstration power plant with demountable magnets. *Fusion Engineering and Design*, 100:378 – 405, 2015.

[11] A.Q. Kuang, N.M. Cao, A.J. Creely, C.A. Dennett, J. Hecla, B. LaBombard, R.A. Tinguely, E.A.

Tolman, H. Hoffman, M. Major, J. Ruiz Ruiz, D. Brunner, P. Grover, C. Laughman, B.N. Sorbom, and D.G. Whyte. Conceptual design study for heat exhaust management in the ARC fusion pilot plant. *Fusion Engineering and Design*, 137:221 – 242, 2018.

[12] A.C.C. Sips, for the Steady State Operation, and the Transport Physics topical groups of the International Tokamak Physics Activity. Advanced scenarios for ITER operation. *Plasma Physics and Controlled Fusion*, 47(5A):A19–A40, 2005.

[13] The interior of Alcator C-Mod as seen from F port. https://commons.wikimedia.org/wiki/Alcator_C-Mod#/media/File:Alcator_C-Mod_Fisheye_from_Fport.jpg. Taken by R. Mumgaard and C. Bolin 2013-09-17. Accessed: 2019-02-13.

[14] L.L. Lao, H. St. John, R.D. Stambaugh, A.G. Kellman, and W. Pfeiffer. Reconstruction of current profile parameters and plasma shapes in tokamaks. *Nuclear Fusion*, 25(11):1611, 1985.

[15] N. Commaux L.R. Baylor D. Brunner C.M. Cooper N.W. Eidietis E.M. Hollmann A.Q. Kuang C.J. Lasnier R.A. Moyer C. Paz-Soldan R. Raman M.L. Reinke D. Shiraki, R.S. Granetz and R.A. Tinguely. Disruption mitigation in the presence of pre-existing MHD instabilities. *Proceedings of the 26th IAEA Fusion Energy Conference*, 2016.

[16] R.A. Tinguely, R.S. Granetz, A. Berg, A.Q. Kuang, D. Brunner, and B. LaBombard. High-resolution disruption halo current measurements using Langmuir probes in Alcator C-Mod. *Nuclear Fusion*, 58(1):016005, 2017.

[17] V.V. Plyusnin, C. Reux, V.G. Kiptily, G. Pautasso, J. Decker, G. Papp, A. Kallenbach, V. Weinzettl, J. Mlynar, S. Coda, V. Riccardo, P. Lomas, S. Jachmich, A.E. Shevelev, B. Alper, E. Khilkevitch, Y. Martin, R. Dux, C. Fuchs, B. Duval, M. Brix, G. Tardini, M. Maraschek, W. Treutterer, L. Giannone, A. Mlynek, O. Ficker, P. Martin, S. Gerasimov, S. Potzel, R. Paprok, P. J. McCarthy, M. Imrisek, A. Boboc, K. Lackner, A. Fernandes, J. Havlicek, L. Giacomelli, M. Vlainic, M. Nocente, U. Kruezi, COMPASS team, TCV team, ASDEX-Upgrade team, EUROFusion MST1 Team, and JET contributors. Comparison of runaway electron generation parameters in small, medium-sized and large tokamaks—a survey of experiments in COMPASS, TCV, ASDEX-Upgrade and JET. *Nuclear Fusion*, 58(1):016014, 2018.

[18] V.V. Plyusnin, V. Riccardo, R. Jaspers, B. Alper, V.G. Kiptily, J. Mlynar, S. Popovichev, E. de La Luna, F. Andersson, and JET EFDA contributors. Study of runaway electron generation during major disruptions in JET. *Nuclear Fusion*, 46(2):277, 2006.

[19] J.R. Martín-Solís, B. Esposito, R. Sánchez, F.M. Poli, and L. Panaccione. Enhanced production of runaway electrons during a disruptive termination of discharges heated with lower hybrid power in the Frascati Tokamak Upgrade. *Phys. Rev. Lett.*, 97:165002, 2006.

[20] M. Hoppe, O. Embréus, R.A. Tinguely, R.S. Granetz, A. Stahl, and T. Fülöp. SOFT: a synthetic synchrotron diagnostic for runaway electrons. *Nuclear Fusion*, 58(2):026032, 2018. SOFT can be downloaded at https://github.com/hoppe93/SOFT, with documentation found at https://soft.readthedocs.io.

[21] R.A. Tinguely, R.S. Granetz, M. Hoppe, and O. Embréus. Measurements of runaway electron synchrotron spectra at high magnetic fields in Alcator C-Mod. *Nuclear Fusion*, 58(7):076019, 2018.

[22] R.A. Tinguely, R.S. Granetz, M. Hoppe, and O. Embréus. Spatiotemporal evolution of runaway electrons from synchrotron images in Alcator C-Mod. *Plasma Physics and Controlled Fusion*, 60(12):124001, 2018.

[23] R.A. Tinguely, M. Hoppe, O. Embréus, R.S. Granetz, S. Scott, and R.T. Mumgaard. Experimental

and synthetic measurements of polarized synchrotron emission from runaway electrons in Alcator C-Mod. 2019. Submitted to *Nuclear Fusion*.

[24] R.A. Tinguely, K.J. Montes, C. Rea, R. Sweeney, and R.S. Granetz. An application of survival analysis to disruption prediction via Random Forests. 2019. Submitted to *Plasma Physics and Controlled Fusion*.

[25] H. Dreicer. Electron and ion runaway in a fully ionized gas. I. *Physical Review*, 115:238–249, 1959.

[26] H. Dreicer. Electron and ion runaway in a fully ionized gas. II. *Physical Review*, 117:329–342, 1960.

[27] J.W. Connor and R.J. Hastie. Relativistic limitations on runaway electrons. *Nuclear Fusion*, 15(3):415, 1975.

[28] J.R. Martín-Solís, R. Sánchez, and B. Esposito. Experimental observation of increased threshold electric field for runaway generation due to synchrotron radiation losses in the FTU tokamak. *Phys. Rev. Lett.*, 105:185002, 2010.

[29] R.S. Granetz, B. Esposito, J.H. Kim, R. Koslowski, M. Lehnen, J.R. Martín-Solís, C. Paz-Soldan, T. Rhee, J.C. Wesley, L. Zeng, and ITPA MHD Group. An ITPA joint experiment to study runaway electron generation and suppression. *Physics of Plasmas*, 21(7):072506, 2014.

[30] R. Jayakumar, H.H. Fleischmann, and S.J. Zweben. Collisional avalanche exponentiation of runaway electrons in electrified plasmas. *Physics Letters A*, 172(6):447 – 451, 1993.

[31] M.N. Rosenbluth and S.V. Putvinski. Theory for avalanche of runaway electrons in tokamaks. *Nuclear Fusion*, 37(10):1355, 1997.

[32] A.H. Boozer. Runaway electrons and ITER. *Nuclear Fusion*, 57(5):056018, 2017.

[33] J.R. Martín-Solís, J.D. Alvarez, R. Sánchez, and B. Esposito. Momentum-space structure of relativistic runaway electrons. *Physics of Plasmas*, 5(6):2370–2377, 1998.

[34] G. Fussmann. On the motion of runaway electrons in momentum space. *Nuclear Fusion*, 19(3):327–334, 1979.

[35] B. Kurzan, K.-H. Steuer, and G. Fussmann. Dynamics of runaway electrons in the magnetic field of a tokamak. *Phys. Rev. Lett.*, 75:4626–4629, 1995.

[36] M. Landreman, A. Stahl, and T. Fülöp. Numerical calculation of the runaway electron distribution function and associated synchrotron emission. *Computer Physics Communications*, 185(3):847 – 855, 2014.

[37] A. Stahl, O. Embréus, G. Papp, M. Landreman, and T. Fülöp. Kinetic modelling of runaway electrons in dynamic scenarios. *Nuclear Fusion*, 56(11):112009, 2016.

[38] H. Knoepfel and D.A. Spong. Runaway electrons in toroidal discharges. *Nuclear Fusion*, 19(6):785, 1979.

[39] J.R. Myra and P.J. Catto. Effect of drifts on the diffusion of runaway electrons in tokamak stochastic magnetic fields. *Physics of Fluids B: Plasma Physics*, 4(1):176–186, 1992.

[40] B. Esposito, J.R. Martín Solís, P. van Belle, O.N. Jarvis, F.B. Marcus, G. Sadler, R. Sánchez, B. Fischer, P. Froissard, J.M. Adams, E. Cecil, and N. Watkins. Runaway electron measurements in the JET tokamak. *Plasma Physics and Controlled Fusion*, 38(12):2035, 1996.

[41] J.R. Martín-Solís, R. Sánchez, and B. Esposito. Effect of magnetic and electrostatic fluctuations on the runaway electron dynamics in tokamak plasmas. *Physics of Plasmas*, 6(10):3925–3933, 1999.

[42] A.B. Rechester and M.N. Rosenbluth. Electron heat transport in a tokamak with destroyed

magnetic surfaces. *Phys. Rev. Lett.*, 40:38–41, 1978.
[43] H.E. Mynick and J.D. Strachan. Transport of runaway and thermal electrons due to magnetic microturbulence. *The Physics of Fluids*, 24(4):695–702, 1981.
[44] P. Helander, L.-G. Eriksson, and F. Andersson. Suppression of runaway electron avalanches by radial diffusion. *Physics of Plasmas*, 7(10):4106–4111, 2000.
[45] A. Wingen, S.S. Abdullaev, K.H. Finken, M. Jakubowski, and K.H. Spatschek. Influence of stochastic magnetic fields on relativistic electrons. *Nuclear Fusion*, 46(11):941, 2006.
[46] G. Papp, M. Drevlak, T. Fülöp, P. Helander, and G.I. Pokol. Runaway electron losses caused by resonant magnetic perturbations in ITER. *Plasma Physics and Controlled Fusion*, 53(9):095004, 2011.
[47] G. Papp, M. Drevlak, T. Fülöp, and G.I. Pokol. The effect of resonant magnetic perturbations on runaway electron transport in ITER. *Plasma Physics and Controlled Fusion*, 54(12):125008, 2012.
[48] G. Papp, M. Drevlak, G.I. Pokol, and T. Fülöp. Energetic electron transport in the presence of magnetic perturbations in magnetically confined plasmas. *Journal of Plasma Physics*, 81(5):475810503, 2015.
[49] O.J. Kwon, P.H. Diamond, F. Wagner, G. Fussmann, and ASDEX Team and NI Team. A study of runaway electron confinement in the ASDEX tokamak. *Nuclear Fusion*, 28(11):1931, 1988.
[50] J.D. Strachan. Runaway electron transport in the LT-3 tokamak. *Nuclear Fusion*, 16(5):743–751, 1976.
[51] O. Embréus, A. Stahl, S. Newton, G. Papp, Ee. Hirvijoki, and T. Fülöp. Effect of bremsstrahlung radiation emission on distributions of runaway electrons in magnetized plasmas. *arXiv preprint arXiv:1511.03917*, 2015.
[52] V.V. Parail and O.P. Pogutse. The kinetic theory of runaway electron beam instability in a tokamak. *Nuclear Fusion*, 18(3):303–314, 1978.
[53] S.C. Luckhardt, K-I. Chen, M.J. Mayberry, M. Porkolab, Y. Terumichi, G. Bekefi, F.S. McDermott, and R. Rohatgi. Particle confinement and the anomalous Doppler instability during combined inductive and lower-hybrid current drive. *The Physics of Fluids*, 29(6):1985–1993, 1986.
[54] D.A. Spong, W.W. Heidbrink, C. Paz-Soldan, X.D. Du, K.E. Thome, M.A. Van Zeeland, C. Collins, A. Lvovskiy, R.A. Moyer, M.E. Austin, D.P. Brennan, C. Liu, E.F. Jaeger, and C. Lau. First direct observation of runaway-electron-driven Whistler waves in tokamaks. *Phys. Rev. Lett.*, 120:155002, 2018.
[55] A Lvovskiy, C Paz-Soldan, N W Eidietis, A Dal Molin, X D Du, L Giacomelli, J L Herfindal, E M Hollmann, L Martinelli, R A Moyer, M Nocente, D Rigamonti, D Shiraki, M Tardocchi, and K E Thome. The role of kinetic instabilities in formation of the runaway electron current after argon injection in DIII-d. *Plasma Physics and Controlled Fusion*, 60(12):124003, nov 2018.
[56] K.C. Westfold. The Polarization of Synchrotron Radiation. *The Astrophysical Journal*, 130:241, 1959.
[57] J. Schwinger. On the classical radiation of accelerated electrons. *Phys. Rev.*, 75:1912–1925, 1949.
[58] I.M. Pankratov. Analysis of the synchrotron radiation spectra of runaway electrons. *Plamsa Physics Reports*, 25(2):145–148, 1999.
[59] I.H. Hutchinson. *Principles of Plasma Diagnostics: Second Edition*. Cambridge University Press, 2002.
[60] A. Stahl, M. Landreman, G. Papp, E. Hollmann, and T. Fülöp. Synchrotron radiation from a

runaway electron distribution in tokamaks. *Physics of Plasmas*, 20(9):093302, 2013.

[61] R. Jaspers, N.J. Lopes Cardozo, A.J.H. Donné, H.L.M. Widdershoven, and K.H. Finken. A synchrotron radiation diagnostic to observe relativistic runaway electrons in a tokamak plasma. *Review of Scientific Instruments*, 72(1):466–470, 2001.

[62] J.H. Yu, E.M. Hollmann, N. Commaux, N.W. Eidietis, D.A. Humphreys, A.N. James, T.C. Jernigan, and R.A. Moyer. Visible imaging and spectroscopy of disruption runaway electrons in DIII-D. *Physics of Plasmas*, 20(4):042113, 2013.

[63] L. Carbajal and D. del Castillo-Negrete. On the synchrotron emission in kinetic simulations of runaway electrons in magnetic confinement fusion plasmas. *Plasma Physics and Controlled Fusion*, 59(12):124001, 2017.

[64] F.M. Levinton, R.J. Fonck, G.M. Gammel, R. Kaita, H.W. Kugel, E.T. Powell, and D.W. Roberts. Magnetic field pitch-angle measurements in the PBX-M tokamak using the motional Stark effect. *Phys. Rev. Lett.*, 63:2060–2063, 1989.

[65] G.R. Boyer, B.F. Lamouroux, and B.S. Prade. Automatic measurement of the Stokes vector of light. *Appl. Opt.*, 18(8):1217–1219, 1979.

[66] R.T. Mumgaard. Engineering upgrades to the Motional Stark Effect diagnostic on Alcator C-Mod, 2015.

[67] R.T. Mumgaard. *Lower Hybrid Current Drive on Alcator C-Mod: Measurements with an upgraded MSE diagnostic and comparisons to simulation*. PhD thesis, Massachusetts Institute of Technology, 2015.

[68] R.T. Mumgaard, S.D. Scott, and M. Khoury. A ten sightline multi-spectral line-polarization MSE system for Alcator C-Mod. *Review of Scientific Instruments*, 87, 2016. https://doi.org/10.1063/1.4959793.

[69] W. Pauli. *Theory of Relativity*. Dover Books on Physics. Dover Publications, 1981.

[70] S.C. Chiu, M.N. Rosenbluth, R.W. Harvey, and V.S. Chan. Fokker-Planck simulations mylb of knock-on electron runaway avalanche and bursts in tokamaks. *Nuclear Fusion*, 38(11):1711, 1998.

[71] A. Stahl. *Momentum-space dynamics of runaway electrons in plasmas*. Chalmers University of Technology, 2017.

[72] C. Liu, E. Hirvijoki, G.-Y. Fu, D.P. Brennan, A. Bhattacharjee, and C. Paz-Soldan. Role of kinetic instability in runaway-electron avalanches and elevated critical electric fields. *Phys. Rev. Lett.*, 120:265001, 2018.

[73] C. Liu, L. Shi, E. Hirvijoki, D.P. Brennan, A. Bhattacharjee, C. Paz-Soldan, and M.E. Austin. The effects of kinetic instabilities on the electron cyclotron emission from runaway electrons. *Nuclear Fusion*, 58(9):096030, jul 2018.

[74] M. Hoppe, O. Embréus, C. Paz-Soldan, R.A. Moyer, and T. Fülöp. Interpretation of runaway electron synchrotron and bremsstrahlung images. *Nuclear Fusion*, 58(8):082001, 2018.

[75] E. Marmar, A. Bader, M. Bakhtiari, H. Barnard, W. Beck, I. Bespamyatnov, A. Binus, P. Bonoli, B. Bose, M. Bitter, I. Cziegler, G. Dekow, A. Dominguez, B. Duval, E. Edlund, D. Ernst, M. Ferrara, C. Fiore, T. Fredian, A. Graf, R. Granetz, M. Greenwald, O. Grulke, D. Gwinn, S. Harrison, R. Harvey, T.C. Hender, J. Hosea, K. Hill, N. Howard, D.F. Howell, A. Hubbard, J.W. Hughes, I. Hutchinson, A. Ince-Cushman, J. Irby, V. Izzo, A. Kanojia, C. Kessel, J.S. Ko, P. Koert, B. LaBombard, C. Lau, L. Lin, Y. Lin, B. Lipschultz, J. Liptac, Y. Ma, K. Marr, M. May, R. McDermott, O. Meneghini, D. Mikkelsen, R. Ochoukov, R. Parker, C.K. Phillips, P. Phillips, Y. Podpaly, M. Porkolab, M. Reinke, J. Rice, W. Rowan, S. Scott, A. Schmidt, J. Sears, S. Shi-

raiwa, A. Sips, N. Smick, J. Snipes, J. Stillerman, Y. Takase, D. Terry, J. Terry, N. Tsujii, E. Valeo, R. Vieira, G. Wallace, D. Whyte, J.R. Wilson, S. Wolfe, G. Wright, J. Wright, S. Wukitch, G. Wurden, P. Xu, K. Zhurovich, J. Zaks, and S. Zweben. Overview of the Alcator C-Mod research program. *Nuclear Fusion*, 49(10):104014, 2009.

[76] V.A. Izzo, E.M. Hollmann, A.N. James, J.H. Yu, D.A. Humphreys, L.L. Lao, P.B. Parks, P.E. Sieck, J.C. Wesley, R.S. Granetz, G.M. Olynyk, and D.G. Whyte. Runaway electron confinement modelling for rapid shutdown scenarios in DIII-D, Alcator C-Mod and ITER. *Nuclear Fusion*, 51(6):063032, 2011.

[77] B. Esposito, J.R. Martín-Solís, F.M. Poli, J.A. Mier, R. Sánchez, and L. Panaccione. Dynamics of high energy runaway electrons in the Frascati Tokamak Upgrade. *Physics of Plasmas*, 10(6):2350–2360, 2003.

[78] Z. Popovic, B. Esposito, J.R. Martín-Solís, W. Bin, P. Buratti, D. Carnevale, F. Causa, M. Gospodarczyk, D. Marocco, G. Ramogida, and M. Riva. On the measurement of the threshold electric field for runaway electron generation in the Frascati Tokamak Upgrade. *Physics of Plasmas*, 23(12):122501, 2016.

[79] B. Esposito, L. Boncagni, P. Buratti, D. Carnevale, F. Causa, M. Gospodarczyk, J.R. Martín-Solís, Z. Popovic, M. Agostini, G. Apruzzese, W. Bin, C. Cianfarani, R. De Angelis, G. Granucci, A. Grosso, G. Maddaluno, D. Marocco, V. Piergotti, A. Pensa, S. Podda, G. Pucella, G. Ramogida, G. Rocchi, M. Riva, A. Sibio, C. Sozzi, B. Tilia, O. Tudisco, M. Valisa, and FTU Team. Runaway electron generation and control. *Plasma Physics and Controlled Fusion*, 59(1):014044, 2017.

[80] M. Hoppe *et al*. SOFT2 can be downloaded at https://github.com/hoppe93/SOFT2.

[81] C. Paz-Soldan, C.M. Cooper, P. Aleynikov, D.C. Pace, N.W. Eidietis, D.P. Brennan, R.S. Granetz, E.M. Hollmann, C. Liu, A. Lvovskiy, R.A. Moyer, and D. Shiraki. Spatiotemporal evolution of runaway electron momentum distributions in tokamaks. *Physical Review Letters*, 118:255002, 2017.

[82] P. Aleynikov and B.N. Breizman. Theory of two threshold fields for relativistic runaway electrons. *Phys. Rev. Lett.*, 114:155001, 2015.

[83] A. Stahl, E. Hirvijoki, J. Decker, O. Embréus, and T. Fülöp. Effective critical electric field for runaway-electron generation. *Phys. Rev. Lett.*, 114:115002, 2015.

[84] M. Vlainic, P. Vondracek, J. Mlynar, V. Weinzettl, O. Ficker, M. Varavin, R. Paprok, M. Imrisek, J. Havlicek, R. Panek, J.-M. Noterdaeme, and the COMPASS Team. Synchrotron radiation from runaway electrons in COMPASS tokamak. *42nd European Physical Society Conference on Plasma Physics*, (P4.108), 2015.

[85] C. Paz-Soldan, C.M. Cooper, P. Aleynikov, N.W. Eidietis, A. Lvovskiy, D.C. Pace, D.P. Brennan, E.M. Hollmann, C. Liu, R.A. Moyer, and D. Shiraki. Resolving runaway electron distributions in space, time, and energy. *Physics of Plasmas*, 25(5):056105, 2018.

[86] C. Paz-Soldan, N.W. Eidietis, R.S. Granetz, E.M. Hollmann, R.A. Moyer, J.C. Wesley, J. Zhang, M.E. Austin, N.A. Crocker, A. Wingen, and Y. Zhu. Growth and decay of runaway electrons above the critical electric field under quiescent conditions. *Physics of Plasmas*, 21(2):022514, 2014.

[87] E.M. Hollmann, P.B. Parks, N. Commaux, N.W. Eidietis, R.A. Moyer, D. Shiraki, M.E. Austin, C.J. Lasnier, C. Paz-Soldan, and D.L. Rudakov. Measurement of runaway electron energy distribution function during high-Z gas injection into runaway electron plateaus in DIII-D. *Physics of Plasmas*, 22(5):056108, 2015.

[88] R.J. Zhou, L.Q. Hu, E.Z. Li, M. Xu, G.Q. Zhong, L.Q. Xu, S.Y. Lin, J.Z. Zhang, and the EAST Team. Investigation of ring-like runaway electron beams in the EAST tokamak. *Plasma Physics and Controlled Fusion*, 55(5):055006, 2013.

[89] R.J. Zhou, I.M. Pankratov, L.Q. Hu, M. Xu, and J.H. Yang. Synchrotron radiation spectra and synchrotron radiation spot shape of runaway electrons in Experimental Advanced Superconducting Tokamak. *Physics of Plasmas*, 21(6):063302, 2014.

[90] Y. Shi, J. Fu, J. Li, Y. Yang, F. Wang, Y. Li, W. Zhang, B. Wan, and Z. Chen. Observation of runaway electron beams by visible color camera in the Experimental Advanced Superconducting Tokamak. *Review of Scientific Instruments*, 81(3):033506, 2010.

[91] Y.P. Zhang, Y. Liu, G.L. Yuan, M. Isobe, Z.Y. Chen, J. Cheng, X.Q. Ji, X.M. Song, J.W. Yang, X.Y. Song, X. Li, W. Deng, Y.G. Li, Y. Xu, T.F. Sun, X.T. Ding, L.W. Yan, Q.W. Yang, X.R. Duan, and Y. Liu. Observation of the generation and evolution of long-lived runaway electron beams during major disruptions in the HuanLiuqi-2A tokamak. *Physics of Plasmas*, 19(3):032510, 2012.

[92] Z.Y. Chen, B.N. Wan, S.Y. Lin, Y.J. Shi, L.Q. Hu, X.Z. Gong, H. Lin, and M. Asif. Measurement of the runaway electrons in the HT-7 tokamak. *Review of Scientific Instruments*, 77(1):013502, 2006.

[93] R.H. Tong, Z.Y. Chen, M. Zhang, D.W. Huang, W. Yan, and G. Zhuang. Observation of runaway electrons by infrared camera in J-TEXT. *Review of Scientific Instruments*, 87(11):11E113, 2016.

[94] A.C. England, Z.Y. Chen, D.C. Seo, J. Chung, Y.S. Leev, J.W. Yoo, W.C. Kim, Y.S. Bae, Y.M. Jeonv, J.G. Kwak, M. Kwon, and the KSTAR Team. Runaway electron suppression by ECRH and RMP in KSTAR. *Plasma Science and Technology*, 15(2):119, 2013.

[95] S.A. Bozhenkov, M. Lehnen, K.H. Finken, M.W. Jakubowski, R.C. Wolf, R. Jaspers, M. Kantor, O.V. Marchuk, E. Uzgel, G. Van Wassenhove, O. Zimmermann, D. Reiter, and the TEXTOR team. Generation and suppression of runaway electrons in disruption mitigation experiments in TEXTOR. *Plasma Physics and Controlled Fusion*, 50(10):105007, 2008.

[96] K. Wongrach, K.H. Finken, S.S. Abdullaev, R. Koslowski, O. Willi, L. Zeng, and the TEXTOR Team. Measurement of synchrotron radiation from runaway electrons during the TEXTOR tokamak disruptions. *Nuclear Fusion*, 54(4):043011, 2014.

[97] K. Wongrach, K.H. Finken, S.S. Abdullaev, O. Willi, L. Zeng, Y. Xu, and the TEXTOR Team. Runaway electron studies in TEXTOR. *Nuclear Fusion*, 55(5):053008, 2015.

[98] I. Entrop, N.J. Lopes Cardozo, R. Jaspers, and K.H. Finken. Scale size of magnetic turbulence in tokamaks probed with 30-MeV electrons. *Physical Review Letters*, 84:3606–3609, 2000.

[99] I. Entrop, N.J. Lopes Cardozo, R. Jaspers, and K.H. Finken. Diffusion of runaway electrons in TEXTOR-94. *Plasma Physics and Controlled Fusion*, 40(8):1513, 1998.

[100] T. Kudyakov, S.S. Abdullaev, S.A. Bozhenkov, K.H. Finken, M.W. Jakubowski, M. Lehnen, G. Sewell, O. Willi, Y. Xu, and the TEXTOR team. Influence of B_t on the magnetic turbulence and on the runaway transport in low-density discharges. *Nuclear Fusion*, 52(2):023025, 2012.

[101] K.H. Finken, J.G. Watkins, D. Rusbüldt, W.J. Corbett, K.H. Dippel, D.M. Goebel, and R.A. Moyer. Observation of infrared synchrotron radiation from tokamak runaway electrons in TEXTOR. *Nuclear Fusion*, 30(5):859, 1990.

[102] R. Jaspers, N.J. Lopes Cardozo, K.H. Finken, B.C. Schokker, G. Mank, G. Fuchs, and F.C. Schüller. Islands of runaway electrons in the TEXTOR tokamak and relation to transport in a stochastic field. *Physical Review Letters*, 72:4093–4096, 1994.

[103] I. Entrop, R. Jaspers, N.J. Lopes Cardozo, and K.H. Finken. Runaway snakes in TEXTOR-94. *Plasma Physics and Controlled Fusion*, 41(3):377, 1999.

[104] L. Carbajal, D. del Castillo-Negrete, D. Spong, S. Seal, and L. Baylor. Space dependent, full orbit effects on runaway electron dynamics in tokamak plasmas. *Physics of Plasmas*, 24(4):042512, 2017.

[105] I. Sobel and G. Feldman. A 3×3 isotropic gradient operator for image processing, 1968. Presented at the Stanford Artificial Intelligence Project.

[106] B. Angelini, S.V. Annibaldi, M.L. Apicella, G. Apruzzese, E. Barbato, A. Bertocchi, F. Bombarda, C. Bourdelle, A. Bruschi, P. Buratti, G. Calabrò, A. Cardinali, L. Carraro, C. Castaldo, C. Centioli, R. Cesario, S. Cirant, V. Cocilovo, F. Crisanti, R. De Angelis, M. De Benedetti, F. De Marco, B. Esposito, D. Frigione, L. Gabellieri, F. Gandini, L. Garzotti, E. Giovannozzi, C. Gormezano, F. Gravanti, G. Granucci, G.T. Hoang, F. Iannone, H. Kroegler, E. Lazzaro, M. Leigheb, G. Maddaluno, G. Maffia, M. Marinucci, D. Marocco, J.R. Martin-Solis, F. Martini, M. Mattioli, G. Mazzitelli, C. Mazzotta, F. Mirizzi, G. Monari, S. Nowak, F. Orsitto, D. Pacella, L. Panaccione, M. Panella, P. Papitto, V. Pericoli-Ridolfini, L. Pieroni, S. Podda, M.E. Puiatti, G. Ravera, G. Regnoli, G.B. Righetti, F. Romanelli, M. Romanelli, F. Santini, M. Sassi, A. Saviliev, P. Scarin, A. Simonetto, P. Smeulders, E. Sternini, C. Sozzi, N. Tartoni, D. Terranova, B. Tilia, A.A. Tuccillo, O. Tudisco, M. Valisa, V. Vershkov, V. Vitale, G. Vlad, and F. Zonca. Overview of the FTU results. *Nuclear Fusion*, 45(10):S227, 2005.

[107] F. Zonca, L. Chen, and R.A. Santoro. Kinetic theory of low-frequency Alfvén modes in tokamaks. *Plasma Physics and Controlled Fusion*, 38(11):2011, 1996.

[108] L. Liu, J. He, Q. Hu, and G. Zhuang. Observation of beta-induced Alfvén eigenmode in J-TEXT tokamak. *Plasma Physics and Controlled Fusion*, 57(6):065007, 2015.

[109] M.A. Vashakidze. On the degree of polarization of the radiation of nearby extragalactic nebulae and of the Crab Nebula. *Astronomical Circular of the USSR*, 147(11), 1954.

[110] V.A. Dombrovsky. On the nature of the radiation from the Crab Nebula. *Proceedings of the USSR Academy of Sciences*, 94:1021, 1954.

[111] I.S. Shklovskii. On the nature of the luminescence of the Crab Nebula. 90(983):1900–1975, 1953.

[112] Ya.M. Sobolev. Polarization of synchrotron radiation from relativistic electrons moving within toroidal magnetic fields. *Problems of Atomic Science and Technology*, 4(86):108–111, 2013.

[113] L. Hesslow, O. Embréus, A. Stahl, T. C. DuBois, G. Papp, S. L. Newton, and T. Fülöp. Effect of partially screened nuclei on fast-electron dynamics. *Phys. Rev. Lett.*, 118:255001, 2017.

[114] L. Hesslow, O. Embréus, G.J. Wilkie, G. Papp, and T. Fülöp. Effect of partially ionized impurities and radiation on the effective critical electric field for runaway generation. *Plasma Physics and Controlled Fusion*, 60(7):074010, 2018.

[115] M. Lehnen, S.S. Abdullaev, G. Arnoux, S.A. Bozhenkov, M.W. Jakubowski, R. Jaspers, V.V. Plyusnin, V. Riccardo, and U. Samm. Runaway generation during disruptions in JET and TEXTOR. *Journal of Nuclear Materials*, 390-391:740 – 746, 2009. Proceedings of the 18th International Conference on Plasma-Surface Interactions in Controlled Fusion Device.

[116] P.T. Bonoli, J. Ko, R. Parker, A.E. Schmidt, G. Wallace, J.C. Wright, C.L. Fiore, A.E. Hubbard, J. Irby, E. Marmar, M. Porkolab, D. Terry, S.M. Wolfe, S.J. Wukitch, J.R. Wilson, S. Scott, E. Valeo, C.K. Phillips, and R.W. Harvey. Lower hybrid current drive experiments on Alcator C-Mod: Comparison with theory and simulation. *Physics of Plasmas*, 15(5):056117, 2008.

[117] R.A. Tinguely, A. Rosenthal, R. Simpson, S.B. Ballinger, A.J. Creely, S. Frank, A.Q. Kuang, B.L.

Linehan, W. McCarthy, L.M. Milanese, K.J. Montes, T. Mouratidis, J.F. Picard, P. Rodriguez-Fernandez, A.J. Sandberg, F. Sciortino, E.A. Tolman, M. Zhou, B.N. Sorbom, Z.S. Hartwig, and A.E. White. Neutron diagnostics for the physics of a high-field, compact, $q \geq 1$ tokamak.

[118] C. Rea, R.S. Granetz, K. Montes, R.A. Tinguely, N. Eidietis, J.M. Hanson, and B. Sammuli. Disruption prediction investigations using machine learning tools on DIII-D and Alcator C-Mod. *Plasma Physics and Controlled Fusion*, 60(8):084004, 2018.

[119] C. Rea, K.J. Montes, R.S. Granetz, R.A. Tinguely, K. Ericksson, et al. A real-time machine learning-based disruption predictor on DIII-D. 2018. Submitted to *Nuclear Fusion*.

[120] K.J. Montes, C. Rea, R.S. Granetz, R.A. Tinguely, N. Eidietis, O.M. Meneghini, D.L. Chen, B. Shen, B.J. Xiao, K. Erickson, and M.D. Boyer. Machine learning for disruption warning on Alcator C-Mod, DIII-D, and EAST tokamaks. 2018. Submitted to *Nuclear Fusion*.

[121] M.L. Reinke, S. Scott, R.S. Granetz, J.W. Hughes, S.G. Baek, S. Shiraiwa, R.A. Tinguely, S. Wukitch, and the Alcator C-Mod Team. Avoidance of impurity-induced current quench using lower hybrid current drive. 2019. Accepted for publication in *Nuclear Fusion*.

[122] Y. Peysson, J. Decker, and R.W. Harvey. Advanced 3-D Electron Fokker-Planck Transport Calculations. In *AIP Conference Proceedings*, volume 694, pages 495–498. AIP, 2003.

[123] J. Decker and Y. Peysson. DKE: A fast numerical solver for the 3D drift kinetic equation. *Euratom-CEA Report No. EUR-CEA-FC-1736*, 2004.

[124] E. Nilsson, J. Decker, Y. Peysson, R.S. Granetz, F. Saint-Laurent, and M. Vlainic. Kinetic modelling of runaway electron avalanches in tokamak plasmas. *Plasma Physics and Controlled Fusion*, 57(9):095006, 2015.

[125] R.W. Harvey, V.S. Chan, S.C. Chiu, T.E. Evans, M.N. Rosenbluth, and D.G. Whyte. Runaway electron production in DIII-D killer pellet experiments, calculated with the CQL3D/KPRAD model. *Physics of Plasmas*, 7(11):4590–4599, 2000.

[126] J. Liu, Y. Wang, and H. Qin. Collisionless pitch-angle scattering of runaway electrons. *Nuclear Fusion*, 56(6):064002, may 2016.

[127] C. Liu, H. Qin, E. Hirvijoki, Y. Wang, and J. Liu. Conservative magnetic moment of runaway electrons and collisionless pitch-angle scattering. *Nuclear Fusion*, 58(10):106018, aug 2018.

[128] A. Stahl, M. Landreman, O. Embréus, and T. Fülöp. NORSE: A solver for the relativistic non-linear Fokker–Planck equation for electrons in a homogeneous plasma. *Computer Physics Communications*, 212:269 – 279, 2017.

[129] J.S. Tyo, D.L. Goldstein, D.B. Chenault, and J. Shaw. Review of passive imaging polarimetry for remote sensing applications. *Applied Optics*, 45:5453–69, 2006.

[130] P. Rodriguez-Fernandez, A.E. White, A.J. Creely, M.J. Greenwald, N.T. Howard, F. Sciortino, and J.C. Wright. VITALS: A Surrogate-Based Optimization Framework for the Accelerated Validation of Plasma Transport Codes. *Fusion Science and Technology*, 74(1-2):65–76, 2018.

[131] K. Kanaya and S. Okayama. Penetration and energy-loss theory of electrons in solid targets. *Journal of Physics D: Applied Physics*, 5(1):43, 1972.

[132] J.C. Wesley, A.W. Hyatt, E.J. Strait, D.P. Schissel, S.M. Flanagan, T.C. Hender, P.C. DeVries, M. Johnson, R. Martin, Y. Gribov, M. Sugihara, E. J. Fredrickson, D.A. Gates, J. Menard, R.S. Granetz, Y. Kawano, J. Lister, and G. Pautasso. *Disruption characterization and database activities for ITER*. IAEA, International Atomic Energy Agency (IAEA), 2007.

[133] C.R. Sovinec, A.H. Glasser, T.A. Gianakon, D.C. Barnes, R.A. Nebel, S.E. Kruger, S.J. Plimpton, A. Tarditi, M.S. Chu, and the NIMROD Team. Nonlinear magnetohydrodynamics with high-order

finite elements. *J. Comp. Phys.*, 195:355, 2004.
[134] J.D. Jackson. *Classical electrodynamics*. John Wiley & Sons, 3 edition, 1999.
[135] V. L. Ginzburg and S. I. Syrovatskii. Developments in the theory of synchrotron radiation and its reabsorption. *Annual Review of Astronomy and Astrophysics*, 7(1):375–420, 1969.
[136] G.G. Stokes. On the composition and resolution of streams of polarized light from different sources. *Transactions of the Cambridge Philosophical Society*, 9:399, 1851.
[137] A. A. Korchakov and S. I. Syrovatskii. Polarization of radiation and the structure of magnetic fields in cosmic sources of radiation. *Soviet Astronomy*, 5:678, 1962.
[138] J.M. Stone. *Radiation and optics: an introduction to classical theory*. McGraw-Hill, 1963.
[139] J. Korger, T. Kolb, P. Banzer, A. Aiello, C. Wittmann, C. Marquardt, and G. Leuchs. The polarization properties of a tilted polarizer. *Optics Express*, 21(22):27032–27042, 2013.